Numerical stability and reduced order chemistry modeling in detonation simulations

Thesis by
Alexandra Baumgart

In Partial Fulfillment of the Requirements for the
Degree of
Doctor of Philosophy

Caltech

CALIFORNIA INSTITUTE OF TECHNOLOGY
Pasadena, California

2025
Defended July 9, 2024

Alexandra Baumgart
ORCID: 0000-0001-8575-3404

ACKNOWLEDGEMENTS

First, I would like to thank my advisor, Professor Guillaume Blanquart, for his endless guidance, support, and enthusiasm throughout my PhD. This work would not have been possible without our many detailed discussions and your seemingly infinite supply of ideas when my simulations kept breaking. Thank you for believing in my research the many times I did not. I would also like to thank my committee members, Professors Tim Colonius, Joanna Austin, and Melany Hunt, for their valuable insights and feedback to improve this thesis.

The Department of Energy Computational Science Graduate Fellowship provided funding and numerous opportunities throughout my PhD. It has been a privilege to be a part of the fellowship program for the past four years.

I would like to thank the past and present members of The FORCE. My experience at Caltech would not have been the same without my officemates, Matthew Yao, Alex Carroll, Liam Heidt, and Aaron Nelson. Your encouragement and willingness to talk through research difficulties is always appreciated. Thank you for convincing me to take breaks to get food, and for all the shenanigans and laughter, especially when I was stressed out about paper revisions. I will miss our late night discussions about side projects none of us have time for (yet). I would also like to thank Guillaume Beardsell for helping me get started on research during my first year.

Others at Caltech have been a great source of support. I would like to thank my friends from the first year MCE office, in particular Rachel Zhou, Stephanie O'Gara, Tracy Lu, and Emily de Jong. Thank you for helping me survive first year (and the pandemic that came with), for the potlucks and hotpot nights, and for all the adventures around LA and elsewhere in California. I would also like to thank the talented musicians of the Caltech Wind Orchestra and Orchestra for providing me with a much needed musical outlet throughout the past five years.

I would like to thank my friends from before Caltech, including my college friends, Emily Weerakkody, Maya D'Souza, Kyla Swain, and Stephanie Sokolyk; and my elementary school friends, Morgan Whitecotton, Emma Boehm, and Lindsey Dzierozynski. Thank you for keeping in touch over the years, I miss you all. Even if infrequent, I always enjoy our phone/video calls and visits.

Finally, I would like to thank my family. My parents have always encouraged me to try anything and everything that interested me, and have been there for every

achievement along the way. Thank you for checking in weekly on Zoom, for all your visits to California, and for the many home-baked goods sent around birthdays, holidays, and exams. My sister, Stephanie, made sure I started learning from day one, reading me books and teaching me all of the dinosaurs. Thank you for encouraging me to start pursuing research opportunities as a clueless undergrad. Watching your academic career has pushed me to do my best, and you set the standard high; I'm glad we have reached an agreement to stop going after more degrees now. To my grandparents, aunts, uncles, and cousins: thank you for always making my visits home for the holidays special. I would not have gotten here without the constant love and support of my family.

ABSTRACT

The coupling between shocks and chemistry in detonations poses a challenge for simulations. In this thesis, a simulation framework is developed to address key components of detonation modeling: numerical stability of shocks and discontinuities, and computational efficiency in chemistry modeling.

To ensure numerical stability in the vicinity of shocks, a variety of methods have been used, including shock-capturing schemes such as weighted essentially non-oscillatory (WENO) schemes, as well as the addition of artificial diffusivities to the governing equations. In this work, all necessary viscous/diffusion terms are derived from first principles, and the performance of these analytical terms is demonstrated within a centered differencing framework. The physical Euler equations are spatially-filtered with a Gaussian-like filter. Sub-filter scale (SFS) terms arise in the momentum and energy equations. Analytical closure is provided for each of them by leveraging the jump conditions for a shock. No SFS terms are present in the continuity or species equations. For contact discontinuities, the analytical SFS terms are identically zero. However, numerically, the transport of a contact discontinuity may result in artificial oscillations due to dispersive errors. To treat contact discontinuities, a WENO-like correction term is applied to the enthalpy transport. Implemented within a centered difference code, this filtered framework performs well for a range of shock-dominated flows without introducing excessive diffusion. In addition to providing new insight into the placement and form of required diffusion terms in the governing equations, this framework is general and may be used with any numerical scheme.

Chemistry modeling in detonations typically relies on two broad approaches: simplified models with one- or two-step chemistry, and detailed chemistry. These approaches require choosing between computational efficiency or physical accuracy. In detailed chemistry simulations, there are physical constraints that must be met when transporting species mass fractions; nonlinear transport schemes such as WENO do not satisfy these constraints automatically. A new method is presented to ensure that the sum of mass fractions equals 1, without penalizing inert species. The approach is better able to capture the physical instability expected for detonations. To reduce the cost of chemistry while maintaining accurate physics, tabulated chemistry has been used extensively for flames/deflagrations in the low Mach number framework. In the simplest tabulated chemistry model for premixed flames, a progress variable, describing the progress of reactions in the system, is transported in the simulation. This progress variable is then used to look up all other species, transport properties, and thermodynamic variables from a pre-computed table. Unfortunately, there is no existing tabulation approach designed specifically for detonations. As such, this work extends the tabulated chemistry method to detonations. To describe the enthalpy and specific heat capacity, the temperature is selected as a second table coordinate. The two table coordinates are able to capture virtually all variations in the progress variable source term. The Zel'dovich-von Neumann-Döring (ZND) model is found to be the most appropriate one-dimensional problem for generation of the table. The ZND tabulation approach is validated for both one-dimensional stable and pulsating and two-dimensional regular and irregular detonations in various hydrogen-oxygen mixtures. The tabulated chemistry simulations are able to reproduce the detailed chemistry results in terms of propagation speed, cellular structures, and source term statistics at a reduced computational cost, demonstrating the benefits of this approach for predictive modeling of detonations.

PUBLISHED CONTENT AND CONTRIBUTIONS

[1] A. Baumgart, G. Beardsell, and G. Blanquart. “Analytical closure to the spatially-filtered Euler equations for shock-dominated flows”. In: *Journal of Computational Physics* 477 (2023), p. 111946. DOI: `https://doi.org/10.1016/j.jcp.2023.111946`.
The author of this thesis developed and implemented the framework, performed all simulations, analyzed the data, made the figures, and wrote the manuscript.

[2] A. Baumgart and G. Blanquart. “A numerical extension of the spatially-filtered Euler equations for contact discontinuities”. In: *Journal of Computational Physics* 491 (2023), p. 112353. DOI: `https://doi.org/10.1016/j.jcp.2023.112353`.
The author of this thesis developed and implemented the method, performed all simulations, analyzed the data, made the figures, and wrote the manuscript.

[3] A. Baumgart and G. Blanquart. “Ensuring $\sum_s Y_s = 1$ in transport of species mass fractions”. In: *Journal of Computational Physics* (2024), p. 113199. DOI: `https://doi.org/10.1016/j.jcp.2024.113199`.
The author of this thesis developed and implemented the method, performed all simulations, analyzed the data, made the figures, and wrote the manuscript.

[4] A. Baumgart, M. X. Yao, and G. Blanquart. “Tabulated chemistry approach for detonation simuations”. In: *Combustion and Flame* (2024). (Under Review).
The author of this thesis developed and implemented the method, performed all simulations, analyzed the data, made the figures, and wrote the manuscript.

TABLE OF CONTENTS

LIST OF ILLUSTRATIONS

LIST OF TABLES

Chapter 1

INTRODUCTION

1.1 Background and motivation

1.1.1 Safety and propulsion

History has seen numerous catastrophes involving accidental detonations. In 2001, leaking ammonium nitrate caused an explosion at the AZote Fertilisant (AZF) chemical plant in France [1]. In 2011 at the Fukushima Daiichi Nuclear Plant, leaking hydrogen gas reacted with oxygen in the air, causing a detonation [2]. Many coal mines have exploded worldwide, as recently as December 2018 in the Czech Republic, in which methane gas and coal dust ignited [3]. In the U.S. alone, there have been hundreds of coal mine explosions since the 1800s [4]. Detonations will always be a safety risk, even though newer energy sources are replacing earlier combustion methods.

Recently, detonations have been explored as an innovative means for energy generation. Detonation engines offer the potential for greatly increased engine efficiency compared to the standard gas turbine engines used in many power and propulsion applications [5, 6]. While gas turbine engines typically rely on the Brayton thermodynamic cycle, switching to a detonation cycle could substantially increase the efficiency. Without the use of a compressor, the Brayton cycle has an efficiency of 0%, whereas detonations are nearly constant volume processes and produce much higher pressures, achieving an efficiency of about 25% [7]. Unfortunately, the same factors that make detonations more efficient (e.g., higher pressures), also make detonation-based engines challenging to design.

Simulations can play an essential role in understanding the conditions that lead to unwanted detonations (deflagration-to-detonation transition, [8, 9]), and can also aid in the development of technologies such as detonation engines [10] by supplementing experimental studies [11, 12]. Simulating these large scale applications necessitates models that accurately capture the inherent structure of detonations in a computationally efficient manner.

1.1.2 Detonation structure

In one dimension, the detonation wave structure can be described by the Zel'dovich-von Neumann-Döring (ZND) model [13–15], in which the post-shock flow consists of a thermoneutral induction zone followed by an exothermic reaction zone. The structure is illustrated in Fig. 1.1 for a detonation wave propagating to the left. The lead shock travels at the Chapman-Jouguet [16, 17] speed (u_{CJ}), heating and compressing the unburnt reactant gases (H_2 and O_2, for hydrogen combustion). In the induction zone (with length $\mathcal{L}$), initial radicals are formed while the thermodynamic state remains approximately constant. This is followed by the reaction zone, where products (H_2O) are formed and heat is released; it is accompanied by an increase in temperature and a decrease in the pressure (and density).

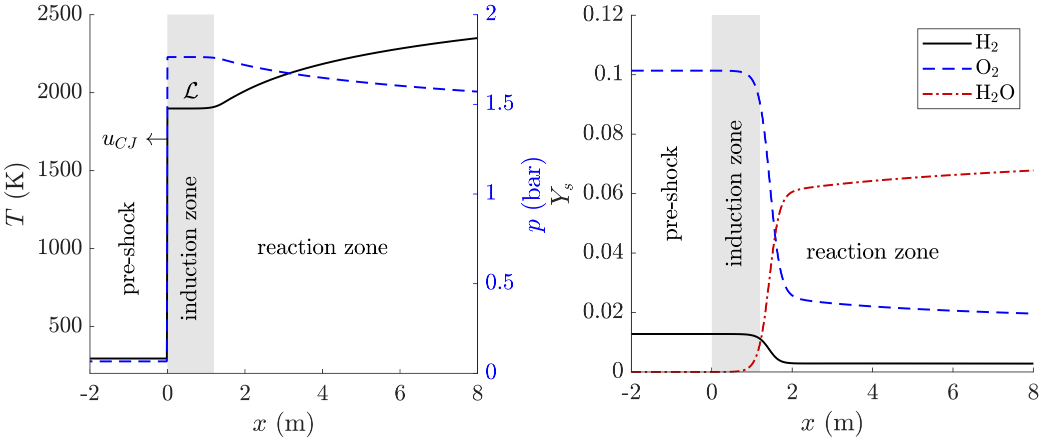

(a) Thermodynamic variables.

(b) Species mass fractions.

Figure 1.1: ZND structure. Temperature (black solid line), pressure (blue dashed line) (a); mass fractions of H_2 (black solid line), O_2 (blue dashed line), H_2O (red dash-dotted line) (b). Induction zone indicated by gray shaded region; shock is at $x = 0$. $2H_2$-O_2-$7Ar$.

In multi-dimensional detonations, the structure is further complicated by the presence of transverse shocks, resulting in substantial variation in the thermodynamic conditions along the unsteady detonation wave front. Figure 1.2 shows an example of the numerical schlieren (density gradient magnitude) for a two-dimensional detonation. Comparing the primary shock front (largest density gradient) with the location of the reaction zone (approximated by the contour of Y_{H_2O}), the induction zone length varies along the detonation front. In portions of the front where the shock is locally propagating above the CJ speed (overdriven), the post-shock temperature and pressure are higher, increasing the reaction rates and shortening the induction length; in regions where the shock is locally underdriven, the reaction rates are smaller and the induction zone lengthens. These regions of locally shorter/longer induction zone lengths are separated by triple point collisions, consisting of the incident shock (locally underdriven), Mach stem (locally overdriven), and transverse waves. Vorticity generated at the triple points propagates into the wake. In three dimensions, there are two sets of transverse waves (oscillating in the *y* and *z* directions, for a detonation propagating in *x*), resulting in an even more complex flow field.

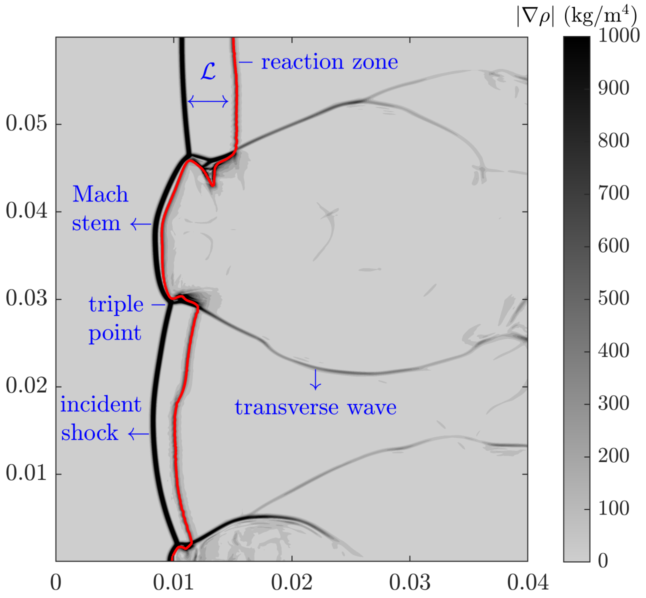

Figure 1.2: Two-dimensional detonation front. Numerical schlieren and contour at half the maximum H_2O mass fraction (red solid line). $2H_2$-O_2-$5.6N_2$.

Experiments provide crucial contributions to our understanding of the structure and dynamics of detonations. However, there are limitations on the data that can be measured. In contrast, simulations provide access to every flow variable at every grid point and time step, increasing the amount of information available. Unfortunately, due to the complex interactions between shock waves and chemical reactions, there are a number of numerical and modeling challenges associated with multi-dimensional detonation simulations. These challenges are the reasons for any observed discrepancies between simulation results and experimental observations [18, 19]. Addressing these challenges is the focus of this thesis. Methods for ensuring the numerical stability of shocks are reviewed in Sec. 1.2. Numerical errors associated with species transport are discussed in Sec. 1.3. Sections 1.4 and 1.5 review strategies for chemistry modeling.

1.2 Numerical treatment of shocks and discontinuities

The Euler equations admit solutions with two different types of discontinuities: shocks and contact discontinuities. These discontinuities are often treated *together* in numerical simulations, with the primary focus on ensuring stable simulations. These approaches may be classified broadly as either shock-capturing numerical schemes or the addition of artificial viscosity/diffusivity.

Essentially non-oscillatory (ENO) and weighted ENO (WENO) schemes are widely used shock-capturing methods [20, 21]. ENO schemes prevent oscillations around shocks by using an adaptive stencil based on the local flow conditions. Near shocks, this stencil is chosen to produce a smooth solution. In WENO schemes, a weighted combination of stencils is used, rather than selecting a single stencil at a given location. While robust, these shock-capturing schemes tend to be dissipative of quantities important for turbulence simulation [22]. Simulations with a combination of shocks and turbulence often rely on a hybrid approach, switching between WENO schemes in the vicinity of discontinuities and high-order accurate centered difference schemes in smooth regions [23]. Such hybrid methods require a shock sensor. However, designing a sensor effective for a variety of problems is challenging [22]. Recent work has explored the use of neural networks for optimizing WENO coefficients to switch effectively between smooth and discontinuous regions [24]. In application to contact discontinuities, shock-capturing schemes tend to smear the discontinuity over time [25]. As such, methods have been developed to sharpen contact discontinuities including subcell resolution [26], artificial compression [27], and anti-diffusive flux corrections [28].

An alternative method, artificial viscosity/diffusivity, eliminates the need for a hybrid scheme and shock sensor, allowing high-order accurate schemes to be used throughout the domain. Artificial viscosity was first introduced by von Neumann and Richtmyer as a method for numerical shock calculations [29]. The addition of artificial viscosity smears the shock such that it can be resolved on a numerical grid using standard finite difference procedures. This approach has been developed and applied to a variety of problems. Based on local flow conditions, artificial shear viscosity, bulk viscosity, conductivity, and/or species diffusivity are computed. For example, to regularize the Euler equations, Cook and Cabot used an artificial viscosity of the form

$$\mu = C_\mu \rho (\Delta x)^{r+1} \overline{\left| \frac{\partial^r u}{\partial x^r} \right|}, \tag{1.1}$$

where C_μ is a constant, ρ is the density, Δx is the grid spacing, r is an integer, u is the velocity, and $\overline{\cdot}$ is a Gaussian filter [30]. This artificial viscosity appears in both the momentum and energy equations. Fiorina and Lele used a similar form to define an artificial viscosity (μ) and an artificial diffusivity (χ_ρ, χ_Y), the latter of which is based on the entropy gradient. Artificial dissipation terms were included in all governing equations, including continuity [31]. Cook extended the artificial viscosity approach in [30] to the full Navier-Stokes equations by introducing artificial shear viscosity (μ^*), artificial bulk viscosity (β^*), artificial conductivity (κ^*), and artificial species diffusivity (D_i^*) [32]. The artificial viscosities, conductivity, and species diffusivities were based on the local gradients of the strain rate tensor, internal energy, and species mass fractions, respectively. These artificial properties are added to the corresponding physical properties wherever they appear in the Navier-Stokes equations. Later, Kawai and Lele generalized the Localized Artificial Diffusivity (LAD) approach to treat shocks and discontinuities on curvilinear and anisotropic meshes [33]. The artificial properties μ^*, β^*, κ^*, and D_k^* introduced by Cook [32] were reformulated for a multi-dimensional generalized coordinate system. Mani et al. demonstrated the benefits of using dilatation instead of the strain rate to define an artificial bulk viscosity [34]. Kawai et al. examined the effects of LAD on simulations of compressible turbulence [35]. The artificial shear viscosity μ^* and artificial conductivity κ^* are the same as those introduced by Cook [32], while the artificial bulk viscosity β^* is based on the dilatation, as recommended by Mani et al. [34]. The addition of switching functions to the definition of the artificial bulk viscosity is found to improve performance away from shocks in regions of weakly compressible turbulence. Finally, Lee and Lele later investigated the application of LAD to reacting flows, including deflagrations and detonations [36].

The previously mentioned LAD studies focused on structured high-order finite difference codes [30–36]. More recent work has extended the use of artificial viscosity to unstructured grids. Premasuthan et al. extended the approach to spectral difference methods with unstructured quadrilateral grids [37]. In line with [34–36], the artificial shear viscosity μ_Δ, artificial bulk viscosity β_Δ, and artificial conductivity κ_Δ are based on the local gradients of the magnitude of the strain rate tensor, dilatation, and internal energy, respectively. It was found that smoothing the artificial viscosity profiles led to more robust performance. Further improvements were made by combining artificial viscosity with local mesh refinement [38]. Haga and Kawai later extended the LAD approach to high-order flux reconstruction methods for unstructured quadrilateral and hexahedral grids [39].

The artificial bulk viscosity β^* and artificial mass diffusivity α^* are based on the local gradients of the dilatation and density, respectively.

As with the shock-capturing schemes, the use of LAD has proven successful for a range of problems and numerical frameworks [30–39]. However, as demonstrated by the above examples summarized in Table 1.1, there is no consistent placement of artificial viscous/diffusion terms in the governing equations. The specific forms of the terms are also arbitrary. Although the physical dimensions of the artificial diffusion terms are consistent with the governing equations, the order of derivatives used as well as the quantities used (i.e. magnitude of strain rate tensor vs. dilatation) varies. Furthermore, all of these artificial diffusivities require the tuning of coefficients to apply a sufficient amount of artificial diffusion.

	Mass	Momentum	Energy	Species
Cook and Cabot [30]	—	μ	μ	—
Cook [32]	—	μ^*, β^*	μ^*, β^*, κ^*	D_i^*
Fiorina and Lele [31]	χ_ρ	μ	μ	χ_Y
Kawai and Lele [33]	—	μ^*, β^*	μ^*, β^*, κ^*	D_k^*
Premasuthan et al. [37]	—	μ_Δ, β_Δ	μ_Δ, β_Δ, κ_Δ	—
Lee and Lele [36]	—	μ^*, β^*	μ^*, β^*, κ^*, D_k^*	D_k^*
Haga and Kawai [39]	α^*	β^*	β^*	—

Table 1.1: Placement of artificial properties in the governing equations.

Most existing shock-capturing and artificial diffusivity methods are *numerical* approaches to spreading the shock interface. Shocks are typically idealized as discontinuities, as their inherent thickness, of the order of a few mean free paths, is much smaller than any practical grid resolution. As a result, the smallest scale feature in the flow—the shock—is not resolved. This is analogous to Large Eddy Simulation (LES), in which the smallest scale features are not resolved but are modeled instead by sub-filter scale (SFS) terms [40, 41]. Adams and Stolz first introduced the idea of exploiting the mathematical framework of LES for shock-capturing, using an approximate deconvolution approach to develop a subgrid-scale model [42, 43]. More recently, Sousa and Scalo explored the mathematical similarity with SFS closure models for LES and proposed closure expressions for both shock-dominated and turbulent flows [44, 45]. While promising, neither the Quasi-Spectral Viscosity model [44], nor the Legendre Spectral Viscosity model [45] leveraged any knowledge of the theoretical shock jump conditions, and the inclusion of an additional explicit filtering operation was found beneficial in attenuating spurious high wavenumber oscillations.

1.3 Numerical transport of species

Reacting flow simulations often require the transport of several species mass fractions. Unfortunately, the solutions of the discretized species equations do not always meet key physical constraints: namely, each mass fraction must be bounded between 0 and 1, and the sum of mass fractions must be equal to 1. First order linear schemes such as upwind meet these constraints, but are too dissipative. High order linear schemes (e.g., QUICK [46]) ensure the sum of mass fractions equals 1, but are not bounded. Nonlinear schemes such as weighted essentially non-oscillatory (WENO) schemes are often preferred for their high order accuracy and non-oscillatory property. However, the sum of mass fractions is not guaranteed to equal 1.

A variety of approaches have been used to address this challenge [47–50]. In detailed chemistry simulations, often $N - 1$ out of the N species equations are transported, with the last inert species being computed to maintain a sum equal to 1 [47]. Alternatively, the mass fractions may be renormalized after computing the reconstruction at the faces [48]. Algorithms have been derived to satisfy both physical constraints [49, 50], although the conditions are scheme-dependent and do not extend easily to multiple dimensions.

1.4 Detonation chemistry modeling

As the chemistry influences the propagation and structure of detonations, detonation simulations require chemical models that are both physically accurate and computationally efficient. Current chemistry modeling approaches for detonations span a range of complexity, from simplified one-step models to detailed chemical mechanisms, resulting in a trade-off between accuracy and efficiency.

The most comprehensive approach considered here, detailed chemistry, requires a separate transport equation for each species. By retaining information about all intermediate species and reactions, this modeling approach is able to reproduce key behavior [19, 51]. For example, detailed chemistry is able to predict quenching limits consistent with experiments [19]. These predictions are possible despite uncertainties in the individual reaction rate constants and neglect of vibrational non-equilibrium effects, both of which may explain discrepancies between detailed chemistry calculations and experimental cell sizes [52, 53]. Unfortunately, detailed chemistry is computationally expensive, and large scale simulations may be impractical. Even the simplest fuel, hydrogen, involves the transport of nine species [54]. For complex hydrocarbon fuels, detailed chemical mechanisms may include tens to hundreds of species [55, 56]. To reduce the cost associated with detailed chemistry, in situ adaptive tabulation (ISAT) has been applied to detonation simulations, tabulating the chemical source terms instead of integrating the stiff ordinary differential equations [57, 58]. Although the evaluation of source terms is accelerated, all chemical species must still be transported throughout the simulation.

At the opposite end, one-step chemistry is a computationally inexpensive method in which a single reaction converts reactants to products. This method uses an Arrhenius-type global reaction to describe the reaction rate, and one transport equation is required for the mass fraction of the reactant [59, 60]. This simplified approach allows for the simulation of complex flow configurations such as deflagration-to-detonation transition (DDT) [8] and detonation-turbulence interaction [61]. Recent work has focused on optimizing the parameters in the Arrhenius reaction expression to reproduce key flame and detonation properties for simulations of DDT [62–64]. Although this inexpensive approach can reliably produce the correct detonation propagation speeds, transient behavior such as quenching limits [19] and re-initiation [65] cannot be reproduced.

The cost of detailed chemistry and the shortcomings of one-step chemistry have led to the development of other simplified models. The detonation structure, consisting of an induction zone followed by a reaction zone, led to the development of the induction parameter model [66]. This model incorporates the induction time of the mixture, delaying the energy release until after the induction period ends. This model has been used for both fundamental studies of detonations [67] as well as larger scale applications such as rotating detonation engine (RDE) simulations [10]. In all cases, the induction parameter must be transported in the simulation; in some simulations [10], the reactant density is also transported.

More complex models describe the reaction process in more detail, using two transport equations to track the chemistry [68–74]. The first step is a thermoneutral induction period, corresponding to chain initiation, chain branching reactions, and the formation of radicals. The second step is an exothermic reaction period, corresponding to chain termination, recombination reactions, and the formation of products. In addition to the induction parameter, a reaction progress variable is transported in the simulation to describe the second reaction step [70–74]. The exothermic reaction rate often takes on an Arrhenius form [69, 71, 73, 74].

To capture additional physics, skeletal chemical models have been developed. For hydrocarbon-air detonations, a two-step approach requires transporting seven species [75]. Three-step mechanisms further split the chemical process into chain-initiation, chain-branching, and termination steps [19, 76]. However, the three-step mechanisms produce weaker transverse waves, larger instantaneous flow structures, and different quenching limits compared to detailed mechanisms. For simulations involving the re-initiation of detonations in ethylene-oxygen mixtures, four-step mechanisms have been used [65, 77]. In such cases, mechanisms with less than four steps were found to be insufficient to reproduce the transverse waves that drive the re-initiation process. As more steps are included, more chemical species need to be included, and the computational cost increases.

1.5 Tabulated chemistry

Tabulated chemistry and flamelet-based methods are commonly used to reduce the cost of low Mach flame simulations without sacrificing the physics [78–80]. In this approach, a progress variable, C, is defined to track the evolution of chemical processes in the simulation. The transport equation for the progress variable is given by

$$\frac{\partial(\rho C)}{\partial t} + \frac{\partial(\rho u_i C)}{\partial x_i} = \frac{\partial}{\partial x_i}\left(\rho D \frac{\partial C}{\partial x_i}\right) + \dot{\omega}_C, \tag{1.2}$$

where ρ is the density, u is the velocity, D is the diffusivity, and $\dot{\omega}_C$ is the progress variable source term. The species mass fractions, transport properties, and thermodynamic variables are tabulated as a function of the progress variable. One-dimensional flamelets are used to pre-compute the information required by the table. This is the simplest model for a premixed flame; other table coordinates may be included in addition to the progress variable. For example, the unburned gas temperature [81] or mixture fraction [80] may be used to describe variations in enthalpy or local equivalence ratio, respectively.

Recent efforts have explored methods of incorporating compressibility effects into the tabulated chemistry approach [82–85]. A challenge common to the various methods is the inconsistency of the thermodynamics between the simulation and the table. In low Mach simulations, there is no need to solve the energy equation, and the temperature is simply an output of the chemistry table. However, in compressible simulations, the temperature must be consistent with the transported energy and the equation of state. In premixed flames, to account for deviations of the transported energy from the tabulated energy, Vicquelin et al. [83] relied on a first-order Taylor expansion to estimate the real temperature from the transported energy (e), tabulated energy ($e_0(C)$), and tabulated temperature ($T_0(C)$),

$$T = T_0(C) + \frac{e - e_0(C)}{c_{v,0}(C)}. \tag{1.3}$$

This expansion is only valid for small temperature and pressure variations, as applicable for acoustics. In non-premixed flames, Oevermann [82] and Saghafian et al. [84] proposed an extension of tabulated chemistry for supersonic combustion. As in [83], they assumed frozen chemistry and included an analytical correction of the tabulated temperature based on the transported and tabulated energies. This compressible formulation has been applied to subsonic flames [86], scramjet [82, 87], and other non-premixed supersonic combustion configurations [84, 88]. More recently, Cisneros-Garibay and Mueller [85] used an iterative approach to solve for the temperature and enforce the consistency between the transported energy and tabulated energy. Within this iterative approach, they solve on the fly the low Mach flamelet equations for all necessary tabulated quantities. As with [84], this iterative method was demonstrated for non-premixed supersonic combustion. While this approach can be adapted to multimodal or premixed combustion, the use of flamelets restricts the framework to the deflagration burning regime. Shunn et al. [89] recently applied the compressible flamelet/progress variable approach of Saghafian et al. to the large eddy simulation of a rotating detonation engine. Although their corrections to the progress variable source term are informed by ZND solutions, their approach still relies on premixed flamelets as the baseline solution. Unfortunately, there is no existing tabulation approach specifically designed for detonations. The application of flamelet-based tabulation to detonations has limited validation; it is unclear if such an approach can reproduce key detonation dynamics, including propagation speeds, the onset of one-dimensional instabilities, and the two-dimensional cell structure.

1.6 Objectives and outline

The goal of this thesis is to develop a modeling framework for detonations that balances numerical stability, physical accuracy, and computational efficiency. Overall, the focus is on two challenges in detonation modeling: shocks and chemistry. The specific objectives are:

- Develop a mathematical and numerical framework to ensure the numerical stability of shocks and contact discontinuities;

- Demonstrate the developed framework in a finite difference solver with a centered spatial discretization, discretely conservative of kinetic energy;
- Improve the physical accuracy and numerical stability of species transport in detailed chemistry simulations;
- Reduce the computational cost of the chemistry in detonations by developing a new tabulated chemistry model;
- Understand the impacts of both the numerics (SFS, species transport) and chemistry model (detailed vs. tabulated) on the detonation physics.

This thesis is organized as follows. Chapters 2-3 focus primarily on non-reacting flows with shocks and discontinuities. In Chapter 2, SFS viscous and diffusion terms are derived from first principles by filtering the Euler equations. The SFS terms are closed analytically by leveraging the shock jump conditions. The resulting mathematical framework is demonstrated for shock-dominated flows. Chapter 3 describes a numerical treatment of the spatially-filtered Euler equations to minimize oscillations when simulating contact discontinuities. The remaining chapters focus on detonations. Chapter 4 presents a new method for correcting the WENO-interpolated mass fractions such that inert species do not change. The tabulated chemistry method is extended to detonations in Chapter 5. Finally, Chapter 6 discusses the influence of the modeling framework on various aspects of the physics in detonations.

Chapter 2

ANALYTICAL CLOSURE TO THE SPATIALLY-FILTERED EULER EQUATIONS FOR SHOCK-DOMINATED FLOWS

[1] A. Baumgart, G. Beardsell, and G. Blanquart. “Analytical closure to the spatially-filtered Euler equations for shock-dominated flows”. In: *Journal of Computational Physics* 477 (2023), p. 111946. DOI: `https://doi.org/10.1016/j.jcp.2023.111946`.

The first objective of this chapter is to derive sub-filter scale (SFS) viscous and diffusion terms by filtering the Euler equations. An analytical closure is provided by leveraging the theoretical shock jump conditions. The filtering procedure will identify unequivocally the placement, form, and magnitude of the required terms. Second, this mathematical framework will be demonstrated numerically using a finite difference solver with a centered spatial discretization. Such schemes are typically avoided for simulations of shock-dominated flows, for they lead to oscillations without adequate diffusion. For this reason, they are the ideal candidate to verify that the analytical diffusion terms are both necessary and sufficient. These simulations will also underscore that the diffusion terms are independent of the numerical scheme.

In Sec. 2.1, analytical SFS diffusion terms are derived for a shock. Sec. 2.2 introduces the numerical methodology. The approach is tested for an assortment of problems in Sec. 2.3-2.5. In Sec. 2.6, the SFS viscosity is compared with Localized Artificial Diffusivity (LAD), and the benefits and limitations of the SFS approach are discussed. A discussion of the so-called “sonic glitch” is included in Sec. 2.7.

2.1 Analytical framework

In this section, the derivation and closure of the SFS terms are presented. The results are independent of any spatial discretization.

2.1.1 Spatial filtering

In their strong form, the Euler equations do not admit solutions that exhibit discontinuities. That is why we consider instead the weak form. More precisely, the equations are filtered, following the same procedure used for LES of compressible flows [40, 41, 90, 91]. In one dimension, filtered variables are defined as

$$\overline{\phi}(x) = \int \phi(x')G(x - x')dx', \tag{2.1}$$

where ϕ is some physical quantity, G is the filter kernel, and the limits of integration span the physical domain. The Favre (density-weighted) average is

$$\tilde{\phi}(x) = \frac{\overline{\rho\phi}}{\overline{\rho}}, \tag{2.2}$$

where ρ is the density.

The unfiltered normal shock profile can be described by

$$\phi(x) = \phi_1 + (\phi_2 - \phi_1)H(x), \tag{2.3}$$

where subscript 1 refers to the pre-shock state, subscript 2 refers to the post-shock state, and $H(x)$ is the unit step (Heaviside) function. The filtered and Favre-averaged shock profiles take the forms

$$\overline{\phi}(x) = \phi_1 + (\phi_2 - \phi_1)\alpha(x) \tag{2.4}$$

and

$$\tilde{\phi}(x) = \frac{\overline{\rho\phi}}{\rho_1 + (\rho_2 - \rho_1)\alpha(x)}, \tag{2.5}$$

respectively. For a Gaussian filter kernel,

$$\alpha(x) = \frac{1}{2}\left(1 + \operatorname{erf}\left(\sqrt{\frac{6}{\delta^2}}x\right)\right), \tag{2.6}$$

$$\alpha(x) \approx \frac{1}{2}\left(1 + \tanh\left(\frac{x}{\Delta}\right)\right), \tag{2.7}$$

where δ is the Gaussian filter width, and $\Delta = \frac{1}{2}\sqrt{\frac{\pi}{6}}\delta$ is the tanh filter width. The relation between δ and Δ ensures that the erf and tanh profiles have matching slopes at $x = 0$. As shown in Fig. 2.1 for a Mach 2 density jump, the erf and tanh functions are virtually identical.

The original, unfiltered governing equations for mass, momentum, energy, and species are given by

$$\frac{\partial \rho}{\partial t} + \frac{\partial}{\partial x_i}(\rho u_i) = 0, \tag{2.8}$$

$$\frac{\partial(\rho u_i)}{\partial t} + \frac{\partial}{\partial x_j}(\rho u_i u_j) = -\frac{\partial p}{\partial x_i}, \tag{2.9}$$

$$\frac{\partial(\rho e_t)}{\partial t} + \frac{\partial}{\partial x_i}(\rho u_i h_t) = -\frac{\partial q_i}{\partial x_i}, \tag{2.10}$$

$$\frac{\partial}{\partial t}(\rho Y_s) + \frac{\partial}{\partial x_i}(\rho u_i Y_s) = -\frac{\partial j_{i,s}}{\partial x_i} + \dot{\omega}_s, \tag{2.11}$$

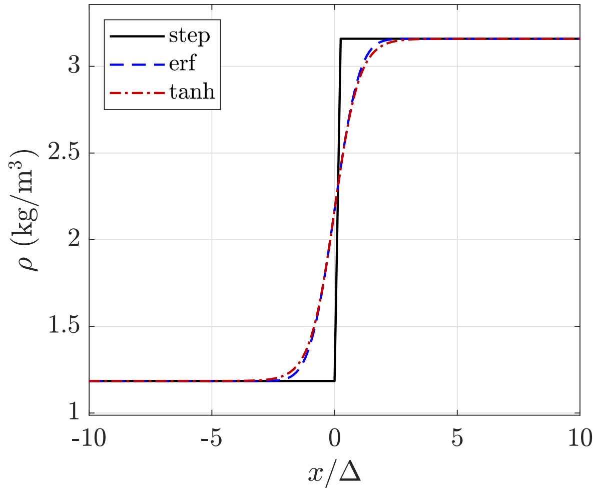

Figure 2.1: Unfiltered (black solid line) and filtered density profile for a Mach 2 shock obtained using Eq. (2.6) (blue dashed line) and Eq. (2.7) (red dash-dotted line).

where u is the velocity, p is the pressure, e_t is the total energy, h_t is the total enthalpy, q is the heat flux, Y_s is the mass fraction, j_s is the species diffusion flux, $\dot{\omega}_s$ is the chemical source term, and the subscript s indicates the species index. The total energy and total enthalpy are given by

$$e_t = e + \frac{1}{2}u_i^2, \tag{2.12}$$

$$h_t = h + \frac{1}{2}u_i^2, \tag{2.13}$$

where e is the specific internal energy, and h is the specific enthalpy. The internal energy and enthalpy are related by

$$h = e + p/\rho. \tag{2.14}$$

The heat flux and species diffusion flux are given by

$$q_i = -\lambda\frac{\partial T}{\partial x_i} + \sum_s h_s j_{i,s} \quad \text{and} \quad j_{i,s} = -\rho Y_s\left(\frac{D_s}{X_s}\frac{\partial X_s}{\partial x_i} + u_{i,c}\right), \tag{2.15}$$

where λ is the conductivity, h_s is the species enthalpy, D_s is the species diffusivity, X_s is the species mole fraction, and u_c is the correction velocity to ensure mass conservation. The system of equations is closed with the ideal gas law,

$$p = \rho RT/W, \tag{2.16}$$

where R is the universal gas constant, and W is the mixture molecular weight.

After filtering, the equations become

$$\frac{\partial \overline{\rho}}{\partial t} + \frac{\partial}{\partial x_i}(\overline{\rho}\tilde{u}_i) = 0, \tag{2.17}$$

$$\frac{\partial}{\partial t}(\overline{\rho}\tilde{u}_i) + \frac{\partial}{\partial x_j}(\overline{\rho}\tilde{u}_i\tilde{u}_j) = -\frac{\partial \overline{p}}{\partial x_i} + \frac{\partial}{\partial x_j}(\overline{\rho}\tilde{u}_i\tilde{u}_j - \overline{\rho u_i u_j}), \tag{2.18}$$

$$\frac{\partial(\overline{\rho}\tilde{e}_t)}{\partial t} + \frac{\partial}{\partial x_i}(\overline{\rho}\tilde{u}_i\tilde{h}_t) = -\frac{\partial \overline{q}_j}{\partial x_i} + \frac{\partial}{\partial x_i}\left(\overline{\rho}\tilde{u}_i\tilde{h}_t - \overline{\rho u_i h_t}\right), \tag{2.19}$$

$$\frac{\partial}{\partial t}(\overline{\rho}\tilde{Y}_s) + \frac{\partial}{\partial x_i}(\overline{\rho}\tilde{u}_i\tilde{Y}_s) = -\frac{\partial \overline{j}_{i,s}}{\partial x_i} + \frac{\partial}{\partial x_i}\left(\overline{\rho}\tilde{u}_i\tilde{Y}_s - \overline{\rho u_i Y_s}\right) + \overline{\dot{\omega}}_s, \tag{2.20}$$

where some variables (e.g. $\overline{\rho}$) appear as Reynolds-averages and other variables (e.g. $\tilde{u}_i$) appear as Favre-averages. Other formulations such as the Reynolds-filtered framework may lead to different closures [92]; however, this is not the focus of the present work. The forms of Eq. (2.17) to (2.20) are standard for LES of reacting, compressible flows. There are no additional terms in the continuity equation (Eq. (2.17)). For Eq. (2.18) to (2.20), the following terms appear and require closure:

$$\tau_{ij,SFS} = \overline{\rho}\tilde{u}_i\tilde{u}_j - \overline{\rho u_i u_j}, \tag{2.21}$$

$$q_{i,SFS} = \overline{\rho}\tilde{u}_i\tilde{h}_t - \overline{\rho u_i h_t}, \tag{2.22}$$

$$j_{i,SFS} = \overline{\rho}\tilde{u}_i\tilde{Y}_s - \overline{\rho u_i Y_s}. \tag{2.23}$$

These SFS terms are discussed in Sec. 2.1.2 for momentum, Sec. 2.1.3 for energy, and Sec. 2.1.4 for species. Closures are developed for two discontinuities of interest: contact discontinuities and shocks.

2.1.2 Momentum equation

2.1.2.1 One-dimensional closure

In one dimension, the SFS term in the momentum equation is

$$\tau_{SFS} = \overline{\rho}\tilde{u}\tilde{u} - \overline{\rho u u} = \overline{\rho}(\tilde{u}\tilde{u} - \widetilde{uu}). \tag{2.24}$$

Across a contact discontinuity, u is constant, so $\tilde{u}\tilde{u}$ and $\widetilde{uu}$ are equal and therefore $\tau_{SFS} = 0$. In other words, no SFS terms are necessary in the momentum equation for a contact discontinuity. For a shock in the shock-fixed frame, ρu ($= \overline{\rho}\tilde{u} = \rho_1 u_1 = \rho_2 u_2$) is constant, so the SFS term can be written equivalently as

$$\tau_{SFS} = \overline{\rho}\tilde{u}\tilde{u} - \overline{\rho u u} = \overline{\rho}\tilde{u}(\tilde{u} - \overline{u}). \tag{2.25}$$

Because u is not constant across the shock, $\tilde{u}$ and $\overline{u}$ are not equal. So, the τ_{SFS} is nonzero.

Using the filtered and Favre-averaged shock profiles from Eq. (2.4) and (2.5), the SFS term becomes

$$\begin{aligned}\tau_{SFS} &= \overline{\rho}\tilde{u}\left(\frac{\rho_1 u_1}{\overline{\rho}} - [u_1 + (u_2 - u_1)\alpha]\right) \\ &= \overline{\rho}\tilde{u}\left(\frac{\alpha(1-\alpha)}{\overline{\rho}}(2\rho_1 u_1 - \rho_1 u_2 - \rho_2 u_1)\right) \\ &= (\rho_2 - \rho_1)(u_2 - u_1)\tilde{u}\alpha(1-\alpha). \end{aligned} \tag{2.26}$$

For the tanh function (Eq. (2.7)), the following expression holds analytically,

$$\alpha(1-\alpha) = \frac{1}{4}\left(1 - \tanh^2\left(\frac{x}{\Delta}\right)\right) = \frac{\Delta}{2}\frac{\partial \alpha}{\partial x}. \tag{2.27}$$

Following the approximation of erf by tanh, τ_{SFS} becomes

$$\tau_{SFS} \approx (\rho_2 - \rho_1)(u_2 - u_1)\tilde{u}\frac{\Delta}{2}\frac{\partial \alpha}{\partial x}. \tag{2.28}$$

Finally, writing $\frac{\partial \alpha}{\partial x}$ in terms of $\frac{\partial \tilde{u}}{\partial x}$ using Eq. (2.4) and (2.5),

$$\frac{\partial \alpha}{\partial x} = -\frac{\rho_1 u_1}{\rho_2 - \rho_1}\frac{1}{\tilde{u}^2}\frac{\partial \tilde{u}}{\partial x}, \tag{2.29}$$

the resulting momentum SFS term for a normal shock is

$$\begin{aligned}\tau_{SFS} &\approx -\frac{\rho_1 u_1}{\rho_2 - \rho_1}\frac{1}{\tilde{u}}(\rho_2 - \rho_1)(u_2 - u_1)\frac{\Delta}{2}\frac{\partial \tilde{u}}{\partial x} \\ &\approx \overline{\rho}(u_1 - u_2)\frac{\Delta}{2}\frac{\partial \tilde{u}}{\partial x}. \end{aligned} \tag{2.30}$$

In other words, the SFS term takes the form of the velocity divergence. Because the SFS term depends on velocity differences and velocity gradients, the model is Galilean invariant and may be applied to both steady and unsteady shocks. In Eq. (2.30), the units of $\overline{\rho}(u_1 - u_2)\frac{\Delta}{2}$ are kg·(m·s)$^{-1}$, corresponding to those of dynamic viscosity. Even though it was derived specifically for a shock, this SFS viscosity is consistent with the closure obtained for a contact discontinuity (as $u_1 = u_2$), $\tau_{SFS} = 0$. As such, the expression will be used for both shocks and contact discontinuities. The only approximation used to derive Eq. (2.30) is the similarity between the erf and tanh function.

2.1.2.2 Multi-dimensional closure

To extend this to two dimensions, Eq. (2.21) may be written in normal-tangential $(n - t)$ coordinates as

$$\boldsymbol{\tau}_{SFS} = \begin{bmatrix} \overline{\rho}\tilde{u}_n\tilde{u}_n - \overline{\rho u_n u_n} & \overline{\rho}\tilde{u}_n\tilde{u}_t - \overline{\rho u_n u_t} \\ \overline{\rho}\tilde{u}_t\tilde{u}_n - \overline{\rho u_t u_n} & \overline{\rho}\tilde{u}_t\tilde{u}_t - \overline{\rho u_t u_t} \end{bmatrix}. \tag{2.31}$$

Across an oblique shock, both ρu_n and u_t are constant, so

$$\tau_{nn,SFS} = \overline{\rho}\tilde{u}_n(\tilde{u}_n - \overline{u}_n), \tag{2.32}$$

$$\tau_{nt,SFS} = \tau_{tn,SFS} = \overline{\rho}\tilde{u}_n(\tilde{u}_t - \overline{u}_t) = 0, \tag{2.33}$$

$$\tau_{tt,SFS} = \overline{\rho}(\tilde{u}_t\tilde{u}_t - \widetilde{u_t u_t}) = 0. \tag{2.34}$$

By the same procedure used to obtain Eq. (2.30), the two-dimensional SFS term in the momentum equation is

$$\boldsymbol{\tau}_{SFS} \approx \begin{bmatrix} \overline{\rho}(u_{1n} - u_{2n})\frac{\Delta}{2}\frac{\partial \tilde{u}_n}{\partial n} & 0 \\ 0 & 0 \end{bmatrix}. \tag{2.35}$$

However, implementing the SFS term in normal-tangential coordinates is not convenient in practice, particularly when multiple shock angles are present in the domain. To identify SFS shear and bulk viscosities that may be used independent of the simulation coordinate system, Eq. (2.35) is compared to the physical viscous stress tensor,

$$\tau_{ij} = \mu\left(\frac{\partial \tilde{u}_i}{\partial x_j} + \frac{\partial \tilde{u}_j}{\partial x_i} - \frac{2}{3}\frac{\partial \tilde{u}_k}{\partial x_k}\delta_{ij}\right) + \kappa\frac{\partial \tilde{u}_k}{\partial x_k}\delta_{ij}, \tag{2.36}$$

where μ and κ are the dynamic and bulk viscosities, respectively. The normal-tangential components of the physical stress tensor are

$$\tau_{nn} = 2\mu\left(\frac{\partial \tilde{u}_n}{\partial n} - \frac{1}{3}\left(\frac{\partial \tilde{u}_n}{\partial n} + \frac{\partial \tilde{u}_t}{\partial t}\right)\right) + \kappa\left(\frac{\partial \tilde{u}_n}{\partial n} + \frac{\partial \tilde{u}_t}{\partial t}\right), \tag{2.37}$$

$$\tau_{nt} = \tau_{tn} = \mu\left(\frac{\partial \tilde{u}_n}{\partial t} + \frac{\partial \tilde{u}_t}{\partial n}\right), \tag{2.38}$$

$$\tau_{tt} = 2\mu\left(\frac{\partial \tilde{u}_t}{\partial t} - \frac{1}{3}\left(\frac{\partial \tilde{u}_n}{\partial n} + \frac{\partial \tilde{u}_t}{\partial t}\right)\right) + \kappa\left(\frac{\partial \tilde{u}_n}{\partial n} + \frac{\partial \tilde{u}_t}{\partial t}\right). \tag{2.39}$$

For an oblique (not curved) shock, u_t is constant and $\frac{\partial}{\partial t} = 0$, so the components of τ are simplified to

$$\tau_{nn} = \left(\kappa + \frac{4}{3}\mu\right)\frac{\partial \tilde{u}_n}{\partial n}, \tag{2.40}$$

$$\tau_{nt} = \tau_{tn} = 0, \tag{2.41}$$

$$\tau_{tt} = \left(\kappa - \frac{2}{3}\mu\right)\frac{\partial \tilde{u}_n}{\partial n}. \tag{2.42}$$

To extract expressions for SFS viscosities, the components of the SFS stress tensor in Eq. (2.35) can be matched with those in Eq. (2.40) and (2.42) such that

$$\tau_{nn,SFS} = \overline{\rho}(u_{1n} - u_{2n})\frac{\Delta}{2}\frac{\partial \tilde{u}_n}{\partial n} = \left(\kappa_{SFS} + \frac{4}{3}\mu_{SFS}\right)\frac{\partial \tilde{u}_n}{\partial n}, \tag{2.43}$$

$$\tau_{tt,SFS} = 0 = \left(\kappa_{SFS} - \frac{2}{3}\mu_{SFS}\right)\frac{\partial \tilde{u}_n}{\partial n}, \tag{2.44}$$

resulting in the SFS dynamic and bulk viscosities,

$$\mu_{SFS} = \overline{\rho}(u_{1n} - u_{2n})\frac{\Delta}{4}, \tag{2.45}$$

$$\kappa_{SFS} = \overline{\rho}(u_{1n} - u_{2n})\frac{\Delta}{6}. \tag{2.46}$$

In Cartesian $(x - y)$ coordinates, the SFS stress tensor components are then

$$\tau_{xx,SFS} = 2\mu_{SFS}\left(\frac{\partial \tilde{u}}{\partial x} - \frac{1}{3}\left(\frac{\partial \tilde{u}}{\partial x} + \frac{\partial \tilde{v}}{\partial y}\right)\right) + \kappa_{SFS}\left(\frac{\partial \tilde{u}}{\partial x} + \frac{\partial \tilde{v}}{\partial y}\right) = \overline{\rho}(u_{1n} - u_{2n})\frac{\Delta}{2}\frac{\partial \tilde{u}}{\partial x}, \tag{2.47}$$

$$\tau_{xy,SFS} = \tau_{yx,SFS} = \mu_{SFS}\left(\frac{\partial \tilde{u}}{\partial y} + \frac{\partial \tilde{v}}{\partial x}\right) = \overline{\rho}(u_{1n} - u_{2n})\frac{\Delta}{4}\left(\frac{\partial \tilde{u}}{\partial y} + \frac{\partial \tilde{v}}{\partial x}\right), \tag{2.48}$$

$$\tau_{yy,SFS} = 2\mu_{SFS}\left(\frac{\partial \tilde{v}}{\partial y} - \frac{1}{3}\left(\frac{\partial \tilde{u}}{\partial x} + \frac{\partial \tilde{v}}{\partial y}\right)\right) + \kappa_{SFS}\left(\frac{\partial \tilde{u}}{\partial x} + \frac{\partial \tilde{v}}{\partial y}\right) = \overline{\rho}(u_{1n} - u_{2n})\frac{\Delta}{2}\frac{\partial \tilde{v}}{\partial y}. \tag{2.49}$$

As expected, the 2D τ_{SFS} simplifies to Eq. (2.30) in the limit of a normal shock.

2.1.3 Energy equation

In one dimension, the SFS term in the energy equation is

$$q_{SFS} = \overline{\rho}\tilde{u}\tilde{h}_t - \overline{\rho u h_t}. \tag{2.50}$$

For the contact discontinuity, it is convenient to use $h_t = c_p T + \frac{1}{2}u^2$, splitting Eq. (2.50) into a SFS conduction term and a SFS viscous dissipation term,

$$q_{SFS} = q_{SFS,c} + q_{SFS,v} = \left(\overline{\rho}\tilde{u}\widetilde{c_p T} - \overline{\rho u c_p T}\right) + \left(\frac{1}{2}\overline{\rho}\tilde{u}\widetilde{u^2} - \frac{1}{2}\overline{\rho u u^2}\right). \tag{2.51}$$

Approximating the specific heat capacity c_p to be constant, and because $u = \tilde{u} = \overline{u}$ across the contact discontinuity,

$$q_{SFS,c} = u c_p(\overline{\rho}\tilde{T} - \overline{\rho T}) = 0, \tag{2.52}$$

$$q_{SFS,v} = \frac{1}{2}u^3(\overline{\rho} - \overline{\rho}) = 0. \tag{2.53}$$

In other words, the SFS heat flux term is zero for a contact discontinuity.

For a shock in the shock-fixed frame, both ρu and h_t are constant, so Eq. (2.50) simplifies to

$$q_{SFS} = 0. \tag{2.54}$$

Alternatively, rather than assuming h_t in Eq. (2.50) is a constant, the two SFS terms in Eq. (2.51) can be rewritten as

$$\begin{aligned} q_{SFS,c} &= \overline{\rho}\tilde{u}c_p(\tilde{T} - \overline{T}), && (2.55)\\ q_{SFS,v} &= \frac{1}{2}\overline{\rho}\tilde{u}\left(\widetilde{u^2} - \overline{u^2}\right), && (2.56)\end{aligned}$$

again assuming constant c_p and ρu. First, looking at the SFS conduction term, the filtered and Favre-averaged shock profiles lead to

$$\begin{aligned} q_{SFS,c} &= \overline{\rho}\tilde{u}c_p(\tilde{T} - \overline{T}) \\ &= \overline{\rho}\tilde{u}c_p\left(\frac{\overline{p}}{\overline{\rho}R/W} - [T_1 + (T_2 - T_1)\alpha]\right) \\ &= \overline{\rho}\tilde{u}c_p\left(\frac{\alpha(1-\alpha)}{\overline{\rho}}(\rho_2 - \rho_1)(T_2 - T_1)\right) \\ &\approx \tilde{u}c_p(\rho_2 - \rho_1)(T_2 - T_1)\frac{\Delta}{2}\frac{\partial \alpha}{\partial x}. \end{aligned} \tag{2.57}$$

Writing $\frac{\partial \alpha}{\partial x}$ in terms of $\frac{\partial \tilde{T}}{\partial x}$,

$$\begin{aligned} \frac{\partial \alpha}{\partial x} &= \frac{\overline{\rho}^2 R/W}{\rho_1 p_2 - \rho_2 p_1}\frac{\partial \tilde{T}}{\partial x} \\ &= \frac{\overline{\rho}^2}{\rho_1\rho_2 T_2 - \rho_2\rho_1 T_1}\frac{\partial \tilde{T}}{\partial x}, \end{aligned} \tag{2.58}$$

and the resulting SFS conduction term is

$$\begin{aligned} q_{SFS,c} &\approx \frac{\overline{\rho}^2}{\rho_1\rho_2(T_2 - T_1)}\tilde{u}c_p(\rho_2 - \rho_1)(T_2 - T_1)\frac{\Delta}{2}\frac{\partial \tilde{T}}{\partial x} \\ &\approx \frac{\overline{\rho}^2 c_p\tilde{u}(\rho_2 - \rho_1)}{\rho_1\rho_2}\frac{\Delta}{2}\frac{\partial \tilde{T}}{\partial x} \\ &\approx \frac{\overline{\rho}^2 c_p\tilde{u}(u_1 - u_2)}{\overline{\rho}\tilde{u}}\frac{\Delta}{2}\frac{\partial \tilde{T}}{\partial x} \\ &\approx \overline{\rho}c_p(u_1 - u_2)\frac{\Delta}{2}\frac{\partial \tilde{T}}{\partial x}, \end{aligned} \tag{2.59}$$

showing that the SFS conductivity, like the SFS viscosity, is proportional to the jump in velocity across the shock.

Using the filtered and Favre-averaged shock profiles, the viscous dissipation term is

$$q_{SFS,v} = \frac{1}{2}\overline{\rho}\tilde{u}\left(\widetilde{u^2} - \overline{u^2}\right) \approx \frac{\tilde{u}}{2}(\rho_2 - \rho_1)(u_2^2 - u_1^2)\frac{\Delta}{2}\frac{\partial \alpha}{\partial x}. \tag{2.60}$$

Writing $\frac{\partial \alpha}{\partial x}$ in terms of $\frac{\partial}{\partial x}\left(\widetilde{u^2}\right)$,

$$\frac{\partial \alpha}{\partial x} = \frac{\overline{\rho}^2}{\rho_1 u_1(\rho_1 u_2 - \rho_2 u_1)}\frac{\partial}{\partial x}\left(\widetilde{u^2}\right), \tag{2.61}$$

and the resulting SFS viscous dissipation term is

$$\begin{aligned} q_{SFS,v} &\approx \frac{\overline{\rho}^2}{\rho_1 u_1(\rho_1 u_2 - \rho_2 u_1)}\frac{\tilde{u}}{2}(\rho_2 - \rho_1)(u_2^2 - u_1^2)\frac{\Delta}{2}\frac{\partial}{\partial x}\left(\widetilde{u^2}\right) \\ &\approx \overline{\rho}(u_1 - u_2)\frac{\Delta}{4}\frac{\partial}{\partial x}\left(\widetilde{u^2}\right). \end{aligned} \tag{2.62}$$

This equation involves $\widetilde{u^2}$, theoretically an unclosed term.

Alternatively, and to be consistent with the momentum equation, the SFS viscous dissipation term may be derived using τ_{SFS} directly, such that

$$\begin{aligned} q_{SFS,v} &\approx \tau_{SFS} \cdot \tilde{u} \\ &\approx \left(\overline{\rho}(u_1 - u_2)\frac{\Delta}{2}\frac{\partial \tilde{u}}{\partial x}\right) \cdot \tilde{u}. \end{aligned} \tag{2.63}$$

Rearranging, the term becomes

$$q_{SFS,v} \approx \overline{\rho}(u_1 - u_2)\frac{\Delta}{4}\frac{\partial \tilde{u}^2}{\partial x}. \tag{2.64}$$

The expressions for $q_{SFS,v}$ in Eq. (2.62) and (2.64) are similar, the only difference being that the former has a derivative of $\widetilde{u^2}$ while the latter has a derivative of $\tilde{u}^2$. Because $\tilde{u}^2$ does not require additional closure, Eq. (2.64) is more practical to implement. This leads to a SFS viscous dissipation error,

$$q_{SFS,v,err} = \overline{\rho}(u_1 - u_2)\frac{\Delta}{4}\frac{\partial}{\partial x}\left(\widetilde{u^2} - \tilde{u}^2\right). \tag{2.65}$$

The SFS conduction term (Eq. (2.59)), the SFS viscous dissipation term (Eq. (2.64)), and the SFS viscous dissipation error (Eq. (2.65)) are all shown in Fig. 2.2 for a Mach 2 shock, using the analytically filtered profiles. The SFS conduction and SFS viscous dissipation counteract each other, and the SFS error term is negligible.

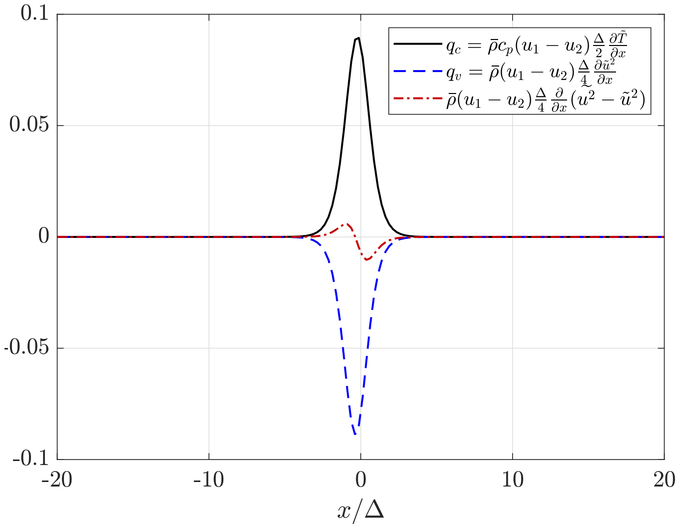

Figure 2.2: SFS flux terms in the energy equation obtained from the analytically filtered profiles for a Mach 2 shock, normalized by the constant $\rho u h_t$. SFS conduction term (Eq. (2.59), black solid line), SFS viscous dissipation term (Eq. (2.64), blue dashed line), and SFS viscous dissipation error (Eq. (2.65), red dash-dotted line).

In two dimensions, the SFS stress tensor is used such that

$$\mathbf{q}_{SFS,v} \approx \begin{bmatrix} \tau_{xx,SFS} & \tau_{xy,SFS} \\ \tau_{yx,SFS} & \tau_{yy,SFS} \end{bmatrix} \begin{bmatrix} u \\ v \end{bmatrix}, \tag{2.66}$$

resulting in the components

$$q_{x,SFS,v} \approx \overline{\rho}(u_{1n} - u_{2n}) \frac{\Delta}{4} \left(\frac{\partial}{\partial x} \left(\tilde{u}^2 + \frac{1}{2}\tilde{v}^2 \right) + \tilde{v} \frac{\partial \tilde{u}}{\partial y} \right), \tag{2.67}$$

$$q_{y,SFS,v} \approx \overline{\rho}(u_{1n} - u_{2n}) \frac{\Delta}{4} \left(\frac{\partial}{\partial y} \left(\frac{1}{2}\tilde{u}^2 + \tilde{v}^2 \right) + \tilde{u} \frac{\partial \tilde{v}}{\partial x} \right). \tag{2.68}$$

In summary, analytically, there are two possible models for the SFS term in the energy equation: $q_{SFS} = 0$ (Eq. (2.54), considering total enthalpy) and $q_{SFS} = q_{SFS,c} + q_{SFS,v}$ (Eq. (2.59) and (2.64), considering enthalpy and kinetic energy separately). Both options will be tested for a variety of shock conditions.

2.1.4 Species equation

The one-dimensional SFS term in the species equation is given by

$$j_{SFS} = \overline{\rho}\tilde{u}\tilde{Y}_s - \overline{\rho u Y_s}. \tag{2.69}$$

Again using $u = \tilde{u} = \overline{u}$ for the contact discontinuity,

$$j_{SFS} = u(\overline{\rho}\tilde{Y}_s - \overline{\rho Y_s}) = 0. \tag{2.70}$$

The shock is assumed to be thin enough that no chemical reactions take place within the shock, such that $Y_s = \tilde{Y}_s = \overline{Y}_s$ and therefore

$$j_{SFS} = \overline{\rho}\tilde{u}(\tilde{Y}_s - \overline{Y}_s) = 0. \tag{2.71}$$

In summary, for the species equation and potentially for the energy equation (depending on the model used), no analytical SFS diffusion terms are required for contact discontinuities or shocks. The reason why a SFS term is present in the momentum equation only is the phenomenon of wave front sharpening. While such phenomenon may arise numerically for temperature and species, it does not come from the analytical equations.

2.1.5 Equation of state

The filtered equation of state (Eq. (2.16)) is

$$\overline{p} = \overline{\rho RT/W} = \overline{\rho}\widetilde{RT/W}. \tag{2.72}$$

As in Sec. 2.1.4, we assume there are no chemical reactions occurring within the shock, and therefore both R and W are constant across the shock. The filtered pressure becomes

$$\overline{p} = \overline{\rho}\tilde{T}R\widetilde{\left(\frac{1}{W}\right)}, \tag{2.73}$$

with

$$\widetilde{\left(\frac{1}{W}\right)} = \sum_{s=1}^{n_s}\frac{\tilde{Y}_s}{W_s}, \tag{2.74}$$

so the ideal gas equation of state is still valid for the filtered quantities. The above expression is also valid through contact discontinuities due to temperature and species discontinuities.

In the governing Eq. (2.17)-(2.20), the quantities solved for are $\overline{\rho}$, $\overline{\rho}\tilde{u}$, $\overline{\rho}\tilde{e}_t$, and $\overline{\rho}\tilde{Y}_s$; the temperature is not solved for directly. Instead, Newton's method is used to solve the equation

$$\tilde{T}_{m+1} = \tilde{T}_m + \left(\frac{\overline{\rho}R\tilde{T}_m}{W} - \left(\overline{\rho}\sum_{s=1}^{n_s}\tilde{h}_s(\tilde{T}_m)\tilde{Y}_s - \overline{\rho}\tilde{e}_t + \frac{1}{2}\overline{\rho}\tilde{u}\tilde{u}\right)\right) \Bigg/ \left(\overline{\rho}\sum_{s=1}^{n_s}c_{v,s}(\tilde{T}_m)\tilde{Y}_s\right), \tag{2.75}$$

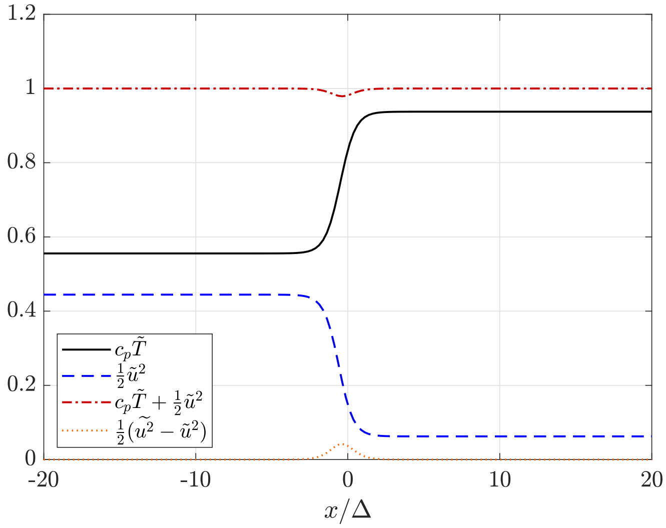

Figure 2.3: Convected quantities in the energy equation for a Mach 2 shock, normalized by the total enthalpy h_t. Enthalpy (black solid line), kinetic energy using $\tilde{u}^2$ (blue dashed line), sum of enthalpy and kinetic energy using $\tilde{u}^2$(red dash-dotted line), and error in filtered kinetic energy (orange dotted line).

where $c_{v,s}$ is the species heat capacity at constant volume and m is the iteration number. Once $\tilde{T}_{m+1}$ is converged, the pressure is computed using the ideal gas law.

A small error is introduced when using the above expression. As discussed previously in Sec. 2.1.3, the filtered total enthalpy ($\tilde{h}_t$) should be a constant through a shock. As shown in Fig. 2.3 for a Mach 2 shock, the increase in $c_p\tilde{T}$ is compensated by the decrease in $\frac{1}{2}\tilde{u}^2$. However, the transported quantity is $\frac{1}{2}\tilde{u}^2$ and not $\frac{1}{2}\widetilde{u^2}$. This approximation introduces a small error that is negligible compared to the total enthalpy.

2.1.6 Entropy equation

For a pure gas, it is common to evaluate entropy from the transported thermodynamic variables using [22, 93]

$$s = c_v \ln \overline{p} - c_p \ln \overline{\rho}. \tag{2.76}$$

This is equivalent to the entropy as defined by the thermodynamic relation (Gibbs equation)

$$\begin{aligned} d\tilde{e} &= \tilde{T} ds - \overline{p} d\tilde{v} \\ &= \tilde{T} ds - \frac{\overline{p}}{\overline{\rho}^2} d\overline{\rho}, \end{aligned} \tag{2.77}$$

where $\tilde{v}$ is the Favre-averaged specific volume. Rearranging the terms, recasting the total derivatives as partial derivatives, and using continuity, in one dimension this leads to

$$\frac{\partial}{\partial t}(\overline{\rho}s) + \frac{\partial}{\partial x}(\overline{\rho}\tilde{u}s) = \frac{1}{\tilde{T}}\left(\frac{\partial}{\partial t}(\overline{\rho}\tilde{e}) + \frac{\partial}{\partial x}(\overline{\rho}\tilde{u}\tilde{e}) + \overline{p}\frac{\partial \tilde{u}}{\partial x}\right). \tag{2.78}$$

The transport equation for $\overline{\rho}\tilde{e}$ may be obtained by subtracting the kinetic energy equation (product of $\tilde{u}$ and the filtered momentum equation) from the filtered energy equation, such that

$$\frac{\partial}{\partial t}(\overline{\rho}\tilde{e}) + \frac{\partial}{\partial x}(\overline{\rho}\tilde{u}\tilde{e}) = \frac{\partial}{\partial x}\left(\lambda_{SFS}\frac{\partial \tilde{T}}{\partial x}\right) + (\tau_{SFS} - \overline{p})\frac{\partial \tilde{u}}{\partial x}, \tag{2.79}$$

where λ_{SFS} is the SFS conductivity corresponding to Eq. (2.59) and τ_{SFS} is the SFS stress given by Eq. (2.30). Combining Eq. (2.78) and (2.79), we obtain

$$\frac{\partial}{\partial t}(\overline{\rho}s) + \frac{\partial}{\partial x}(\overline{\rho}\tilde{u}s) = \frac{1}{\tilde{T}}\left(\frac{\partial}{\partial x}\left(\lambda_{SFS}\frac{\partial \tilde{T}}{\partial x}\right) + \tau_{SFS}\frac{\partial \tilde{u}}{\partial x}\right). \tag{2.80}$$

The entropy profile for a steady shock, shown in Fig. 2.4a, is computed using a high resolution numerical solution ($M = 2$ and $\Delta/\Delta x = 16$ from Sec. 2.3.3). The entropy is smooth and not monotonic, reaching a peak in the middle of the shock. This behavior has been observed previously for viscous shock layers with resolution smaller than the mean free path [93]. The entropy peak will be visible in the solution to the Shu-Osher problem in Sec. 2.4. This evolution is a result of the two source terms in Eq. (2.80). Examining the entropy budget in Fig. 2.4b, the viscous term is always positive while the conduction term has both positive and negative regions. Together, the SFS terms balance the convective term. If the scaling or ratio of the SFS viscosity and SFS conductivity were altered, the SFS terms would no longer balance the convective term, leading to a source or sink of entropy. Furthermore, including additional diffusion terms elsewhere in the governing equations may disrupt the entropy balance (e.g., inclusion of a mass diffusivity in continuity [31, 39]; see Table 1.1).

2.2 Numerical methods

In the previous section, no assumptions were made about either the grid spacing (Δx) or the discretization of spatial derivatives. The analytical SFS terms are general and can be used with any spatial discretization. The numerical discretization used for the validation test cases (to be presented in Sec. 2.3-2.5) is reviewed in this section first.

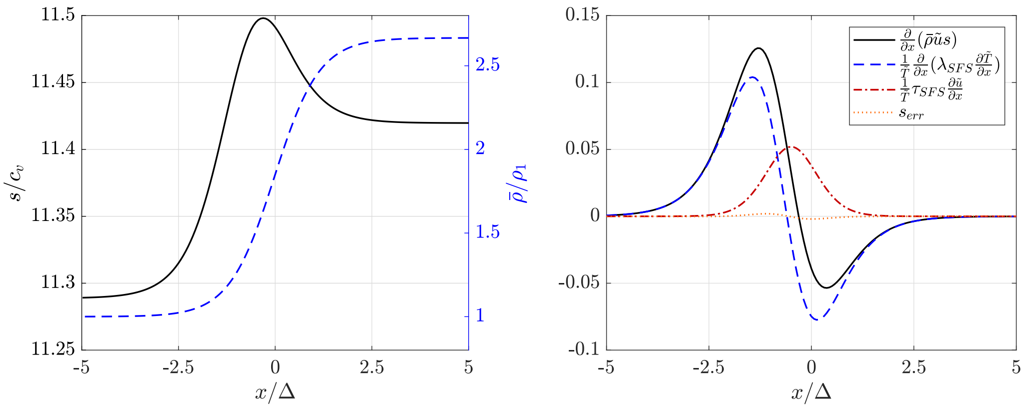

(a) Entropy and density.

(b) Entropy budget.

Figure 2.4: Nondimensional entropy (black solid line) and density (blue dashed line) profiles (left). Balance of terms in the entropy transport equation: convective term (black solid line), SFS conduction term (blue dashed line), SFS viscous term (red dash-dotted line), and the error (orange dotted line), all nondimensionalized by the constant $\overline{\rho}\tilde{u}c_v/\Delta$ (right).

Simulations are performed using the compressible formulation [94] of the conservative finite difference solver NGA [95]. The reader is referred to [95] for a complete description of the spatial discretization (common to the low Mach and compressible formulations) and to [94] for the time integration (specific to the compressible formulation). Only a brief overview will be provided here. A uniform Cartesian grid is used, with variables staggered such that all scalar quantities are stored at the cell centers and vector components are stored at the cell faces, as shown in Fig. 2.5. Second-order accurate interpolation and differentiation operators are defined by

$$\overline{\phi}^x = \frac{\phi(x+\Delta x/2, y, z) + \phi(x-\Delta x/2, y, z)}{2}, \tag{2.81}$$

$$\left.\frac{\partial \phi}{\partial x}\right|_x = \frac{\phi(x+\Delta x/2, y, z) - \phi(x-\Delta x/2, y, z)}{\Delta x}, \tag{2.82}$$

respectively, for a quantity ϕ. For instance, the discretized continuity equation takes the form

$$\frac{\partial \rho}{\partial t} + \sum_{i=1}^{3} \frac{\partial g_i}{\partial x_i} = 0, \tag{2.83}$$

where $g_i = \rho u_i$, consistent with the low Mach number formulation. The discretization for the momentum equation also matches that of [95]. Differences in the discretization specific to the compressible formulation of the code are described in [94]. Second-order accurate operators are used to discretize all convective, viscous, and diffusive terms in the governing equations.

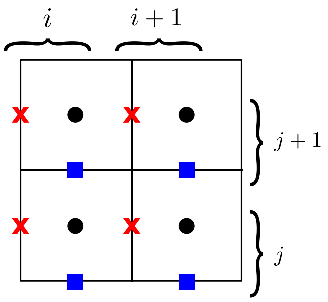

Figure 2.5: Two-dimensional staggered grid (adapted from [94]); black circles indicate scalar quantities, and vector quantities are marked by red crosses and blue squares for the x- and y-components, respectively.

The NGA code was demonstrated to discretely conserve kinetic energy by Desjardins et al. [95]. The non-dissipative nature of the discretization is an important property for simulations involving turbulence and remains true for the present compressible formulation. However, the code does not discretely conserve total enthalpy. Computing the kinetic energy at the cell centers requires interpolations, while the enthalpy h is already cell-centered; this discrepancy leads to an error in h_t in the vicinity of shocks. As a consequence, it is expected that the energy equation will require some diffusion to achieve numerical stability without changing the underlying discretization of the code. For this reason, the SFS energy model given by Eq. (2.59) and (2.64) may be more robust against the code's discretization.

The explicit RK4 scheme is used for the time integration of the equations for ρ, ρu, ρe_t, and ρY_s. A semi-implicit RK4 method may be used to advance the species mass fractions to reduce chemistry constraints on the timestep [94]. However, here the timestep is restricted most by the shock velocity, not the chemistry, so the explicit RK4 is used for all transported quantities.

2.3 Results of steady normal shock tests

The first flow configuration tested is a steady normal shock, with shock Mach numbers ranging from $M_1 = 1.01$ to $M_1 = 20$. For all Mach numbers tested, the pre-shock conditions are $T_1 = 298$ K and $p_1 = 101325$ Pa. The initial profiles are given by Eq. (2.4), (2.5), and (2.7), using the Rankine-Hugoniot jump conditions with $\gamma = 1.4$ to calculate the post-shock conditions. The inflow uses Dirichlet boundary conditions set to the pre-shock values, with an inflow velocity u_1 set to the shock speed to ensure that the shock location is fixed. The outflow uses Navier-Stokes Characteristic Boundary Conditions (NSCBCs) [96, 97]. The domain length is $L = 1$ mm. A filter width of $\Delta = 1 \cdot 10^{-6}$ m is used along with three different grid resolutions: $\Delta/\Delta x = 1, 2$, and 4. The total simulation time is $2 \cdot 10^{-6}$ s, allowing the simulation to reach a stationary state. The timestep is given by a maximum CFL of 0.8. All the simulations reach a stationary state and did not exhibit the 1D carbuncle effect observed in [98].

2.3.1 Moderate and strong normal shocks

Results for a Mach 2 shock are shown in Fig. 2.6 to compare the performance of the two SFS models for the energy equation. Using the SFS term based on total enthalpy ($q_{SFS} = 0$, Eq. (2.54)) leads to severe cell-to-cell oscillations. A steady solution could not be reached for shock Mach numbers 5 and higher.

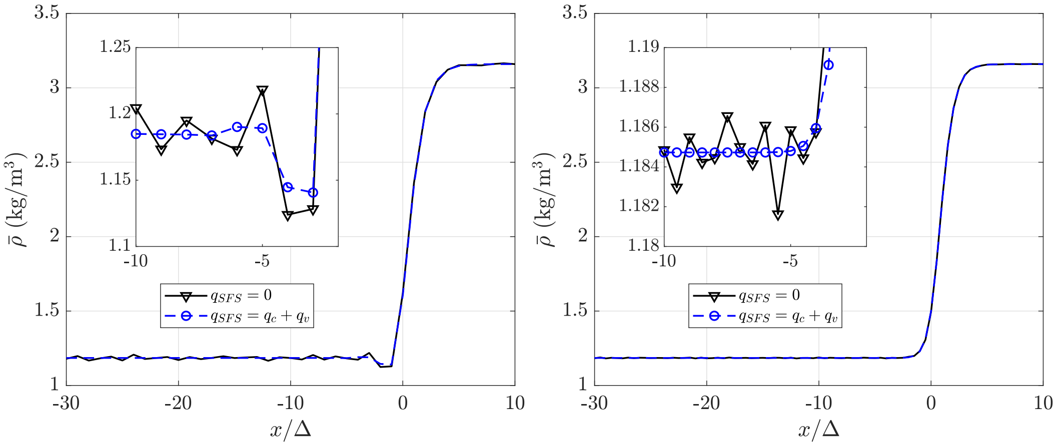

(a) $\Delta/\Delta x = 1$.

(b) $\Delta/\Delta x = 2$.

Figure 2.6: Density profiles for a Mach 2 shock with two different grid resolutions: $\Delta/\Delta x = 1$ (left) and $\Delta/\Delta x = 2$ (right). Comparison of using $q_{SFS} = 0$ (black solid line and triangles) and $q_{SFS} = q_c + q_v$ (blue dashed line and circles). The insets show the oscillations just before the shock.

The SFS term that acts as a combination of conduction and viscous dissipation ($q_{SFS} = q_c + q_v$, Eq. (2.59) and (2.64)) leads to stable simulations for all shock Mach numbers tested. For a grid resolution $\Delta/\Delta x = 1$ (shown in Fig. 2.6a), cell-to-cell oscillations are present, as shown in the inset. These cell-to-cell oscillations are observed to have a wavelength of $2\Delta x$ for Mach numbers 2 and higher (see Fig. 2.7). Therefore, using a filter width/resolution ratio of $\Delta/\Delta x = 2$ filters over these cell-to-cell oscillations.

To compare the simulation shock profiles to the analytically filtered profile, the shock thicknesses are evaluated to quantify the amount the shock is spread. The

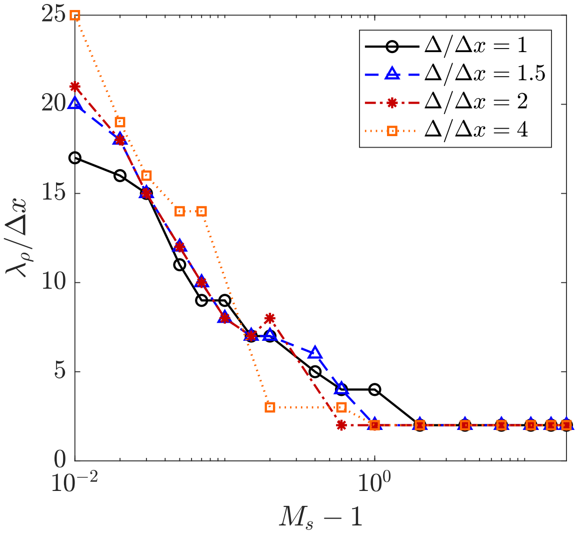

Figure 2.7: Wavelength of density oscillations using $q_{SFS} = q_c + q_v$ for grid resolutions of $\Delta/\Delta x = 1$ (black solid line and circles), $\Delta/\Delta x = 1.5$ (blue dashed line and triangles), $\Delta/\Delta x = 2$ (red dash-dotted line and asterisks), and $\Delta/\Delta x = 4$ (orange dotted line and squares).

shock thickness is computed as

$$\ell_\phi = \frac{\phi_2 - \phi_1}{\left(\frac{\partial \phi}{\partial x}\right)_{max}}, \tag{2.84}$$

where ϕ may be the density, pressure, velocity, or temperature. Using Eq. (2.84) with the analytical expressions for $\overline{\phi}(x)$ and $\tilde{\phi}(x)$ leads to an analytical shock thickness of $\ell_\phi = 2\Delta$. The lack of dependence of the filtered shock thickness on the Mach number deserves further discussion. For common gases, a Reynolds number can be defined as a function of the theoretical shock thickness and the jump in velocity across the shock [99],

$$Re = \frac{\ell(u_1 - u_2)}{\nu} \approx 1. \tag{2.85}$$

The theoretical shock thickness is then expressed as

$$\ell \propto \frac{\nu}{(u_1 - u_2)}. \tag{2.86}$$

Using the SFS viscosity for ν in the above expression,

$$\ell \propto \frac{(u_1 - u_2)\frac{\Delta}{2}}{(u_1 - u_2)} \propto \Delta, \tag{2.87}$$

so the shock thickness is expected to be proportional to the filter width Δ, and constant across shock Mach number. This result comes from the specific form of the SFS viscosity, namely Eq. (2.30).

Figure 2.8a shows the shock thicknesses computed using $\overline{\rho}$, $\overline{p}$, $\tilde{u}$, and $\tilde{T}$ for a filter width $\Delta/\Delta x = 1$. The thickness is approximately constant across the range of Mach numbers (from 2 to 20) and is close to the theoretical value of 2Δ. The effect of grid resolution is investigated in Fig. 2.8b using the shock thickness based on density, ℓ_ρ. As $\Delta/\Delta x$ increases, the shock thickness decreases and is closer to the theoretical thickness. However, the thickness appears to converge to a value slightly large than 2Δ. The specific discretization used in NGA requires various interpolations that may result in additional numerical diffusion and/or dispersion.

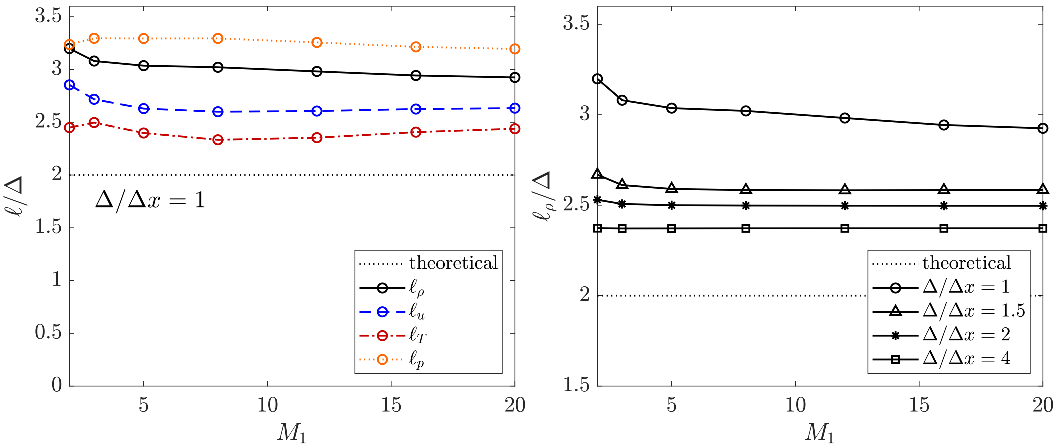

(a) Impact of choice of variable ($\Delta/\Delta x = 1$). (b) Impact of grid resolution.

Figure 2.8: Impact of the choice of flow variable (left at $\Delta/\Delta x = 1$) and grid resolution (right for ρ) on the shock thickness for moderate and strong shocks. Analytical shock thickness (black dotted line); shock thickness computed from density (black symbols/solid line), velocity (blue symbols/dashed line), temperature (red symbols/dash-dotted line), pressure (orange symbols/dotted line); grid resolution of $\Delta/\Delta x = 1$ (circles), $\Delta/\Delta x = 1.5$ (triangles), $\Delta/\Delta x = 2$ (asterisks), and $\Delta/\Delta x = 4$ (squares).

2.3.2 Weak normal shocks

For weak shocks ($M \approx 1$), the jump in velocity ($u_1 - u_2$) is small, and therefore the SFS viscosity is small. For instance, a Mach 1.01 shock has a SFS viscosity on the order of 10^{-6} Pa·s. Under these conditions, two numerical artifacts are observed.

First and as shown in Fig. 2.9, numerical oscillations develop ahead of the shock. These oscillations are relatively large (of the order of the jump) but absolutely

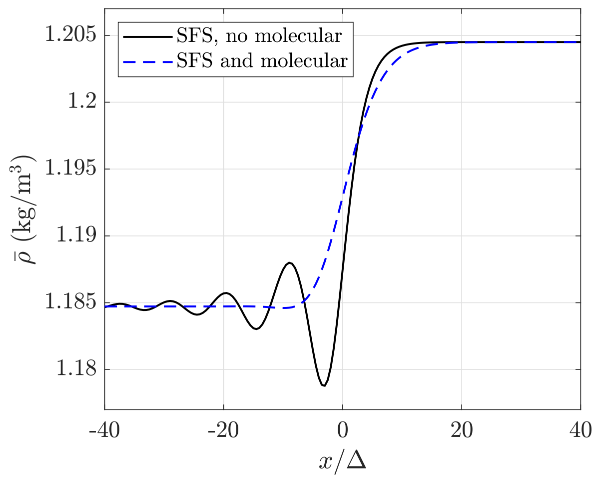

Figure 2.9: Density profile for Mach 1.01 shock ($\Delta/\Delta x = 2$) with SFS viscosity only (black solid line) and with SFS and molecular viscosity (blue dashed line).

small (compared to the pre-shock values). For the full range of shocks tested, the relative amplitude of oscillations is shown in Fig. 2.10. The absolute oscillations (shown in Fig. 2.10a) are small, and increasing with Mach number for $\Delta/\Delta x = 1$. Using $\Delta/\Delta x = 1.5$ reduces the oscillations, but still shows an increasing trend at higher Mach numbers. For $\Delta/\Delta x = 2$, these oscillations virtually disappear for moderate/strong shocks, as was observed in Fig. 2.6b. The relative oscillations (shown in Fig. 2.10b) decrease with Mach number for all grid resolutions. Especially for stronger shocks, increasing from $\Delta/\Delta x = 1$ to 2 leads to a substantial reduction of the oscillations.

Increasing the ratio $\Delta/\Delta x$ also leads to a more restrictive CFL condition. The viscous CFL is given by

$$\sigma = \frac{4\nu\Delta t}{(\Delta x)^2}, \tag{2.88}$$

where ν is the physical kinematic viscosity. The SFS viscosity also has a corresponding CFL given by

$$\begin{aligned}\sigma_{SFS} &= \frac{4\nu_{SFS}\Delta t}{(\Delta x)^2} \\ &= \frac{2(u_1 - u_2)\Delta t}{\Delta x}\left(\frac{\Delta}{\Delta x}\right)\end{aligned} \tag{2.89}$$

in one dimension. This CFL restriction is not unique to the framework here, and is also present for artificial viscosity/diffusivity approaches [35, 100]. As $\sigma_{SFS} \propto \Delta/\Delta x$, it is best to keep $\Delta/\Delta x$ as small as possible while still filtering

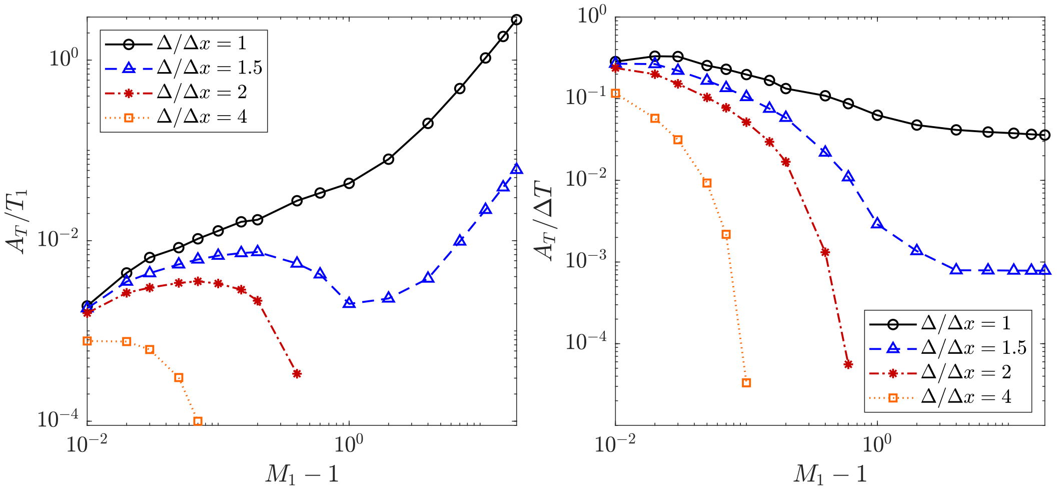

(a) Absolute oscillation amplitude.

(b) Relative oscillation amplitude.

Figure 2.10: Impact of grid resolution on the maximum temperature oscillation amplitude, A_T, normalized by the pre-shock temperature (left) and by the jump in temperature across the shock (right). $\Delta/\Delta x = 1$ (black circles/solid line), $\Delta/\Delta x = 1.5$ (blue triangles/dashed line), $\Delta/\Delta x = 2$ (red asterisks/dash-dotted line), and $\Delta/\Delta x = 4$ (orange squares/dotted line).

the oscillations. Referring back to the oscillation wavelengths in Fig. 2.7, there is no need to use $\Delta/\Delta x > 2$ to manage the oscillations for moderate and strong shocks. However, weaker shocks have oscillations spread over more points, and as such require a larger $\Delta/\Delta x$ to filter over the full oscillation wavelength. To avoid increasing the resolution requirements—and thus the timestep restriction—for weak shocks, this may be addressed by including molecular viscosity, which is on the order of 10^{-5} Pa·s for air. This physical diffusion is sufficient to prevent oscillations for the weaker shocks, as illustrated in Fig. 2.9, where a constant value of $\mu_{mol.} = 1.81 \cdot 10^{-5}$ Pa·s is used.

Second, and as shown in Fig. 2.11, the simulation results of weak shocks appear thicker than the analytical/theoretical value of 2Δ. Because the overall jump across the shock is small for weak shocks, the impact of the numerical discretization is much more pronounced here. More precisely, the theoretical shock thickness scaling (i.e. Eq. (2.84)) for weak shocks becomes [99]

$$\ell \propto \frac{\nu}{c(M_1 - 1)}. \tag{2.90}$$

As the SFS viscosity tends towards zero, other spurious viscous effects may become dominant. Assigning them a constant ν_{err} value, the shock thickness now becomes

$$\ell \propto \frac{\nu_{SFS} + \nu_{err}}{c(M_1 - 1)} \propto 2\Delta + \frac{\nu_{err}}{c(M_1 - 1)}. \tag{2.91}$$

So for weak shocks the thickness is expected to depend on the Mach number M_1 in addition to the filter width Δ.

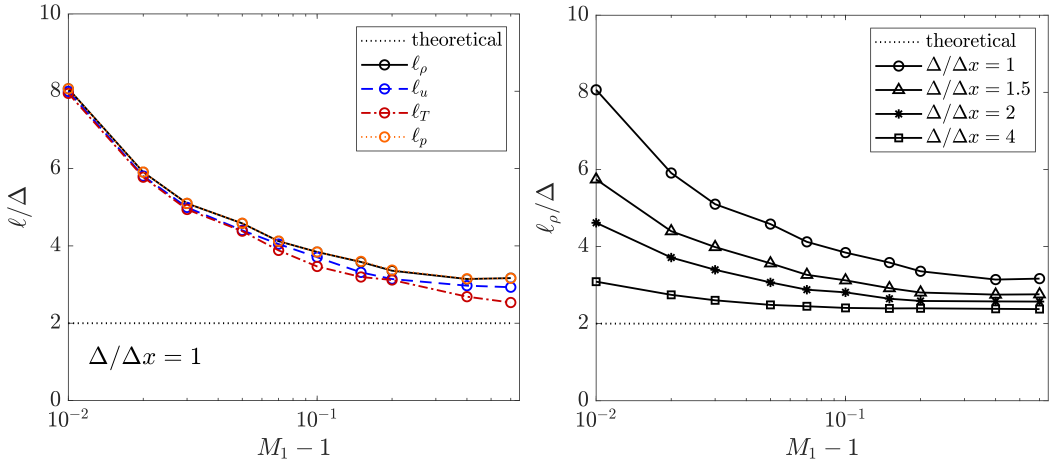

(a) Impact of choice of variable ($\Delta/\Delta x = 1$). (b) Impact of grid resolution.

Figure 2.11: Impact of the choice of variable (left at $\Delta/\Delta x = 1$) and grid resolution (right for ρ) on shock thickness for weak shocks. Analytical shock thickness (black dotted line); shock thickness computed from density (black symbols/solid line), velocity (blue symbols/dashed line), temperature (red symbols/dash-dotted line), pressure (orange symbols/dotted line); grid resolution of $\Delta/\Delta x = 1$ (circles), $\Delta/\Delta x = 1.5$ (triangles), $\Delta/\Delta x = 2$ (asterisks), and $\Delta/\Delta x = 4$ (squares).

The results of Fig. 2.11b confirm that the ν_{err} is of a numerical origin as its impact reduces with increased grid resolution ($\Delta/\Delta x = 2$ and 4).

2.3.3 Order of convergence

The original Euler equations admit discontinuities, i.e., shocks are infinitely thin. This lack of length scale in the original equations leads to poor convergence of most numerical solutions with grid refinement. Even with higher order schemes, first-order convergence is often observed in the vicinity of shocks [31, 101]. In contrast, the filtered Euler equations are regularized, and a length scale has been introduced: namely, the filter width Δ. As discussed in Sec. 2.3.1, the filter width controls the shock thickness. By fixing Δ, the shock profile is expected to converge with sufficiently high grid resolution (larger $\Delta/\Delta x$).

To assess the effect of the grid resolution, a much finer simulation of the Mach 2 shock is performed with $\Delta/\Delta x = 16$ and the same filter width $\Delta = 1 \cdot 10^{-6}$ m. After running this high resolution case for $t = 1 \cdot 10^{-6}$ s, the solution is interpolated onto the coarser grids for $\Delta/\Delta x = 1$, 2, and 4. Transient effects at the simulation startup can lead to a slight drift in the shock position. Initializing from the same numerical solution ensures this drift is the same for each $\Delta/\Delta x$. All four cases are run for another $t = 2 \cdot 10^{-6}$ s.

The error in the density profile is calculated using the L_∞, L_1, and L_2 norms. The highest resolution case ($\Delta/\Delta x = 16$) is taken to be the exact solution (referred to as ρ_∞). As shown in Fig. 2.12, all three error norms exhibit a quadratic dependence on Δx. A second-order convergence is expected as the code uses second-order interpolation and derivative operators in space (see Sec. 2.2).

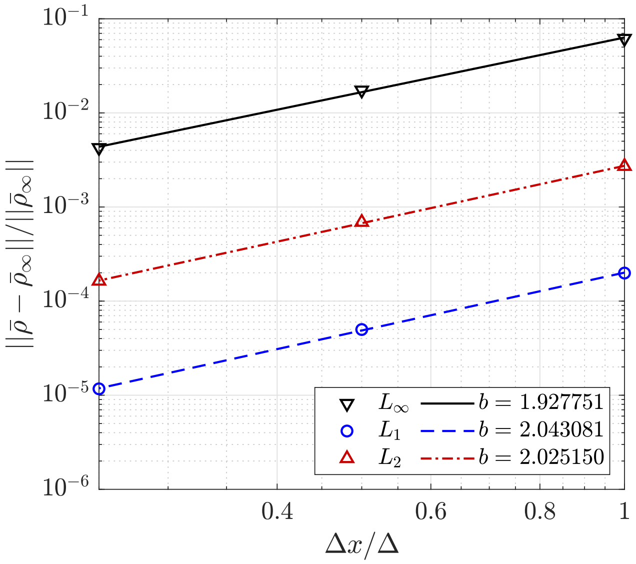

Figure 2.12: Impact of grid resolution, Δx, on the L_∞ error norm (black triangles/solid line), L_1 error norm (blue circles/dashed line), and L_2 error norm (red triangles/dash-dotted line) of the density profile for a Mach 2 shock. Fixed $\Delta = 1 \cdot 10^{-6}$ m.

2.3.4 Estimating the velocity across a shock

For simulations of steady normal shocks with a prescribed Mach number, the theoretical jump in velocity ($u_1 - u_2$) can be used directly to compute the SFS terms in Eq. (2.30), (2.59), and (2.64). This was done in the previous two subsections. However, the jump in velocity is not always known a priori. For all general cases, the velocity jump is estimated by considering the local densities and velocities.

The shock normal vector can be defined using the density gradient as

$$\hat{\mathbf{n}} = \frac{\nabla\rho}{|\nabla\rho| + \epsilon}, \tag{2.92}$$

where $\epsilon = 10^{-15}$ to avoid dividing by zero in uniform regions. The velocity vector in $(x - y)$ coordinates is

$$\mathbf{u} = u\hat{\mathbf{x}} + v\hat{\mathbf{y}}. \tag{2.93}$$

The normal velocity is given by

$$\begin{aligned} u_n &= \mathbf{u} \cdot \hat{\mathbf{n}} \\ &= u\hat{n}_x + v\hat{n}_y, \end{aligned} \tag{2.94}$$

and the change in the normal velocity across an oblique shock is

$$u_{1n} - u_{2n} = (u_1 - u_2)\hat{n}_x + (v_1 - v_2)\hat{n}_y. \tag{2.95}$$

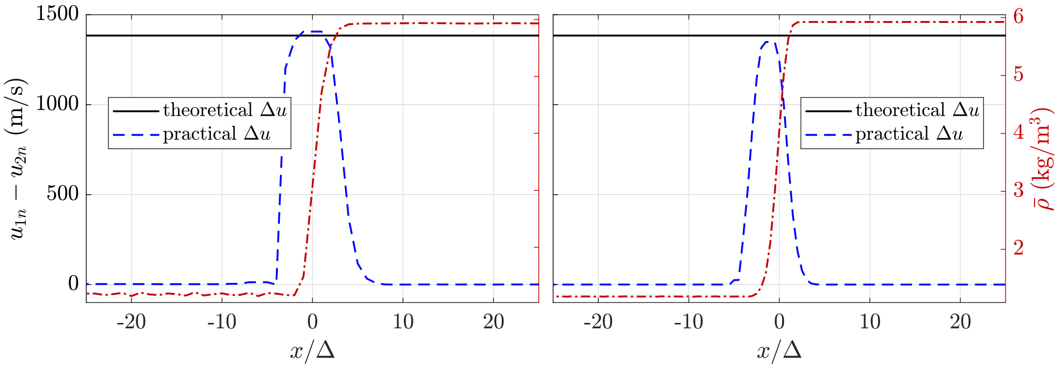

(a) $\Delta/\Delta x = 1$.

(b) $\Delta/\Delta x = 2$.

Figure 2.13: Comparison of theoretical $(u_1 - u_2)$ (black solid line) with the practical $(u_1 - u_2)$ computed using Eq. (2.95) through (2.104) (blue dashed line). The density profile for a Mach 5 shock using the practical $(u_1 - u_2)$ is shown for reference (red dash-dotted line).

To compute this at runtime, first we identify the pre-shock and post-shock locations, (x_1, y_1) and (x_2, y_2) respectively, using the local density such that

$$\rho(x_1, y_1) = \min_{\substack{x'=x\pm3\Delta x \\ y'=y\pm3\Delta y}} \{\rho(x', y')\}, \tag{2.96}$$

$$\rho(x_2, y_2) = \max_{\substack{x'=x\pm3\Delta x \\ y'=y\pm3\Delta y}} \{\rho(x', y')\}, \tag{2.97}$$

with the points at ±3Δx based on the number of grid points observed across moderate to strong shocks for $\Delta/\Delta x = 1$ (see Fig. 2.8a). The corresponding velocities at these locations,

$$(u_1, v_1) = (u(x_1, y_1), v(x_1, y_1)), \tag{2.98}$$

$$(u_2, v_2) = (u(x_2, y_2), v(x_2, y_2)), \tag{2.99}$$

are then used in Eq. (2.95). To avoid picking up changes in density and velocity due to shear layers or rarefaction fans, as well as to avoid adding SFS antidiffusion, $(u_{1n} - u_{2n})$ is updated as

$$u_{1n} - u_{2n} = \max\{u_{1n} - u_{2n}, 0\}. \tag{2.100}$$

For filter width ratios larger than $\Delta/\Delta x = 1$, there may be more points within the shock, and so the velocity jump is underestimated. To correct this, assuming the filtered shock profile takes the form of a hyperbolic tangent, the difference in velocities at ±3Δx is

$$u(-3\Delta x) - u(3\Delta x) = (u_1 - u_2) \tanh\left(3\frac{\Delta x}{\Delta}\right), \tag{2.101}$$

so the result from Eq. (2.100) is updated to

$$u_{1n} - u_{2n} = \frac{u_{1n} - u_{2n}}{\tanh\left(3\frac{\Delta n}{\Delta}\right)}, \tag{2.102}$$

where the shock-normal grid spacing is given by

$$\Delta n = \Delta x \cdot \hat{n}_x + \Delta y \cdot \hat{n}_y \tag{2.103}$$

in two dimensions.

Finally, so that the largest value computed for $(u_{1n} - u_{2n})$ is used at more than one grid point in the shock, the velocity jump at each point is updated as

$$(u_{1n} - u_{2n})(x, y) = \max_{\substack{x'=x-\Delta x \le x \le x+\Delta x \\ y'=y-\Delta y \le y \le y+\Delta y}} \{(u_{1n} - u_{2n})(x', y')\}. \tag{2.104}$$

As illustrated in Fig. 2.13, this calculation of $(u_{1n} - u_{2n})$ acts as a shock sensor, achieving the theoretical velocity jump at the shock and dropping to zero away from the shock.

The remaining simulations in this work do not have a theoretically-prescribed velocity jump. Therefore, the calculation described in Eq. (2.95) through (2.104) is used for all tests presented in Sec. 2.3.5, 2.4, and 2.5.

2.3.5 Moderate and strong shocks with temperature-dependent properties

In the previous simulations, it was assumed that thermodynamic properties such as the specific heat capacity are constant. However, for shocks with a substantial temperature change, there is a non-negligible change in the heat capacities. To investigate their impacts and the ability of the code to handle changes in properties, a sample of Mach numbers is rerun with temperature-dependent properties for air ($Y_{N_2} = 0.768$ and $Y_{O_2} = 0.232$). The shock Mach numbers and the corresponding post-shock specific heat ratios are shown in Table 2.1. Starting from the same initial conditions as before, a total run time of $3 \cdot 10^{-6}$ s is sufficient for the profiles to adjust from the perfect gas (constant c_p) to the $c_p(\tilde{T})$ jump conditions. The timestep restriction and boundary conditions are the same as in the previous shocks. The filter width $\Delta = 1 \cdot 10^{-6}$ m with $\Delta/\Delta x = 2$.

The steady-state profiles for a Mach 5 shock are compared in Fig. 2.14. For consistency, both the constant c_p and variable c_p cases shown here use the practical $(u_1 - u_2)$ described in Sec. 2.3.4. Accounting for changes in c_p and the species enthalpies h_s with temperature, the post-shock density increases and the post-shock temperature decreases relative to the perfect gas post-shock conditions. These changes do not affect the smoothness of the resulting profiles.

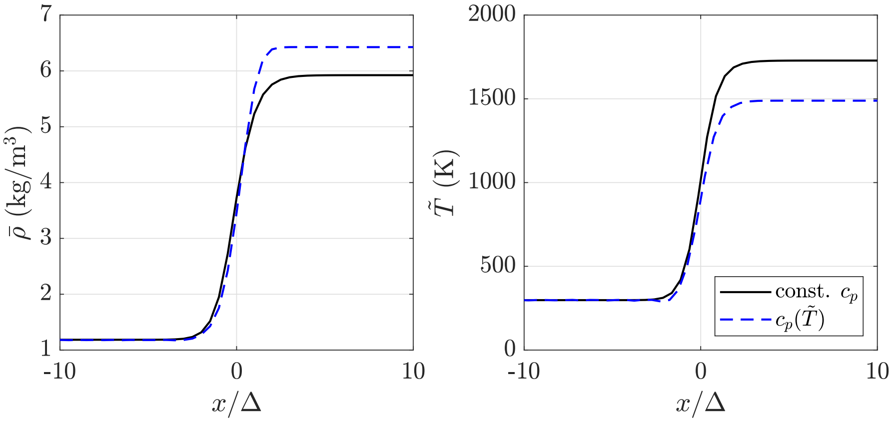

Figure 2.14: Density (left) and temperature (right) profiles for the Mach 5 shock, using constant c_p (black solid line) and variable $c_p(\tilde{T})$ (blue dashed line).

2.4 Other 1D results

2.4.1 Shu-Osher problem

The Shu-Osher problem is often used as a one-dimensional test for shock-turbulence interaction. A Mach 3 shock propagates through a sinusoidal density field, generating acoustic and entropy waves downstream. In the present work, this problem

M_1	γ_2
2	1.39
3	1.36
5	1.31
8	1.28
12	1.27

Table 2.1: Post-shock specific heat capacity ratio γ_2 for variable $c_p(\tilde{T})$ shocks. The pre-shock ratio $\gamma_1 = 1.4$ for all cases.

is used to isolate the effects of two parameters: the filter width, Δ, and the grid resolution, Δx. The initial conditions are listed in Table 2.2. The boundaries use NSCBCs, with the inlet conditions corresponding to the left state in Table 2.2. The timestep is restricted by a CFL of 0.8.

	Left	Right
ρ	3.857143	$1.0 + 0.2\sin(5x)$
p	10.33333	1.0
u	2.629369	0.0

Table 2.2: Initial conditions for the Shu-Osher problem.

First, to test the impact of the filtering without introducing numerical errors, a fine resolution $\Delta x = 0.005$ is tested, using a filter width $\Delta/\Delta x = 10$ (i.e. $\Delta = 0.05$). Results are shown at $t = 1.8$ in Fig. 2.15. The density profile, shown in Fig. 2.15a, is compared with a reference solution obtained using a fifth-order ENO scheme [42]. The entropy profile, shown in Fig. 2.15b, is compared with a reference solution obtained using a seventh-order WENO scheme [22]. To validate the numerical solution of the filtered Euler equations, both reference solutions are filtered with a Gaussian corresponding to $\Delta = 0.05$. The entropy is computed from the simulation data as $\Delta s/c_v \equiv \ln(\overline{p}/\overline{\rho}^{\gamma})$. As shown in Fig. 2.15, the shock, acoustic wave, and entropy waves are all captured accurately, with limited damping of the entropy wave in the post-shock region. Unlike the reference solution from [22], the entropy reaches a maximum within the shock, near $x = 2.5$, consistent with the discussion from Sec. 2.1.6.

Next, to test the impact of the numerical discretization, the simulation is performed on a coarse grid, with $\Delta x = \Delta = 0.05$. Results are shown in Fig. 2.16, again at $t = 1.8$. To compare across resolutions, the previously discussed $\Delta x = 0.005$ case is also shown. At this resolution, the shock and acoustic wave are still captured well. However, the results in Fig. 2.16b show a substantial change in the wavelength

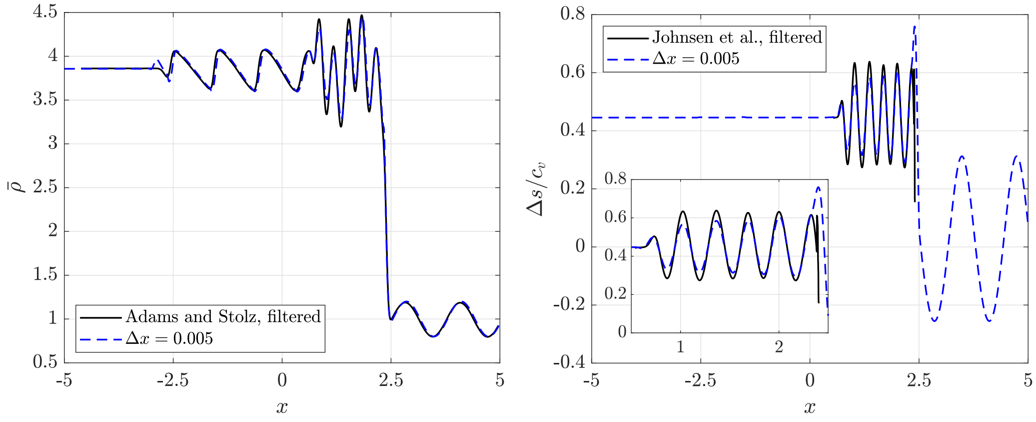

(a) Density. Reference solution from [42]. (b) Entropy. Reference solution from [22].

Figure 2.15: Shu-Osher problem at $t = 1.8$. Reference solution filtered with $\Delta = 0.05$ (black solid line), simulation solution with $\Delta x = 0.005$, $\Delta = 0.05$ (blue dashed line).

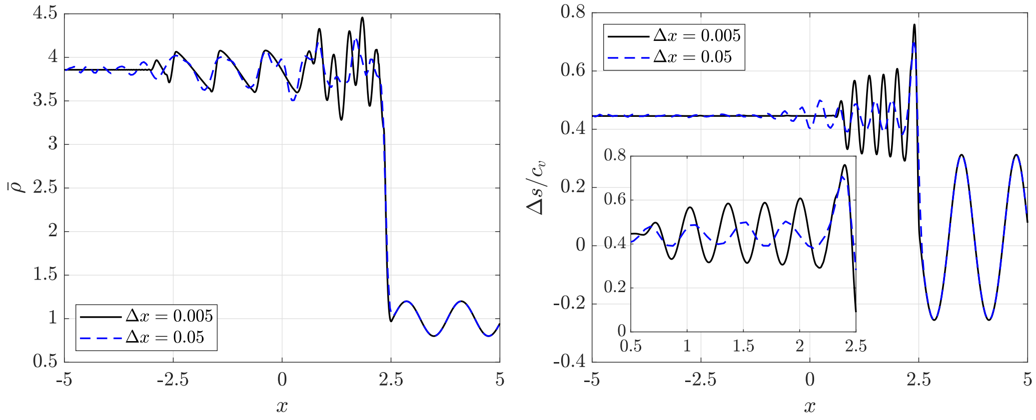

(a) Density. (b) Entropy.

Figure 2.16: Shu-Osher problem at $t = 1.8$. Simulation solution with $\Delta x = 0.005$, $\Delta = 0.05$ (black solid line), simulation solution with $\Delta x = 0.05$, $\Delta = 0.05$ (blue dashed line).

and amplitude of the post-shock entropy wave for the coarser grid ($\Delta x = 0.05$). This is purely a result of dispersion errors stemming from the present second-order centered spatial discretization. From conservation of mass, the relationship between the pre-shock wavelength, λ_1, and the post-shock wavelength, λ_2, is

$$\lambda_2 = \frac{u_s - u_2}{u_s - u_1}\lambda_1, \tag{2.105}$$

where u_s, u_1, and u_2 are the shock, pre-shock, and post-shock velocities in the lab frame of reference, respectively. For a second-order centered scheme, the modified wave speed is given by

$$u' = \frac{\sin(k\Delta x)}{k\Delta x} u, \tag{2.106}$$

where k is the wavenumber. Applying this dispersion relation to Eq. (2.105), the modified wavelength is

$$\lambda_2' = \frac{u_s - \frac{\sin(k\Delta x)}{k\Delta x} u_2}{u_s - u_1} \lambda_1. \tag{2.107}$$

For the Shu-Osher problem, $\lambda_2 \approx 0.33$. From Eq.(2.107), the modified wavelengths $\lambda_2'(\Delta x = 0.005) \approx 0.34$ and $\lambda_2'(\Delta x = 0.05) \approx 0.47$, in agreement with the profiles shown in Fig. 2.15b and 2.16b. Although $\Delta x = 0.05$ is commonly used in the literature for the Shu-Osher problem, the schemes used were high-order compact schemes, greatly reducing the dispersion errors [30–33, 35]. These dispersion errors on the entropy waves are unrelated to the SFS viscosity.

A more detailed discussion of the dispersion errors observed for the Shu-Osher problem is included here. The discretized expressions for first derivatives in second order centered, fourth order centered, fourth order compact, and sixth order compact schemes are given by

$$\phi_i' = \frac{1}{2\Delta x} \left(\phi_{i+1} - \phi_{i-1} \right), \tag{2.108}$$

$$\phi_i' = \frac{1}{48\Delta x} \left(-\phi_{i+2} + 26\phi_{i+1} - 26\phi_{i-1} + \phi_{i-2} \right), \tag{2.109}$$

$$\frac{1}{4}\phi_{i-1}' + \phi_i' + \frac{1}{4}\phi_{i+1}' = \frac{3}{2} \frac{\phi_{i+1} - \phi_{i-1}}{2\Delta x}, \tag{2.110}$$

$$\frac{1}{3}\phi_{i-1}' + \phi_i' + \frac{1}{3}\phi_{i+1}' = \frac{14}{9} \frac{\phi_{i+1} - \phi_{i-1}}{2\Delta x} + \frac{1}{9} \frac{\phi_{i+2} - \phi_{i-2}}{4\Delta x}, \tag{2.111}$$

respectively. The corresponding modified wave speeds u' are

$$u' = \left(\frac{\sin(k\Delta x)}{k\Delta x} \right) u, \tag{2.112}$$

$$u' = \left(\frac{\sin(k\Delta x)}{k\Delta x} \right) \left(\frac{13 - \cos(k\Delta x)}{12} \right) u, \tag{2.113}$$

$$u' = \left(\frac{\sin(k\Delta x)}{k\Delta x} \right) \left(\frac{3}{2 + \cos(k\Delta x)} \right) u, \tag{2.114}$$

$$u' = \left(\frac{\sin(k\Delta x)}{k\Delta x} \right) \left(\frac{14 + \cos(k\Delta x)}{9 + 6\cos(k\Delta x)} \right) u. \tag{2.115}$$

To illustrate the dispersion errors, a sinusoidal entropy wave is tested, based on the conditions for the post-shock region of the Shu-Osher problem. The velocity $u = 2.629369$, pressure $p = 10.33333$, and the density is given by

$$\rho(x) = 3.857143 + 0.2 \sin\left(\frac{2\pi x}{0.33}\right). \tag{2.116}$$

The boundary conditions are periodic. The simulation is run at different grid resolutions: $\Delta x = 0.05$, 0.025, 0.0125, and 0.005. The results at $t = 1 \cdot 10^{-1}$ are shown in Fig. 2.17, along with the initial condition.

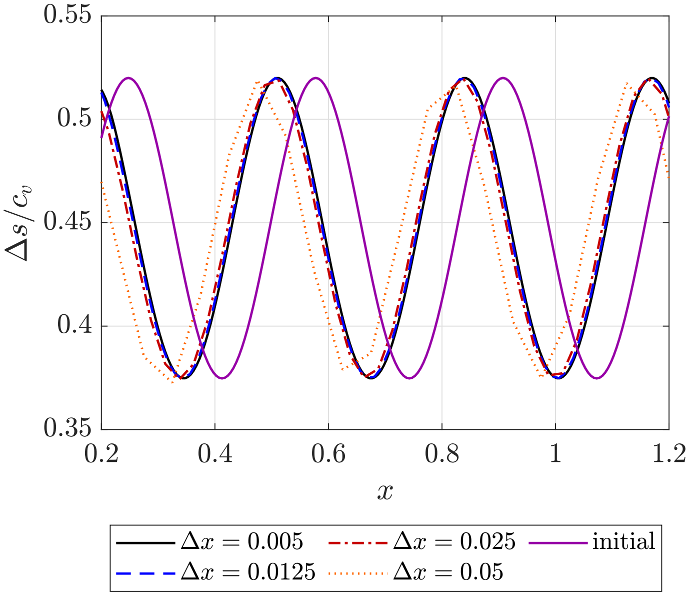

Figure 2.17: Right-moving entropy wave at varying grid resolutions. $\Delta x = 0.005$ (black solid line), 0.0125 (blue dashed line), 0.025 (red dash-dotted line), and 0.05 (orange dotted line). The initial wave is shown in solid purple.

From Fig. 2.17, the wave speeds at each resolution can be computed. The measured wave speed ratio is shown along with the theoretical dispersion relations in Eq. (2.112) to (2.115) in Fig. 2.18. As expected, the simulation results correspond to the second order dispersion errors.

2.4.2 1D detonation

A detonation is tested in hydrogen and air with an equivalence ratio $\phi = 0.6$, using an H_2/O_2 mechanism with 9 species and 54 reactions [54]. The simulation is initialized with a Mach 5 normal shock with $T_1 = 298$ K and $p_1 = 101325$ Pa. The post-shock state has sufficiently high temperature and pressure to ignite, after which the shock evolves into a Zel'dovich-Neumann-Döring (ZND) detonation profile. The ignition of the post-shock state results in an increase in the shock speed, so first

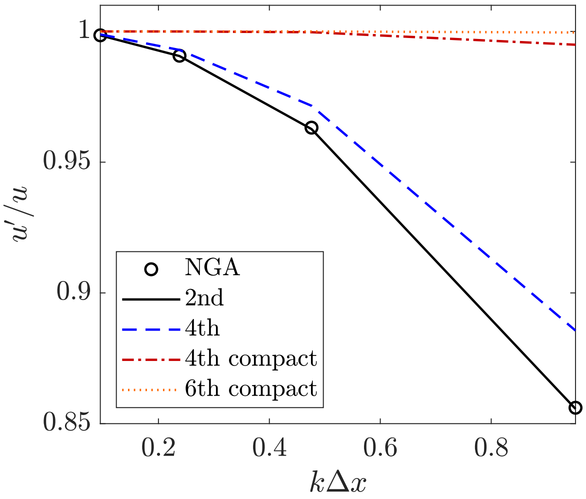

Figure 2.18: Dispersion errors for 2nd order centered (black solid line), 4th order centered (blue dashed line), 4th order compact (red dash-dotted line), and 6th order compact (orange dotted line). The numerical results are shown in black circles.

the simulation is run for $2 \cdot 10^{-6}$ s, allowing the ignition to begin and strengthen the shock. Then, the velocity field and inflow velocity are shifted by 390 m/s to keep the detonation wave fixed, and the simulation is run for an additional $2 \cdot 10^{-6}$ s, allowing the shock, induction zone, and post-ignition profile to reach a steady state. Various grid resolutions are tested; based on the results from Sec. 2.3.1, a fixed ratio of $\Delta/\Delta x = 2$ is used for all resolutions. The coarsest grid ($\Delta x = 1 \cdot 10^{-6}$) is chosen such that the filter width is about an order of magnitude smaller than the expected induction zone length. For all resolutions, the timestep is restricted by a maximum CFL of 0.8. The boundaries are treated with NSCBCs, with the inflow conditions specified as the pre-shock, unburnt values.

The shock portion of the steady ZND profile behaves similarly to the normal shock test case, and so the shock thickness will not be discussed again here. The coarsest resolution case is compared to the ZND calculation from the Shock and Detonation Toolbox [102] using Cantera [103] in Fig. 2.19. The ZND calculation takes the shock front speed (measured from the simulation) along with the chemical mechanism and the pre-shock conditions (temperature, pressure, species mass fractions) and outputs the ZND detonation profiles. The simulation profiles match the Cantera profiles closely. While the filtering framework spreads the shock to maintain numerical stability, it does not spread the ignition portion of the ZND profile.

For detonations, the induction zone length is another important length scale. Com-

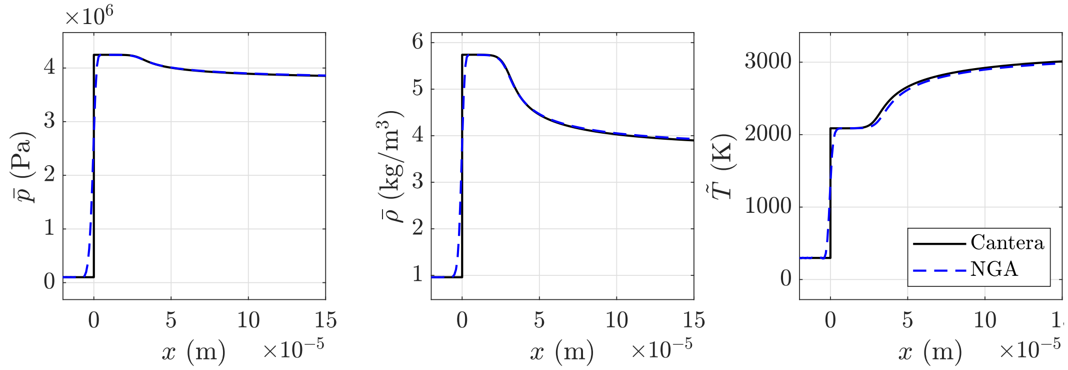

Figure 2.19: Comparison of the coarsest resolution ($\Delta x = 1 \cdot 10^{-6}$ m) case (NGA, blue dashed line) with ZND calculation from the Shock and Detonation Toolbox (Cantera, black solid line).

puting the induction zone length requires the shock location, post-shock temperature, and the maximum temperature gradient during the ignition (post-shock). First, the location of the overall maximum temperature gradient is identified as the shock location x_0. Using a least-squares regression, the hyperbolic tangent profile

$$\overline{T}(x) = T_1 + \frac{1}{2}(T_2 - T_1)\left(1 + \tanh\left(\frac{x - x_0}{\Delta}\right)\right) \tag{2.117}$$

is fit to the temperature data in the vicinity of the shock, with the post-shock temperature T_2, shock location x_0, and Δ as parameters. The pre-shock temperature is fixed at $T_1 = 298$ K. The maximum temperature gradient during ignition, $\frac{\partial T_3}{\partial x}$, and the temperature T_3 at the same location x_3, are used to calculate the induction zone length as follows:

$$\mathcal{L} = x_3 - \frac{T_3 - T_2}{\frac{\partial T_3}{\partial x}} - x_0. \tag{2.118}$$

The quantities used in Eq. (2.118) are illustrated in Fig. 2.20, and the calculated induction zone lengths are shown in Table 2.3 for each resolution tested. For the finer resolution cases, the induction zone lengths calculated from the simulation results differ from Cantera by less than $1 \cdot 10^{-6}$ m. From the different grid resolutions tested, the order of accuracy can be examined. Using the highest resolution case ($\Delta x = 1.25 \cdot 10^{-7}$ m) as the "exact" length $\mathcal{L}_\infty$, the relative error in $\mathcal{L}$ is shown in Table 2.3 and plotted against the nondimensional grid spacing $\Delta x/\mathcal{L}_\infty$ in Fig. 2.21. The induction zone length is found to be approximately first-order accurate.

2.5 Multi-dimensional tests

Finally, multi-dimensional cases are considered to assess the formulation of the SFS terms (Eq. (2.36) with (2.45) and (2.46)) in capturing oblique and curved shocks.

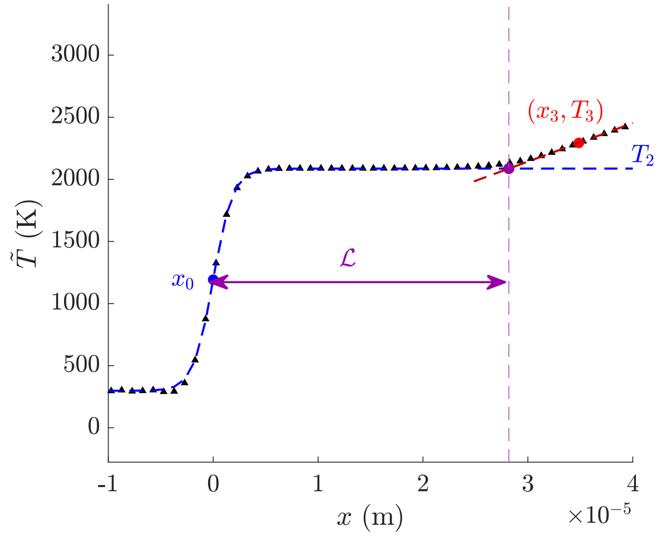

Figure 2.20: Temperature data points (black triangles); hyperbolic tangent curve fit (blue dashed line); maximum temperature gradient during ignition $\left(\frac{\partial T_3}{\partial x}\right)$ (red dashed line); x location of tanh fit and $\frac{\partial T_3}{\partial x}$ intersection (purple dashed line); the induction zone length $\mathcal{L}$ is the distance from x_0 to this intersection (purple arrow).

Δx [$\cdot 10^{-6}$ m]	Δ [$\cdot 10^{-6}$ m]	$\mathcal{L}$ [$\cdot 10^{-5}$ m]	$\Delta\mathcal{L}/\mathcal{L}_\infty$
1	2	2.82	0.133
0.667	1.33	2.69	0.083
0.5	1	2.63	0.058
0.25	0.5	2.54	0.019
0.125	0.25	2.49	0
Cantera		2.54	

Table 2.3: Comparison of simulation induction zone length with Cantera. The result for the finest resolution case is taken to be $\mathcal{L}_\infty$.

2.5.1 Forward facing step

A Mach 3 supersonic inflow interacts with a forward facing step located at $x = 0.6$ with a height of 0.2 [104]. The simulation uses a 240×80 grid on a 3×1 domain, as in [104]. The Mach 3 flow is initially uniform throughout the domain with $p = 1$ and $\rho = 1.4$ (resulting in a sound speed $c = 1$ using $\gamma = 1.4$). The inlet conditions are $p_1 = 1$, $\rho_1 = 1.4$, and $u_1 = 3$, and the inflow (left) and outflow (right) boundaries are treated with NSCBCs. The upper boundary is a symmetry plane. The walls are inviscid. A timestep $\Delta t = 1 \cdot 10^{-3}$ is used. Results are shown for $t = 4$ in Fig. 2.22. This test features a rarefaction fan at the corner of the step interacting with the reflecting shock waves. Numerical errors at this corner may lead to substantial changes in the downstream flow behavior, as thoroughly detailed

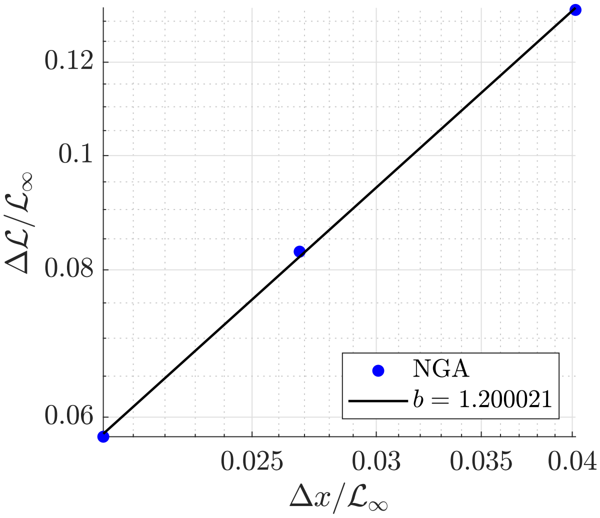

Figure 2.21: Order of accuracy of calculated induction zone length with changes in grid resolution Δx (blue circles). The line of fit (black solid line) for $\Delta\mathcal{L}$ vs. Δx is given by $\Delta\mathcal{L}_{fit} = a \cdot (\Delta x)^b$, where b indicates the order of accuracy.

in [104]. The framework here captures the expected flow features well. Particularly, the Mach stems at the upper boundary and at the wall reflection are free of numerical oscillations and kinks that have been observed in previous studies [105].

2.5.2 Shock diffraction over 90 degree corner

A Mach 5.09 normal shock diffracts around the corner of a step with a height of 0.45 and with the right edge located at $x = 0.05$ [106]. The simulation uses a 400×400 grid on a 1×1 domain, as in [105]. Initially, the portion of the domain to the right of the step has uniform flow set to the pre-shock conditions, $p_1 = 1$ and $\rho_1 = 1.4$ (resulting in a sound speed $c_1 = 1$ using $\gamma = 1.4$). The portion of the domain above the step has uniform flow set to the post-shock conditions. The inlet values at the left boundary are set to the post-shock conditions, and NSCBCs are used for both the inflow and outflow boundary conditions. The walls are inviscid, and the remaining boundaries use Neumann boundary conditions. The timestep is restricted by a maximum CFL of 0.4. Results are shown for $t = 0.1561$ in Fig. 2.23. Previous studies have shown that if insufficient diffusion is applied, the normal portion of the shock front is subject to severe numerical instabilities (referred to as the carbuncle phenomenon) [105, 106]. As seen in Fig. 2.23, the shock front is smooth along the entire curvature, so the SFS diffusion is sufficient to avoid this numerical instability.

The shock diffraction is used to assess the effect of the grid resolution in two

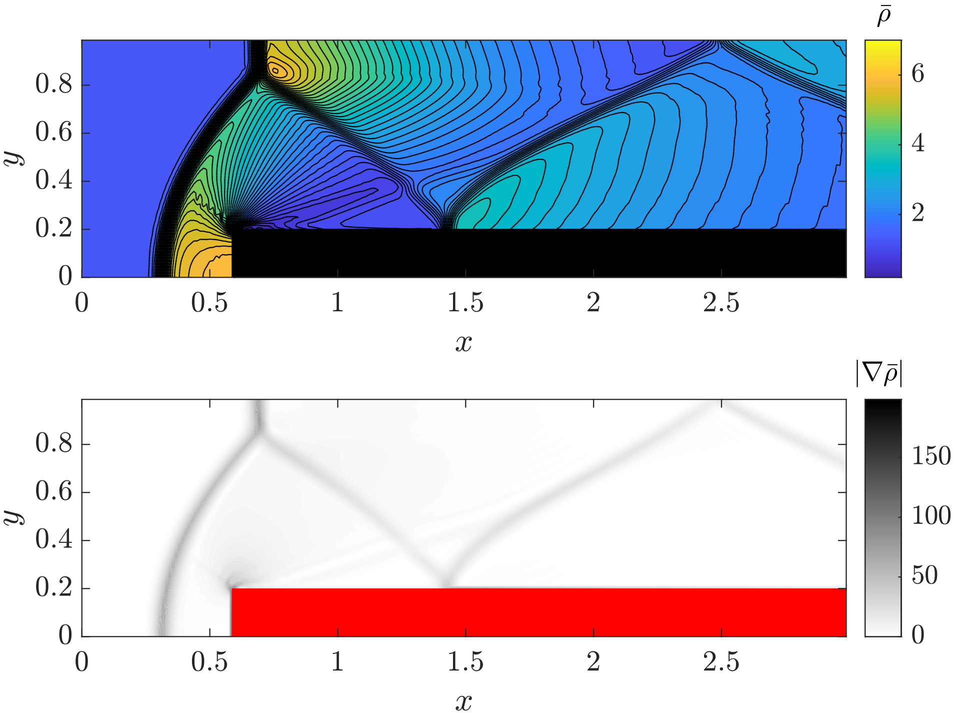

Figure 2.22: Contours of density (top) and density gradient magnitude (bottom). Step shown in black (top) or red (bottom). The density plot shows 40 contour levels spanning 0.2 to 7, as in [105]. ($\Delta/\Delta x = 2$).

dimensions. Keeping the filter width constant at $\Delta = 0.005$ (corresponding to $\Delta/\Delta x = 2$ for the 400×400 case), three additional simulations are performed with $\Delta/\Delta x = 1$, $\Delta/\Delta x = 3$, and $\Delta/\Delta x = 4$. The density and pressure along a vertical cut are compared in Fig. 2.24. The cut passes through the primary shock, the contact discontinuity, the secondary shock, and the expansion. As shown in Fig. 2.24, the profiles are virtually identical for each of these flow features, with the exception of the coarsest case. This further highlights the observation in Sec. 2.3.1 that a filter width/resolution ratio of $\Delta/\Delta x = 2$ is sufficient, even in more complex flow configurations.

2.5.3 Blunt-body flow

An inviscid Mach 2 flow past a square obstacle is tested. The grid size is 1000×200, the domain length and width are $L = 1$ mm and $W = 0.2$ mm, respectively. The obstacle is a $2 \cdot 10^{-5}$ m square located $4 \cdot 10^{-4}$ m from the inlet and centered vertically in the domain. The initial flow field is uniform $M = 2$ flow with $p = 101325$ Pa and $T = 298$ K, and these conditions are also imposed at the inlet. The inflow (left) and outflow (right) boundaries are treated with NSCBCs. The walls are inviscid. The

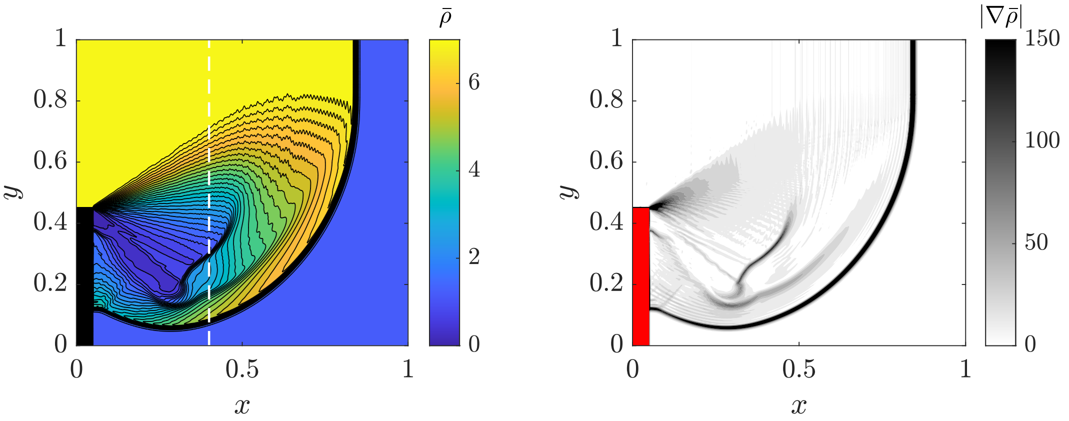

Figure 2.23: Contours of density (left) and density gradient magnitude (right). Corner step shown in black (left) or red (right). The density plot shows 30 contour levels spanning 0 to 7, as in [105]. ($\Delta/\Delta x = 2$).

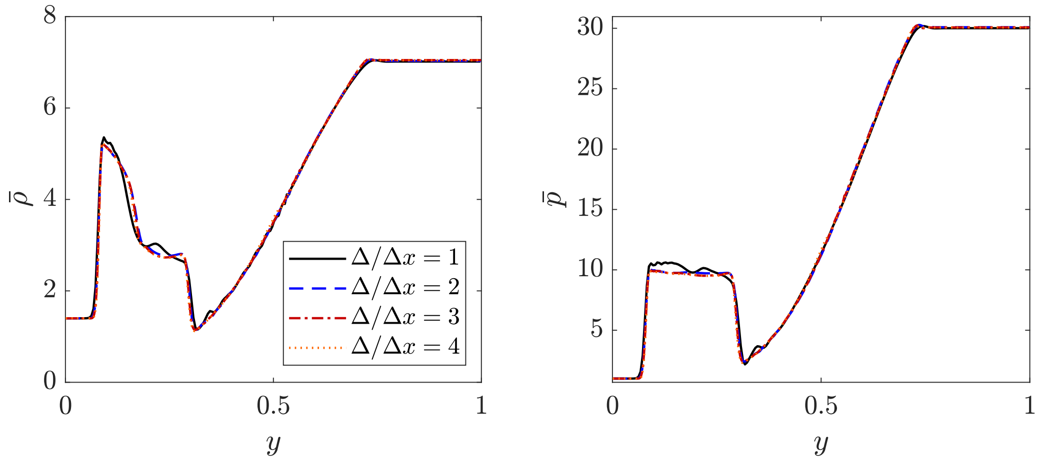

Figure 2.24: Density (left) and pressure (right) at $x = 0.4$ (cut shown in white dashed line in Fig. 2.23). Grid resolution of $\Delta/\Delta x = 1$ (black solid line), $\Delta/\Delta x = 2$ (blue dashed line), $\Delta/\Delta x = 3$ (red dash-dotted line), and $\Delta/\Delta x = 4$ (orange dotted line). Fixed $\Delta = 0.005$.

transverse (y) boundaries are periodic such that shocks are reflected downstream of the body. The timestep is restricted by a maximum CFL of 0.4. The resulting simulated Schlieren (density gradient magnitude) and SFS viscosity after $2 \cdot 10^{-6}$ s are shown in Fig. 2.25. Similar to the forward facing step, there is a bow shock followed by rarefaction fans at the left corners of the obstacle. The wake of the obstacle features two shear layers followed by vortex shedding. Since the flow is inviscid, the effective Reynolds number comes from the SFS viscosity. Farther downstream of the obstacle, the vortices interact with the reflected shocks. Due to the change in flow direction at the start of the wake region, a pair of secondary weak oblique shock waves form at the right corners of the obstacle. Both the primary (bow) shock and these secondary shocks reflect off the periodic boundaries and the centerline.

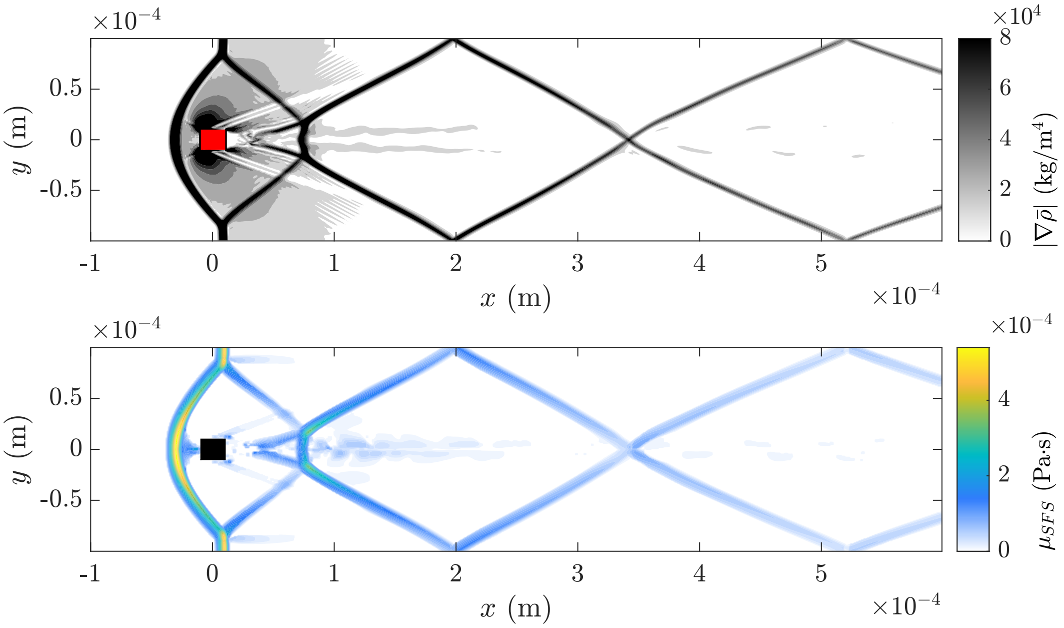

Figure 2.25: Contours of density gradient magnitude (top) and the SFS viscosity (bottom). Obstacle shown in red (top) or black (bottom). ($\Delta/\Delta x = 2$).

Comparing the simulated Schlieren with the μ_{SFS} contours, the larger values of μ_{SFS} are in the vicinity of the shocks (as expected). The shock locations and strengths are not known ahead of runtime, so Fig. 2.25 illustrates the ability of the SFS viscosity to detect shocks as they form. Minimal SFS viscosity is applied to the vortices in the wake, on the order of 10^{-5} Pa·s. At the rarefaction fans and in uniform regions (e.g. in the inflow before the bow shock), the SFS viscosity is on the order of 10^{-7} Pa·s, negligible compared to typical physical viscosity values for air.

2.6 Discussion

2.6.1 Comparison with localized artificial diffusivity (LAD)

The expressions for the SFS viscosity and conductivity derived in Sec. 2.1 resemble previously developed artificial fluid properties. To compare the effect of SFS properties with the effect of artificial properties, the oscillation amplitude and shock thickness are computed for a 1D shock using the same conditions from Kawai and Lele [33]. A Mach 2 shock is run at three grid resolutions: $\Delta x = 0.02$, 0.01, and 0.005 m. For each Δx, three filter widths are tested: $\Delta/\Delta x = 1$, 1.5, and 2. The timestep is restricted by a maximum CFL of 0.8, and the simulations are run to a steady state at $t = 3 \cdot 10^{-2}$ s. The initial and boundary conditions are specified as in Sec. 2.3. For consistency with the previous results shown for oscillation amplitude and shock thickness (Fig. 2.10 and 2.8, respectively), the theoretical velocity jump has been used again here.

The results computed from the pressure profiles are shown in Fig. 2.26 along with results obtained from the LAD scheme LADG-E4 [33]. The maximum pressure oscillation amplitude, normalized by the jump in pressure across the shock in Fig. 2.26a, shows that the ratio $\Delta/\Delta x$ has a much stronger impact on the oscillations compared to Δx alone. The $\Delta/\Delta x = 1$ cases have larger oscillations than the LADG-E4 results; this is expected as the filter width is insufficient to prevent cell-to-cell oscillations. Increasing the filter width to $\Delta/\Delta x = 1.5$ brings the amplitude slightly below that of the LADG-E4 oscillations, and increasing to $\Delta/\Delta x = 2$ leads to a larger drop in the amplitude. The shock thickness, normalized by Δx, also shows a stronger dependence on the ratio $\Delta/\Delta x$ than on Δx, as shown in Fig. 2.26b. The shocks with $\Delta/\Delta x = 1$ are thinner than the LADG-E4 shocks. The $\Delta/\Delta x = 1.5$ shocks are slightly thicker than the LADG-E4 shocks, and the $\Delta/\Delta x = 2$ shocks are the thickest. The LADG-E4 results are from simulations using a sixth-order compact differencing scheme, not a second-order centered differencing scheme. The minimum required $\Delta/\Delta x$ is likely scheme dependent. The results in Fig. 2.26 illustrate the trade-off between oscillation amplitude and shock thickness; reducing the magnitude of the oscillations leads to an increase in the number of grid points per shock thickness.

The SFS properties and localized artificial viscosities/diffusivities can also be computed and compared directly. For fair comparison, the SFS viscosities are computed with a filter width ratio $\Delta/\Delta x = 1.5$, as this value had the closest results to the LAD method (see Fig. 2.26). To isolate the properties from the specific numerical schemes used (i.e., second-order staggered vs. tenth-order compact), the same gradient operators (second-order centered) are used in computing both the SFS and LAD properties. The artificial fluid properties introduced by Cook [32] are defined as

$$\mu^* = C_\mu \overline{\rho |\nabla^r S|} \Delta^{(r+2)}, \tag{2.119}$$

$$\beta^* = C_\beta \overline{\rho |\nabla^r S|} \Delta^{(r+2)}, \tag{2.120}$$

$$\kappa^* = C_\kappa \overline{\frac{\rho c_s}{T} |\nabla^r e|} \Delta^{(r+1)}, \tag{2.121}$$

where $C_\mu = 0.002$, S is the magnitude of the strain rate tensor, Δ is the local grid

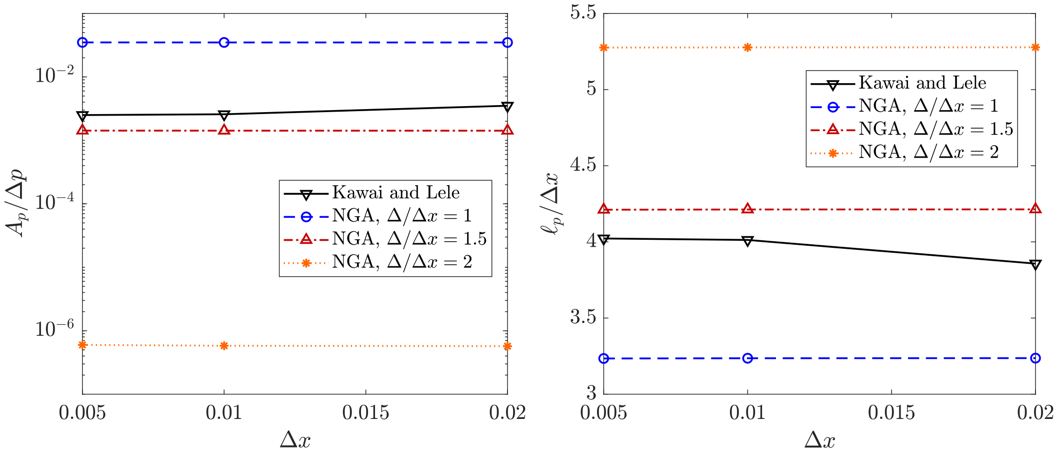

(a) Relative oscillation amplitude.

(b) Shock thickness.

Figure 2.26: Results for a Mach 2 shock comparing SFS properties with LADG-E4 properties from Kawai and Lele [33]. Maximum pressure oscillation amplitude normalized by the jump in pressure across the shock (left). Shock thickness computed from pressure normalized by the grid spacing (right). LADG-E4 (black triangles/solid line) and SFS with $\Delta/\Delta x = 1$ (blue circles/dashed line), $\Delta/\Delta x = 1.5$ (red triangles/dash-dotted line), and $\Delta/\Delta x = 2$ (orange asterisks/dotted line).

spacing, $C_\beta = 1$, $C_\kappa = 0.01$, and c_s is the sound speed. For details on the stencil used for the truncated Gaussian filter $(\bar{\cdot})$, the reader is referred to [32]. Lee and Lele [36] used the same definitions for the artificial shear viscosity μ^* and artificial conductivity κ^*, but used an artificial bulk viscosity based on the dilatation,

$$\beta^* = C_\beta \overline{\rho |\nabla^r \nabla \cdot \mathbf{u}|} \Delta^{(r+2)}, \tag{2.122}$$

similar to the form recommended by Mani et al. [34]. Data for the density, velocity, energy, and temperature from a Mach 2 shock are used to calculate the artificial properties given by Eq. (2.119) to (2.122). The same data is used to compute the SFS properties, with the velocity jump estimated using Eq. (2.95) to (2.104). The properties are compared in Fig. 2.27.

The SFS shear viscosity and conductivity are much larger than their artificial counterparts, while the SFS bulk viscosity is comparable to the artificial bulk viscosity. To analyze these results, it is insightful to consider ratios of two of these properties. The ratio of shear to bulk viscosity depends on the tuning parameters C_μ and C_β for the LAD method. For Cook's model [32], it is a constant, namely $\mu^*/\beta^* = C_\mu/C_\beta = 0.002$. In contrast, for the SFS viscosities, this ratio is derived analytically to be $3/2$ (as shown in Sec. 2.1.2.2). Similarly, a Prandtl number may

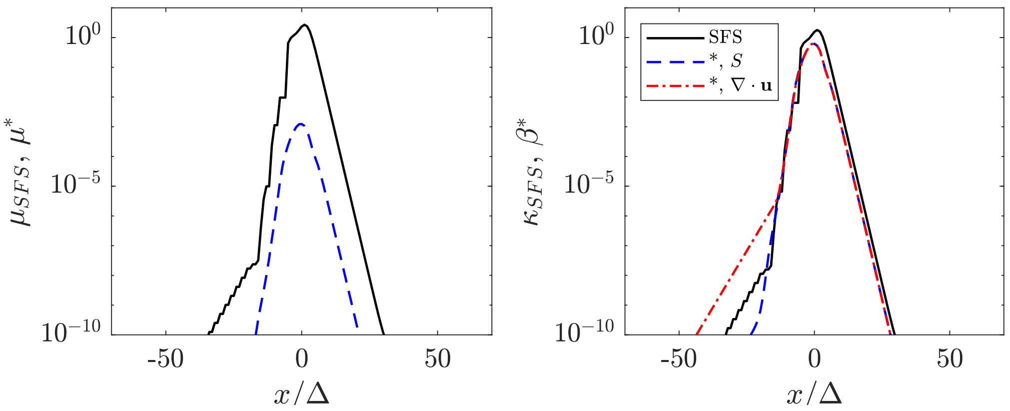

(a) Viscosities.

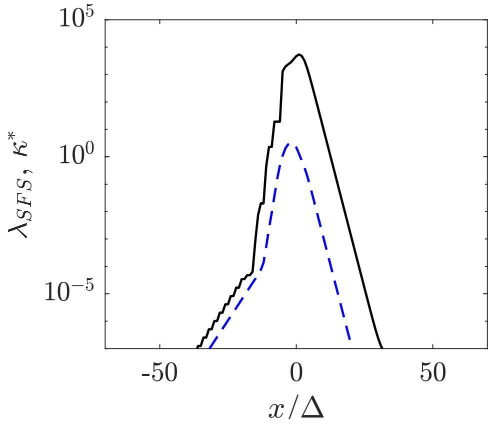

(b) Conductivity.

Figure 2.27: SFS properties (black solid line), artificial properties from [32] (blue dashed line), artificial bulk viscosity from [36] (red dash-dotted line). SFS/artificial shear viscosity (a, left), bulk viscosity (a, right), and conductivity (b). The shock is located at $x/\Delta = 0$.

be computed as the ratio of kinematic viscosity and thermal diffusivity. The Prandtl number for the artificial properties is given by

$$Pr^* = \frac{\nu^*}{\alpha^*} = \frac{\mu^* c_p}{\kappa^*} = \frac{C_\mu \overline{\rho |\nabla^r S|} \Delta c_p}{C_\kappa \overline{\frac{\rho c_s}{T} |\nabla^r e|}}. \tag{2.123}$$

This Prandtl number varies by several orders of magnitude, as can be seen in Fig. 2.28. In contrast, for the SFS properties, the Prandtl number is shown mathematically to be constant and, once again, order unity.

$$Pr_{SFS} = \frac{\nu_{SFS}}{\alpha_{SFS}} = \frac{(u_1 - u_2)\frac{\Delta}{4}}{(u_1 - u_2)\frac{\Delta}{2}} = \frac{1}{2}. \tag{2.124}$$

To compare the SFS and artificial viscosities in a more complex configuration, the data from the forward facing step is used to compute the properties. The bulk

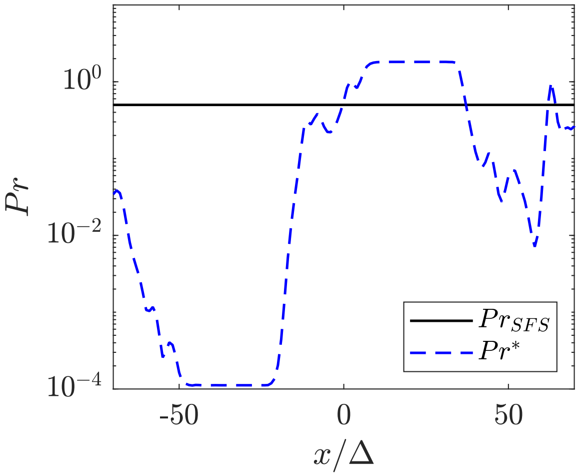

Figure 2.28: Prandtl number computed using SFS properties (black solid line) and artificial properties (blue dashed line). The shock is located at $x/\Delta = 0$.

viscosities are shown in Fig. 2.29 for the full domain, and along $y = 0.3$ in Fig. 2.30. Overall, the larger values of bulk viscosity appear in similar regions around the shocks, as expected. However, the artificial bulk viscosity (using both definitions) is much larger than the SFS bulk viscosity between the bow shock and leading edge of the step, and in parts of the expansion around the corner. The higher order velocity derivatives used in computing β^* detect changes through expansions, whereas the method for computing $u_{1n} - u_{2n}$ in κ_{SFS} does not. Also, although the artificial bulk viscosity has smoother variation throughout the domain, the SFS bulk viscosity is about an order of magnitude lower in the uniform inflow and in some regions away from shocks, $O(10^{-5})$ and $O(10^{-4})$ for the SFS and artificial viscosities, respectively.

2.6.2 Limitations

As demonstrated in the test cases in Sec. 2.3 to 2.5, the proposed SFS closure of the filtered Euler equations has a wide range of applicability. All 1D shocks tested ($M = 1.01$ to 20) reach a steady solution. For most of this range, the SFS viscosity is sufficient to prevent cell-to-cell oscillations. The formulation also works for both steady and unsteady shocks. The 1D shock and detonation simulations are performed in the shock-fixed frame (steady), while the remaining test cases are performed in the lab frame (unsteady). Using the multi-dimensional closure, the method is shown to be robust for a range of shock angles and curvatures. Finally, the SFS terms also perform well near walls at reflecting shocks and Mach stems.

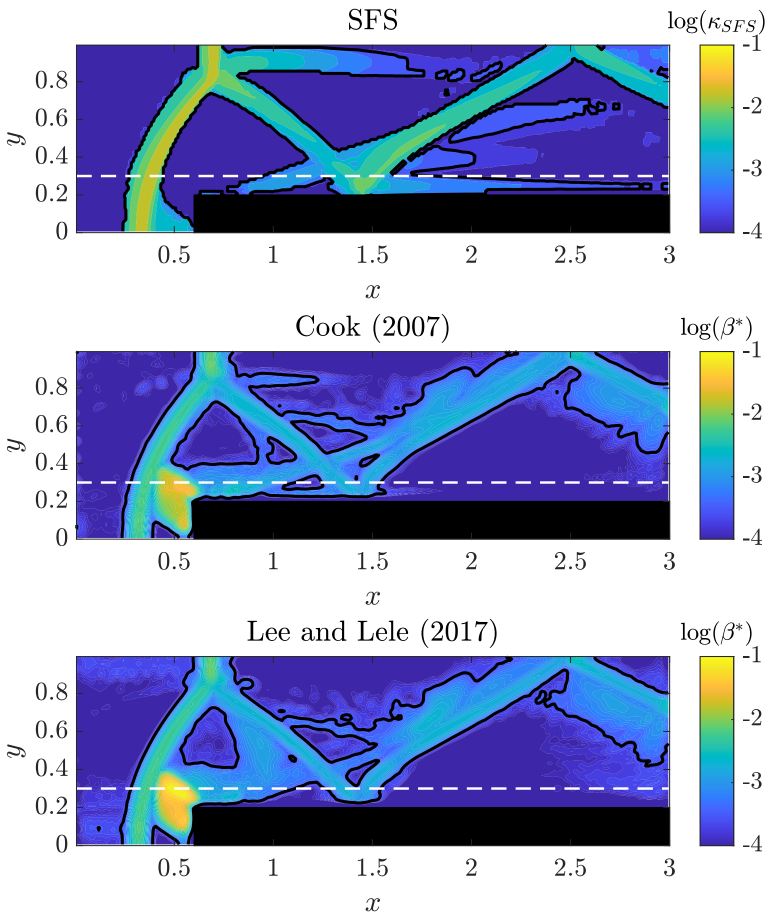

Figure 2.29: Bulk viscosities for the forward facing step. SFS (top), artificial based on S [32] (middle), artificial based on $\nabla \cdot \mathbf{u}$ [36] (bottom). Contour at a value of $\log(\kappa_{SFS}) = \log(\beta^*) = -3.5$ (black line).

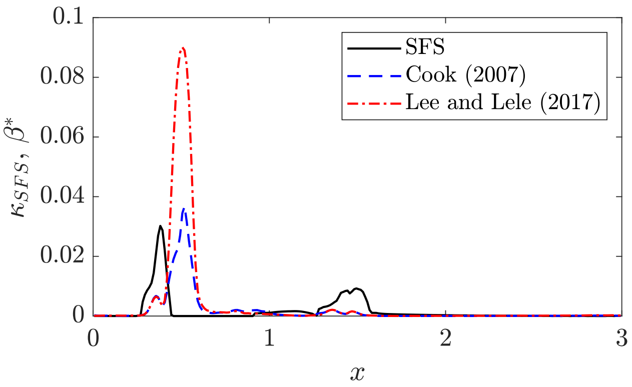

Figure 2.30: Bulk viscosities for the forward facing step at $y = 0.3$ (cut shown in white dashed line in Fig. 2.29). SFS (black solid line), artificial based on S [32] (blue dashed line), artificial based on $\nabla \cdot \mathbf{u}$ [36] (red dash-dotted line).

Despite these successes, there are a few limitations to the presented closure of the SFS terms. First, as shown in Sec. 2.3.2, the weaker shocks ($M < 1.4$) are too spread, thicker than the analytical shock thickness. For the weakest shocks ($M < 1.1$), the absolute oscillation amplitude decreases as expected as the Mach number is reduced. However, the relative oscillation amplitude remains large and the SFS viscosity is not sufficient; so molecular viscosity is required to prevent oscillations. Second, for the blunt-body flow in Sec. 2.5, the presence of SFS viscosity leads to viscous vortex shedding that should not exist in inviscid flow simulations. There is some SFS viscosity detected in these vortices, although much smaller in magnitude, $O(10^{-5})$ Pa·s, compared to $O(10^{-4})$ Pa·s in shocks. Lastly, the analytical closure leads to zero SFS terms for contact discontinuities. As a result, the SFS properties do not treat numerical errors associated with the transport of contact discontinuities. The treatment of contact discontinuities within the filtered framework will be discussed in Chapter 3.

2.7 Burgers' equation and the sonic glitch

The sonic glitch is a well-known numerical artifact observed near the sonic point in rarefaction waves for many shock capturing schemes, including the Godunov and Roe schemes [107]. In the present work, the SFS framework is demonstrated to prevent oscillations near shocks in a centered finite difference solver. However, this methodology is not limited to the Euler equations or any specific numerical framework. To demonstrate this, we apply the methodology to Burgers' equation and solve the numerical simulations with the Godunov scheme. Following the same mathematical procedure as in Sec. 2.1, the filtered Burgers' equation is

$$\frac{\partial \bar{u}}{\partial t} + \bar{u}\frac{\partial \bar{u}}{\partial x} = \frac{\partial}{\partial x}\left(\tau_{SFS}\right), \tag{2.125}$$

where the SFS stress is given by

$$\begin{aligned} \tau_{SFS} &= \frac{1}{2}\left(\bar{u}\bar{u} - \overline{uu}\right) &(2.126)\\ &= (u_1 - u_2)\frac{\Delta}{4}\frac{\partial \bar{u}}{\partial x}. &(2.127) \end{aligned}$$

Because there is no density present in Burgers' equation, rather than following the full procedure outlined in Sec. 2.3.4, the jump $(u_1 - u_2)$ is simply estimated by

$$(u_1 - u_2)(x) \approx \max_{x'=x\pm 3\Delta x}\{\bar{u}(x')\} - \min_{x'=x\pm 3\Delta x}\{\bar{u}(x')\}. \tag{2.128}$$

First, we consider the sonic rarefaction wave, for which Godunov's scheme is known to exhibit a sonic glitch [107]. The sonic rarefaction wave is given by

$$u(x,t) = \begin{cases} u_L, & x < u_L t, \\ x/t, & u_L t \leq x \leq u_R t, \\ u_R, & x > u_R t, \end{cases} \tag{2.129}$$

where $u_R = 1$ and $u_L = -u_R$ [107]. The domain spans $-2 \leq x \leq 2$ with 150 grid cells, and the simulation is run from $t = 0.1$ to $t = 1$ with the CFL limited to 0.9. Figure 2.31a compares the exact solution (both unfiltered and filtered) with the numerical solutions obtained using the Godunov scheme alone, and the Godunov scheme with the SFS viscosity using $\Delta/\Delta x = 2$. The inset illustrates the sonic point at $x = 0$. Without SFS viscosity (i.e. Godunov scheme alone), the sonic glitch is observed. With the addition of SFS viscosity, the sonic glitch is no longer visible.

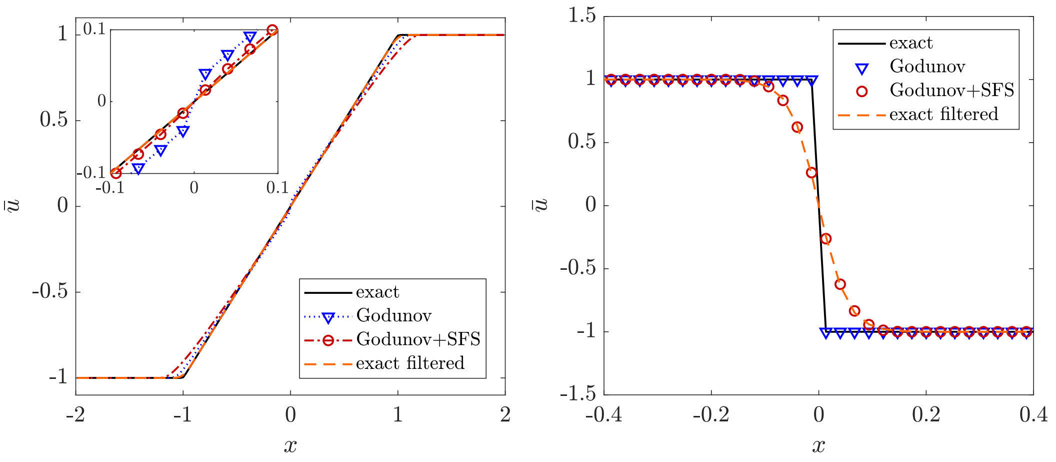

(a) Expansion.

(b) Shock.

Figure 2.31: Burgers' equation solved for an expansion (left) and shock (right). Exact solution (black solid line), solution using Godunov scheme (blue dotted line and triangles), solution using Godunov scheme with SFS (red dash-dotted line and circles), exact filtered shock (orange dashed line).

Second, Burgers' equation is also tested with a shock wave, whose initial condition is given by

$$u(x,t) = \begin{cases} u_L, & x < 0, \\ u_R, & x > 0, \end{cases} \tag{2.130}$$

where $u_L = 1$ and $u_R = -u_L$. The domain and grid size are the same as for the sonic rarefaction, and the simulation is run from $t = 0$ to $t = 1$ with the CFL limited to 0.9. The sonic point is once again located at $x = 0$. Figure 2.31b compares the exact solution with the numerical solution using the Godunov scheme alone, and the exact filtered solution with the numerical solution using the Godunov scheme with SFS viscosity using $\Delta/\Delta x = 2$. No numerical issues are observed at the sonic point. While the SFS viscosity spreads the shock over more points than the Godunov scheme alone, the numerical solution closely matches the analytically filtered solution.

2.8 Conclusion

This chapter introduced a physical approach to spreading the shock interface, which can be applied to any computational framework. Drawing from the methodology of Large Eddy Simulation to model small-scale flow features, the necessary and sufficient diffusion terms were derived by spatially-filtering the Euler equations. Analytical closure was provided for the SFS terms by leveraging the shock jump conditions. The framework was validated for several shock-dominated flow configurations.

Chapter 3

A NUMERICAL EXTENSION OF THE SPATIALLY-FILTERED EULER EQUATIONS FOR CONTACT DISCONTINUITIES

[1] A. Baumgart and G. Blanquart. “A numerical extension of the spatially-filtered Euler equations for contact discontinuities”. In: *Journal of Computational Physics* 491 (2023), p. 112353. DOI: `https://doi.org/10.1016/j.jcp.2023.112353`.

In Chapter 2, the spatially-filtered framework was developed and validated for shock-dominated flows. The treatment of contact discontinuities within the spatially-filtered Euler equation framework deserves special consideration. Contact discontinuities take the form of a jump in density without any associated discontinuities in velocity or pressure. This density discontinuity may come from a jump in either temperature or species composition, or both. From a theoretical point of view, these contact discontinuities are fundamentally different from shocks because the density profile is not subject to front sharpening and remains unaffected by transport. That is why the SFS terms are identically zero for contact discontinuities (see Sec. 2.1). In numerical simulations, the situation is different. Even if the initial density profile is smooth and adequately resolved on a given grid, its numerical transport (even in a one-dimensional uniform flow field) leads to either artificial oscillations or artificial smearing [108]. The first phenomenon is due to dispersive errors; the second is due to diffusive errors.

The objective of this chapter is to formulate a WENO-like correction term for the energy equation to counteract dispersive errors encountered in contact discontinuities and inherent to centered schemes. By using a WENO interpolation, there is no need to tune coefficients, as required by artificial diffusivities. Furthermore, unlike Riemann solvers that treat the entire system of Euler equations, this approach allows for an isolated treatment of the enthalpy transport. This is analogous to the use of the WENO scheme for the convective flux in the species transport equation (to be discussed in detail in Chapter 4).

A numerical extension of the framework for contact discontinuities is described in Sec. 3.1. A variety of tests involving contact discontinuities (both in temperature and composition) are included in Sec. 3.2.

3.1 Numerical extension for contact discontinuities

As demonstrated in Chapter 2, the present numerical framework leads to numerically smooth solutions of shock-dominated flows thanks to the SFS terms,

$$\tau_{ij,SFS} = \overline{\rho}(u_{1n} - u_{2n})\frac{\Delta}{4}\left(\frac{\partial \tilde{u}_i}{\partial x_j} + \frac{\partial \tilde{u}_j}{\partial x_i}\right), \tag{3.1}$$

$$q_{i,SFS} = \overline{\rho} c_p (u_{1n} - u_{2n})\frac{\Delta}{2}\frac{\partial \tilde{T}}{\partial x_i} + \tau_{ij,SFS} \cdot \tilde{u}_j. \tag{3.2}$$

However, the numerical solutions of contact discontinuities are not smooth (see Fig. 3.2). As mentioned in Sec. 2.1, analytically, there is no SFS diffusivity for contact discontinuities. From a numerical perspective, the conservative centered scheme introduces dispersive errors, resulting in unphysical oscillations. The convective flux in the energy equation is discretized at each face as $\overline{(\rho e_t + p)}^x u$, in theory allowing the pressure to remain constant across a contact after the interpolation operation. However, this is not sufficient to prevent oscillations. To effectively switch to a less dispersive scheme for the enthalpy without impacting the kinetic energy, an “anti-dispersion” term is constructed by modifying the convective fluxes as

$$\begin{aligned} \overline{(\rho e_t + p)}^x u \quad &\rightarrow \quad \overline{(\rho e_t + p)}^x u + q_{W5}, \\ q_{W5} &= (\rho u)\overline{h}^{W5} - \overline{\rho h}^x u, \end{aligned} \tag{3.3}$$

where $\overline{\phi}^x$ is the second-order central difference interpolation, and $\overline{\phi}^{W5}$ is the fifth-order WENO interpolation [21]. This deferred correction term, q_{W5}, subtracts off the central difference interpolation of the enthalpy component of the convective flux, replacing it with the WENO interpolation of the flux. The WENO component is discretized to be consistent with continuity, using the face-centered momentum (ρu). The divergence of the modified fluxes is then computed, maintaining primary conservation of total energy.

The total energy is given by $e_t = e + \frac{1}{2}u^2$, and the enthalpy is given by $h = e + p/\rho$, so the original convective flux can be written as

$$\overline{(\rho e_t + p)}^x u = \overline{\rho h}^x u + \frac{1}{2}\overline{\rho u^2}^x u. \tag{3.4}$$

Adding the deferred correction term (q_{W5}) from Eq. (3.3) to Eq. (3.4), the new convective flux becomes

$$\begin{aligned} \overline{(\rho e_t + p)}^x u + q_{W5} &= \overline{\rho h}^x u + \frac{1}{2}\overline{\rho u^2}^x u + (\rho u)\overline{h}^{W5} - \overline{\rho h}^x u \\ &= (\rho u)\overline{h}^{W5} + \frac{1}{2}\overline{\rho u^2}^x u. \end{aligned} \tag{3.5}$$

In summary, the enthalpy flux is practically replaced with the non-dispersive WENO interpolation of the flux.

As written above, the WENO interpolation is performed on the enthalpy with stencil coefficients computed from the same profile. For a contact discontinuity of a single component fluid at constant c_p, the enthalpy is given by $h = c_p T$, so the correction term may be written equivalently as

$$q_{W5} = (\rho u)\overline{c_p}^{x}\overline{T}^{W5} - \overline{\rho c_p T}^{x} u, \tag{3.6}$$

where the WENO interpolation is performed directly on T. For simulations with constant c_p (as in the test problems in Sec. 3.2.1 and 3.2.2), there is no difference between the discretizations in Eq. (3.3) and (3.6). In Sec. 3.2.3, the two interpolations ($\overline{h}^{W5}$ vs. $\overline{c_p}^{x}\overline{T}^{W5}$) will be compared in temperature and enthalpy discontinuities with variable c_p and mixture composition to evaluate the performance of the two discretizations.

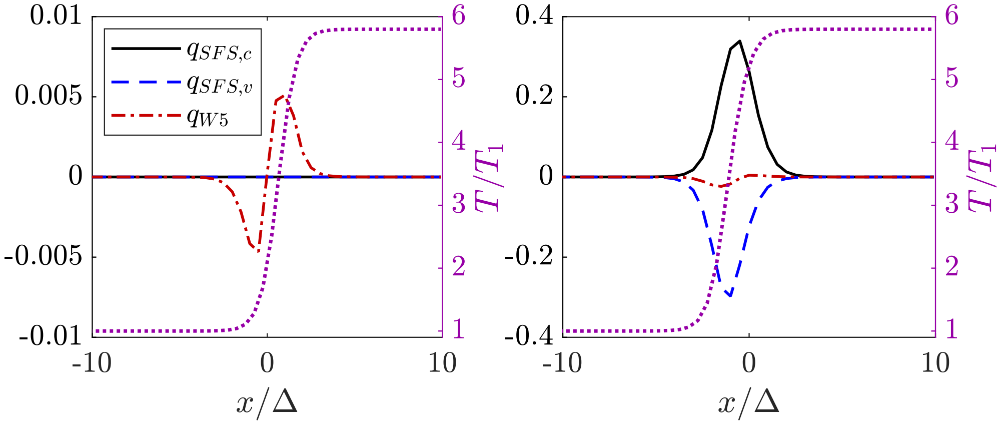

(a) Contact discontinuity.

(b) Shock.

Figure 3.1: Flux terms in the energy equation, normalized by $\rho_1 u_1 c_p \Delta T$. SFS conduction term ($q_{SFS,c} = \overline{\rho} c_p (u_{1n} - u_{2n}) \frac{\Delta}{2} \frac{\partial \tilde{T}}{\partial x}$, black solid line), SFS viscous term ($q_{SFS,v} = \tau_{SFS} \cdot \tilde{u}$, blue dashed line), and WENO correction term (q_{W5}, red dash-dotted line). Normalized temperature (purple dotted line, right axis). ($\Delta/\Delta x = 2$).

Comparison of the additional term in Eq. (3.3) with the SFS terms (Eq. (3.2)) is shown in Fig. 3.1a for a contact discontinuity and in Fig. 3.1b for a shock, both with a temperature jump corresponding to a Mach 5 shock. The WENO correction term is the only active term for the contact discontinuity, but it is negligible compared to the SFS terms for the shock. In both cases, the shape of the correction term is consistent with a dispersive error.

The WENO scheme was selected for its non-oscillatory property to counteract dispersive errors specific to our schemes; the deferred correction approach itself is not restricted to standard WENO schemes. Other schemes, such as upwind differencing or TVD schemes, also prevent oscillations at discontinuities and could be used in a similar manner. WENO schemes are preferred as they allow for a high order of accuracy to be achieved. In our case, the fifth-order WENO interpolation is used because it is the highest order WENO interpolation that does not require additional ghost cells; the SFS terms in Eq. (3.1) and (3.2) already require a stencil of ±3 grid points to estimate the shock-normal velocity jump (see Sec. 2.3.4 for details). Despite these advantages, it is well-documented that WENO schemes require additional sharpening to prevent excessive smearing of contacts [21, 26–28]. Such sharpening methods may be incorporated readily into the deferred correction; however, that is outside the scope of this work.

3.2 Contact discontinuity results

3.2.1 Sod shock tube problem

The Sod problem is a standard test for shocks and contact discontinuities. Initially, a diaphragm divides the domain into high and low pressure regions. On the left, the pressure and density are both 1.0; on the right, the pressure is 0.1 and density is 0.125. The initial velocity is 0. When the diaphragm ruptures at $t = 0$, a rarefaction wave propagates to the left, and a shock and a contact discontinuity propagate to the right. The domain length $L = 4$, grid spacing $\Delta x = 0.002$, and filter width $\Delta = 0.004$. The timestep is restricted by a CFL of 0.8. Results at $t = 0.25$ are shown in Fig 3.2. An exact filtered solution is obtained by integrating the exact solution [109] with a Gaussian filter kernel of width Δ. As expected, the SFS terms are sufficient to treat the shock, but not the contact. Including the WENO correction term prevents oscillations in the contact without additional spreading of the shock. The shock location is also unchanged with the addition of the correction term, indicating that the modification in Eq. (3.3) has not affected the propagation speed of the shock.

3.2.2 Shock diffraction over 90 degree corner

The diffraction of a shock over a corner involves a curved contact discontinuity. The setup was described previously in Sec. 2.5. The grid size $\Delta x = 0.0025$, and the timestep $\Delta t = 10^{-5}$ s. Figure 3.3 shows the results at $t = 0.1561$ both without and with the WENO correction term. The contact discontinuity, located behind the lead

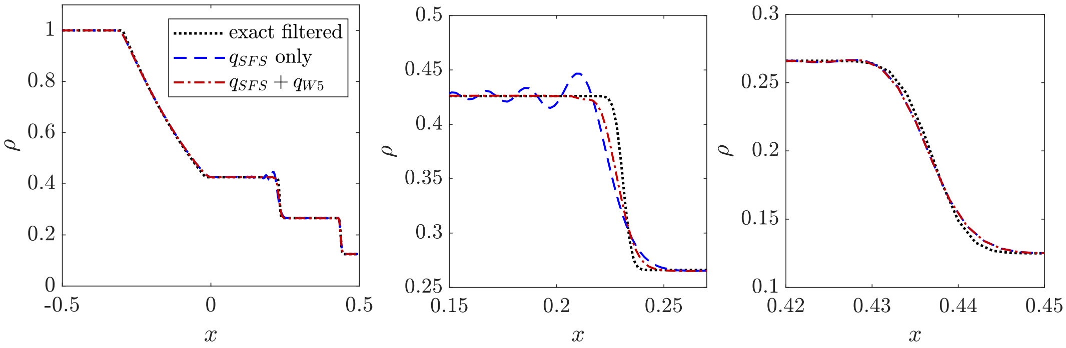

(a) Sod problem. (b) Contact. (c) Shock.

Figure 3.2: Comparison of Sod shock tube results with the exact filtered Riemann solution. Exact filtered solution (black dotted line), q_{SFS} with no WENO (blue dash-dotted line), q_{SFS} with WENO (red dash-dotted line). ($\Delta/\Delta x = 2$).

shock, exhibits oscillations that pollute the expansion region when the WENO term is not included. When the term is added, the post-contact oscillations are prevented and the shocks are unaffected. As in the Sod problem, neither the shock location nor its thickness have been altered.

3.2.3 Contact discontinuities in variable mixture compositions

In the Sod problem and shock diffraction, no species are present, and the specific heat capacity is a constant. In such cases, there is no difference between using $\overline{c_p}^x \overline{T}^{W5}$ or $\overline{h}^{W5}$ in the WENO correction term. To determine which interpolation is best, two types of contact discontinuities with species are tested: a discontinuity in temperature with constant mixture enthalpy, and a discontinuity in mixture enthalpy with constant temperature. For both cases, the uniform pressure and velocity are $p_0 = 101325$ Pa and $u_0 = 100$ m/s, respectively. Mixtures of Ar and H are used to obtain the desired changes in T and h; both these gases are monatomic and therefore have constant c_p. Chemical reactions are not included in the simulations. The left and right initial states are summarized in Table 3.1.

	T_1 (K)	h_1 (J/g)	$Y_{Ar,1}$	$Y_{H,1}$	T_2 (K)	h_2 (J/g)	$Y_{Ar,2}$	$Y_{H,2}$
$T(Y_i)$, const. h	300	21630	0.9	0.1	1500	21630	0.913	0.087
$h(Y_i)$, const. T	2000	885.5	1.0	0.0	2000	8855	0.968	0.032

Table 3.1: Initial conditions for the temperature and enthalpy discontinuities; subscripts 1 and 2 indicate the left and right states, respectively.

The domain length $L = 1$ m, $\Delta x = 0.005$ m, and the discontinuity is initialized at

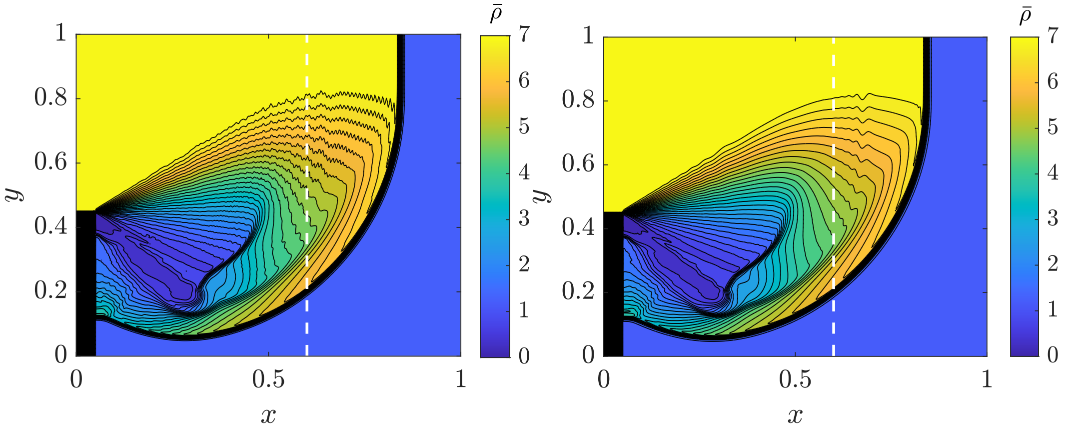

(a) Without WENO correction term.

(b) With WENO correction term.

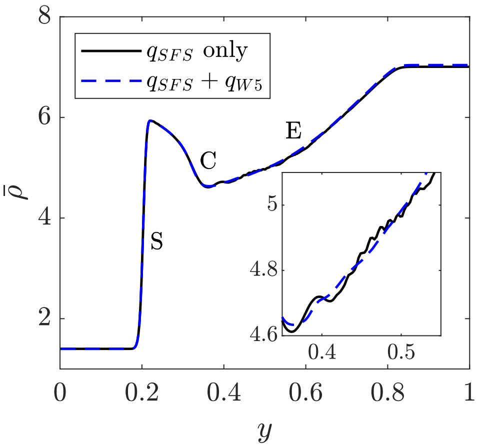

(c) 1D cut along $x = 0.6$.

Figure 3.3: Contours of density (left and center), with 30 contour levels from 0 to 7 (as in [105]). Vertical cut (white dashed line/right) showing the primary shock (S), contact (C), and expansion (E); q_{SFS} with no WENO (black solid line) and q_{SFS} with WENO (blue dashed line. ($\Delta/\Delta x = 2$).

$L/2$. The timestep is $\Delta t = 10^{-6}$ s, and the simulations are run for a total time 10^{-3} s. The results are shown in Fig. 3.4 for the temperature discontinuity and Fig. 3.5 for the enthalpy discontinuity. For both cases, using a WENO interpolation on h instead of T leads to smoother density profiles and smaller errors in the constant quantity (h in Fig. 3.4 and T in Fig. 3.5). Based on these results, using $\overline{h}^{W5}$ is preferable, as in Eq. (3.3).

3.3 Conclusion

Solving the spatially-filtered Euler equations with a kinetic energy-preserving centered discretization is an efficient framework for simulating shock-dominated flows. In this chapter, a numerical extension was presented for simulating contact discon-

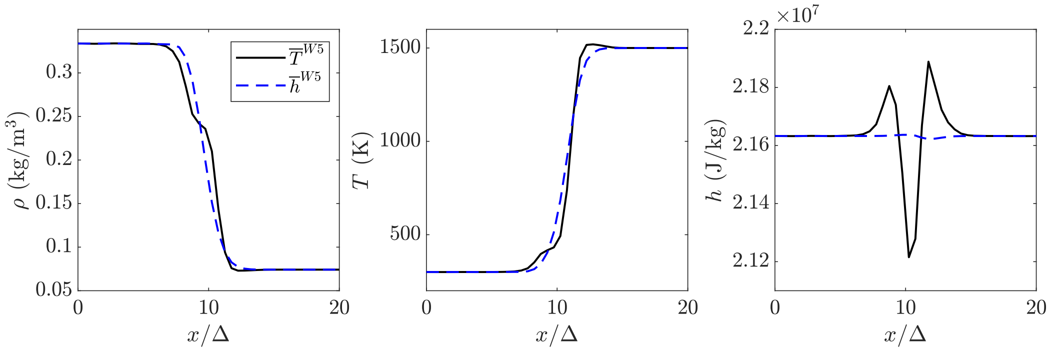

(a) Density. (b) Temperature. (c) Enthalpy.

Figure 3.4: Profiles for a variable temperature, constant enthalpy contact discontinuity. Deferred correction term with WENO interpolation on temperature (black solid line), correction term with WENO interpolation on enthalpy (blue dashed line). ($\Delta/\Delta x = 2$).

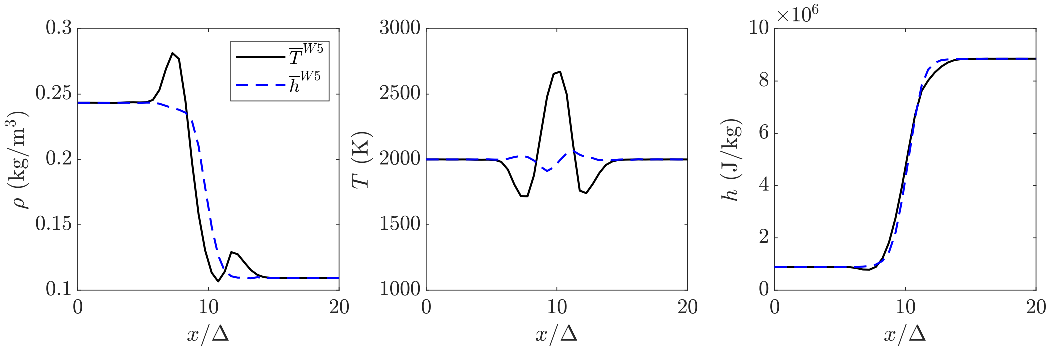

(a) Density. (b) Temperature. (c) Enthalpy.

Figure 3.5: Profiles for a variable enthalpy, constant temperature contact discontinuity. Deferred correction term with WENO interpolation on temperature (black solid line), correction term with WENO interpolation on enthalpy (blue dashed line). ($\Delta/\Delta x = 2$).

tinuities. The enthalpy transport was treated with a WENO-like deferred correction term, while the overall spatial discretization remained centered. The method was demonstrated for the Sod shock tube problem in one dimension and the shock diffraction in two dimensions.

Chapter 4

DETONATION SIMULATIONS WITH DETAILED CHEMISTRY

[1] A. Baumgart and G. Blanquart. “Ensuring $\sum_s Y_s = 1$ in transport of species mass fractions”. In: *Journal of Computational Physics* (2024), p. 113199. DOI: `https://doi.org/10.1016/j.jcp.2024.113199`.

[2] A. Baumgart, M. X. Yao, and G. Blanquart. “Tabulated chemistry approach for detonation simuations”. In: *Combustion and Flame* (2024). (Under Review).

Detonation simulations with detailed chemistry typically rely on solving $N-1$ species transport equations to maintain a sum of mass fractions equal to 1; unfortunately, this forces inert species to absorb any numerical errors in the species transport. In this chapter, a simple method for preserving the sum of mass fractions without penalizing the inert species is proposed. The approach is demonstrated to improve detailed chemistry simulations of detonations. In Sec. 4.1, a correction to the species discretization is proposed to ensure that the transported mass fractions sum to 1. The simulation setup for the detonation simulations is described in Sec. 4.2. One- and two-dimensional results are presented in Sec. 4.3 and 4.4, respectively, for both regular and irregular H_2-O_2 mixtures. The two-dimensional argon-diluted case that will be used to inform the methodology in Chapter 5 is presented in Sec. 4.5.

4.1 Species discretization

Analytically, summing over the species transport equations (Eq. (2.11)) results in the continuity equation (Eq. (2.8)),

$$\sum_{s=1}^{N}\left(\frac{\partial(\rho Y_s)}{\partial t}+\frac{\partial(\rho u_i Y_s)}{\partial x_i}=-\frac{\partial j_{i,s}}{\partial x_i}+\dot{\omega}_s\right)\rightarrow\left(\frac{\partial \rho}{\partial t}+\frac{\partial(\rho u_i)}{\partial x_i}=0\right), \tag{4.1}$$

with the conditions

$$\sum_{s=1}^{N} Y_s = 1, \quad \sum_{s=1}^{N} j_s = 0, \quad \sum_{s=1}^{N} \dot{\omega}_s = 0, \tag{4.2}$$

where N is the number of species. Unfortunately, when all N species equations are solved in addition to the continuity equation, Eq. (4.1) is not guaranteed discretely.

In one dimension, the convective terms in Eq. (2.8) and (2.11) are spatially discretized as

$$\begin{aligned} \frac{\partial(\rho u)}{\partial x} &\approx \frac{(\rho u)_{i+1/2} - (\rho u)_{i-1/2}}{\Delta x_i}, \\ \frac{\partial(\rho u Y_s)}{\partial x} &\approx \frac{(\rho u)_{i+1/2} Y_{s,i+1/2} - (\rho u)_{i-1/2} Y_{s,i-1/2}}{\Delta x_i}, \end{aligned} \tag{4.3}$$

where $(\rho u)_{i+1/2}$ is known naturally due to the staggering, and $Y_{s,i+1/2}$ is the face value that requires interpolation from the cell averages ($Y_{s,i}$, $Y_{s,i+1}$,...).

When a linear scheme, such as first order upwind, is used to interpolate the mass fractions, the stencil coefficients, c_i, are independent of the species s. For instance, for an interpolation between two cells,

$$\begin{aligned} & Y_{s,i+1/2} = c_i \cdot Y_{s,i} + c_{i+1} \cdot Y_{s,i+1} \\ \rightarrow \quad & \sum_s Y_{s,i+1/2} = c_i \sum_s Y_{s,i} + c_{i+1} \sum_s Y_{s,i+1} = c_i + c_{i+1} = 1, \end{aligned} \tag{4.4}$$

the summation of the interpolated values equals 1 as long as the initial cell-centered sums are also equal to 1. When a nonlinear scheme is used, the sum of the interpolated Y_s is not guaranteed to equal 1, because the stencil coefficients, $f(Y_{s,i})$, are dependent on the species. For instance, for an interpolation between two cells,

$$\begin{aligned} & Y_{s,i+1/2} = f(Y_{s,i}) \cdot Y_{s,i} + f(Y_{s,i+1}) \cdot Y_{s,i+1} \\ \rightarrow \quad & \sum_s Y_{s,i+1/2} = \sum_s \left(f(Y_{s,i}) \cdot Y_{s,i} + f(Y_{s,i+1}) \cdot Y_{s,i+1} \right) \neq 1. \end{aligned} \tag{4.5}$$

In practice, this can lead to an error in $\sum_s Y_s$ that grows throughout the simulation. Commonly used scalar transport schemes, including WENO schemes [21], fall into this category. The methodology is illustrated for the fifth order WENO scheme and can be easily extended to other nonlinear schemes. As mentioned earlier, there are a few options to improve the sum of mass fractions.

Option 1: Recognizing that Eq. (2.8) and Eq. (2.11) are over-constrained, $N-1$ species equations may be solved instead of N equations. Then, the Nth mass fraction is computed as $Y_N = 1 - \sum_{s=1}^{N-1} Y_s$ (e.g., [47]). However, this requires selecting *one species* to absorb all of the error in $\sum_s Y_s$.

Option 2: Another simple approach involves normalizing the WENO-interpolated mass fractions by their sum (e.g., [48]), $\overline{Y_s} = \overline{Y_s}^W \Big/ \sum_s \overline{Y_s}^W$, where $\overline{Y_s} = Y_{s,i+1/2}$ is the final interpolated mass fraction, and $\overline{\cdot}^W$ indicates the WENO-interpolated value. This approach distributes the error in the sum of mass fractions *over all species.*

However, as in option 1, this approach leads to errors in inert species, such as N_2 or Ar.

Option 3: Here, we propose a third option consisting of weighting between the WENO and upwind interpolations to enforce $\sum_s Y_s = 1$ without altering inert species. The key observation is that

$$\min\{\overline{Y_s}^W, \overline{Y_s}^U\} \le \overline{Y_s}^W \le \max\{\overline{Y_s}^W, \overline{Y_s}^U\}, \tag{4.6}$$

where $\overline{\cdot}^U$ indicates the upwind-interpolated value. Within this range, we aim to find a correction ϵ_s to $\overline{Y_s}^W$ such that $\sum_s(\overline{Y_s}^W + \epsilon_s) = 1$. The procedure is as follows:

1. Evaluate the WENO ($\overline{Y_s}^W$) and upwind ($\overline{Y_s}^U$) interpolations for all Y_s.
2. If $\sum_s \overline{Y_s}^W > 1$, we seek to decrease $\overline{Y_s}^W$
    - The largest decrease within the range of Eq. (4.6) is:
      $\sum^- = \sum_s(\min\{\overline{Y_s}^W, \overline{Y_s}^U\} - \overline{Y_s}^W) < 0$
    - The relative decrease in $\sum_s \overline{Y_s}^W$ required is: $\alpha = (1 - \sum_s \overline{Y_s}^W)/\sum^-$
    - The correction to each species is: $\epsilon_s = \alpha(\min\{\overline{Y_s}^W, \overline{Y_s}^U\} - \overline{Y_s}^W)$
3. If $\sum_s \overline{Y_s}^W < 1$, we seek to increase $\overline{Y_s}^W$
    - The largest increase within the range of Eq. (4.6) is:
      $\sum^+ = \sum_s(\max\{\overline{Y_s}^W, \overline{Y_s}^U\} - \overline{Y_s}^W) > 0$
    - The relative increase in $\sum_s \overline{Y_s}^W$ required is: $\alpha = (1 - \sum_s \overline{Y_s}^W)/\sum^+$
    - The correction to each species is: $\epsilon_s = \alpha(\max\{\overline{Y_s}^W, \overline{Y_s}^U\} - \overline{Y_s}^W)$
4. Update the interpolated mass fractions to $\overline{Y_s} = \overline{Y_s}^W + \epsilon_s$ prior to computing the convective fluxes in Eq. (4.3).

In this way, spatially-uniform species are unaffected, as the upwind and WENO-interpolated values are equal. For such species, the resulting flux is $F_{s,i+1/2} = (\rho u)_{i+1/2} Y_s$; this consistency is essential for ensuring convergence of the scheme. For the non-uniform species, a value between $\overline{Y_s}^W$ and $\overline{Y_s}^U$ is used.

The proposed algorithm is equivalent to a flux limiting algorithm,

$$\begin{aligned} F_{s,i+1/2} &= F^U_{s,i+1/2} + \phi_{s,i+1/2}[F^W_{s,i+1/2} - F^U_{s,i+1/2}] \\ &= F^W_{s,i+1/2} + (1-\phi_{s,i+1/2})[F^U_{s,i+1/2} - F^W_{s,i+1/2}] \\ &= (\rho u)_{i+1/2}\left(\overline{Y_s}^W + (1-\phi_{s,i+1/2})[\overline{Y_s}^U - \overline{Y_s}^W]\right) \\ &= (\rho u)_{i+1/2}\left(\overline{Y_s}^W + \epsilon_s\right), \end{aligned} \tag{4.7}$$

where $F^U_{s,i+1/2}$ is the upwind flux, $F^W_{s,i+1/2}$ is the WENO flux, and $\phi_{s,i+1/2}$ is the limiter function. The definitions for ϵ_s and α can be related to the flux limiting algorithm to find $\phi_{s,i+1/2}$. If $\sum_s \overline{Y_s}^W > 1$,

$$\begin{aligned} \epsilon_s = (1-\phi_{s,i+1/2})[\overline{Y_s}^U - \overline{Y_s}^W] &= \alpha(\min\{\overline{Y_s}^W, \overline{Y_s}^U\} - \overline{Y_s}^W) \\ \phi_{s,i+1/2} &= 1 - \alpha\left(\frac{\min\left\{\overline{Y_s}^W, \overline{Y_s}^U\right\} - \overline{Y_s}^W}{\overline{Y_s}^U - \overline{Y_s}^W}\right) \\ &= 1 - \frac{\alpha}{2}\left(1 + \operatorname{sgn}(\overline{Y_s}^W - \overline{Y_s}^U)\right), \end{aligned} \tag{4.8}$$

and if $\sum_s \overline{Y_s}^W < 1$,

$$\begin{aligned} \epsilon_s = (1-\phi_{s,i+1/2})[\overline{Y_s}^U - \overline{Y_s}^W] &= \alpha(\max\{\overline{Y_s}^W, \overline{Y_s}^U\} - \overline{Y_s}^W) \\ \phi_{s,i+1/2} &= 1 - \alpha\left(\frac{\max\left\{\overline{Y_s}^W, \overline{Y_s}^U\right\} - \overline{Y_s}^W}{\overline{Y_s}^U - \overline{Y_s}^W}\right) \\ \phi_{s,i+1/2} &= 1 - \frac{\alpha}{2}\left(1 - \operatorname{sgn}(\overline{Y_s}^W - \overline{Y_s}^U)\right). \end{aligned} \tag{4.9}$$

The form of the flux correction is similar in concept to the rescaling of the dominant fluxes introduced in [110] to ensure the correct sum.

4.2 Physical configuration

The Shock and Detonation Toolbox [102] and Cantera [103] are used to compute a Zel'dovich-von Neumann-Döring (ZND) detonation solution propagating at the Chapman-Jouguet (CJ) speed. The unburnt conditions and relevant length scales for all test cases included in Chapter 4 and 5 are listed in Table 4.1 and 4.2. In this chapter, the 7Ar and 5.6N_2-diluted mixtures will be used as representative regular and irregular detonations, respectively. The detailed chemical mechanism contains 9 species and 54 reactions [54, 111, 112] (counting forward and backward reactions separately).

Mixture	p_1 (kPa)	u_{CJ} (m/s)	Δt (s)
$2H_2$-O_2-7Ar	6.67	1616	$5 \cdot 10^{-9}$
$2H_2$-O_2-12Ar	20	1516	$5 \cdot 10^{-9}$
$2H_2$-O_2-17Ar	20	1413	10^{-8}
$2H_2$-O_2-3.5N_2	20	1962	$2.5 \cdot 10^{-9}$
$2H_2$-O_2-5.6N_2	20	1799	$5 \cdot 10^{-9}$

Table 4.1: Unburnt conditions, CJ speeds, and time steps for detonation test cases. The unburnt temperature $T_1 = 295$ K for all tables. Conditions taken from [113].

The shock-fixed referenced frame is used, with the inflow velocity matching the CJ speed. The minimum grid spacing is $\Delta x_{\min} = \mathcal{L}/20$, where $\mathcal{L}$ is the temperature-based induction zone length (listed in Table 4.2 and defined below); this falls within the range of values used in the literature for multi-dimensional detonations [19, 61, 63, 114–116]. The domain length, given in Table 4.2, corresponds to the maximum integration distance of the ZND solver [102]. The first 0.05 m in x is uniformly spaced at the minimum Δx, after which a 1% stretch factor is used. The initial condition is filtered with a filter width $\Delta = 2\Delta x_{\min}$, consistent with the numerical framework used (see Chapter 2).

Mixture	$\mathcal{L}(T)$ (mm)	$\mathcal{L}(\dot{\sigma})$ (mm)	$\frac{L_y}{\mathcal{L}(\dot{\sigma})}$	ℓ_r (mm)	$\frac{\mathcal{L}(T)}{\ell_r}$	L_x (m)
$2H_2$-O_2-7Ar	1.20	1.50	60	1.05	1.14	0.83
$2H_2$-O_2-12Ar	0.69	0.89	67	0.50	1.37	0.83
$2H_2$-O_2-17Ar	1.36	1.73	60	0.90	1.52	0.75
$2H_2$-O_2-3.5N_2	0.78	0.90	67	0.36	2.17	0.89
$2H_2$-O_2-5.6N_2	1.56	1.78	60	0.67	2.32	0.97

Table 4.2: Induction and reaction lengths, channel heights, and domain lengths for each mixture.

For the two-dimensional simulation, this one-dimensional solution is mapped onto a two-dimensional grid, perturbing the detonation front according to

$$x_s(y) = x_0 + \mathcal{L} \cdot \left(\sin\left(\frac{2\pi y}{L_y}\right) + \sin\left(\frac{2\pi y}{L_y/2}\right) + \sin\left(\frac{2\pi y}{L_y/4}\right) \right), \tag{4.10}$$

where the shock location x_s is centered at $x_0 = 0.0125$ m. The domain height, given in Table 4.2, is based on the distance to the maximum thermicity, with uniform spacing $\Delta y = \Delta x_{\min} = \mathcal{L}/20$; for the 7Ar-diluted case, this L_y is expected to allow for about 6 cells across the channel height, based on experimental measurements [113]. The inflow and outflow boundaries use Navier-Stokes Characteristic Boundary Conditions (NSCBCs) [96, 97], with the outflow pressure p_∞ relaxing to the

CJ pressure. The upper and lower y boundaries use symmetry conditions. The simulation is run for a total time of $6 \cdot 10^{-4}$ s, requiring 16000 CPU hours for the 7Ar-diluted case.

The relevant length scales for each mixture are included in Table 4.2. The temperature-based induction zone length (i.e., the distance for which the temperature remains essentially constant), is defined as follows:

$$\mathcal{L}(T) = x_3 - \frac{T_3 - T_2}{(\nabla T)_3}, \tag{4.11}$$

where subscript 2 indicates the von Neumann state, subscript 3 indicates the location of the maximum temperature gradient during ignition. The shock is located at $x = 0$. Alternatively, the induction zone length is commonly defined in terms of the location of maximum thermicity, $\dot{\sigma}$. Both $\mathcal{L}(T)$ and $\mathcal{L}(\dot{\sigma})$ are included in Table 4.2; the smaller estimate ($\mathcal{L}(T)$) was used to determine Δx, while the larger estimate ($\mathcal{L}(\dot{\sigma})$) was used to assess the domain height.

The progress variable at the end of the main reaction zone is computed as

$$C_r = C_4 - \frac{\dot{\omega}_{C,4}}{(\nabla \dot{\omega}_C)_4}, \tag{4.12}$$

where subscript 4 indicates the location of the minimum progress variable source term gradient. The reaction zone length is then

$$\ell_r = x_r - \mathcal{L}(T), \tag{4.13}$$

where x_r is the location corresponding to C_r.

4.3 One-dimensional detonations

The procedure outlined in Sec. 4.1 will be demonstrated for the $2H_2$-O_2-7Ar and $2H_2$-O_2-$5.6N_2$ mixtures. Four scalar discretizations are tested: the standard WENO with no corrections, WENO with $N - 1$ species transport equations (WENO-N1), WENO normalized by the sum of interpolated mass fractions (WENO-NORM) and the weighted WENO/upwind correction (WENO-UP) proposed in the present work.

Figure 4.1 illustrates the WENO-UP approach for the one-dimensional argon-diluted detonation. The largest errors in $\sum_s \overline{Y_s}^W$ as well as the largest magnitudes of $\sum^+$ and $\sum^-$ are found in the reaction zone of the detonation. The range $\left[\sum^-, \sum^+\right]$ is much larger than the required adjustment to $\sum_s \overline{Y_s}^W$, indicating that the correction ϵ_s will introduce only a small deviation from the standard WENO interpolation.

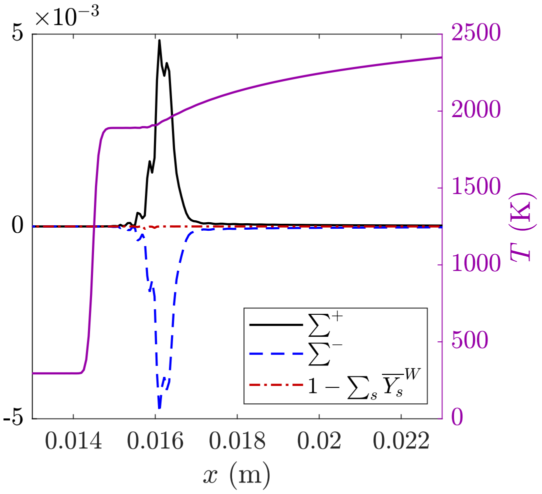

Figure 4.1: Allowable adjustments to $\sum_s \overline{Y}_s^W$ for one-dimensional Ar-diluted detonation. Quantities used in the correction ϵ_s (a): maximum allowable increase (black solid line), maximum allowable decrease (blue dashed line), error in $\sum_s \overline{Y}_s^W$ (red dash-dotted line), temperature (purple solid line).

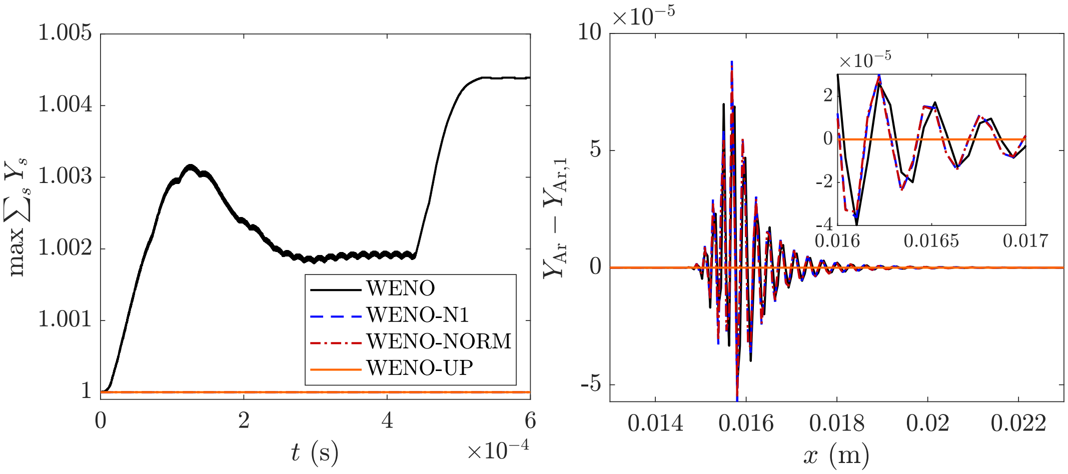

(a) Maximum $\sum_s Y_s$.

(b) Ar mass fraction error.

Figure 4.2: One-dimensional Ar-diluted detonation. Maximum $\sum_s Y_s$ over time (b) and Ar mass fraction error at $t = 6 \cdot 10^{-4}$ s (c) using WENO (black solid line), WENO-N1 (blue dashed line), WENO-NORM (red dash-dotted line), and WENO-UP (orange solid line).

The maximum $\sum_s Y_s$ over time, along with the Ar mass fraction at the end of the simulation, are compared for the four scalar discretizations in Fig. 4.2a and 4.2b. WENO-N1, WENO-NORM, and WENO-UP are able to enforce $\sum_s Y_s = 1$. However, WENO, WENO-N1, and WENO-NORM have oscillatory errors in the Ar mass fraction; only WENO-UP is able to maintain both constant Y_{Ar} and $\sum_s Y_s = 1$.

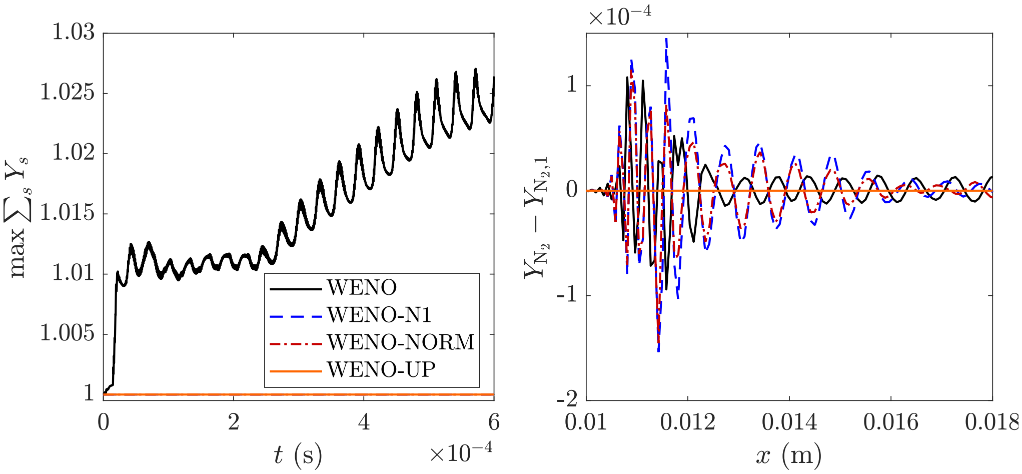

(a) Maximum $\sum_s Y_s$.

(b) N_2 mass fraction error.

Figure 4.3: One-dimensional N_2-diluted detonation. Maximum $\sum_s Y_s$ over time (a) and N_2 mass fraction at $t = 6 \cdot 10^{-4}$ s (b) using WENO (black solid line), WENO-N1 (blue dashed line), WENO-NORM (red dash-dotted line), and WENO-UP (orange solid line).

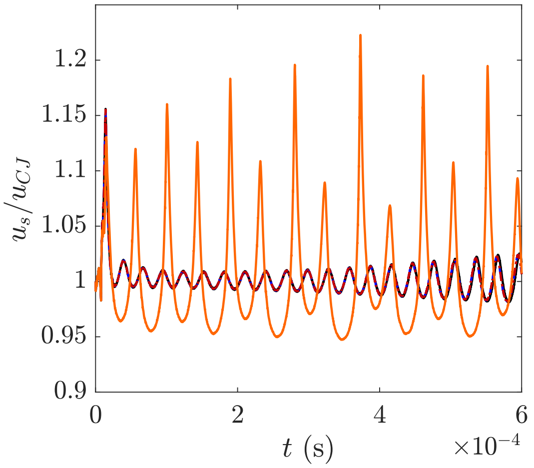

Figure 4.4: One-dimensional N_2-diluted detonation. Detonation propagation speed normalized by the CJ speed using WENO (black solid line), WENO-N1 (blue dashed line), WENO-NORM (red dash-dotted line), and WENO-UP (orange solid line).

The Ar-diluted case is known to be a relatively stable, regular mixture. In contrast, the N_2-diluted case is known to exhibit instabilities in 1D and irregular cellular structures in 2D. Once again, WENO-UP is the only scheme able to ensure $\sum_s Y_s = 1$ (Fig. 4.3a) and constant Y_{N_2} (Fig. 4.3b). The errors in $\sum_s Y_s$ are larger compared to the argon mixture when WENO is used. For this mixture, there is also a clear difference in the limit cycle of the instability depending on the discretization (Fig. 4.4). WENO,

WENO-N1, and WENO-NORM show small oscillations that grow gradually over time. WENO-UP reproduces the expected pulsating detonation behavior, with larger oscillations and period-doubling [117].

4.4 Two-dimensional detonations

4.4.1 Numerical soot foils

In the lab frame of reference, numerical soot foils are computed by recording the maximum pressure over time at each (x, y) location in the domain,

$$Q(x, y, t) = \max\{Q(x, y, t - n\Delta t), p(x, y, t)\}, \tag{4.14}$$

where Q is the soot foil record in the lab frame and p is the simulation pressure field. Because our simulations are performed in the shock frame of reference, the generation of soot foils requires more elaboration. The array containing the soot foil record in the shock frame is termed $\mathcal{P}$. The following coordinate transformation is used for time and the streamwise coordinate,

$$s = t, \quad \zeta = x - u_{CJ}t. \tag{4.15}$$

The y coordinate is unchanged. With this transformation, the shock frame and lab frame soot foils are related by

$$\begin{aligned} \mathcal{P}(\zeta, y, s) &= Q(x, y, t), \\ \mathcal{P}(\zeta - u_{CJ}n\Delta t, y, s - n\Delta t) &= Q(x, y, t - n\Delta t). \end{aligned} \tag{4.16}$$

In practice, $\mathcal{P}$ is computed with the following procedure:

1. At $t = s = t_0$, set $\mathcal{P}(\zeta_i, y_j, t_0) = p(x_i, y_j, t_0)$
2. Every time interval $n\Delta t$, update the record
    - $\mathcal{P}(\zeta_i, y_j, s) = \max\{\mathcal{P}(\zeta_{i-1}, y_j, s - n\Delta t), p(x_i, y_j, t)\}$
    - At a given (ζ_i, y_j) coordinate, this updates the recorded pressure if $p(x_i, y_j, t)$ is a new maximum, or else advects the previously recorded pressure $\mathcal{P}(\zeta_{i-1}, y_j, s - n\Delta t)$ to the right at the inflow velocity (u_{CJ})
    - n is an integer to avoid interpolations in t, s
3. After N updates to the soot foil record, the streamwise grid for $\mathcal{P}$ is
    - $\Delta\zeta = u_{CJ}n\Delta t$ is uniform

- $L_\zeta = N\Delta\zeta$

For convenience, $N = nx$; the integer n, which may be expressed as

$$n = \frac{L_\zeta}{u_{CJ} N \Delta t} \tag{4.17}$$

is chosen for each mixture such that $L_\zeta \approx 0.2$ m. This transformation from x to ζ does not account for the grid stretching present for $x > 0.05$ m. Because the pressure decreases away from the detonation front, and the detonation front is always contained within the uniform grid region, it is assumed that there are no new maxima in p in the stretched region of the domain, so $\mathcal{P}$ can simply be advected downstream.

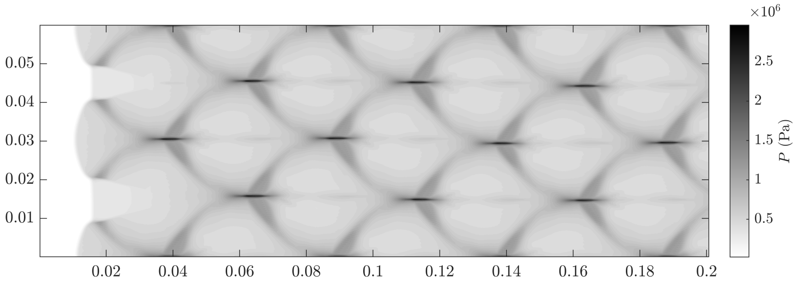

(a) Soot foil using WENO.

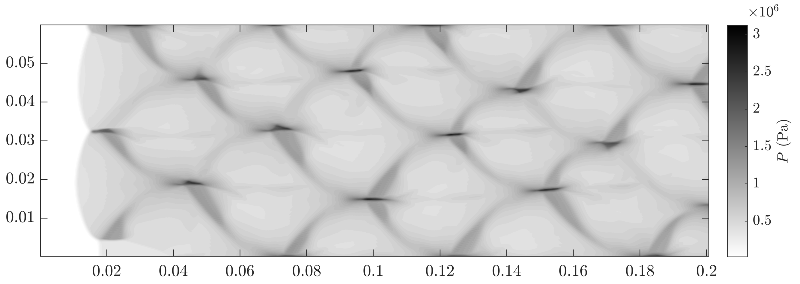

(b) Soot foil using WENO-UP.

Figure 4.5: Two-dimensional N_2-diluted detonation. Soot foils using WENO (a) and WENO-UP (b).

4.4.2 Validation case - Nitrogen-diluted detonation

In one dimension, the nitrogen-diluted detonation had more severe errors in the sum of mass fractions, and is therefore a more informative validation case for the corrected species transport. To assess the impact of the scalar discretization on the cellular structure of the detonation, the N_2 mixture is also tested in 2D. To exaggerate errors in the sum of mass fractions, a coarser grid is used, with the minimum $\Delta x = \Delta y = \mathcal{L}/10$.

The numerical soot foils are shown for WENO and WENO-UP in Fig. 4.5a and 4.5b. With WENO-UP, the cell structure is more irregular, as is expected for N_2-diluted mixtures. Using WENO, the sums of mass fractions, shown over time (Fig. 4.6a) and vs. temperature at the end of the simulation (Fig. 4.6b), have substantial errors compared to the 1D simulations, up to about 15%. As in the 1D simulations, WENO-UP is able to ensure that $\sum_s Y_s = 1$ throughout the simulation. WENO also results in larger errors in the N_2 mass fraction, as seen in Fig. 4.6c; WENO-UP maintains the inert species at a constant value, as intended.

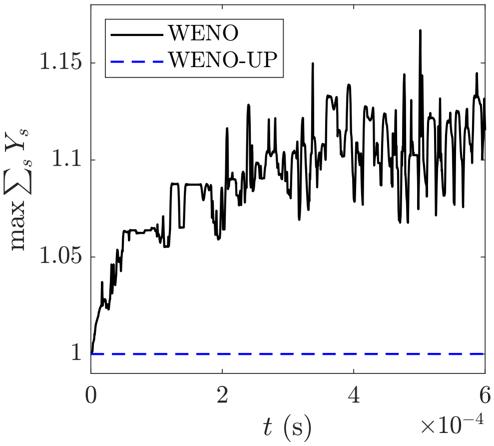

(a) Maximum $\sum_s Y_s$.

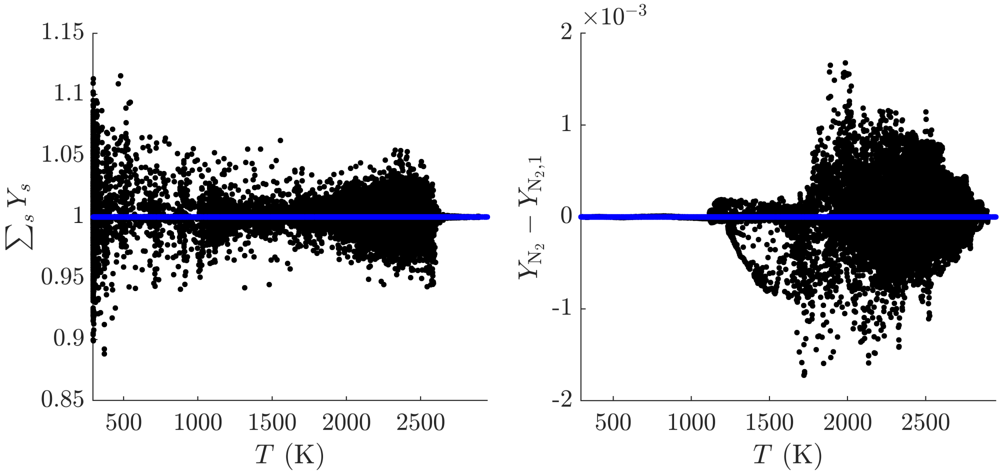

(b) $\sum_s Y_s$.

(c) N_2 mass fraction error.

Figure 4.6: Two-dimensional N_2-diluted detonation. Maximum $\sum_s Y_s$ over time (a), $\sum_s Y_s$ vs. temperature at $t = 6 \cdot 10^{-4}$ s (b), and N_2 mass fraction error vs. temperature at $t = 6 \cdot 10^{-4}$ s (c) using WENO (black solid line/points) and WENO-UP (blue dashed line/points).

4.5 Example - Argon-diluted detonation

Detailed chemistry data will be required to inform the chemistry model development in Chapter 5. While the nitrogen-diluted case in Sec. 4.4.2 was a useful stress-test for the scalar transport, the regular cell structure of argon-diluted detonations is anticipated to be a simpler configuration for a priori analysis of the tabulation framework. The 7Ar-diluted mixture is simulated in 2D with a minimum grid spacing $\Delta x = \mathcal{L}/20$.

The numerical schlieren and temperature fields are shown at three time snapshots in Fig. 4.7, and the propagation speed is shown in Fig. 4.8,

$$u_s = \frac{\langle \rho \rangle_2 \left(\langle u \rangle_2 - \langle u \rangle_1 \right)}{\langle \rho \rangle_1 - \langle \rho \rangle_2}, \quad u_s(y_0) = \frac{\rho_2(y_0)(u_2(y_0) - u_1(y_0))}{\rho_1(y_0) - \rho_2(y_0)}, \tag{4.18}$$

where u_s is the y-averaged speed and $u_s(y_0)$ is the local speed on the mid-plane at $y_0 = L_y/2$. The planar averages $\langle \rho \rangle_1$ and $\langle \rho \rangle_2$ correspond to the pre-shock and von Neumann state (maximum $\langle \rho \rangle$) densities, respectively. $\langle u \rangle_1$ and $\langle u \rangle_2$ are the corresponding planar Favre-averaged velocities. Similarly, the local $\rho_1(y_0)$ and $\rho_2(y_0)$ are the pre-shock and von Neumann state (maximum $\rho(y_0)$) densities, and $u_1(y_0)$ and $u_2(y_0)$ are the corresponding local velocities. The relation in Eq. (4.18) comes from the conservation of mass across a normal shock. The resulting shock propagation speed indicates the extent of overdrive compared to the CJ velocity, both on average and instantaneously.

The initial perturbation is shown as a numerical schlieren in Fig. 4.7a. The contour at the H_2O mass fraction corresponding to the peak 1D source term illustrates the local changes in reaction zone length along the detonation front. Later in the simulation (Fig. 4.7b and 4.7c), the detonation front is observed to have a regular spacing between triple point collisions, as expected for the $2H_2$-O_2-7Ar mixture, with about 3-4 cells across the vertical domain; this will be discussed further using soot foils in Sec. 5.3. As seen in Fig. 4.7d and 4.7e, higher temperatures at the detonation front result in shorter induction lengths, while lower temperatures delay the reactions. Both the planar-averaged propagation speed (Fig. 4.8a) and the local propagation speed at the mid-plane ($y = L_y/2$) (Fig. 4.8b) oscillate about the CJ propagation speed. These oscillations have a period of about 10^{-5} s. Because there is always some portion of the front propagating above u_{CJ}, and some portion propagating below u_{CJ}, the average remains within 1-2% of the CJ speed. The local propagation speed shows larger fluctuations, as this shows the change in propagation

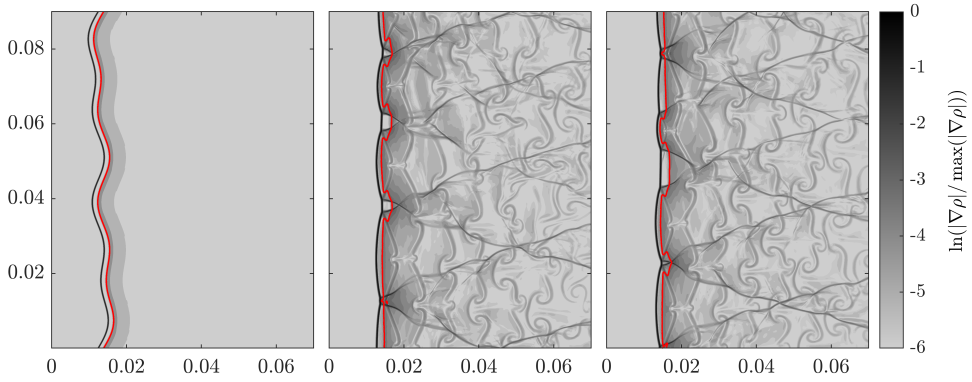

(a) Schlieren, 0 s. (b) Schlieren, $4 \cdot 10^{-4}$ s. (c) Schlieren, $6 \cdot 10^{-4}$ s.

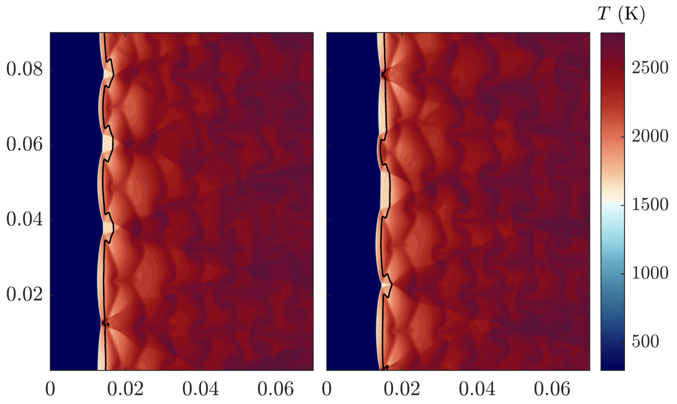

(d) Temperature, $4 \cdot 10^{-4}$ s. (e) Temperature, $6 \cdot 10^{-4}$ s.

Figure 4.7: Numerical Schlieren (normalized density gradient magnitude, a-c) and temperature field (d-e); contour indicating $Y_{\mathrm{H_2O}}$ at the peak $\dot{\omega}_{\mathrm{H_2O},CJ}$ (red line, a-c; black line, d-e).

speed through a given cell. The velocity peaks at the triple point and decays through the cell until it is reshocked at the next triple point.

The detailed chemistry results for the one- and two-dimensional detonations will be used to inform the construction of the table in Sec. 5.2, and to validate the tabulation approach in Sec. 5.3.

4.6 Conclusion

In this chapter, we described a procedure for correcting the sum of mass fractions when nonlinear schemes such as WENO are used. Unlike common existing approaches, our procedure does not lead to errors in the inert species. The method was successfully demonstrated for one-dimensional detonations in hydrogen and oxygen, diluted with either argon or nitrogen, as well as a two-dimensional detonation diluted with nitrogen. Errors in the sum of mass fractions present with the standard fifth-order WENO scheme were prevented when the correction is used. Further-

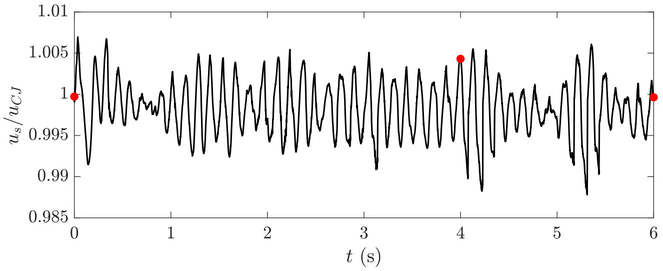

(a) Planar-averaged propagation speed vs. time.

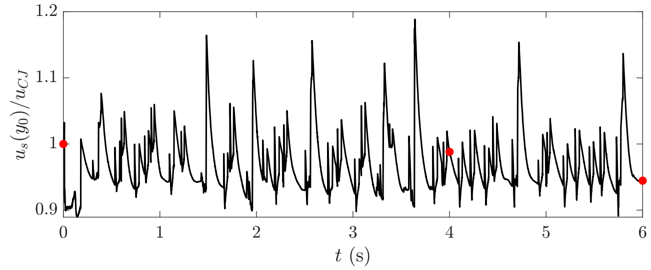

(b) Local propagation speed vs. time.

Figure 4.8: Planar-averaged and local propagation speeds (normalized by CJ speed) over time. Red markers correspond to the time snapshots shown in Fig. 4.7.

more, the diluent species do not absorb the errors and remain constant. For the nitrogen-diluted detonations, the correction results in a more pronounced physical instability/irregularity. While demonstrated here for the fifth-order WENO scheme, the current approach is generalizable to other nonlinear transport schemes.

Chapter 5

TABULATED CHEMISTRY APPROACH FOR DETONATION SIMULATIONS

[1] A. Baumgart, M. X. Yao, and G. Blanquart. "Tabulated chemistry approach for detonation simuations". In: *Combustion and Flame* (2024). (Under Review).

The detailed chemistry simulations in Chapter 4 required transporting nine species mass fractions. For flame simulations, tabulated chemistry is a common approach to modeling chemistry at a lower computational cost. In this chapter, a tabulated chemistry model suitable for detonations is developed. Analogous to the flamelets used to generate chemistry tables for flames, one-dimensional detonations will be used to pre-compute the table. In Sec. 5.1, the analytical framework for compressible flow simulations is reviewed. The proposed tabulation method is described in Sec. 5.2. Validation of the chemistry model is presented for various H_2-O_2 mixtures in Sec. 5.3 for both one- and two-dimensional simulations.

5.1 Compressible flow simulation framework

To motivate the tabulated chemistry approach, the requirements for compressible flow simulations are reviewed here.

5.1.1 Pure substance - Ideal gas

The spatially-filtered governing equations for mass, momentum, and energy are given by

$$\frac{\partial \overline{\rho}}{\partial t} + \frac{\partial \overline{\rho}\tilde{u}_i}{\partial x_i} = 0, \tag{5.1}$$

$$\frac{\partial (\overline{\rho}\tilde{u}_i)}{\partial t} + \frac{\partial (\overline{\rho}\tilde{u}_i\tilde{u}_j)}{\partial x_j} = -\frac{\partial \overline{p}}{\partial x_i} + \frac{\partial \overline{\tau}_{ij}}{\partial x_j} + \frac{\partial \tau_{ij,SFS}}{\partial x_j}, \tag{5.2}$$

$$\frac{\partial (\overline{\rho}\tilde{e}_t)}{\partial t} + \frac{\partial (\overline{\rho}\tilde{u}_i\tilde{h}_t)}{\partial x_i} = -\frac{\partial \overline{q}_i}{\partial x_i} + \frac{\partial}{\partial x_i}\left(\overline{\tau}_{ij}\tilde{u}_j\right) + \frac{\partial q_{i,SFS}}{\partial x_i}, \tag{5.3}$$

where ρ is the density, u is the velocity, p is the pressure, τ is the viscous stress tensor, e_t is the total energy, and h_t is the total enthalpy. The heat flux, q, is defined as

$$\overline{q}_i = -\lambda \frac{\partial \tilde{T}}{\partial x_i}, \tag{5.4}$$

where λ is the thermal conductivity and T is the temperature. The system is closed with the ideal gas equation of state,

$$\overline{p} = \frac{\overline{\rho} R \tilde{T}}{\tilde{W}}, \tag{5.5}$$

where R is the universal gas constant and W is the molecular weight. For a pure substance, W is constant.

Equations (5.1) to (5.3) and (5.5) form an almost complete set of equations to describe any compressible flow of a pure substance. What remains is an expression to relate the enthalpy (or the internal energy) to temperature and pressure, namely $h = h(T, P)$. For a single ideal gas, enthalpy is only a function of temperature, generally expressed as

$$h(T) = h_{ref} + \int_{T_{ref}}^{T} c_p(T) dT. \tag{5.6}$$

When c_p is constant, the enthalpy is often expressed as $h = c_p T$. If c_p is not constant, the NASA polynomials [118] may be used to describe $c_p(T)$ and hence $h(T)$. Using such expressions, the temperature is computed from the transported quantities using a Newton iteration,

$$\tilde{T}_{m+1} = \tilde{T}_m + \frac{\frac{\overline{\rho} R \tilde{T}}{\tilde{W}} - \left(\overline{\rho} \tilde{h} - \overline{\rho} \tilde{e}_t + \frac{1}{2} \overline{\rho} \tilde{u} \tilde{u} \right)}{\overline{\rho} \left(\tilde{c}_p - \frac{R}{\tilde{W}} \right)}, \tag{5.7}$$

where m is the iteration number.

5.1.2 Non-reacting mixtures

For mixtures, Eq. (5.1) to (5.3) must be accompanied by a transport equation for each species, given by

$$\frac{\partial (\overline{\rho} \tilde{Y}_s)}{\partial t} + \frac{\partial (\overline{\rho} \tilde{u}_i \tilde{Y}_s)}{\partial x_i} = -\frac{\partial \overline{j}_{i,s}}{\partial x_i}, \tag{5.8}$$

where Y_s is the mass fraction of species s and n_s is the number of species. The species diffusion flux, j_s, and the updated heat flux (in Eq. (5.3)) are defined as

$$\begin{aligned} \overline{j}_{i,s} &= -\overline{\rho} D \frac{\partial \tilde{Y}_s}{\partial x_i}, \\ \overline{q}_i &= -\lambda \frac{\partial \tilde{T}}{\partial x_i} + \sum_s \tilde{h}_s \overline{j}_{i,s}, \end{aligned} \tag{5.9}$$

where D is the species diffusivity and h_s is the species enthalpy. For simplicity, the Lewis number $Le = \alpha/D$ (where $\alpha = \lambda/\rho c_p$ is the thermal diffusivity) is assumed to be unity.

To fully close the set of governing equations, expressions for the mixture molecular weight and the mixture enthalpy are necessary. For ideal gases, the mixture molecular weight is only a function of the species mass fractions and is given by

$$W(Y_s) = \left(\sum_s Y_s / W_s \right)^{-1}, \tag{5.10}$$

and the mixture enthalpy and heat capacity are functions of only T and Y_s,

$$\begin{aligned} h(T, Y_s) &= \sum_s h_s(T) Y_s, \\ c_p(T, Y_s) &= \sum_s c_{p,s}(T) Y_s, \end{aligned} \tag{5.11}$$

where $h_s(T)$ and $c_{p,s}(T)$ are evaluated using the NASA polynomials for each species. In practice, only h is required in simulations, as c_p is evaluated as

$$c_p = \left. \frac{\partial h}{\partial T} \right|_{Y_s}. \tag{5.12}$$

The above expressions for W, h, and c_p are then used for the temperature inversion; no modifications to Eq. (5.7) are required.

5.1.3 Reacting flows - Detailed chemistry

In reacting flows, the previous requirements described in Sec. 5.1.1 and 5.1.2 still hold. W is still a function of Y_s, and h and c_p are still functions of T and Y_s. However, the species transport equation must be modified to include the chemical source terms,

$$\frac{\partial (\overline{\rho} \tilde{Y}_s)}{\partial t} + \frac{\partial (\overline{\rho} \tilde{u}_i \tilde{Y}_s)}{\partial x_i} = -\frac{\partial \overline{j}_{i,s}}{\partial x_i} + \dot{\omega}_s, \tag{5.13}$$

where $\dot{\omega}_s$ is the net source term for species s. These source terms are complex functions of temperature and the species concentrations and may be expressed generally as $\dot{\omega}_s(\rho, T, Y_s)$. It is through the density that the effects of pressure are felt on the combustion processes.

5.1.4 Reacting flows - Tabulated chemistry

In the tabulated chemistry framework, rather than solving Eq. (5.13) for each chemical species present, a single scalar equation is solved,

$$\frac{\partial(\overline{\rho}\tilde{C})}{\partial t} + \frac{\partial(\overline{\rho}\tilde{u}_i\tilde{C})}{\partial x_i} = \frac{\partial}{\partial x_i}\left(\overline{\rho}D\frac{\partial\tilde{C}}{\partial x_i}\right) + \dot{\omega}_C, \tag{5.14}$$

where C is the progress variable. As in Eq. (5.9), the progress variable diffusivity is evaluated assuming a unity Lewis number. The progress variable is often the mass fraction of one of the products [80, 119] or a linear combination of species mass fractions [78]. In low Mach number chemistry tabulation, it is assumed that all thermochemical variables including the species mass fractions and temperature may be reconstructed as a function of the progress variable, namely, $Y_s \approx Y_s(C)$ and $T \approx T(C)$. The energy equation and temperature inversion (Eq. (5.3) and (5.7)) are not needed for low Mach number flow simulations.

In compressible flows, the temperature is an independent variable extracted from the energy equation. If it is assumed that the species mass fractions may be entirely described by the progress variable, namely $Y_s \approx Y_s(C)$, the mixture enthalpy (see Eq. (5.11)) would become a function of temperature and progress variable,

$$h \approx h(T, C). \tag{5.15}$$

However, this functional dependence for Y_s is unnecessarily restrictive. Because the temperature is already required to compute h, here the assumption on the mass fractions is relaxed such that the species mass fractions (at a given temperature) may be reconstructed as a function of the progress variable, namely $Y_s \approx Y_s(T, C)$. Using this approximation in Eq. (5.10), the mixture molecular weight becomes a function of temperature and progress variable,

$$W \approx W(T, C). \tag{5.16}$$

Similarly, the source term of the progress variable becomes a function of density, temperature, and progress variable,

$$\dot{\omega}_C \approx \dot{\omega}_C(\rho, T, C)\,. \tag{5.17}$$

Evaluating these three functions is the goal of the present work and is detailed in the following two sections.

5.2 Chemistry tabulation method

The progress variable definition is discussed in Sec. 5.2.1. The choice of table coordinates is assessed in Sec. 5.2.2. Section 5.2.3 describes the procedure for generating the chemistry tables. Finally, Sec. 5.2.4 investigates the chemical reactions built into the table. The detailed chemistry data from Chapter 4 (Sec. 4.5) is used for all a priori analysis.

5.2.1 Choice of progress variable

In deflagrations, the flame structure is primarily influenced by diffusion, so the mass fraction of the products is sufficient to define the progress variable. However, in detonations, ignition, not diffusion, becomes the driving process [75]. Because ignition plays a key role in determining the detonation structure (e.g., induction zone length), the progress variable definition requires further consideration.

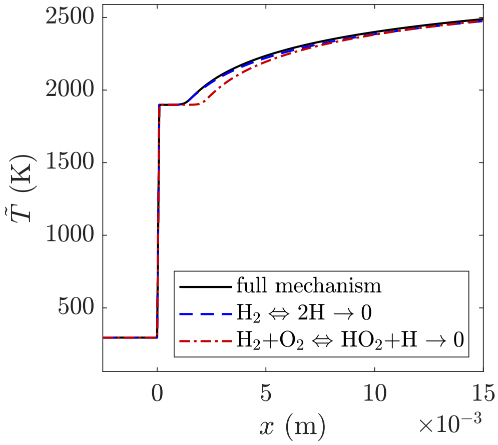

Figure 5.1: Steady temperature profiles for the full mechanism (black solid line), with the rate constant for Eq. (5.18) set to zero (blue dashed line), and with the rate constant for Eq. (5.19) set to zero (red dash-dotted line).

In order for ignition to occur behind the shock wave, the source term of the progress variable, $\dot{\omega}_C$, must be nonzero at $C = 0$. This could be accomplished by using a reactant species for C, or by considering the initial radical species. The two initiation reactions for hydrogen combustion are

$$H_2 + M \rightarrow 2H, \tag{5.18}$$

$$H_2 + O_2 \rightarrow HO_2 + H. \tag{5.19}$$

The only nonzero source terms in the unburnt mixture are $\dot{\omega}_H$ and $\dot{\omega}_{HO_2}$. To identify which initiation reaction is more important for reproducing the correct induction zone length, the original mechanism [54] is modified and the impact on the ZND structure is examined. The resulting temperature profiles are compared in Fig. 5.1. When the rate constant for Eq. (5.18) is set to zero, the temperature profile is virtually identical to that of the full mechanism with the original rate constants. However, when the rate constant for Eq. (5.19) is set to zero, the induction zone is much longer than that of the full mechanism. In other words, the initiation reaction in Eq. (5.19) controls the induction zone length. This initiation reaction involves the formation of two radicals, H and HO_2; either of them could be added to the progress variable definition (e.g., $C = Y_{H_2O} + Y_H$). These initial radicals are then involved in competing reaction pathways, as described in [120]; chain-branching for H, and chain-termination for HO_2.

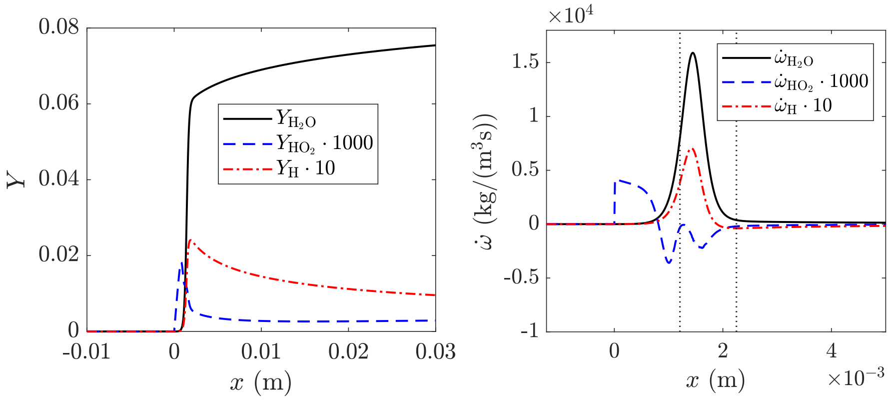

(a) Species mass fractions.

(b) Species source terms.

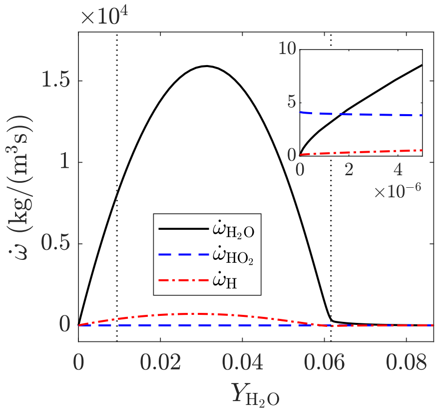

(c) Species source terms.

Figure 5.2: Species mass fractions (a) and corresponding source terms (b, c) of H_2O (black solid line), HO_2 (blue dashed line), and H (red dash-dotted line). Vertical dotted lines in (b, c) indicate the end of the induction zone and the end of the main reaction zone. Inset shows near $Y_{H_2O} = 0$ (c).

The mass fractions of H_2O, HO_2, and H from the ZND solution are shown in

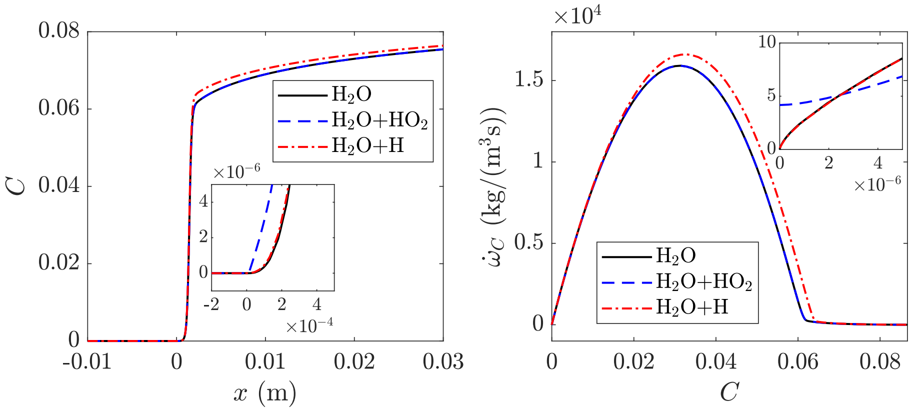

(a) Progress variable.

(b) Progress variable source term.

Figure 5.3: Progress variable (a) and corresponding source term (b) when defined as H_2O (black solid line), H_2O+HO_2 (blue dashed line), and H_2O+H (red dash-dotted line). Insets show near $C = 0$.

Fig. 5.2a. Ideally, the progress variable is a monotonically increasing quantity, as seen for the mass fraction of H_2O. Although the mass fractions of HO_2 and H are non-monotonic, their magnitudes are much smaller than Y_{H_2O}: three orders of magnitude for Y_{HO_2}, and one order of magnitude for Y_H. The sum of the mass fractions remains monotonic whether HO_2 or H is used with HO_2, as shown in Fig. 5.3a.

The net source terms for H_2O, HO_2, and H are shown in physical space in Fig. 5.2b. The source term of HO_2 jumps at the shock (at $x = 0$), while the source term of H_2O remains zero into the post-shock. The induction zone, where temperature remains essentially constant, spans from about $x = 0$ to $x = 1.2$ mm (marked by the first vertical dotted line). For most of this region, $\dot{\omega}_{HO_2}$ is the dominant source term; near the end of the induction zone, the other source terms begin to increase. The main reaction zone then spans from $x = 1.2$ mm to $x = 2.3$ mm (marked by the second vertical dotted line); here, the H_2O source term is dominant. (Induction/reaction lengths for other mixtures, as well as details on their calculation, are included in the supplementary material.) These source terms are shown as a function of Y_{H_2O} in Fig. 5.2c, and the net progress variable source term is shown in C space for the three definitions of C (H_2O only, H_2O with HO_2, and H_2O with H) in Fig. 5.3b. The vertical dotted lines in Fig. 5.2c again correspond to the end of the induction zone ($Y_{H_2O} = 0.009$) and reaction zone ($Y_{H_2O} = 0.06$). In Fig. 5.2c and 5.3b, $Y_{H_2O} = 0$ and $C = 0$ correspond to the von Neumann state; the pre-shock is well below the autoignition limit, so $\dot{\omega}_s \approx 0$ for all species. For the majority of the range of C, the contribution of $\dot{\omega}_{\mathrm{HO_2}}$ is small compared to the contribution of $\dot{\omega}_{\mathrm{H_2O}}$, so the first two definitions of $\dot{\omega}_C$ are indistinguishable. The main difference is near $C = 0$, where the source term for $C = Y_{\mathrm{H_2O}}$ goes to zero, but the source term for $C = Y_{\mathrm{H_2O}} + Y_{\mathrm{HO_2}}$ does not. Although the source term is also nonzero at $C = 0$ for H (though an order of magnitude smaller than the $\mathrm{HO_2}$ source term), the contribution of $\dot{\omega}_{\mathrm{H}}$ is not negligible compared to $\dot{\omega}_{\mathrm{H_2O}}$ for a large range of C. Therefore, it is preferable to include $\mathrm{HO_2}$, rather than H, in the progress variable definition to improve the behavior near $C = 0$ without impacting the rest of the domain in C:

$$C = Y_{\mathrm{H_2O}} + Y_{\mathrm{HO_2}}, \tag{5.20}$$

$$\dot{\omega}_C = \dot{\omega}_{\mathrm{H_2O}} + \dot{\omega}_{\mathrm{HO_2}}. \tag{5.21}$$

Unless otherwise specified, this definition of C is used for all following sections.

5.2.2 Table coordinates

As discussed in Sec. 5.1.4, the key assumption behind tabulated chemistry is that the mass fractions may be described as functions of progress variable and temperature: $Y_s \approx Y_s(C,T)$. From a mathematical point of view, the optimal estimator of any bivariate function, $\phi(C,T)$, is the 2D conditional mean, namely $\langle \phi | C,T \rangle$. The quality of this estimator is measured by the 2D conditional standard deviation, namely $\sigma(\phi | C,T)$. Using the detailed chemistry data from Sec. 4.5, conditional statistics are used to extract the 2D functions. Unless otherwise specified, statistics are computed using snapshots from $t = 4 \cdot 10^{-4}$ to $6 \cdot 10^{-4}$ s in intervals of 10^{-5} s. The (C,T) bins used for the conditional statistics correspond to the (C,T) coordinates of the chemistry table, which will be described in Sec. 5.2.3.

The two-dimensional conditional mean species mass fractions, $\langle Y | C,T \rangle$, and relative standard deviations, $\sigma(Y|C,T)/Y^{\mathrm{1D}}_{\max}$, are shown in Fig. 5.4 for the fuel and a key radical. The standard deviations are normalized by the maximum value from the one-dimensional CJ solution. Both conditional mean mass fractions are smooth functions which vary mostly with C. The $\mathrm{H_2}$ mass fraction decreases almost linearly with the progress variable in the initial reaction zone (i.e., $C < 0.06$) and is virtually zero thereafter. The OH profile increases gradually through the detonation with a weak temperature dependence. At a given (C,T), the standard deviations of the mass fractions are small, with a maximum around 1% for both species. These results confirm the assumption that $Y_s \approx Y_s(T,C)$.

The same conditional statistics are computed for all the quantities required in the tabulated chemistry simulations, namely W, h, and $\dot{\omega}_C$, and are shown in Fig. 5.5.

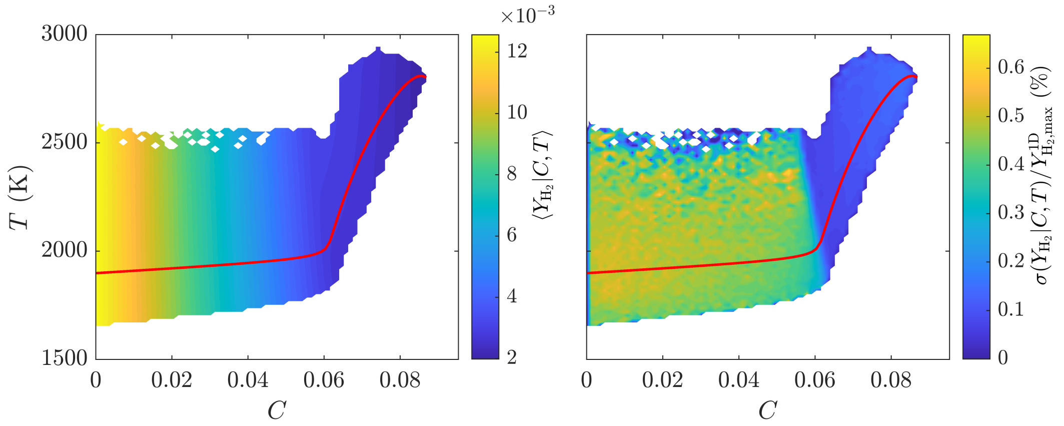

(a) H_2 mass fraction mean.

(b) H_2 mass fraction rms.

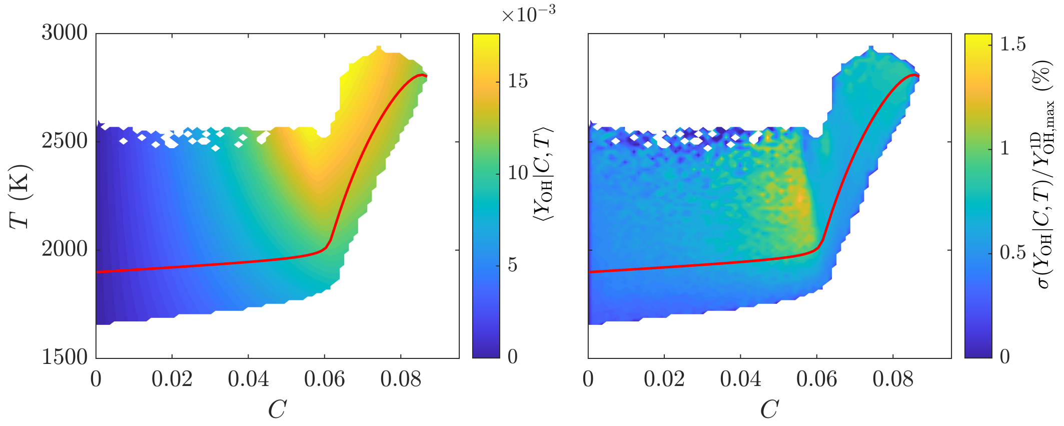

(c) OH mass fraction mean.

(d) OH mass fraction rms.

Figure 5.4: Conditional statistics computed on the two-dimensional detailed chemistry data. Conditional means (a, c) and standard deviations normalized by the maximum value from the 1D CJ solution (b, d), conditioning on both C and T. CJ solution for reference (red solid line).

The mixture molecular weight and enthalpy both have relatively small standard deviations at a given (C, T) (around 0.1% for W and 1% for h). The chemical source term for the progress variable deserves more consideration.

For a binary reaction $A + B \longrightarrow D$ (such as the initiation reactions discussed in the previous section), the chemical source term is

$$\dot{\omega}_r = [A] \cdot [B] \cdot k_r(T) = \frac{\rho Y_A}{W_A} \cdot \frac{\rho Y_B}{W_B} \cdot k_r(T), \tag{5.22}$$

where $[\cdot]$ indicates the species concentration and k_r is the temperature-dependent reaction rate constant. Rearranging as

$$\frac{\dot{\omega}_r}{\rho^2} = \frac{Y_A}{W_A} \cdot \frac{Y_B}{W_B} \cdot k_r(T), \tag{5.23}$$

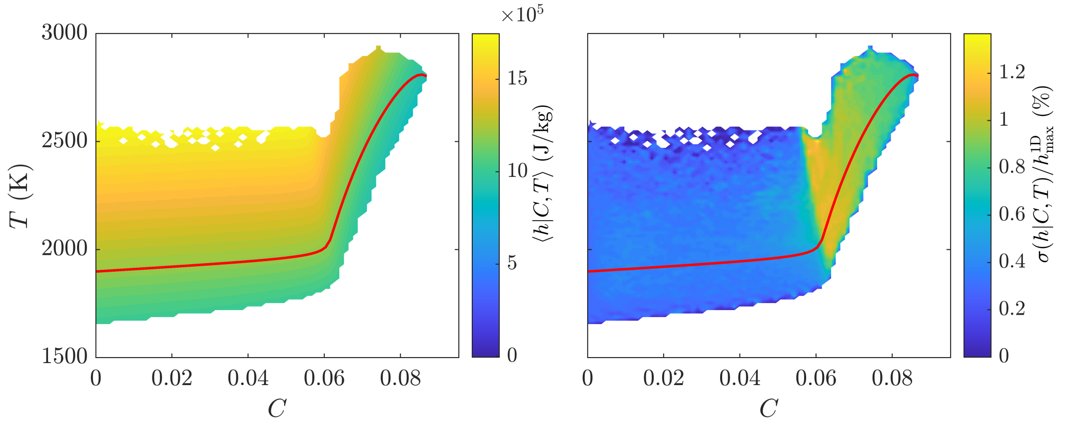

(a) Mixture enthalpy mean.

(b) Mixture enthalpy rms.

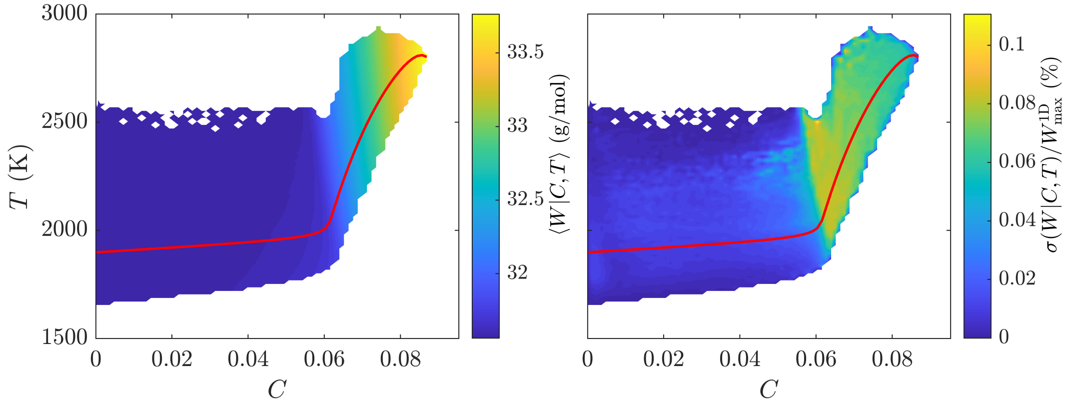

(c) Mixture molecular weight mean.

(d) Mixture molecular weight rms.

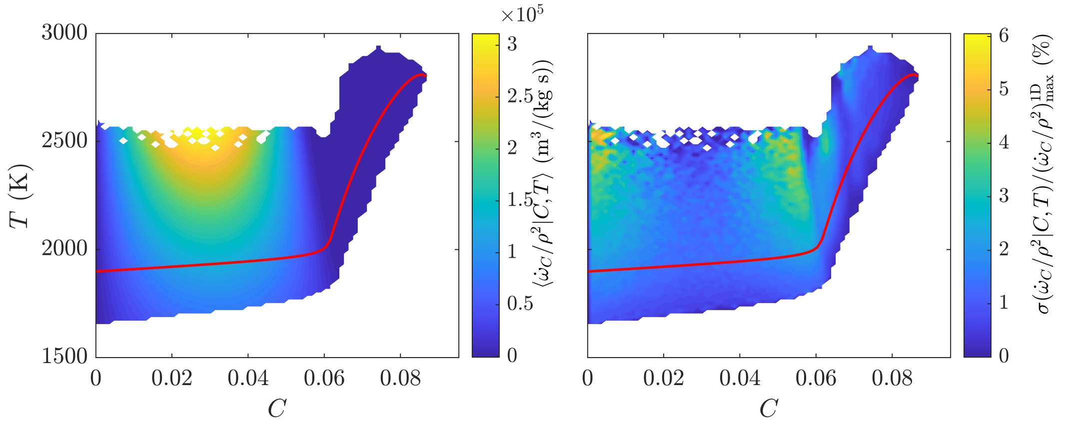

(e) Source term mean.

(f) Source term rms.

Figure 5.5: Conditional statistics computed on the two-dimensional detailed chemistry data for the $2H_2$-O_2-7Ar mixture. Conditional means (a, c, e) and standard deviations normalized by the maximum value from the 1D CJ solution (b, d, f), conditioning on both C and T. CJ solution for reference (red solid line).

the right-hand side is now dependent only on the mixture composition (Y_A and Y_B)

and the temperature. In hydrogen combustion, the majority of the reactions are second order, suggesting that a density exponent of 2 is an appropriate scaling for the progress variable source term.

More generally and without assuming the reaction order, the source term and density are related by

$$\dot{\omega}_C \propto \rho^{a_\rho} \cdot f(T, Y_s). \tag{5.24}$$

The sensitivity of the source term to density perturbations, namely a_ρ, may be extracted using the CJ solution as the baseline. At each point in C, the density is perturbed over a range of ±10% while maintaining the temperature and mixture composition. The progress variable source term is then recomputed at the new densities. Finally, the exponent is extracted by fitting

$$\ln \dot{\omega}_C(C) = a_\rho \ln \rho(C). \tag{5.25}$$

The resulting exponent is shown in Fig. 5.6 along with the source term. The detailed mechanism used here consists of only second and third order reactions [54, 111, 112], so the exponent is expected to vary between 2 and 3. For the range of C where $\dot{\omega}_C$ is largest, $a_\rho \approx 2$. At higher C where $a_\rho > 2$, the source term is orders of magnitude smaller than the peak $\dot{\omega}_C$, approaching zero as chemical equilibrium is reached. The dominant reactions at specific C locations (denoted by the symbols) will be discussed in Sec. 5.2.4. The scaling found in Fig. 5.6 depends on the detailed mechanism used. For example, a mechanism including non-thermal termolecular reactions (which may be influential on the detonation structure [121, 122]) may scale differently. While possible to tabulate a_ρ as a varying function of C and T (as done in compressible flamelet/progress variable models [84]), we can reduce the preprocessing requirements by noting the behavior of the source term relative to a_ρ. Based on this observation, we seek to tabulate the progress variable source term as $\dot{\omega}_C/\rho^2 = f(C, T)$. The tabulated value would then be multiplied by ρ^2 in the simulation.

Examining the conditional mean $\langle \dot{\omega}_C/\rho^2 | C, T \rangle$ in Fig. 5.5e, the progress variable source term is a smooth function with a strong C and T dependence. In the reaction zone, it exhibits a bell-shape dependence on the progress variable and a monotonic increase with temperature. After $C > 0.06$, the source term is small, but not zero. Figure 5.5f shows the standard deviation in the source term at a given (C, T). This standard deviation compounds two separate errors: errors due to deviations in the

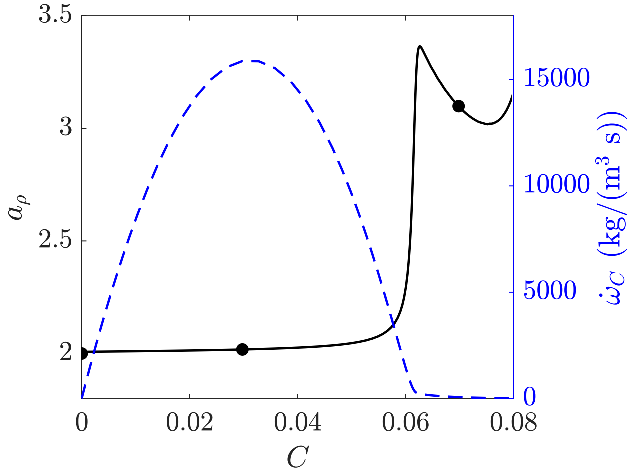

Figure 5.6: Density scaling for the source term along the CJ solution (left axis, black solid line); progress variable source term for reference (right axis, blue dashed line). Symbols indicate C locations to be discussed in Sec. 5.2.4.

species profiles (i.e., $Y_s \neq Y_s(C,T)$) and contributions of elementary reactions which are not second order (i.e. $\omega_r \not\propto \rho^2$). Although it is slightly larger compared to the mass fraction standard deviations, it is still small relative to the peak source term from the CJ solution (at most 5%). Based on these conditional statistics, the (C,T) table coordinates are expected to be sufficient.

Figure 5.7 illustrates how a (C,T) chemistry table fits into the simulation framework described in Sec. 5.1. Computing the right hand side (RHS) for the progress variable transport equation requires a table lookup for the progress variable source term. During the Newton iteration (Eq. (5.7)) to extract the temperature from the transported energy, table lookups for the mixture enthalpy, molecular weight, and specific heat capacity are required. Once the Newton iteration converges, both the temperature and pressure are updated.

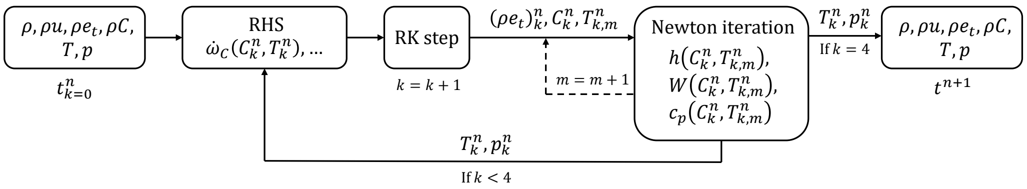

Figure 5.7: Solution procedure using a (C,T) table. Superscript n indicates the timestep, subscript k indicates the RK step, and subscript m indicates the Newton iteration number (see Eq. (5.7)). Quantities written as $f(C^n_k, T^n_k)$ indicate where table lookups are required.

5.2.3 Table generation

The optimal (C, T) chemistry table consists of the conditional means $\langle \phi | C, T \rangle$ evaluated from the detailed chemistry data. However, this defeats the purpose of tabulating the chemistry, as a two-dimensional detailed chemistry simulation would be required for each mixture *prior* to generating the table. We propose an alternative approach to filling in the (C, T) coordinate space, analogous to what is done for flames.

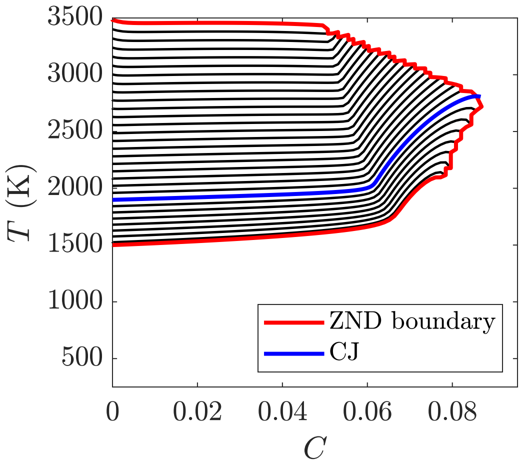

Figure 5.8: One-dimensional ZND solutions in (C, T) space (black solid lines), equilibrium boundary (red solid line), and CJ solution (blue solid line).

For premixed flames, chemistry tables are typically generated using one-dimensional flamelets [80, 119]. However, a steady premixed flamelet cannot exist at the relevant post-shock conditions in a detonation; due to the autoignition limits of the fuel/oxidizer mixture, the unburnt side of the flame would ignite. In detonations, the representative one-dimensional problem is the ZND model. To generate the table, a set of 60 one-dimensional ZND detonation solutions are computed with the Shock and Detonation Toolbox using the same unburnt conditions ($2H_2$-O_2-7Ar, $p_1 = 6.67$ kPa, and $T_1 = 295$ K). Using the shock speed as the varying parameter is motivated by the conditions found along multi-dimensional detonation fronts, where the local propagation speed varies but the unburnt/pre-shock conditions are fixed. The propagation speeds range from $u_1 = 1400$ to 2300 m/s, including both under- and over-driven detonations ($u_{CJ} = 1616$ m/s, so $0.87 \leq (u_1/u_{CJ}) \leq 1.42$). Generally, a range of $0.8 \leq u_1/u_{CJ} \leq 1.4$ is recommended to span the velocities observed in multi-dimensional detonations [120, 123]; for the cases in the present work, it was verified that the ZND solutions cover the range observed in the detailed chemistry data. These detonations are shown in (C, T) space in Fig. 5.8. The boundary of the ZND profiles will be referred to as $(C_{\mathrm{ZND}}, T_{\mathrm{ZND}})$. In addition to the progress variable and temperature, along these profiles, the density, pressure, all species mass fractions, mixture weight, enthalpy, and chemical source terms are known. These variables are interpolated onto the C and T coordinates of the table. There are $N_C = 100$ points in C ranging from 0 to $1.1 \cdot \max\{Y_{\mathrm{H_2O,CJ}}\}$ (referred to hereafter as $C_{\max}$). The points near $C = 0$ use a logarithmic spacing and the remaining points use a linear spacing,

$$C(i) = \frac{C_{\max}}{N_C - n - 1} \cdot \left(\frac{1}{2}\right)^{n+2-i} \quad \text{for} \quad 2 \le i \le n+1, \tag{5.26}$$

$$C(i) = \frac{C_{\max}}{N_C - n - 1} \cdot (i - n - 1) \quad \text{for} \quad n+2 \le i \le N_C, \tag{5.27}$$

where n is the number of logarithmically spaced points and i is the C index. A value of $n = 20$ was found to provide sufficient resolution at low C. The T coordinate ranges from 250 to 3500 K, with 200 linearly spaced points. This range covers all temperatures observed in the two-dimensional detailed chemistry simulation.

For all (C, T) coordinates inside the ZND boundary, the table outputs $\phi(C, T)$ (for $\phi = Y_s, W, h, \dot{\omega}_C$) are found using a bi-linear interpolation in C and T, using the nearest ZND solutions. Outside the ZND boundary, extrapolation is required. The extrapolation is done differently for the mixture composition and the thermodynamic variables.

The mixture composition is extrapolated assuming all Y_s are primarily influenced by C, not T. Specifically, for (C, T) coordinates below the ZND boundary, the mass fractions are copied down from the boundary, such that $Y_s(C, T < T_{\mathrm{ZND}}) = Y_s(C, T_{\mathrm{ZND}})$. Similarly, for (C, T) coordinates above the ZND boundary, the mass fractions are copied up from the boundary, such that $Y_s(C, T > T_{\mathrm{ZND}}) = Y_s(C, T_{\mathrm{ZND}})$. For C coordinates to the right of the CJ endpoint, the mass fractions are copied to the right, such that $Y_s(C > C_{\mathrm{CJ}}, T) = Y_s(C_{\mathrm{CJ}}, T)$. Then, the mixture weight $W(C, T)$ is computed using the extrapolated $Y_s(C, T)$.

The mixture thermodynamic variables are primarily influenced by T. For all T coordinates, the species enthalpies, h_s, are computed using the NASA polynomials [118]. Because h_s are functions of T only, there is no need to extrapolate outside the ZND boundary. The mixture h is computed using the exact $h_s(T)$ along with the extrapolated mass fractions $Y_s(C, T)$. For the denominator in the Newton iteration (Eq. (5.7)), the heat capacity is computed as $c_p = \frac{\partial h}{\partial T}\big|_C$; this is not the true mixture heat capacity, but the derivative required for the Newton solver (which assumes

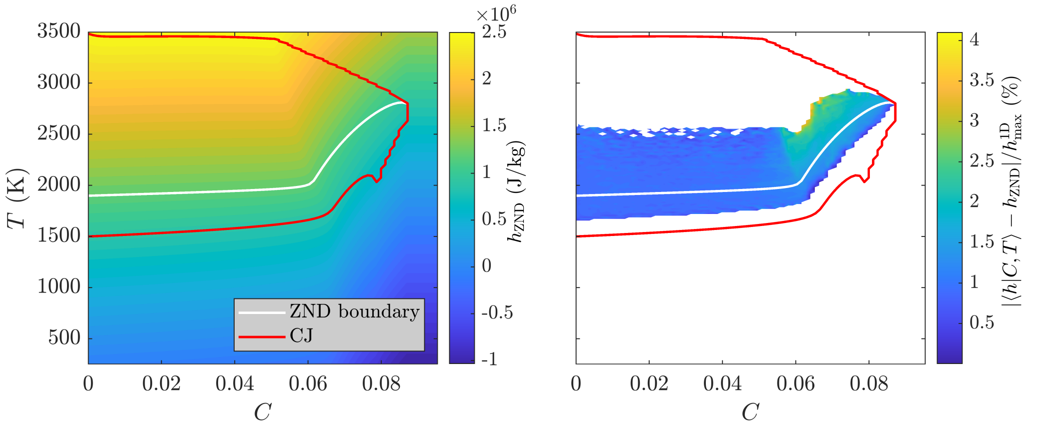

(a) ZND table mixture enthalpy.

(b) ZND table mixture enthalpy error.

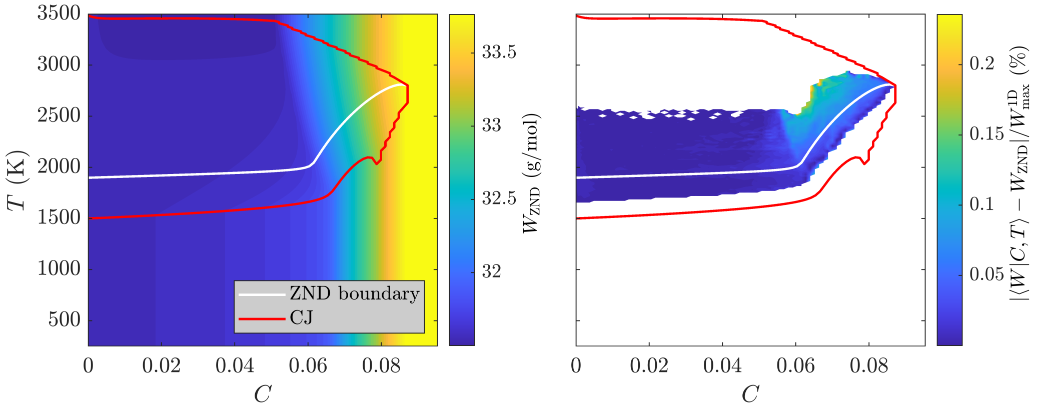

(c) ZND table mixture molecular weight.

(d) ZND table mixture molecular weight error.

Figure 5.9: Tabulated mixture enthalpy (a) and molecular weight (c) using ZND solutions. Error in the tabulated mixture enthalpy (b) and molecular weight (d) compared to the conditional means, normalized by the maximum value from the 1D CJ solution. Equilibrium boundary (red solid line) and CJ solution (white solid line).

constant ρ, ρe_t, and ρC). Both W and h vary smoothly throughout the table, as seen in Fig. 5.9; this is particularly important for the convergence of the Newton iteration in Eq. (5.7).

The boundary points $(C_{\mathrm{ZND}}, T_{\mathrm{ZND}})$ are located at chemical equilibrium for each of the ZND solutions; extrapolating the progress variable source term from inside the ZND equilibrium boundary would be unphysical. Therefore, the source term is set to zero outside the ZND boundary. The tabulated progress variable source term is shown in Fig. 5.10a, with the ZND boundary and CJ profile overlaid for reference. The source term varies smoothly throughout the table. Figure 5.10b

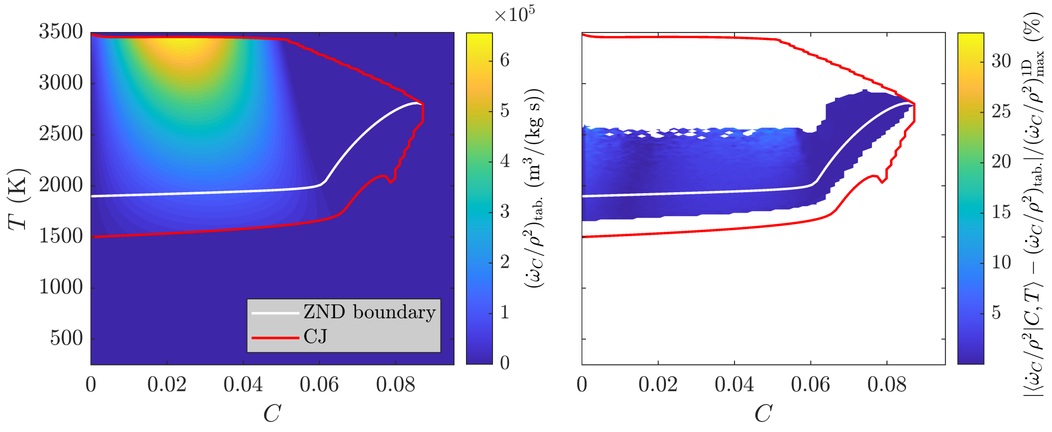

(a) ZND table source term. (b) ZND table error.

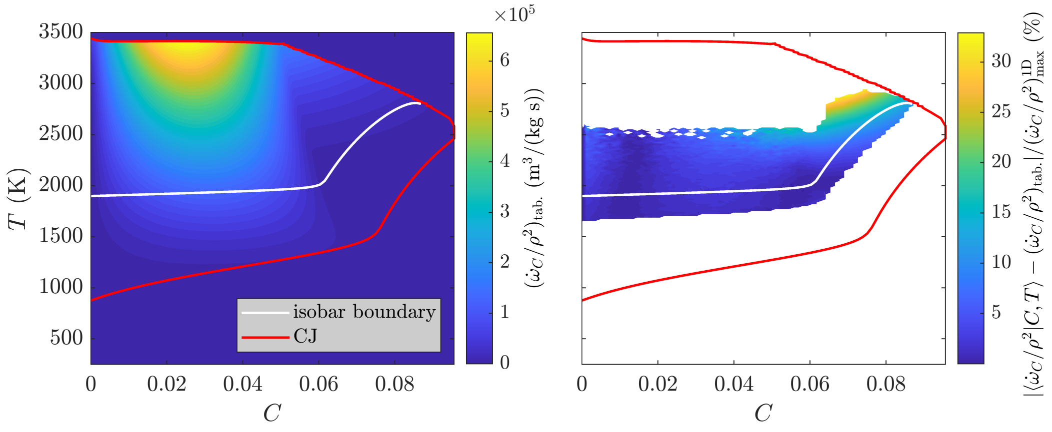

(c) Isobar table source term. (d) Isobar table error.

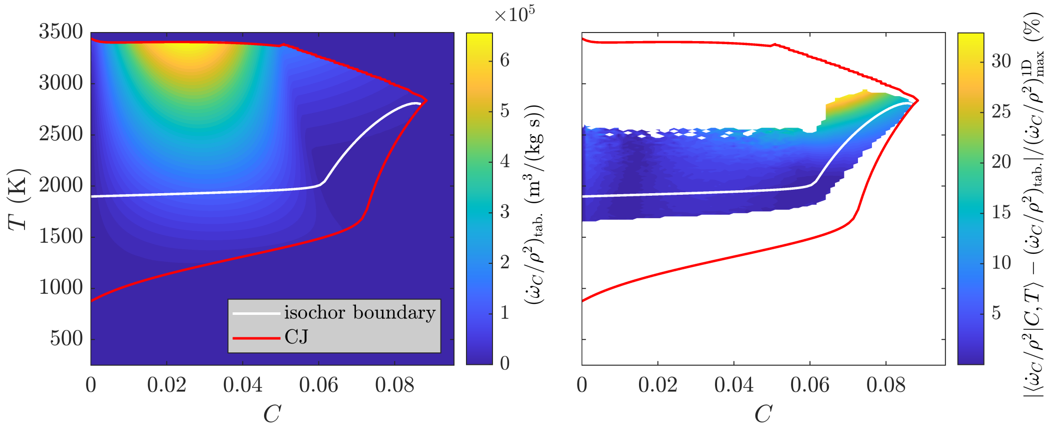

(e) Isochor table source term. (f) Isochor table error.

Figure 5.10: Tabulated progress variable source term, normalized by ρ^2, using ZND solutions (a), isobaric ignitions (c), and isochoric ignitions (e). Error in the tabulated source term compared to the conditional means $\langle \cdot | C, T \rangle$, normalized by the maximum value from the 1D CJ solution (b, d, f). Equilibrium boundary (red solid line) and CJ solution (white solid line).

shows the relative error of the progress variable source term predicted by the ZND table against that from the conditional mean $\langle \dot{\omega}_C/\rho^2 | C, T\rangle$. The errors remain small with a maximum of 7%. The errors in the other required table outputs, namely W and h, are even smaller and peak at 0.2% and 4% respectively.

As discussed in Sec. 5.2.1, the ignition process is important to reproduce the structure and propagation of the detonation. Therefore, it is worth considering if other ignition solutions (i.e. isobaric and isochoric ignitions) would predict equally well the conditional means. A series of ignition cases, with initial T and p corresponding to the von Neumann states of the ZND solutions, are computed using FlameMaster [124]. The individual ignitions are shown in (C, T) space in Fig. 5.11. From these solutions, two additional tables are generated: an isobaric and an isochoric. The procedure for interpolating and extrapolating the ignitions onto the (C, T) table coordinates is the same as was done for the ZND table.

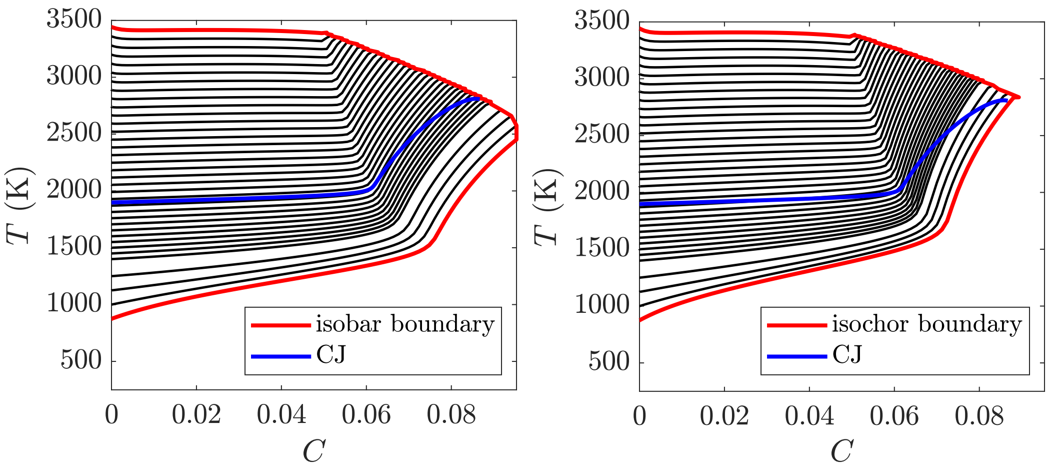

(a) Isobaric ignitions.

(b) Isochoric ignitions.

Figure 5.11: One-dimensional ignition solutions in (C, T) space (black solid lines), equilibrium boundary (red solid line), and CJ solution (blue solid line).

The progress variable source terms show the largest sensitivity to the choice of ignition solutions and are shown in (C, T) space in Fig. 5.10. Qualitatively, the dependence of the source term on C and T appears similar between the three tables. Figure 5.10 also shows the relative errors in the three tables compared to the conditional mean. The ZND table exhibits the lowest errors throughout the range of (C, T) coordinates. For both ignition tables, beyond the reaction zone and approaching the CJ state, the errors increase up to 30%. These tables would likely result in an overproduction of C in regions of the flow that should be nearing chemical equilibrium. From this comparison with the conditional means, the ZND table is found to be the best option for tabulating in (C, T) coordinates without relying on two-dimensional detailed chemistry calculations.

The ignition tables further highlight that premixed flamelets cannot be used for table generation. Premixed flamelets require the unburnt temperature to be below the ignition limit. As shown in Fig. 5.10d and 5.10f, the lower boundaries on the both the isobaric and isochoric ignition tables have an initial temperature of 875 K. Unfortunately, for the CJ detonation, the von Neumann state temperature, $T_{vN} = 1898$ K, is well above this ignition threshold. While a premixed flamelet table could be generated in (C, T) coordinates, the flamelet solutions could not fill the (C, T) space relevant to detonations.

In addition to the 7Ar-diluted mixture used to illustrate the methodology in Sec. 5.2.2-5.2.3, the tabulation approach is demonstrated for four other H_2-O_2 mixtures. The parameters used for table generation are listed in Table 5.1. The same procedure outlined in Sec. 5.2.3 is used for each mixture. The resulting tabulated source terms are shown in Fig. 5.12.

Mixture	p_1 (kPa)	u_{CJ} (m/s)	u_s (m/s)	u_s/u_{CJ}
$2H_2$-O_2-12Ar	20	1516	1300-2200	0.84-1.45
$2H_2$-O_2-17Ar	20	1413	1200-2000	0.85-1.42
$2H_2$-O_2-$3.5N_2$	20	1962	1540-2800	0.78-1.43
$2H_2$-O_2-$5.6N_2$	20	1799	1450-2800	0.81-1.56

Table 5.1: Unburnt conditions and range of ZND shock velocities used for each chemistry table. The unburnt temperature $T_1 = 295$ K for all tables.

5.2.4 Reaction rates in *(C,T)* space

In one step chemistry models, typically the reaction rate is assumed to take an Arrhenius form with a fixed parameter to describe the global activation energy. Recent compressible tabulation approaches still assume an Arrhenius form, but allow parameters to vary with the composition [84, 89]. Here, we explore the more complex description of the chemical reactions inherently built into the table.

Figure 5.13 shows Arrhenius plots of the tabulated progress variable chemical source term at the von Neumann state, the location of peak source term, and at 80% of the maximum C. These three locations correspond to the symbols marked on Fig. 5.6. To remove the offset between each mixture due to the varying amount of diluent vs. reactants, the source term is normalized depending on the local reaction order.

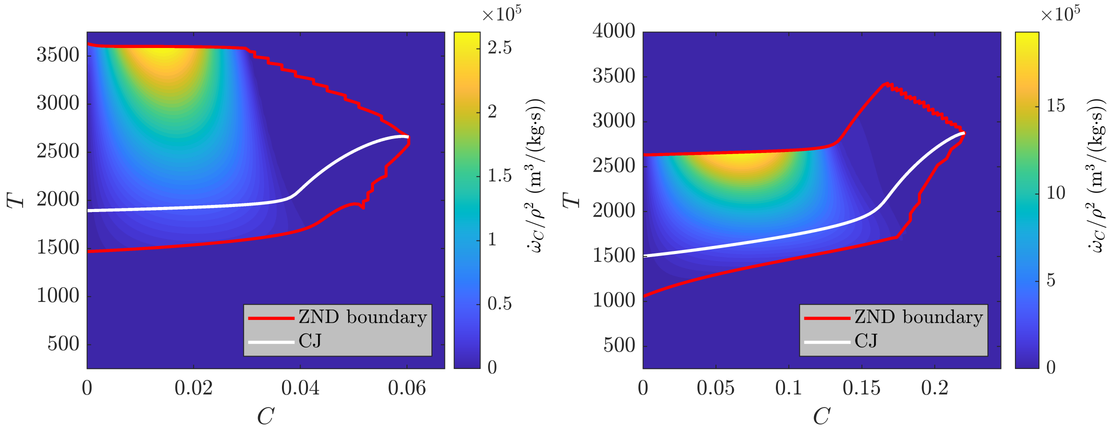

(a) 12Ar table source term.

(b) 3.5N_2 table source term.

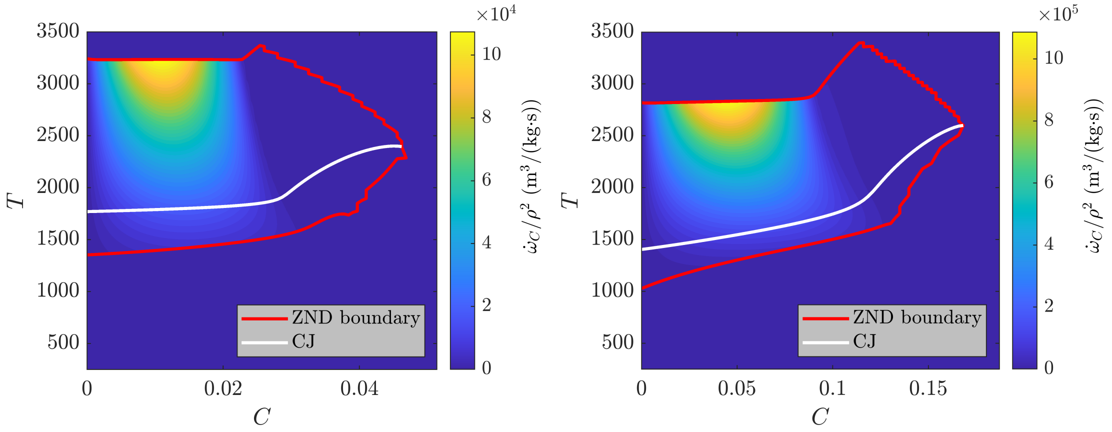

(c) 17Ar table source term.

(d) 5.6N_2 table source term.

Figure 5.12: Tabulated progress variable source term, normalized by ρ^2, using ZND solutions for the mixtures/conditions listed in Table 5.1. Equilibrium boundary (red solid line) and CJ solution (white solid line).

At the first two locations, $\dot{\omega}_C/\rho^2$ is normalized by $(1 - Y_{\text{dil.}})^2$, where $Y_{\text{dil.}}$ is either Y_{Ar} or Y_{N_2}, and the exponent of 2 comes from the general form for binary reactions, Eq. (5.22). The third location was found to have $a_\rho \approx 3$ (see Fig. 5.6), so $\dot{\omega}_C$ is normalized instead by ρ^3 and $(1 - Y_{\text{dil.}})^3$. These three locations in the detonation can be linked to specific reactions in the detailed chemical mechanism.

As discussed for detailed chemistry in Sec. 5.2.1, the initiation reactions are dominant in the post-shock region where $C \approx 0$. In particular, the following reaction,

$$H_2 + O_2 \rightarrow HO_2 + H, \tag{5.28}$$

was found to have a significant influence on the induction zone length (see Fig. 5.1). The slope corresponding to the Arrhenius rate for this reaction is indicated in Fig. 5.13a (note the reaction rate constant follows the modified Arrhenius form with a T^n term). Given the definition of the progress variable (Eq. (5.20)-(5.21)), the only initiation reaction built into the progress variable source term is Eq. (5.28). As a result, the same slope is found for each chemistry table regardless of the amount or type of diluent, closely matching the slope from the detailed reaction rate.

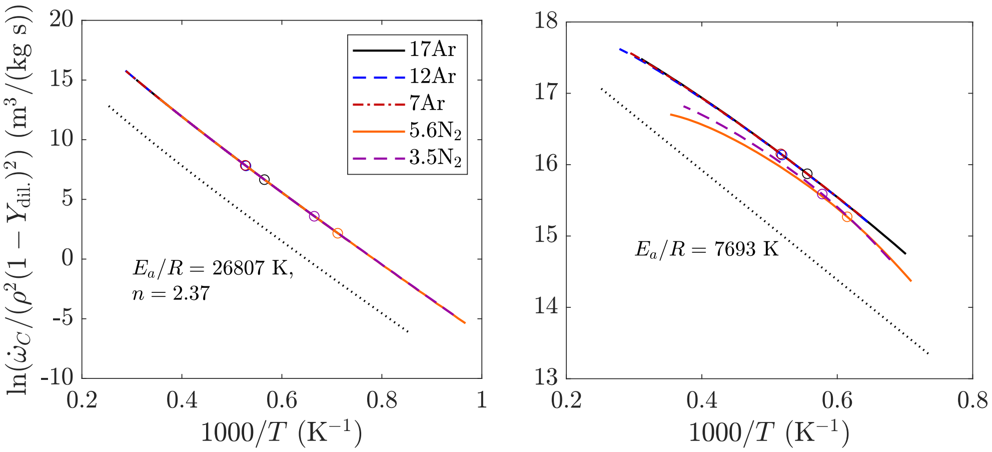

(a) von Neumann state ($C = 0$).

(b) C at peak source term.

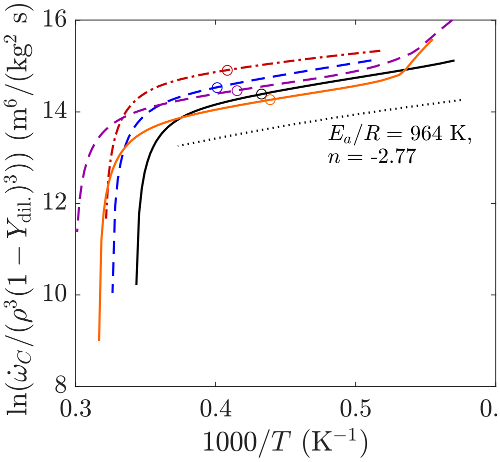

(c) $C = 0.8 \cdot \max\{C\}$.

Figure 5.13: Activation energy extracted from the chemistry tables along $C = 0$, C at the peak source term, and $C = 0.8 \cdot \max\{C\}$. Tables for stoichiometric H_2-O_2 diluted with 17Ar (black solid line), 12Ar (blue dashed line), 7Ar (red dash-dotted line), 5.6N_2 (orange solid line), and 3.5N_2 (purple dashed line). Symbols correspond to the (C, T) coordinate from the CJ ZND. Slopes corresponding to the rates for $H_2+O_2 \rightarrow HO_2+H$ (a), $H+O_2 \rightarrow O+OH$ (b), and $H+OH+H_2O \rightarrow 2H_2O$ (c) shown for reference (black dotted line).

At the peak source term, there are several intermediate species and elementary reactions involved. The following reaction,

$$H + O_2 \rightarrow O + OH, \tag{5.29}$$

was identified as the controlling reaction in determining ignition delay times [125]. The slope corresponding to the Arrhenius rate for this reaction is indicated in Fig. 5.13b. The rate corresponding to Eq. (5.29) is a decent approximation for the tabulated rates, albeit with some differences. Particularly for the N_2-diluted tables, there is some change in slope with temperature.

Near the maximum C, the termination reaction

$$\mathrm{H} + \mathrm{OH} + \mathrm{H_2O} \rightarrow 2\mathrm{H_2O}, \tag{5.30}$$

becomes important, so the assumption that second order reactions control the overall progress variable source term no longer holds. This is consistent with the observed source term-density dependence in Fig. 5.6. As for Eq. (5.28), the reaction rate for Eq. (5.30) follows the modified Arrhenius form, now with the rate decreasing as temperature increases. The tabulated source terms match this slope for a majority of the temperature range, before quickly dropping off at high T. These drops correspond to approaching the ZND boundaries, as the source term goes to zero at chemical equilibrium.

As evident from the changing slopes (indicative of changing activation energies), the present chemistry tabulation captures the richness of the detailed chemistry (i.e, different activation energy) while requiring only one additional transported scalar, as in one-step chemistry. By tabulating ZND solutions directly in both C and T coordinates, there is no need to assume the functional form of the temperature dependence of the source term.

5.3 A posteriori model validation

First, the chemistry model is tested for 1D argon-diluted detonations with two different configurations in Sec. 5.3.1. Then, a 1D pulsating detonation in a nitrogen-diluted mixture is demonstrated in Sec. 5.3.2. The model is validated for a variety of two-dimensional detonations in Sec. 5.3.3. The numerical convergence of the two-dimensional simulations is discussed in Sec. 5.3.4. Finally, Sec. 5.3.5 examines the computational cost of the simulations.

5.3.1 One-dimensional argon-diluted detonation

The tabulation approach is verified in several one-dimensional simulations. First, the table is tested using the ZND solution as the initial condition, propagating at the CJ speed. The setup is consistent with the one-dimensional solution and grid (in x) described in Sec. 4.2. The detailed and tabulated chemistry solutions, compared at $t = 6 \cdot 10^{-4}$ s in Fig. 5.14, are almost indistinguishable. As noted previously in Sec. 4.1, the progress variable solution varies monotonically in x.

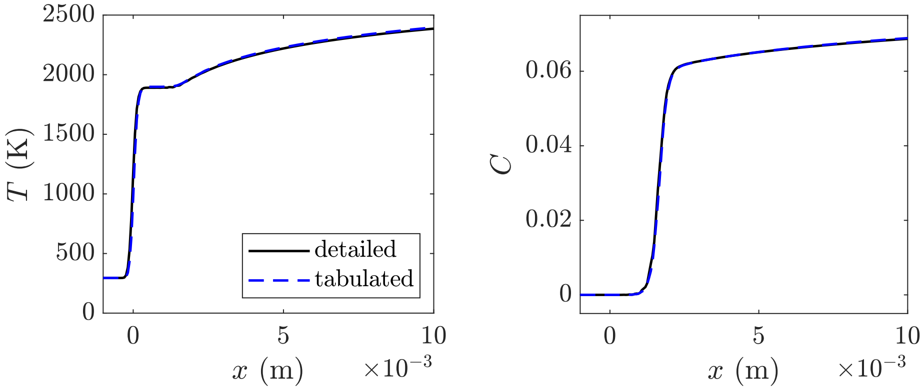

(a) Temperature.

(b) Progress variable ($Y_{H_2O} + Y_{HO_2}$).

Figure 5.14: One-dimensional CJ detonation in 7Ar-diluted mixture. Detailed chemistry (black solid line) and tabulated chemistry (blue dashed line). The profiles are shifted in x such that the shock (identified by the maximum temperature gradient) is located at $x = 0$.

Next, to confirm the choice of progress variable, a non-stationary case is used to compare two definitions: $C = Y_{H_2O}$ and $C = Y_{H_2O} + Y_{HO_2}$. Rather than using the ZND solution as the initial condition, a detonation may be triggered by a strong shock propagating through the unburnt mixture. In this configuration, the initial progress variable is 0 throughout the domain. A 1 m long shock tube configuration is used, with a 0.01 m driver section followed by a 0.99 m test section. A uniform grid with $\Delta x = \mathcal{L}/20$ is used for the entire domain. The initial conditions in the driver section are $T = 2500$ K and $p = 10^6$ Pa, and the initial conditions in the test section are $T = 295$ K and $p = 6.67$ kPa. The initial velocity is equal to 0. At the start of the simulation, a shock propagates to the right and an expansion propagates to the left. As the unburnt mixture ignites, the shock wave transitions into a detonation wave that propagates the length of the channel.

The evolution of the lead shock speed as it propagates down the channel is shown in Fig. 5.15a. The solutions using both detailed chemistry and tabulated chemistry with $C = Y_{H_2O} + Y_{HO_2}$ relax towards the CJ speed, whereas the tabulated chemistry with $C = Y_{H_2O}$ propagates at a slower speed and decays without reaching an asymptote. When the shock has reached $x_s = 0.9$ m, the detailed and tabulated (including HO_2) cases are within 2-3% of the CJ speed. At this shock location, the instantaneous profiles are compared in Fig. 5.15b and 5.15c. When the progress variable only

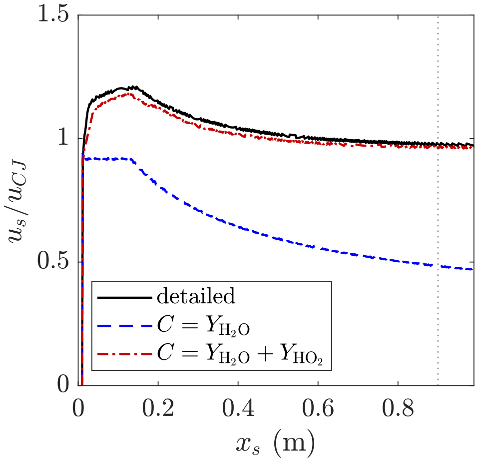

(a) Shock speed.

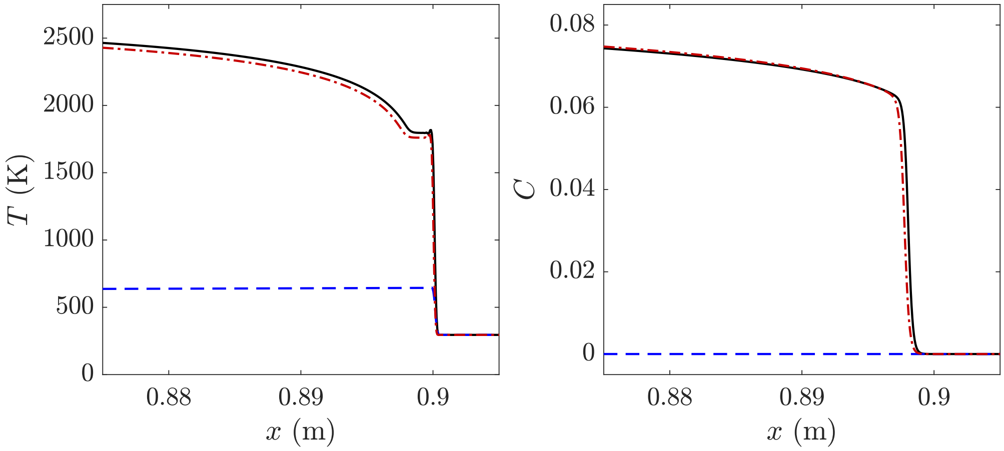

(b) Temperature.

(c) Progress variable.

Figure 5.15: Shock tube-initiated 1D detonation; shock propagation speed (normalized by the CJ speed) shown as a function of the shock location x_s (a), instantaneous temperature and progress variable profiles shown when the shock has reached $x_s = 0.9$ (b,c). Detailed chemistry (black solid line), tabulated chemistry with $C = Y_{H_2O}$ (blue dashed line), and tabulated chemistry with $C = Y_{H_2O} + Y_{HO_2}$ (red dash-dotted line); $x_s = 0.9$ (a, vertical black dotted line).

includes H_2O, ignition never occurs; the post-shock temperature is uniform and the progress variable stays at 0. Including HO_2 in the definition of the progress variable results in temperature and progress variable profiles that closely match the detailed chemistry solution. Slight differences in the detonation strength are likely due to discrepancies in the initial transient. Due to the range of (C, T) conditions encountered during the initial ignition process, this case is more sensitive to the lower ZND boundary in the table. The lower bound of $u_s = 1400$ m/s was sufficient for cases initialized with the steady CJ solution; here, the lower bound is reduced to

$u_s = 1150$ m/s. Other details of the table generation are the same as described in Sec. 5.2.3; the modified table is shown in Fig. 5.16.

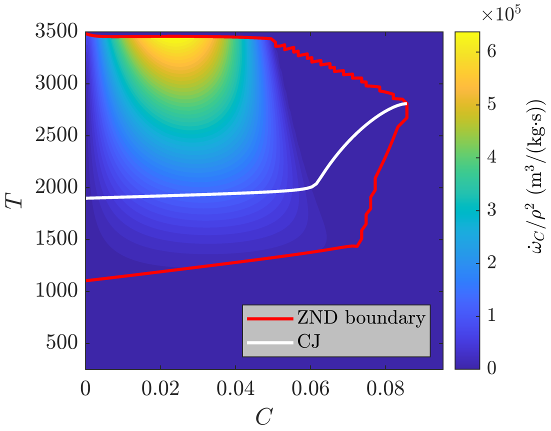

Figure 5.16: Tabulated progress variable source term for the non-stationary 7Ar-diluted detonation, normalized by ρ^2, using a lower ZND boundary of $u_s = 1150$ m/s. Equilibrium boundary (red solid line) and CJ solution (white solid line).

These one-dimensional results illustrate the importance of including HO_2 in the progress variable definition. In the tabulation of hydrogen flames, using $C = Y_{H_2O}$ was sufficient due to the role of diffusion [80]. Because detonations are driven by ignition, not diffusion, it is necessary for the table to include the effects of the initiation reactions. Therefore, all remaining test cases in this paper use $C = Y_{H_2O} + Y_{HO_2}$.

5.3.2 One-dimensional nitrogen-diluted detonation

To test the ability of the tabulation to capture additional unsteady 1D behavior, a more unstable mixture is tested, this time diluting with nitrogen instead of argon: $2H_2$-O_2-$5.6N_2$. Once again, the steady ZND solution is used as the initial condition, with the minimum $\Delta x = \mathcal{L}/20$. Figure 5.17 shows the time evolution of the detonation propagation speed. Both the detailed and tabulated chemistry solutions oscillate about the CJ speed due to the physical instability of the detonation front. Although the amplitude of the oscillations is somewhat reduced in the tabulated simulation, the periods closely match between the two chemistry models. This indicates that the tabulation approach is able to capture the limit cycle behavior expected for unstable mixtures. The impact of grid resolution on this period-2 limit cycle is discussed in Sec. 6.1.

Traditional stability analyses of 1D pulsating detonations have relied on one-step chemistry characterized by a single activation energy (valid throughout the reaction

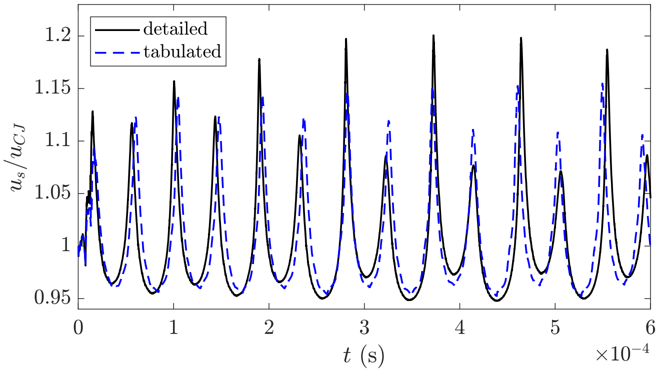

Figure 5.17: 1D pulsating detonation in 5.6N_2-diluted mixture; propagation velocity normalized by the CJ speed. Detailed chemistry (black solid line) and tabulated chemistry (blue dashed line).

process) [59, 126–134]. These studies identified the reduced activation energy (E_a/RT_0, where E_a is the activation energy and the reference temperature T_0 is typically the unburnt, pre-shock temperature [126]) as a controlling parameter in separating stability limits/regimes. At lower activation energies, oscillations in the shock pressure/speed are dampened out over time. As the activation energy increases, a periodic limit cycle is achieved. In contrast, detailed chemistry is composed of a multitude of elementary reactions, each with their own activation energy. As a result, the overall/effective activation energy will be different in different regions of the detonation, as discussed previously in Sec. 5.2.4. Because the table contains information about the local reaction rates/activation energies, it captures the onset of irregularity intrinsically. Other reduced models of two or three steps have used the chain-branching cross-over temperature [135] or the ratio of the reaction to induction zone lengths [136] as bifurcation parameters. More generally, the ratio of the induction zone to reaction zone length influences the degree of instability, regardless of the chemistry model used; these length scales and their ratios are provided in Sec. 5.3.3 for various H_2-O_2 mixtures.

These results further highlight that a density scaling of 2 is a reasonable approximation for the progress variable source term; the 1D instability originates within the induction zone (from the von Neumann state, Fig. 5.13a, to the reaction zone, around Fig. 5.13b), where second order reactions dominate the chemistry. While there are third order reactions in the detailed mechanism, these are more important further into the burnt region (Fig. 5.13c), and therefore have little impact on the limit cycle behavior.

5.3.3 Two-dimensional detonations

The chemistry table is validated for two-dimensional detonations using the same configuration described in Sec. 4.2. Along with the H_2-O_2-7Ar mixture, four additional mixtures are tested: $2H_2$-O_2-12Ar, $2H_2$-O_2-17Ar, $2H_2$-O_2-$3.5N_2$, and $2H_2$-O_2-$5.6N_2$. These conditions correspond to experimental mixture parameters from [113]. Parameters for each mixture are included in Table 4.1, 4.2, and 5.1. As described in Sec. 4.2, a uniform grid is used up to $x = 0.05$ m, after which 1% stretching is applied; because Δx is dependent on the induction zone length, this results in a different number of grid points in x and y for each mixture. To focus on the late-time behavior, rather than discrepancies in the initial transient period, the tabulated simulations are initialized from the detailed solutions at $t = 4 \cdot 10^{-4}$ s before running to $t = 6 \cdot 10^{-4}$ s.

For each mixture, the time evolution of the propagation speed is shown in Fig. 5.18; in all cases, the tabulated chemistry simulations sustain the CJ speed. Compared to the planar-averaged propagation speed, the local propagation speed varies more throughout the cell cycle, and is therefore useful for comparing the detonation dynamics produced by the two chemistry models. For all mixtures tested, the tabulated simulations are able to capture a majority of the variation within a cell cycle. Both the amplitude and period of the velocity oscillations are similar between the detailed and tabulated simulations.

The time evolution can be further examined by comparing numerical soot foils from the two sets of simulations. The maximum pressure history is recorded over the time range $t = 4 \cdot 10^{-4}$ to $6 \cdot 10^{-4}$ s and shown in Fig. 5.19. The sizes of the observed cell structures are similar between the detailed and tabulated simulations, indicating that the evolution of the triple point collisions is not impacted by the chemistry tabulation. Additionally, the tabulation is able to reproduce the regularity of the cell structure. The argon-diluted mixtures have more regular cells; while the nitrogen-diluted mixtures have more irregular cell structures. The cell sizes can be compared more quantitatively for the different mixtures and chemistry models through histograms of the length scales observed. Figure 5.20 shows the distributions of the length scales measured from the soot foils in Fig. 5.19. Length scales are measured manually across a cell from triple point to triple point, both in the streamwise and transverse directions. For all mixtures, the streamwise length scales are longer than the transverse length scales; this is consistent between the detailed and tabulated chemistry results. The widths and means of the distributions

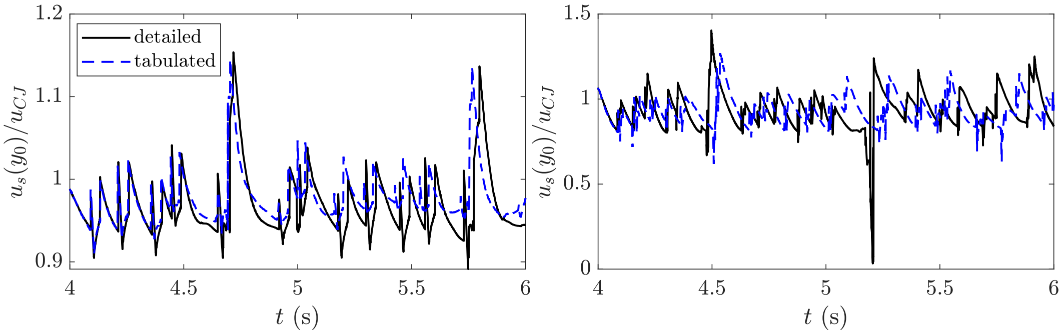

(a) 7Ar

(b) 3.5N$_2$

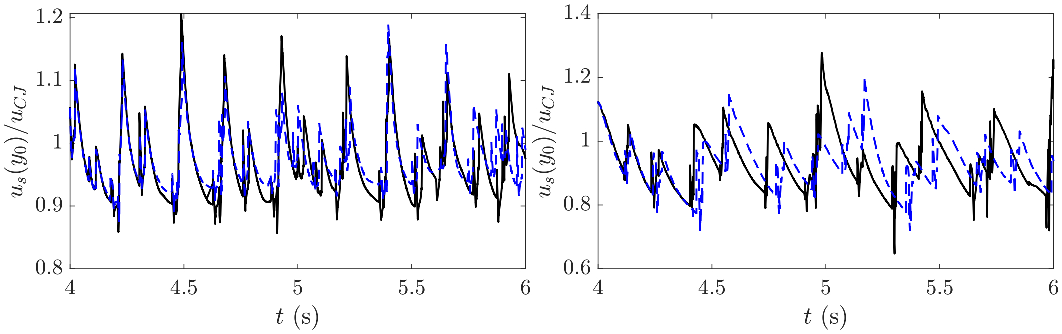

(c) 12Ar

(d) 5.6N$_2$

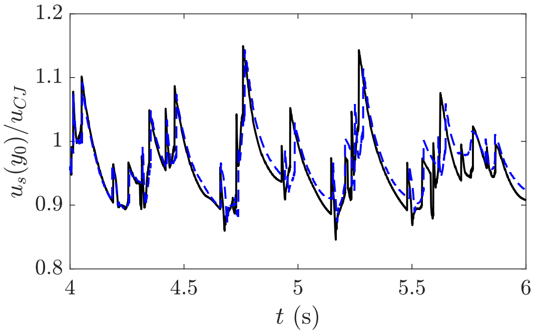

(e) 17Ar

Figure 5.18: Time evolution of the local propagation speed (normalized by the CJ speed). Detailed chemistry (black solid line) and tabulated chemistry (blue dashed line).

are also similar between the chemistry models. The soot foils are shown for comparison between the detailed chemistry and tabulated chemistry simulations only. To compare the cell structure with that observed in experiments, the simulation boundary conditions and domain size should match that of the experiment. While the unburnt conditions in this work are taken from experiments [113], the channel heights ($L_y = 0.06 - 0.107$ m) are smaller than that of the experimental facility ($L_y = 0.152$ m), and the simulations are two-dimensional, not three-dimensional. As such, direct comparisons to experimental cell sizes are outside the scope of the

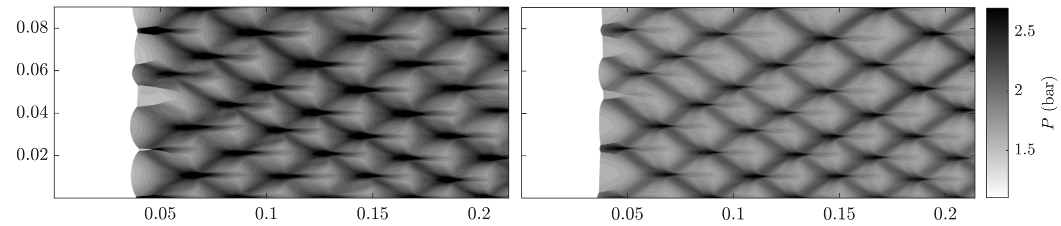

(a) 7Ar, detailed chemistry. (b) 7Ar, tabulated chemistry.

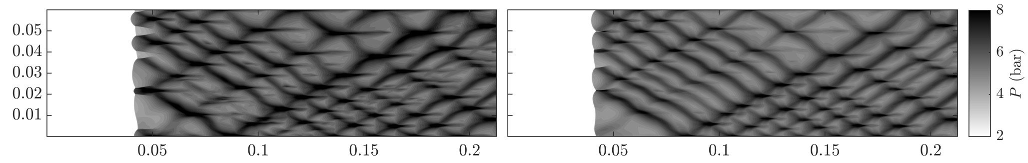

(c) 12Ar, detailed chemistry. (d) 12Ar, tabulated chemistry.

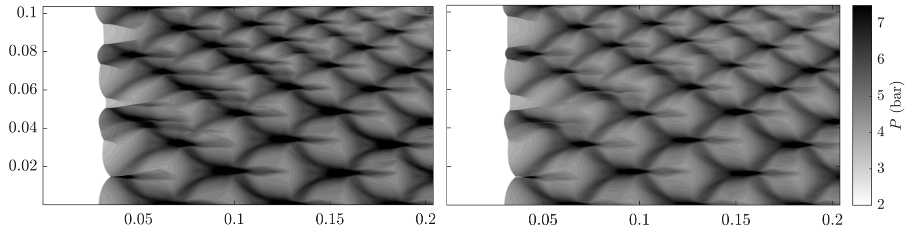

(e) 17Ar, detailed chemistry. (f) 17Ar, tabulated chemistry.

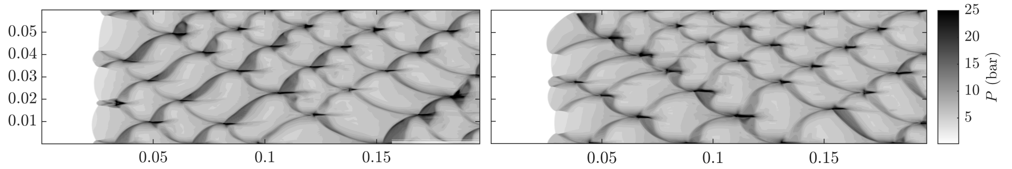

(g) 3.5N_2, detailed chemistry. (h) 3.5N2, tabulated chemistry.

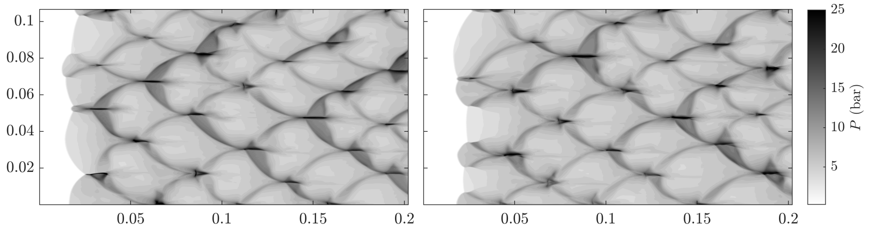

(i) 5.6N_2, detailed chemistry. (j) 5.6N2, tabulated chemistry.

Figure 5.19: Numerical soot foils (maximum pressure trace) for the detailed (a, c, e, g, i) and tabulated (b, d, f, h, j) simulations.

present work.

Instantaneous snapshots may be used to examine the detonation structure in more detail. The numerical schlieren and temperature fields are shown for both N_2 cases in Fig. 5.21. Contour lines at the C corresponding to the peak progress variable source term (from the CJ solution in 1D) are shown to illustrate both the location

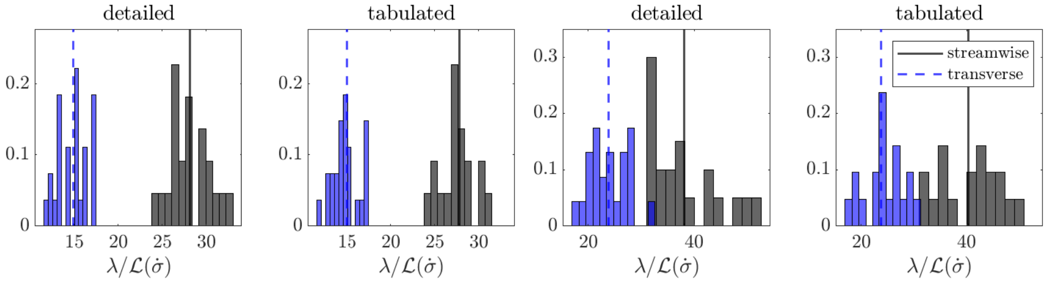

(a) 7Ar

(b) $3.5N_2$

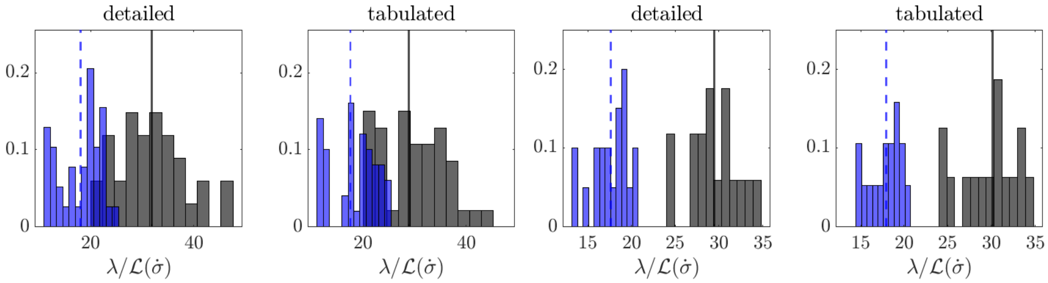

(c) 12Ar

(d) $5.6N_2$

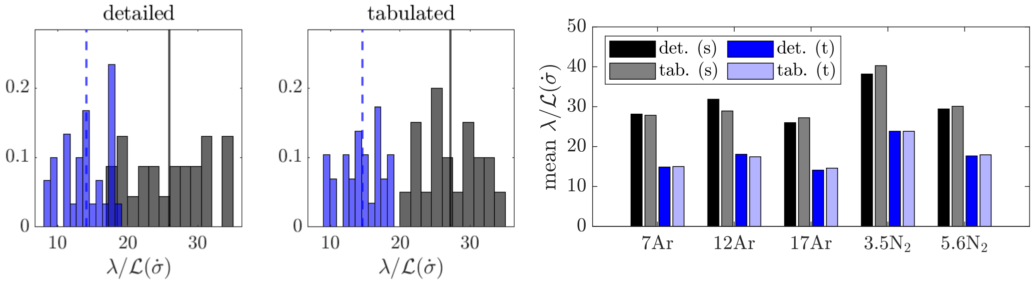

(e) 17Ar

(f) Mean cell sizes.

Figure 5.20: Distributions (a-e) of the length scales observed in the soot foils in Fig. 5.19, normalized by the 1D induction zone length defined by the maximum thermicity location. Streamwise cell lengths (gray histograms) and their mean (black solid line), transverse cell heights (blue histograms) and their mean (blue dashed line). Comparison of mean length scales for all cases (f).

of the reaction front relative to the shock front, as well as the unburnt pockets behind the reaction front. Comparing the schlieren with the C contour, the unburnt pockets form next to transverse waves soon after a new triple point collision. As the time evolution does not match instantaneously between the detailed and tabulated simulations (see Fig. 5.18), these snapshots primarily offer a qualitative comparison between the detailed and tabulated chemistry simulations. For both the $5.6N_2$ and $3.5N_2$-diluted mixtures, the sizes and shapes of the unburnt pockets are similar. For both chemistry models, the unburnt pockets are found only near the most recent triple point collisons; as the transverse waves propagate away from the triple point,

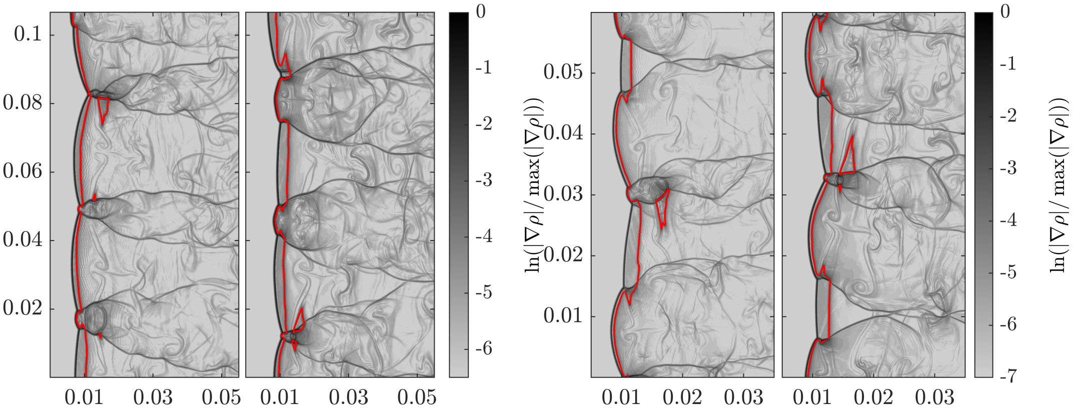

(a) 5.6N$_2$, detailed. (b) 5.6N$_2$, tabulated. (c) 3.5N$_2$, detailed. (d) 3.5N$_2$, tabulated.

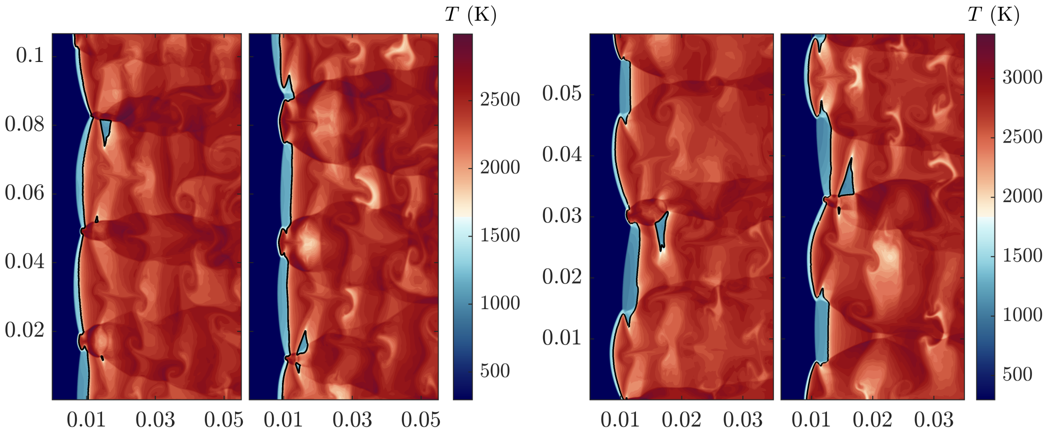

(e) 5.6N$_2$, detailed. (f) 5.6N$_2$, tabulated. (g) 3.5N$_2$, detailed. (h) 3.5N$_2$, tabulated.

Figure 5.21: Instantaneous schlieren (top) and temperature (bottom) for the N$_2$-diluted cases; contour at the C corresponding to the peak $\dot{\omega}_{C,CJ}$ (red solid line, a-d; black solid line, e-h).

the unburnt pockets are re-shocked and then burnt.

The time-averaged joint PDFs and conditional means of the progress variable source term are shown in Fig. 5.22 and 5.23. For both the 7Ar (regular) and 5.6N$_2$ (irregular) diluted cases, the tabulated chemistry simulation results closely reproduce the detailed chemistry results. There are two small differences in the results. At the source term peak, the tabulated distribution is slightly narrower than the detailed distribution. At larger C, the tabulation does not capture all the variation in the source term. These discrepancies are more easily seen in the conditional standard deviations of the source term, shown in Fig. 5.24a and 5.24d. To separate the errors introduced by the ZND table from the errors associated with the solution of the progress variable transport equation, an a priori comparison is also shown. From the detailed chemistry data, the progress variable $Y_{H_2O} + Y_{HO_2}$ and the temperature

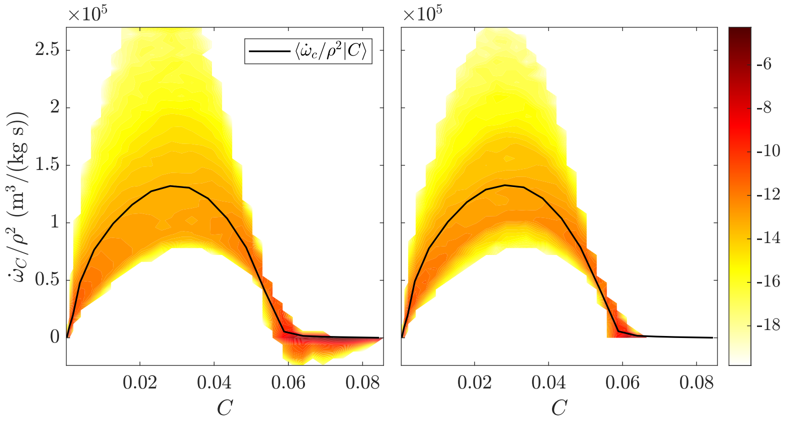

(a) 7Ar, detailed chemistry. (b) 7Ar, tabulated chemistry.

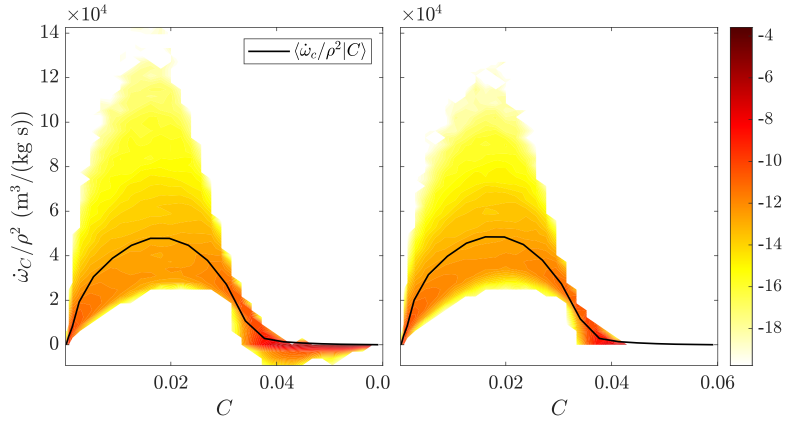

(c) 12Ar, detailed chemistry. (d) 12Ar, tabulated chemistry.

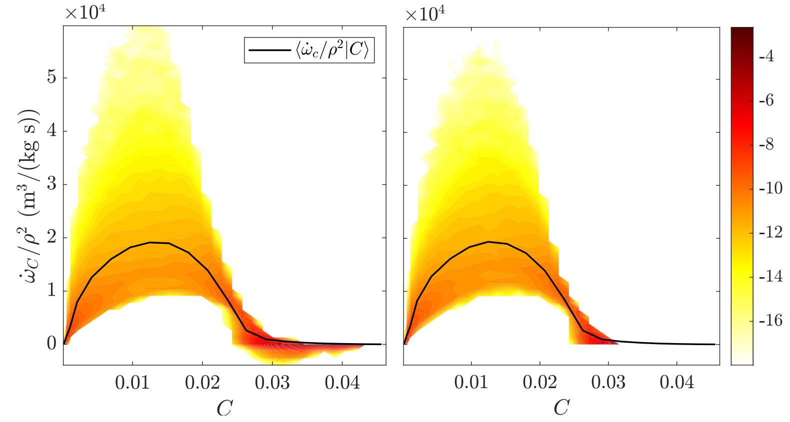

(e) 17Ar, detailed chemistry. (f) 17Ar, tabulated chemistry.

Figure 5.22: Two-dimensional Ar-diluted detonations. Comparison of detailed (a, c, e) and a posteriori tabulated (b, d, f) progress variable source term time-averaged over $t = 4 \cdot 10^{-4}$ to $6 \cdot 10^{-4}$ s. Joint PDF (red/yellow colormap showing the natural log of the PDF) and conditional mean on C (black solid line).

are used to look up the progress variable source term from the table. The a priori tabulated conditional standard deviations closely match the detailed ones. This

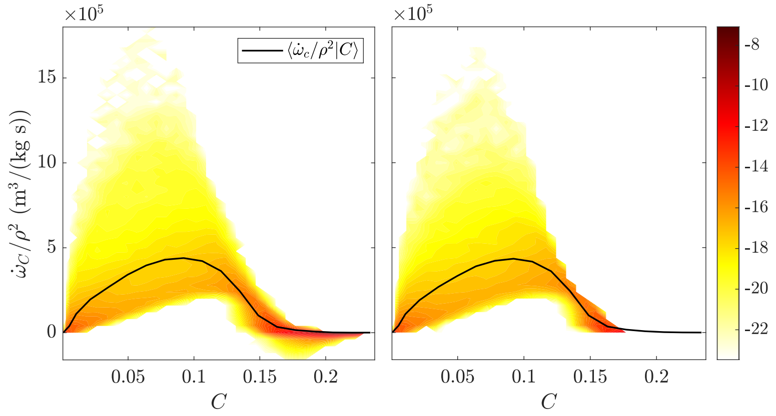

(a) 3.5N$_2$, detailed chemistry. (b) 3.5N$_2$, tabulated chemistry.

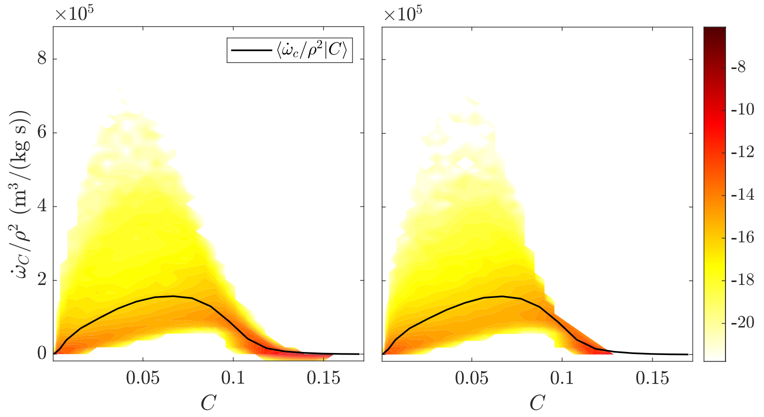

(c) 5.6N$_2$, detailed chemistry. (d) 5.6N$_2$, tabulated chemistry.

Figure 5.23: Two-dimensional N$_2$-diluted detonations. Comparison of detailed (a, c) and a posteriori tabulated (b, d) progress variable source term time-averaged over $t = 4 \cdot 10^{-4}$ to $6 \cdot 10^{-4}$ s. Joint PDF (red/yellow colormap showing the natural log of the PDF) and conditional mean on C (black solid line).

indicates that the table itself is able to describe virtually all the variation in the source term present in the detailed chemistry simulations. Minor differences in the results emerge primarily due to a buildup of errors over time of the simulation. Specifically, the slight underprediction of the standard deviations (up to about 5% at the peak source term) for the a posteriori tabulated source term reflects slight differences in the dynamical evolution of the 2D detonation (as shown in the previous soot foils). These results indicate that even with the cumulative errors from the table coordinates, table generation, and numerical transport of the progress variable, the tabulation is still able to reproduce a majority of the variation in the source term for both regular and irregular mixtures.

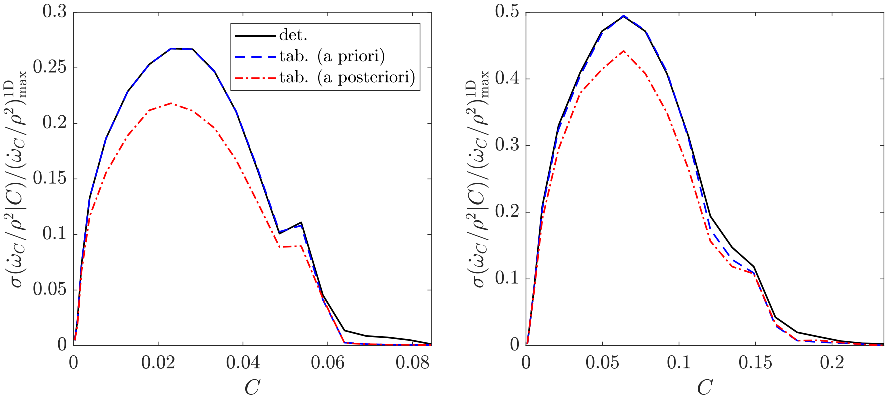

(a) 7Ar, source term rms. (b) $3.5N_2$, source term rms.

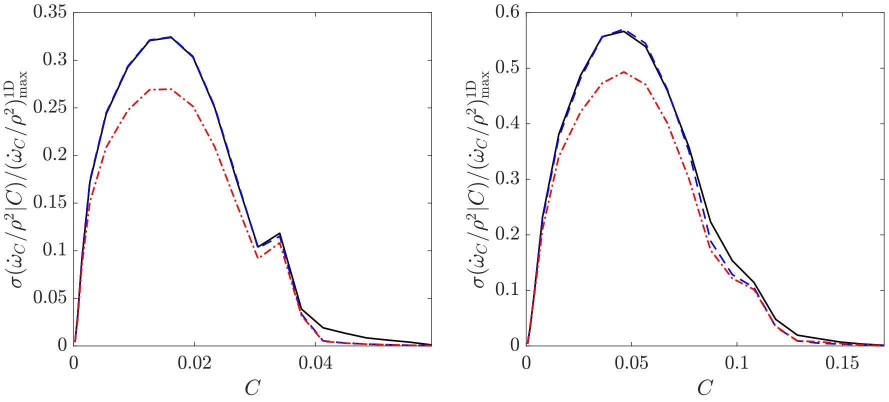

(c) 12Ar, source term rms. (d) $5.6N_2$, source term rms.

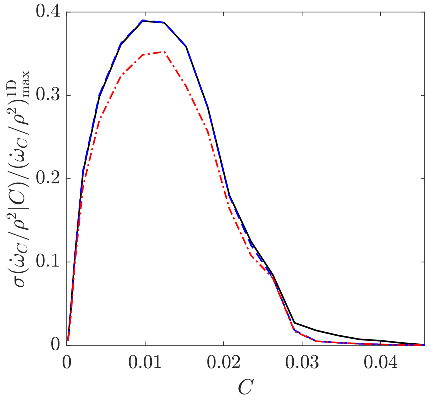

(e) 17Ar, source term rms.

Figure 5.24: Conditional standard deviation of the source term normalized by the maximum value from the 1D CJ solution from detailed chemistry (black solid line), a priori tabulated chemistry (blue dashed line), and a posteriori tabulated chemistry (red dash-dotted line).

5.3.4 Numerical convergence

To assess the impact of grid resolution on the two-dimensional simulations, one regular case ($2H_2$-O_2-7Ar) and one irregular case ($2H_2$-O_2-$5.6N_2$) are tested at varying resolutions: 10, 20, and 32 points per induction length. The resulting soot foils are shown in Fig. 5.25 and 5.26. In the 7Ar-diluted cases, refining the grid primarily sharpens the cell structures; the sizes/shapes of the cells are fairly consistent. The resolution has a stronger influence on the 5.6N_2-diluted cases. At 10 points per induction length, the cell structure is more regular compared to the two finer grids. While the irregular structures are sharper in the finest case (32 points per induction length), 20 points per induction length is sufficient to reproduce sizes/shapes of the cells. Therefore, the results presented in this chapter use a resolution of 20 points per induction length. It is also worth noting that for both mixtures, the resolution effects are similar between the detailed chemistry and tabulated chemistry simulations. The influence of the resolution on the one-dimensional instability will be investigated in Sec. 6.1.

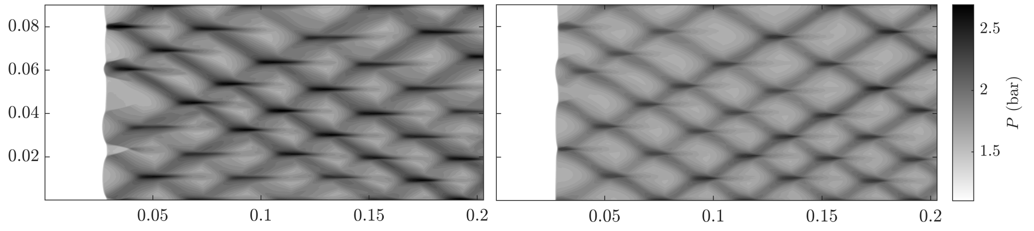

(a) $\Delta x = \mathcal{L}/10$, detailed (b) $\Delta x = \mathcal{L}/10$, tabulated

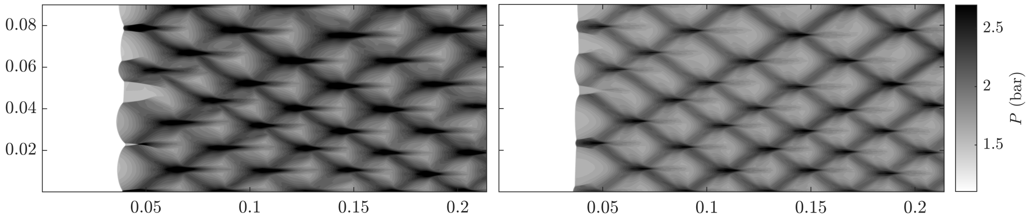

(c) $\Delta x = \mathcal{L}/20$, detailed (d) $\Delta x = \mathcal{L}/20$, tabulated

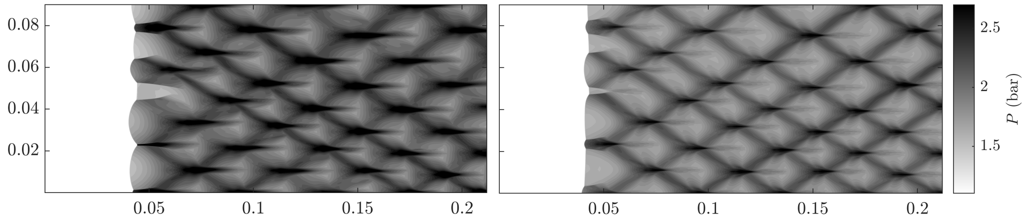

(e) $\Delta x = \mathcal{L}/32$, detailed (f) $\Delta x = \mathcal{L}/32$, tabulated

Figure 5.25: $2H_2$-O_2-7Ar soot foils at varying grid resolutions.

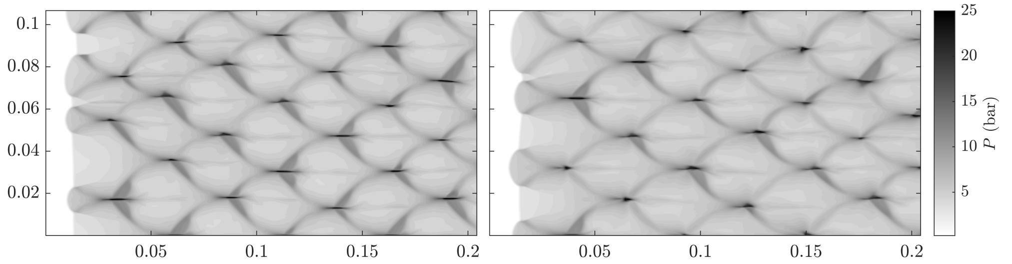

(a) $\Delta x = \mathcal{L}/10$, detailed (b) $\Delta x = \mathcal{L}/10$, tabulated

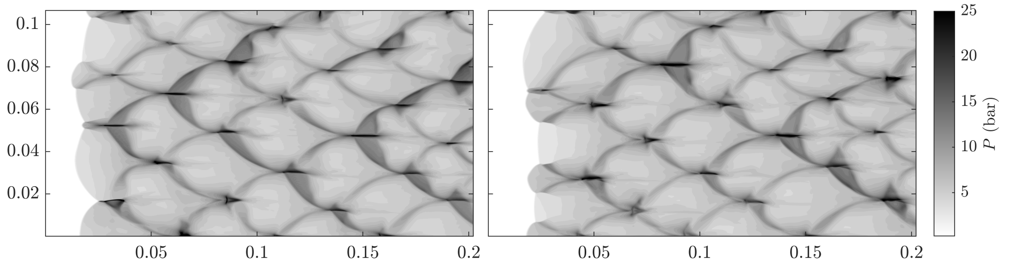

(c) $\Delta x = \mathcal{L}/20$, detailed (d) $\Delta x = \mathcal{L}/20$, tabulated

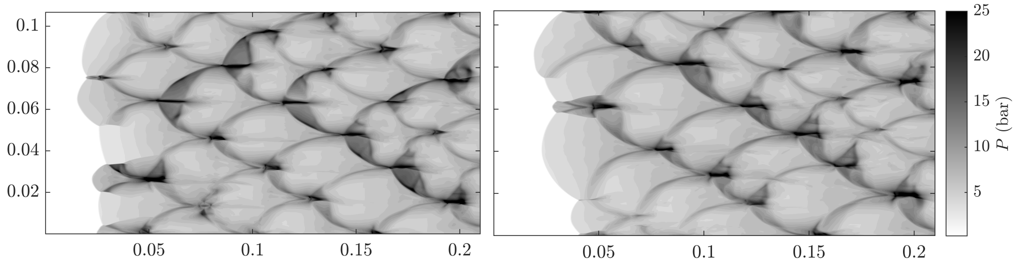

(e) $\Delta x = \mathcal{L}/32$, detailed (f) $\Delta x = \mathcal{L}/32$, tabulated

Figure 5.26: $2H_2$-O_2-$5.6N_2$ soot foils at varying grid resolutions.

5.3.5 Computational cost

One of the main reasons for using a tabulated chemistry model in place of a detailed mechanism is to reduce the computational cost. The computational time requirements for each component of the code are shown in Fig. 5.27, using the average over 20 timesteps from the two-dimensional simulations. The combustion timing includes computation of all chemistry-related source terms and thermodynamic properties; the continuity, momentum, and energy timings include computation of the convective and viscous terms in the respective equations, as well as the time integration; the scalar timing includes all species equations for the detailed simulation, and the progress variable equation for the tabulated simulation; the SFS timing accounts for all terms related to the treatment of shocks and discontinuities; the rest timing accounts for everything else, a large portion of which is the temperature inversion (Eq. (5.7)). This computational budget does not include the pre-processing time required for table generation. For one mixture, the table generation takes 2 minutes running Matlab in serial on a desktop. Relative to the total CPU hours required for the two-dimensional simulation, the cost of table generation is negligible.

Overall, the computational time is reduced by a factor of 4.1 when using the tabulated chemistry model. A substantial reduction in the CPU-time per point is observed for both the combustion and scalar timings. In the tabulated simulation, the combustion cost is reduced to a table lookup for the progress variable source term, rather than computing chemical source terms for all 9 species and 54 reactions present in the detailed hydrogen mechanism. The scalar cost is reduced because only one transport equation (for the progress variable) is required instead of the 9 species equations. The scalar timing shows an absolute speedup by a factor of 9.4, going from 51% of the total computational cost to 21%. The combustion timing shows an absolute speedup by a factor of about 17.3, going from 32% of the total computational cost to 8%.

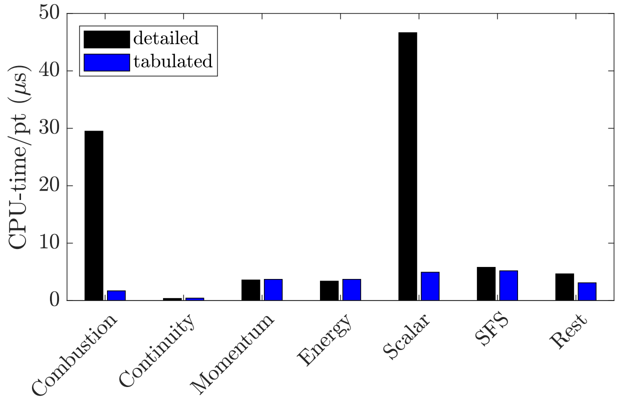

Figure 5.27: Computational time per grid point. Detailed simulation (black shaded bars) and tabulated simulation (blue shaded bars).

All the detailed chemistry results presented used a corrected WENO scheme to ensure that $\sum_s Y_s = 1$ (see Sec. 4.1); this was necessary to capture the pulsating behavior in Sec. 5.3.2 and the irregular cell structures in Sec. 5.3.3 for the N_2-diluted cases. The timings shown correspond to this scalar transport scheme for the detailed chemistry simulations, and the standard fifth order WENO scheme for the tabulated chemistry simulations; the same spatial and temporal resolution was used for both chemistry models. The scalar transport scheme has some effect on the scalar timing; when the standard WENO scheme is used with detailed chemistry, the scalar transport is about 10% faster. However, as discussed in more detail in

Sec. 6.1, when the standard WENO scheme is used, detailed chemistry requires a finer grid for the same level of error as tabulated chemistry. This is an additional source of computational savings.

The current work focuses on hydrogen combustion. More substantial computational savings are expected for larger chemical mechanisms required for hydrocarbons, and for state-to-state thermochemical models that incorporate vibrational non-equilibrium effects [53]. The timings in Fig. 5.27 can be used to estimate potential cost reduction for more complex fuels. For example, a reduced chemical model for *n*-heptane (regularly used in turbulent premixed flames) requires 35 species and 217 reactions (forward and backward reactions counted separately) [55]. In general, for detailed chemical kinetic models there is a linear correlation between the number of species and number of reactions [137]. If it is assumed that the combustion and scalar timings scale linearly with the number of species, we expect speedup factors of about 37 and 67 for the scalar and combustion timings, respectively. This would result in an overall speedup of approximately 14. Other factors may affect the ultimate performance for larger mechanisms; future work is required to confirm the estimated speedup of the tabulated chemistry model with more complex fuels.

5.4 Conclusion

This chapter proposed a new tabulated chemistry approach valid for detonations. One-dimensional ZND solutions were selected as the relevant physical problem to be tabulated, with progress variable and temperature as the table coordinates. The new model reproduced critical parameters such as induction zone length, detonation velocity, and cell structure compared to the detailed chemistry results. The total cost of simulations was reduced by over 4 times for hydrogen-oxygen detonations.

Chapter 6

DISCUSSIONS

Chapters 2 and 3 presented the mathematical framework used for the numerical simulations of shock-dominated flows. Using this framework, one- and two-dimensional detonations with detailed finite-rate chemistry were performed in Chapter 4. In Chapter 5, the tabulated chemistry method was formulated for detonations and validated by comparing to detailed chemistry results. The performance and limitations of the overall computational framework are reviewed here by focusing on three specific topics. First, the limit cycle of the one-dimensional detonation instability is revisited in Sec. 6.1. In Sec. 6.2, the evolution of regular and irregular detonations are examined in more detail in thermo-chemical space (i.e., (C, T) space). Finally, the potential impact of the SFS viscosity is investigated by analyzing the flow field behind the detonation front through the vorticity in Sec. 6.3. The objective is not to perform an in-depth analysis of the mathematical or physical phenomena, but to assess the impact of the numerical and modeling choices introduced in the previous chapters.

6.1 One-dimensional instability

One-dimensional pulsating detonations were used as validation cases in Sec. 4.3 and 5.3.2. These pulsating detonations are perfect examples of bifurcations, sometimes referred to as non-classical Hopf bifurcations [138] or period-doubling bifurcations [134], and have been the subject of previous numerical and theoretical studies. The detonation instability is revisited here for both N_2-diluted mixtures to assess the relative impacts of the numerical transport (see Chapter 4) and chemistry modeling (see Chapter 5).

The peak pressure for the limit cycle behavior is shown as a function of time in Fig. 6.1. For both $5.6N_2$ and $3.5N_2$, the cases with detailed chemistry and corrected WENO scheme (i.e., WENO-UP in Chapter 4) display the strongest instability. The tabulated chemistry cases show oscillations with a similar period, although the amplitude is somewhat reduced. In contrast, the detailed chemistry cases using the standard WENO scheme have oscillations with much lower amplitudes (by about an order of magnitude) and shorter periods; in the $5.6N_2$ case, this amplitude grows slowly, while in the $3.5N_2$ case, the oscillations are dampened over time. For both mixtures, the tabulated chemistry cases have almost the same period as the detailed WENO-UP cases; the time between peaks is about 1-5% shorter in the tabulated cases. This is an improvement from the detailed WENO cases, which have much shorter periods, about 70% those of the detailed WENO-UP. The estimated periods (and corresponding frequencies) are listed in Table 6.1.

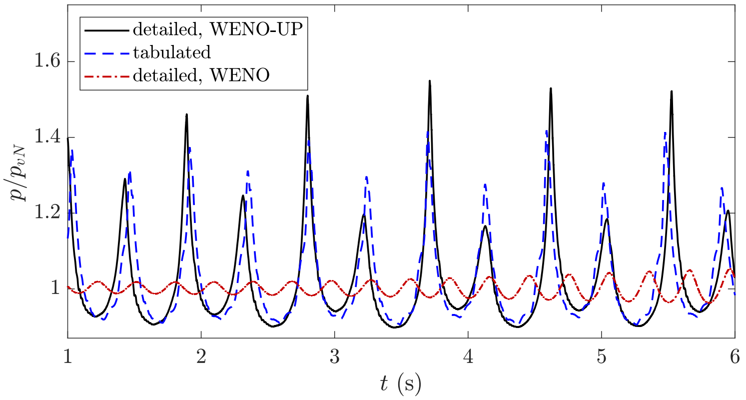

(a) 5.6N$_2$.

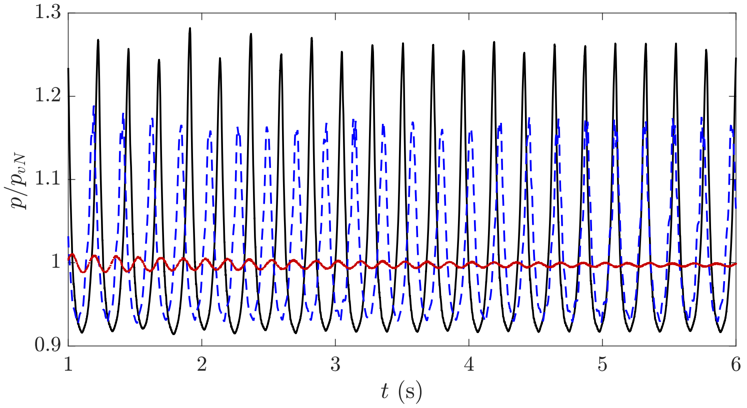

(b) 3.5N$_2$.

Figure 6.1: Shock pressure over time, normalized by the steady von Neumann state pressure (p_{vN}). Detailed chemistry with WENO-UP (black solid line), tabulated chemistry (blue dashed line), and detailed chemistry with WENO (red dash-dotted line).

Two periods of the shock oscillation are shown in Fig. 6.2 to illustrate the differences in the limit cycle behavior. In the 5.6N$_2$ case, the detailed chemistry case using standard WENO spans the smallest region in phase space (see Fig. 6.2b). When the species transport scheme is changed to WENO-UP, two different modes are observed. This is referred to as period-doubling [117, 134]. The tabulated chemistry case also shows two modes, with amplitudes between the two modes of the detailed WENO-UP case. In the 3.5N$_2$ case, both the detailed WENO-UP and tabulated chemistry cases have a single instability mode, with a slightly lower amplitude in the tabulated case (see Fig. 6.2d). The detailed case with WENO shows almost no deviation from the von Neumann state pressure.

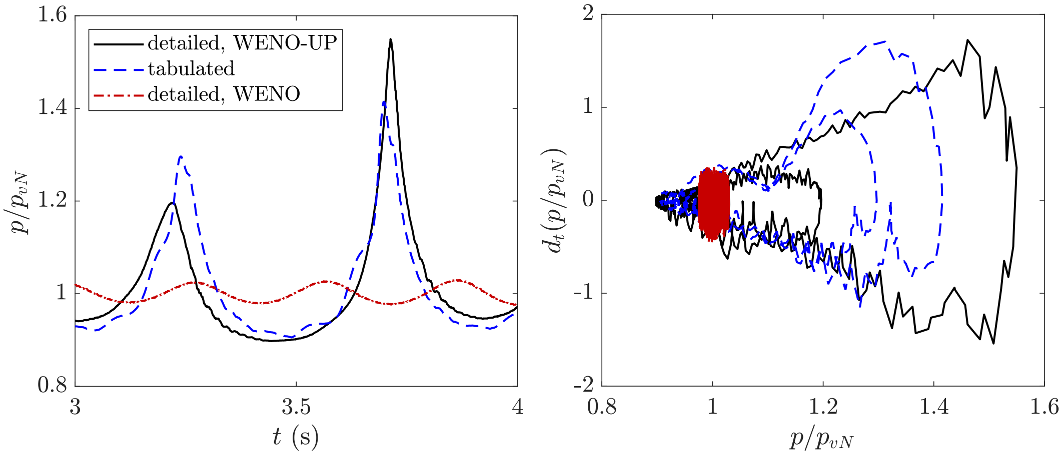

(a) 5.6N_2.

(b) 5.6N_2.

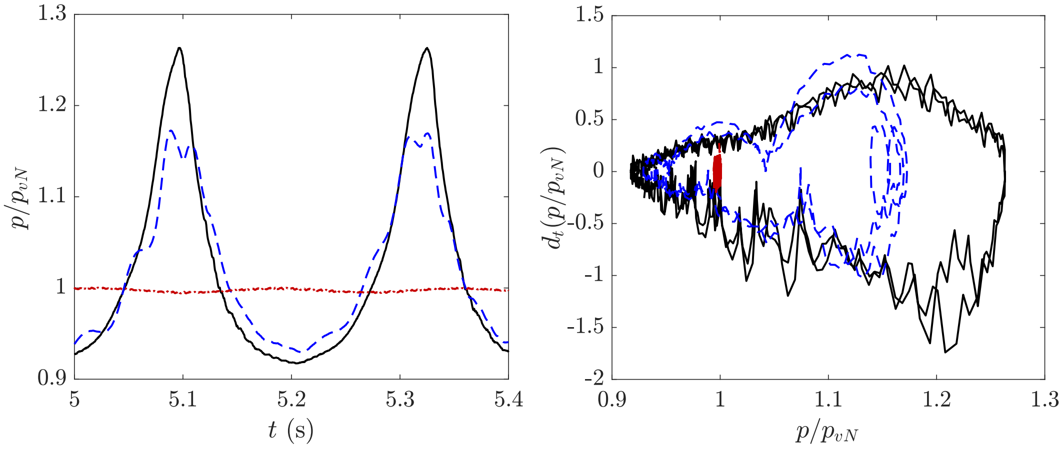

(c) 3.5N_2.

(d) 3.5N_2.

Figure 6.2: Limit cycle over two periods. Shock pressure vs. time (a, c) and time derivative of pressure vs. pressure (b, d). Detailed chemistry with WENO-UP (black solid line), tabulated chemistry (blue dashed line), and detailed chemistry with WENO (red dash-dotted line).

The limit cycle can also be analyzed through the power spectral density (PSD), shown in Fig. 6.3. The PSD is computed using Welch's overlapped segment averaging estimator with two different window sizes: 9000Δt (spanning approximately two periods in t) and 30000Δt (spanning several periods, to include more variations in the peak amplitude). When the smaller window is used, the tabulated case closely matches the detailed case with WENO-UP for a large range of frequencies; while the detailed case with WENO is orders of magnitude lower, especially at the lower

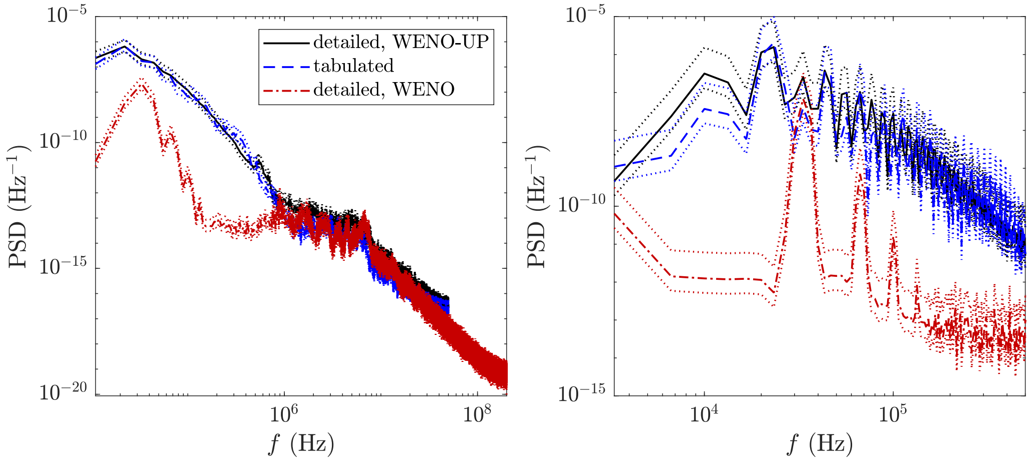

(a) 5.6N$_2$, window of $9 \cdot 10^{-5}$ s. (b) 5.6N$_2$, window of $3 \cdot 10^{-4}$ s.

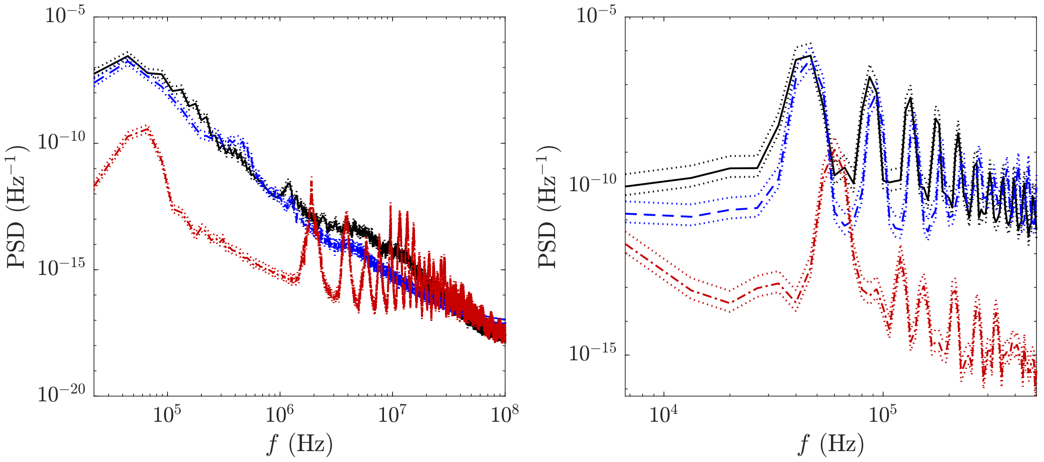

(c) 3.5N$_2$, window of $4.5 \cdot 10^{-5}$ s. (d) 3.5N$_2$, window of $1.5 \cdot 10^{-4}$ s.

Figure 6.3: Welch's PSD estimate. Detailed chemistry with WENO-UP (black solid line), tabulated chemistry (blue dashed line), and detailed chemistry with WENO (red dash-dotted line). Dotted lines indicate the 95% confidence interval for the PSD estimate.

frequencies. When the larger window is used, differences between the detailed WENO-UP and tabulated cases become evident at the low frequencies. The lowest peak frequencies from the PSD (with the larger window) are included in Table 6.1 for comparison with the frequencies estimated from Fig. 6.1. For all cases, the peak frequencies from the PSD closely match the corresponding frequencies estimated from Fig. 6.1. For 5.6N$_2$, the first peak in Fig. 6.3b corresponds to the double period; the second peak corresponds to the period between adjacent peaks. The detailed WENO case does not show the first peak frequency; this is consistent with the lack of period-doubling seen in Fig. 6.2. The tabulated case matches both peak frequencies closely, while the detailed WENO case peaks at a higher frequency.

These observations are similar for $3.5N_2$ in Fig. 6.3d. Both the detailed WENO-UP and tabulated cases match the first peak, while the detailed WENO case peaks at a higher frequency.

	detailed, WENO-UP	tabulated	detailed, WENO
$5.6N_2$			
1-period, est. (s)	$4.52 \cdot 10^{-5}$	$4.43 \cdot 10^{-5}$	$2.95 \cdot 10^{-5}$
Frequency, est. (Hz)	$2.21 \cdot 10^{4}$	$2.26 \cdot 10^{4}$	$3.39 \cdot 10^{4}$
Frequency, PSD (Hz)	$2.33 \cdot 10^{4}$	$2.33 \cdot 10^{4}$	$3.33 \cdot 10^{4}$
2-period, est. (s)	$9.09 \cdot 10^{-5}$	$8.89 \cdot 10^{-5}$	–
Frequency, est. (Hz)	$1.10 \cdot 10^{4}$	$1.12 \cdot 10^{-4}$	–
Frequency, PSD (Hz)	10^{4}	10^{4}	–
$3.5N_2$			
Period, est. (s)	$2.27 \cdot 10^{-5}$	$2.16 \cdot 10^{-5}$	$1.67 \cdot 10^{-5}$
Frequency, est. (Hz)	$4.40 \cdot 10^{4}$	$4.62 \cdot 10^{4}$	$5.99 \cdot 10^{4}$
Frequency, PSD (Hz)	$4.67 \cdot 10^{4}$	$4.67 \cdot 10^{4}$	$6 \cdot 10^{4}$

Table 6.1: Periods and frequencies estimated from the time plots (Fig. 6.1) and the PSD (Fig. 6.3). 2-period refers to the period/frequency describing the period-doubling; 1-period refers to the time between two adjacent peaks.

The results in Fig. 6.1 to 6.3 and Table 6.1 all used a grid resolution of 20 points per induction length. However, the one-dimensional instability is sensitive to the grid resolution, as excessive numerical diffusion can alter the limit cycle behavior [139]. To understand the impact of the grid resolution on the one-dimensional instability, resolutions of 10, 20, 32, 50, and 100 points per induction length were tested for the $5.6N_2$-diluted mixture.

For all three methods, 10 points per induction length is not sufficient to establish the limit cycle, and peak frequencies could not be extracted. At 20 points per induction length (shown in Fig. 6.1), detailed chemistry with standard WENO has much weaker oscillations than the other two cases. Both the detailed chemistry with WENO-UP and the tabulated chemistry cases show a period-2 limit cycle, although there are some discrepancies in the peak amplitudes. If the standard WENO scheme had been used for all detailed chemistry simulations in Chapters 4 to 5, a finer grid would be required to observe any period-doubling (in one dimension); it is also likely a finer grid would be needed to achieve the same degree of irregularity in the N_2 soot foils (in two dimensions). The WENO-UP scheme lessens the resolution requirements for detailed chemistry, as 20 points per induction length is sufficient for period-doubling. Interestingly, the tabulated chemistry simulation exhibits period-doubling at 20 points per induction length, even though the standard WENO scheme is used.

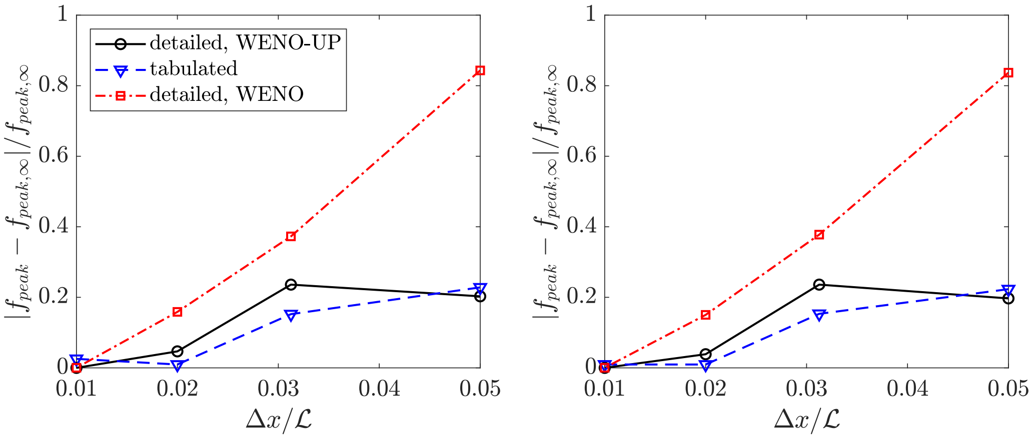

(a) Mean frequency for all peaks.

(b) Mean frequency for upper peaks.

Figure 6.4: 1D pulsating detonation ($2H_2$-O_2-$5.6N_2$) at varying grid resolutions. Detailed chemistry with WENO-UP (black solid line, circles), tabulated chemistry (blue dashed line, triangles), and detailed chemistry with standard WENO (red dash-dotted line, squares).

For resolutions of 20, 32, 50, and 100 points per induction length, the average peak frequency (between all peaks in Fig. 6.4a, and between the upper peaks in Fig. 6.4b) are extracted from the pressure-time data. (In the detailed WENO case, period-doubling does not occur until 32 points per induction length, hence the much larger errors at 20 points per induction length.) The frequency errors are computed relative to the frequencies extracted from the detailed WENO-UP case at the finest resolution, $f_{peak,\infty}$. As Δx decreases, the frequencies for all three methods generally converge towards $f_{peak,\infty}$. Going from $\Delta x = \mathcal{L}/20$ to $\mathcal{L}/32$, there is not much difference in the error for both the detailed WENO-UP and tabulated cases. While there is a large decrease in the error for the detailed WENO case, the error at $\Delta x = \mathcal{L}/32$ is still larger than both the detailed WENO-UP and tabulated errors at $\Delta x = \mathcal{L}/20$. By $\Delta x = \mathcal{L}/50$, the detailed WENO case finally shows errors below those of the detailed WENO-UP and tabulated at $\Delta x = \mathcal{L}/20$. This highlights another advantage of the tabulation approach: given the same numerical scheme (standard fifth-order WENO), a coarser grid may be used when using tabulated chemistry in place of detailed chemistry. A larger Δx allows for a larger Δt while still satisfying the CFL condition, and fewer grid points are required for a given domain. These computational cost savings are in addition to those discussed in

Sec. 5.3.5, in which the comparison used the same Δx and Δt for both chemistry models.

Summary Overall, the tabulated chemistry models reproduce a majority of the pulsating behavior observed in the detailed chemistry (WENO-UP) results, with only one degree of freedom (one progress variable, compared to nine species required for detailed chemistry). Furthermore, it does not suffer from the same numerical sensitivity to the scalar transport scheme as detailed chemistry. When the standard WENO scheme is used, the resolution requirements are less strict for tabulated chemistry than for detailed chemistry.

6.2 Detonation behavior in (C, T) space

The conditional means and standard deviations in Sec. 5.2 provided an overall assessment of the (C, T) ZND table's ability to reproduce the thermo-chemical states in a two-dimensional detonation. Such analysis may be referred as a "static" analysis. The present section expands with an investigation of the dynamic behavior in (C, T) space.

First, a detonation with a regular cell structure is examined. The numerical schlieren, temperature field, and (C, T) curves are shown for the 7Ar-diluted mixture in Fig. 6.5 and 6.6. In Fig. 6.5, four y locations are marked, corresponding to different conditions at the detonation front. As seen in the (C, T) diagram at $C = 0$, locations y_1 and y_2 are initially overdriven, y_3 is initially underdriven, and y_4 is near the CJ von Neumann state. On each horizontal cut, a specific point is marked in (x, y) coordinates (Fig. 6.5a and 6.5b) and (C, T) coordinates (Fig. 6.5c). Both the markers on y_1 and y_2 indicate the transition across a previous shock collision, going from a locally overdriven region to a decaying region at the end of a previous cell. In (C, T) space, this is seen as a sudden drop in temperature. Because y_2 is nearer the primary shock front, the drop in T is accompanied by a drop in C as the line cut goes from a hotter region with faster reactions to a cooler region with slower reactions. The line cuts y_3 and y_4 start at locally decaying regions on the detonation front; the markers indicate where a previous triple point (y_3) or transverse shock wave (y_4) is crossed, resulting in an increase in temperature. Aside from the locations where triple points or shocks are crossed, within the reaction zone up to $C = 0.06$, the (C, T) "trajectories" vary smoothly, roughly parallel to the tabulated ZND solutions.

In Fig. 6.6, three x locations are marked, corresponding to different distances from the primary shock front. Location x_1 is nearest the shock front, in the reaction

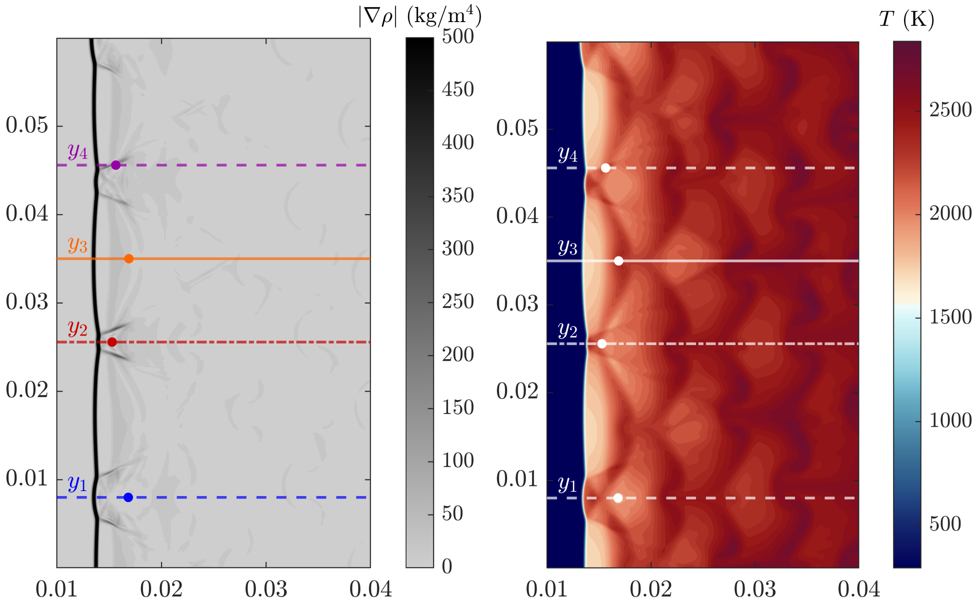

(a) Schlieren. (b) Temperature field.

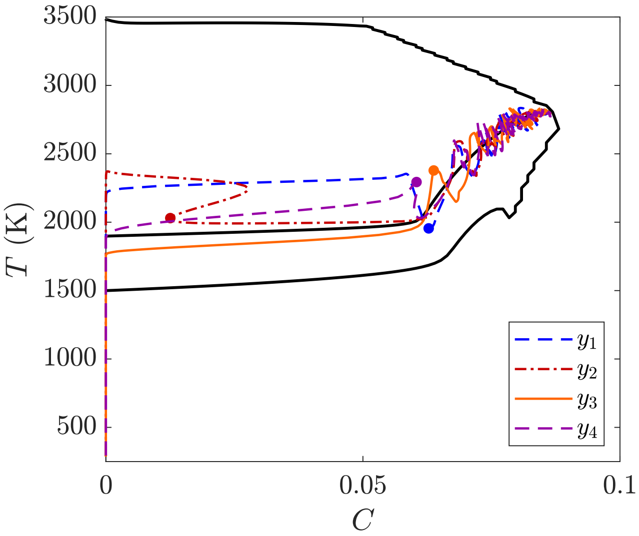

(c) Line cuts in (C, T) space.

Figure 6.5: 7Ar tabulated chemistry solution at $t = 5 \cdot 10^{-4}$ s. Horizontal cuts at four locations across the detonation front (a-b) and corresponding curves in (C, T) space (c); y_1 (blue dashed line), y_2 (red dash-dotted line), y_3 (orange solid line), and y_4 (purple dashed line). Symbols correspond to the same locations in (x, y) (a-b) and (C, T) (c) coordinates. The CJ ZND solution and the ZND boundary are indicated by the black solid lines.

zone, and therefore spans a wide range of C values in (C, T) space. Between shock collisions, this line cut varies smoothly in (C, T) space. Three points are marked on the cut at x_1. Points a and b correspond to locally overdriven portions of the detonation front; a is farther from the shock front than b, and has progressed farther

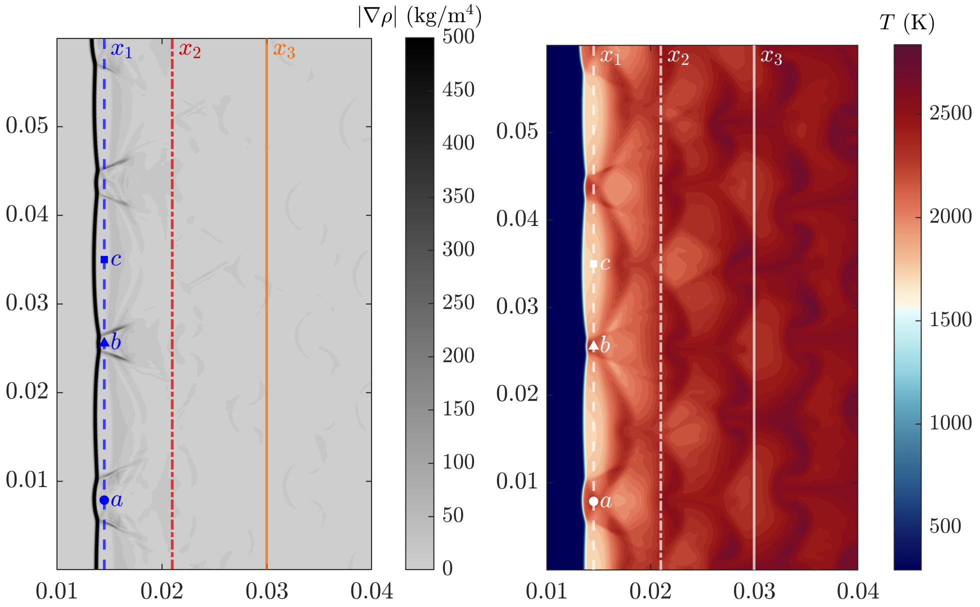

(a) Schlieren.

(b) Temperature field.

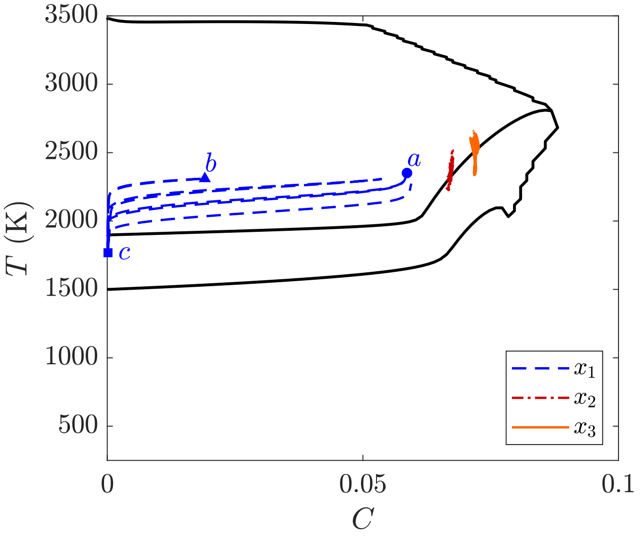

(c) Line cuts in (C, T) space.

Figure 6.6: 7Ar tabulated chemistry solution at $t = 5 \cdot 10^{-4}$ s. Vertical cuts at three locations in the wake of the detonation front (a-b) and corresponding curves in (C, T) space (c); x_1 (blue dashed line), x_2 (red dash-dotted line), and x_3 (orange solid line). Symbols/letters correspond to the same locations in (x, y) (a-b) and (C, T) (c) coordinates. The CJ ZND solution and the ZND boundary are indicated by the black solid lines.

in C. Point c corresponds to a locally underdriven portion of the detonation front, and is near $C = 0$. Locations x_2 and x_3 are in the wake past the main reaction front; in (C, T) space, there is almost no change in C, and the temperature fluctuates about the CJ ZND solution. The results in Fig. 6.6 illustrate that most of the production of C occurs over a short distance; portions of x_1 nearly reach $C = 0.06$. Beyond this main reaction zone, there is only a gradual increase in C; from x_2 to x_3, C increases by about 0.005.

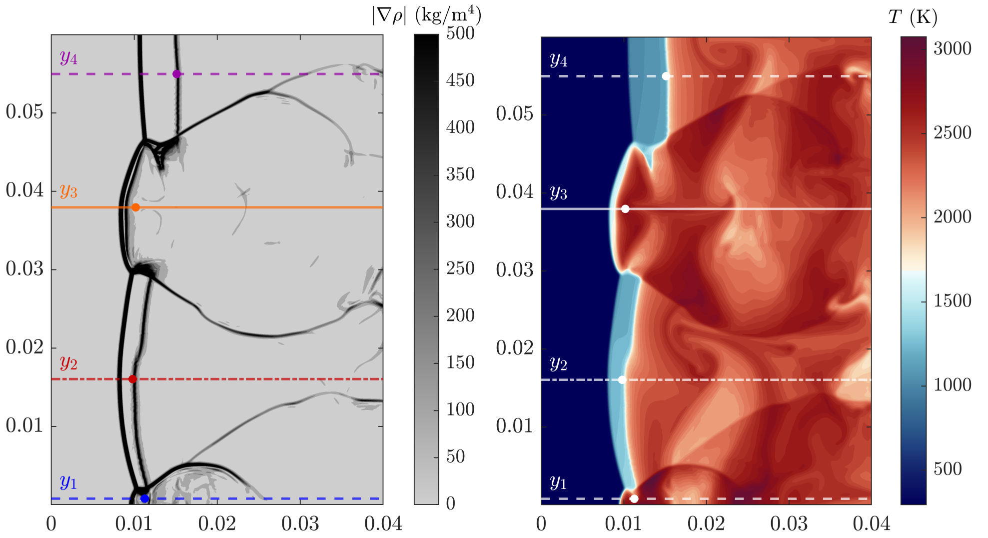

(a) Schlieren. (b) Temperature field.

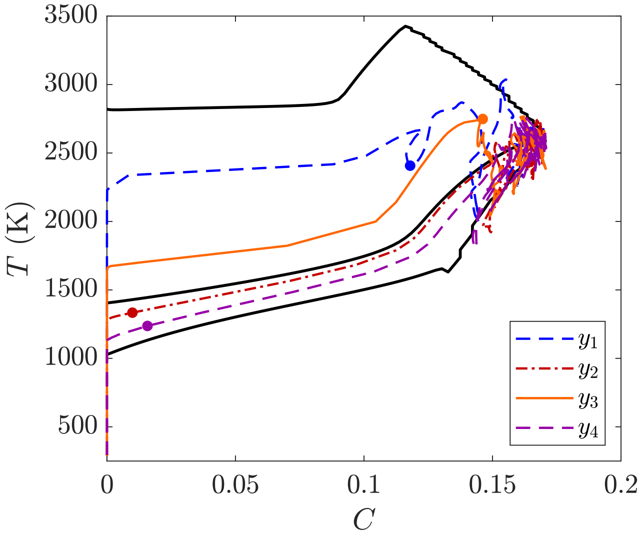

(c) Line cuts in (C, T) space.

Figure 6.7: $5.6N_2$ tabulated chemistry solution at $t = 4.7 \cdot 10^{-4}$ s. Horizontal cuts at four locations across the detonation front (a-b) and corresponding curves in (C, T) space (c); y_1 (blue dashed line), y_2 (red dash-dotted line), y_3 (orange solid line), and y_4 (purple dashed line). Symbols correspond to the same locations in (x, y) (a-b) and (C, T) (c) coordinates. The CJ ZND solution and the ZND boundary are indicated by the black solid lines.

The same analysis is performed for the $5.6N_2$-diluted mixture in Fig. 6.7 and 6.8. Once again, in Fig. 6.7, four y locations are selected and mapped onto (C, T) space.

At $C = 0$, locations y_1 and y_3 are initially overdriven, while locations y_2 and y_4 are initially underdriven. The marker on y_1 indicates a local drop in temperature as one transverse shock wave is crossed, prior to being reshocked upon crossing another shock, after which the temperature increases again. The other three line cuts have smooth (C, T) profiles for a majority of the range of C, again roughly parallel to the tabulated ZND solutions; they extend farther in C space before encountering any additional shocks. Due to variations in the detonation strength along the front, the physical distance from the shock front does not directly translate to distance in progress variable space. The markers on y_2 and y_4 indicate the end of a relatively low temperature region post-shock; despite the distance from the shock front, these points still have small values of C, as seen in (C, T) space. The marker on y_3, however, is much closer to the shock front but is near the fully burnt side of the C range.

In Fig. 6.8, three x locations are shown at different distances from the shock front, with the corresponding curves in (C, T) space. As with the 7Ar-diluted case, the cut at x_1 is nearest the front and crosses over locally over- and underdriven regions, spanning a variety of conditions in C and T. The locations farther in the wake, x_2 and x_3, primarily fluctuate in T, and show slightly more variation in C than in the 7Ar case. Four points are marked along x_1. Point a is in the vicinity of multiple shock collisions and is at both high C and T. Points b and d are in locally underdriven regions; b is past the main reaction zone, and therefore at higher C, and d is nearest the shock front, near $C = 0$. Point c is on a transverse shock between an underdriven and overdriven region; in (C, T) space, this is a turning point as the curve crosses the CJ ZND solution.

Summary The table was generated from one-dimensional steady ZND solutions. Sometimes the two-dimensional detonation structure locally resembles that of underdriven or overdriven ZND solutions, but features such as triple points are clearly not one-dimensional. Despite this, the (C, T) table is able to capture the two-dimensional and unsteady behavior.

6.3 Vorticity and the impact of SFS viscosity

The soot foils in Sec. 5.3.3 were a useful means of comparing the evolution of triple points over time of the simulation. The tabulated chemistry simulations were found to reproduce the cell structures of the detailed chemistry simulations; the argon-diluted mixtures were characterized by regular cell structures, while the

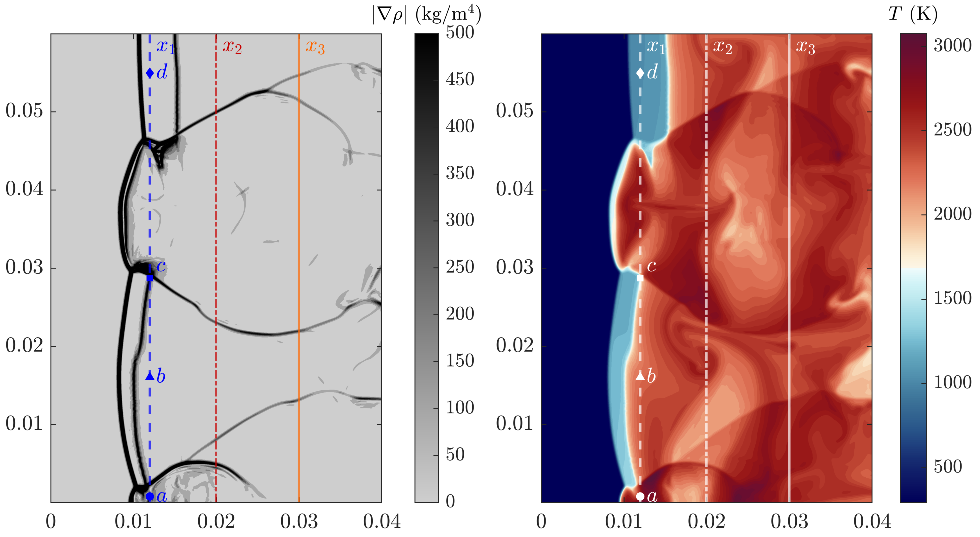

(a) Schlieren.

(b) Temperature field.

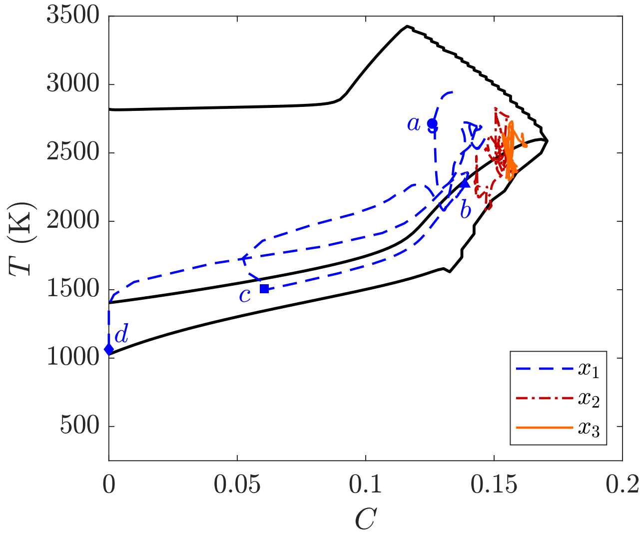

(c) Line cuts in (C, T) space.

Figure 6.8: $5.6N_2$ tabulated chemistry solution at $t = 4.7 \cdot 10^{-4}$ s. Vertical cuts at three locations in the wake of the detonation front (a-b) and corresponding curves in (C, T) space (c); x_1 (blue dashed line), x_2 (red dash-dotted line), and x_3 (orange solid line). Symbols/letters correspond to the same locations in (x, y) (a-b) and (C, T) (c) coordinates. The CJ ZND solution and the ZND boundary are indicated by the black solid lines.

nitrogen-diluted mixtures had irregular cells. Vorticity is cited as one mechanism by which soot foils are generated in experiments [117, 140]. As such, the differences in regularity can also be observed by looking at the vorticity fields. Vorticity is also a great means to investigate the impact of the numerical methods and the SFS viscosity.

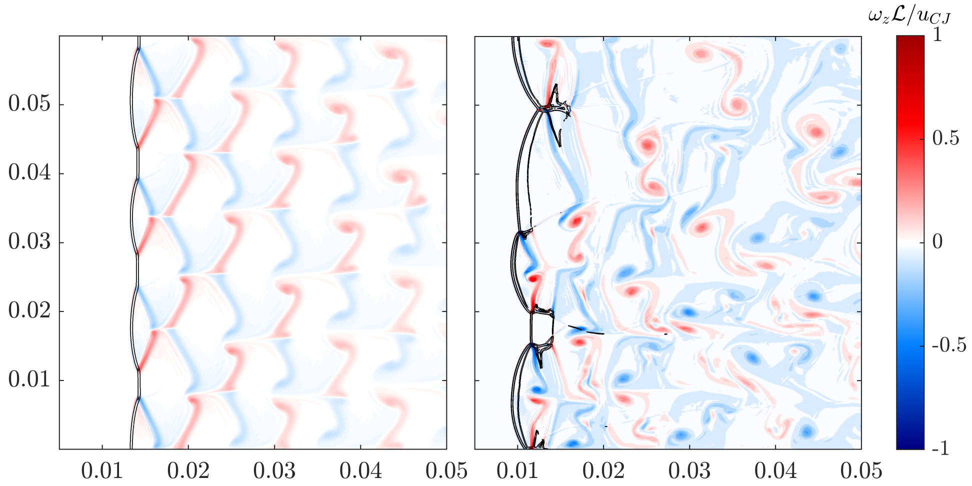

(a) 7Ar, $t = 6 \cdot 10^{-4}$ s.

(b) 3.5N$_2$, $t = 5.1 \cdot 10^{-4}$ s.

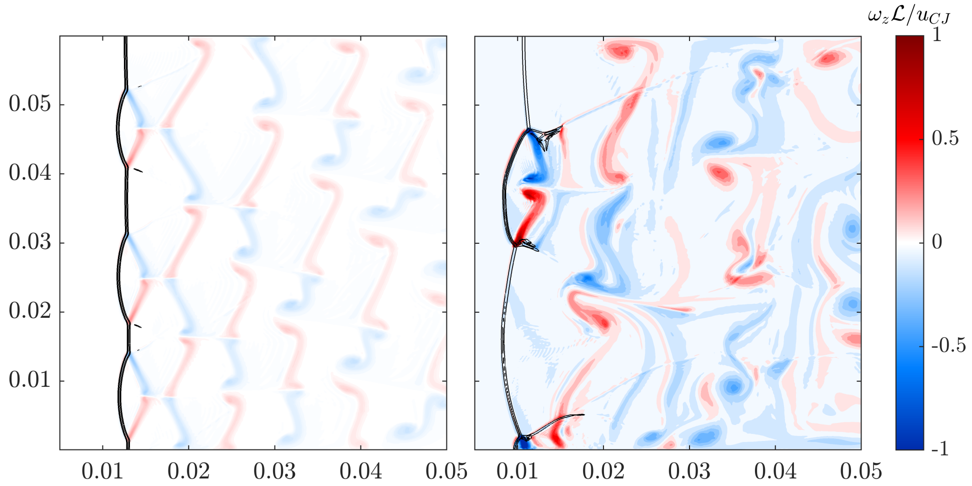

(c) 12Ar, $t = 5.5 \cdot 10^{-4}$ s.

(d) 5.6N$_2$, $t = 4.7 \cdot 10^{-4}$ s.

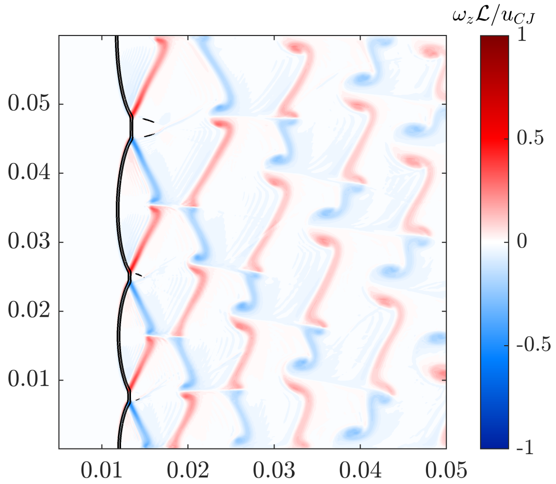

(e) 17Ar, $t = 5.4 \cdot 10^{-4}$ s.

Figure 6.9: Vorticity field for regular (a, c, e) and irregular (b, d) detonations. Isocontours of $|\nabla\rho|$ indicate the shock front (black solid lines).

Representative instantaneous vorticity fields for each of the mixtures are shown in Fig. 6.9. Vorticity is generated at the detonation front through mechanisms including triple point collisions and baroclinic torque [117, 140–142] and is then advected downstream. For the argon-diluted mixtures, these vortical structures are fairly uniform, consistent with the regular cell structure observed in the soot foils. There is some loss in the symmetry of the vortices downstream; because the soot foils track the maximum pressure at the primary shock front/triple point collisions, this loss of symmetry in the wake was not observed in Fig. 5.19. In contrast, the nitrogen-diluted mixtures exhibit a more chaotic vorticity field; the sizes of the vortices and the spacing between neighboring vortices vary throughout the wake.

To compare the magnitude of vorticity generated between different mixtures, the vorticity, ω_z, was non-dimensionalized as $\omega_z \mathcal{L}/u_{CJ}$, where $\mathcal{L}$ and u_{CJ} are specific to the mixture. The induction zone length and the CJ speed are relevant length and velocity scales at the detonation front; because vorticity is generated just behind the detonation front, these quantities are natural choices for normalization. The non-dimensional vorticity fields in Fig. 6.9 illustrate that the nitrogen-diluted mixtures experience relatively higher vorticity magnitudes immediately behind the detonation front.

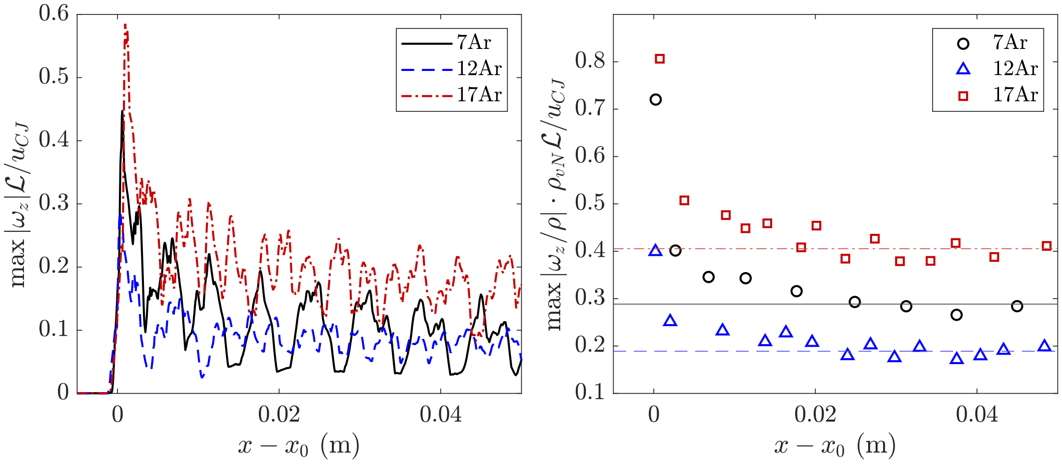

(a) Unscaled vorticity magnitude.

(b) Density-scaled vorticity magnitude.

Figure 6.10: Maximum vorticity magnitude vs. distance from the detonation front, corresponding to the time snapshots in Fig. 6.9; diluted with 7Ar (black solid line/circles), 12Ar (blue dashed line/triangles), and 17Ar (red dash-dotted line/squares). Horizontal lines in (b) show the average of local peaks between $x - x_0 = 0.02$ and 0.05 m.

The evolution of the vorticity in the wake of the detonation front can be quantified by looking at the maximum vorticity magnitude in Fig. 6.10a for the argon-diluted cases. As in Fig. 6.9, the induction length and CJ speed are used for non-dimensionalization to compare across mixtures. At the shock ($x = x_0$), there is a peak in vorticity for all mixtures. In the wake, the vorticity shows several local peaks corresponding to the vortical structures advecting downstream. The magnitudes of the peaks decrease gradually with distance from the shock front, indicating a decay of vorticity. However, it is important to account for the decrease in the density through the wake of the detonation. In the absence of vortex stretching, baroclinic torque, viscous diffusion, and body forces, the vorticity transport equation simplifies to

$$\frac{D(\omega_z/\rho)}{Dt} = 0, \tag{6.1}$$

suggesting that ω_z/ρ, not ω_z, should be conserved as vortices are advected downstream. Figure 6.10b shows the maximum magnitude of vorticity scaled by the density. After an initial drop in vorticity immediately after the shock front (where the vorticity is generated), by about 0.02 m into the wake, the density-scaled vorticity fluctuates around a steady value. This evolution is a direct consequence of the numerical and mathematical framework used. The numerical formulation (described in Sec. 2.2) discretely conserves kinetic energy; as such, the numerical scheme does not introduce artificial viscosity and should have minimal impact on the decay of vorticity in the wake.

Vorticity may still be impacted by physical viscosity and the SFS terms. In Sec. 2.6.2, it was observed that the velocity gradients due to vortical structures could lead to nonzero SFS viscosity. Given the vorticity generation at the detonation front, and the propagation of vortices throughout the wake, it is important to consider the SFS viscosity again here and contrast it to the physical viscosity. Using the same snapshots from Fig. 6.9 for the 7Ar- and 5.6N_2-diluted mixtures, the SFS shear viscosity is shown in Fig. 6.11. As expected, the largest SFS viscosity is at the primary shock front, followed by the transverse shocks. The magnitudes of SFS and physical viscosity are compared along horizontal line cuts in Fig. 6.11c and 6.11d. Across the primary shock, the SFS viscosity is about two orders of magnitude larger than the physical viscosity. In the wake for the 7Ar-diluted case, the physical viscosity is larger than the SFS for a majority of the domain. For the 5.6N_2-diluted case, due to the stronger transverse waves, there are some locations in the wake where the SFS viscosity exceeds the physical viscosity. Taken together, the results in Fig. 6.10b and 6.11 demonstrate that the SFS viscosity has minimal impact on the vorticity field in the wake.

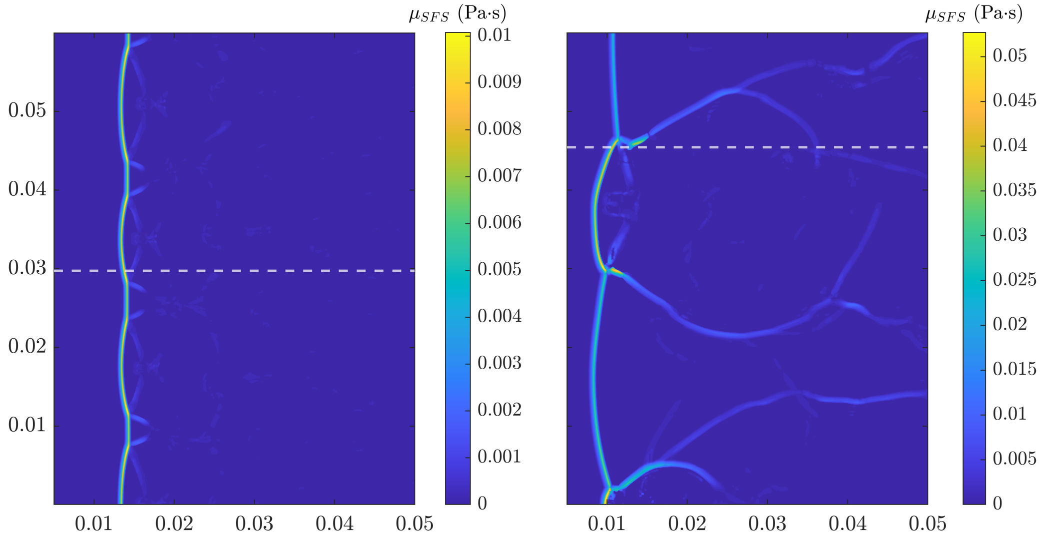

(a) 7Ar, $6 \cdot 10^{-4}$ s.

(b) 5.6N_2, $4.7 \cdot 10^{-4}$ s.

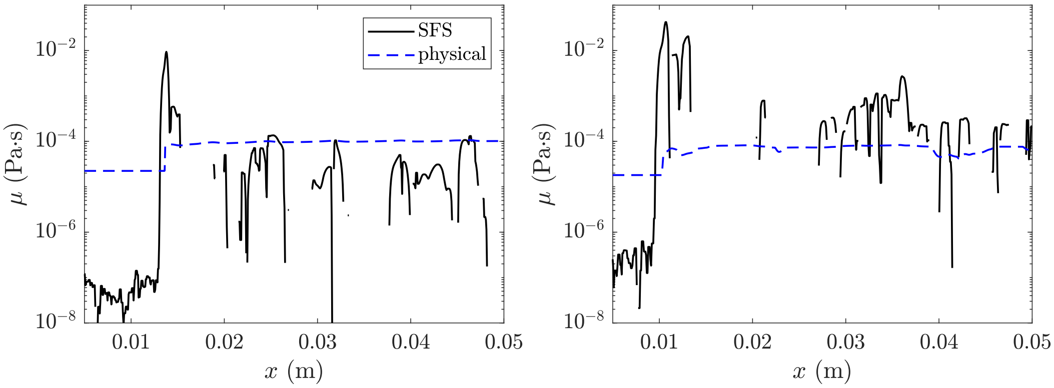

(c) 7Ar, .

(d) 5.6N_2, $y = 0.045$ m.

Figure 6.11: SFS shear viscosity in the detonation. Comparison to physical viscosity along the horizontal cuts (marked in white dashed lines on the contour plots); SFS viscosity (black solid line), and physical viscosity (blue dashed line). Discontinuities in the SFS viscosity correspond to regions where the SFS terms are zero.

Summary The detonation simulations in this thesis are idealized, propagating in two-dimensional channels. In practical configurations, the flow is three-dimensional and turbulent. As such, it is important to assess the impact of the numerical framework on vorticity. This analysis is intended as a first step towards future work to understand detonation-turbulence interactions.

Chapter 7

CONCLUSIONS AND FUTURE WORK

This thesis focused on developing methods to address challenges in detonation simulations. Methods that are able to balance numerical stability, physical accuracy, and computational efficiency are essential for predictive modeling in applications including safety and propulsion. To enable numerically stable simulations of shocks and contact discontinuities, a mathematical framework was developed and demonstrated in a central finite difference code. Chemistry modeling was investigated first by improving the physical accuracy of detailed chemistry species transport, and second by developing a tabulated chemistry model to reduce the cost of simulations.

7.1 Numerical stability of shocks and contact discontinuities

Chapters 2 and 3 established a simulation framework to ensure the numerical stability of shocks and other discontinuities. To perform stable simulations involving shocks, the Euler equations were spatially-filtered, resulting in SFS terms in the momentum, energy, and species equations that required closure. For a contact discontinuity, these SFS terms were found to be zero for all equations. Using analytical expressions for a normal shock, a nonzero SFS term was derived for the momentum equation. This term resembles previously used artificial viscosity, and in multiple dimensions, acts as a combination of dynamic and bulk viscosity. Conservation of total enthalpy across the shock resulted in no SFS term for the energy equation. An alternative closure model for the energy equation led to a SFS conduction term and a SFS viscous dissipation term. As chemical reactions do not occur over the thickness of the shock, no SFS terms were required for the species equation.

The SFS terms were implemented within a conservative, centered difference numerical framework. The normal shock test cases were numerically stable for the full range of Mach numbers tested, and the filtered shock thickness was independent of Mach number for moderate and strong shocks. Cell-to-cell oscillations were prevented for a large range of shock Mach numbers. The one-dimensional formulation was also validated for more complex configurations, including the Shu-Osher test problem. The ZND detonation demonstrated both the accuracy and stability of this approach when applied to reacting flows with shocks. The extension to multiple dimensions was demonstrated for supersonic flow over a forward facing step, shock diffraction over a corner, and blunt-body flow. The implementation of the SFS terms is similar to that of the LAD approach, the main difference being how the terms are derived/constructed. Unlike hybrid WENO schemes, using SFS (or LAD) does not require modifying the underlying discretization of the solver. For example, this thesis uses a kinetic-energy conserving scheme throughout the domain; only the magnitude of the SFS terms varies depending on the local flow conditions.

To treat numerical oscillations that arise at contact discontinuities, a WENO-like deferred correction term was included for the enthalpy flux. The numerical treatment of contact discontinuities was demonstrated for the Sod shock tube problem, as well as other temperature and species discontinuities. In Chapter 6, the impact of the SFS viscosity on the structure of two-dimensional detonations was examined, with particular focus on the diffusion of vorticity.

In practical applications, shock waves are not isolated but interact with other flow phenomena, including turbulence. For example, in accidental explosions, turbulent flames may transition to detonation. Simulations intended to predict, and thus help prevent, such explosions must be able to model both turbulence and shocks accurately. Because the SFS terms were derived analytically, they are general and may be implemented within any numerical framework, including codes designed for high fidelity turbulence simulations.

7.2 Chemistry modeling for detonations

The existing approaches to modeling the chemistry in detonations often require either the oversimplification of the chemical processes or prohibitive computational costs. The most accurate approach, detailed chemistry, has additional numerical challenges associated with species transport. When nonlinear transport schemes are used, there is no guarantee that physical constraints on the species mass fractions are satisfied. In Chapter 4, a procedure was introduced to ensure that the sum of mass fractions equals 1. In addition to conserving inert species, this approach resulted in a more pronounced physical instability for detonations in nitrogen-diluted mixtures.

To reduce the cost of chemistry without neglecting the physics, tabulated chemistry has been used with much success for a variety of flame simulations. Originally developed for low Mach combustion, there have been recent extensions of the method to compressible reacting flows. However, the majority of supersonic combustion tabulation has been for non-premixed configurations and relied on flamelets for table generation, which is not applicable to detonation burning.

Chapter 5 presented a tabulation approach for detonations. A two-dimensional chemistry table was constructed, using a progress variable and temperature as the inputs. Conditional statistics of the detailed chemistry data indicated that these two coordinates are able to capture at least 95% of the variations in the source term observed in two-dimensional detonations. To ensure ignition can occur, the progress variable consisted of both the combustion product, H_2O, as well as an intermediate species formed by the initiation reactions, HO_2. Rather than using flamelets to generate the table, as in low Mach chemistry tables, one-dimensional ZND detonations were used. Comparison of the conditional mean of the progress variable source term with the tabulated source term demonstrated that the ZND model is preferred over other one-dimensional model problems (i.e., ignitions), introducing at most a 7% error.

Both a priori and a posteriori analysis showed promising results for the tabulation framework for one- and two-dimensional detonation simulations. In one dimension, the tabulation was able to reproduce unsteady behavior including initiating a detonation with a shock. For two-dimensional channel propagation, the detailed and tabulated chemistry simulations produced similar detonation dynamics for both regular and irregular H_2-O_2 mixtures. Even for the simplest fuel, hydrogen, the total computational cost was reduced by about 4 times. This reduction was mainly due to costs associated with the scalar transport and combustion, which were reduced by factors of 9 and 17, respectively. These computational savings are expected to increase for larger detailed mechanisms. In Chapter 6, the impact of both the chemistry model and scalar transport on the physical limit cycle of unstable mixtures was investigated. To further understand the performance of the tabulated chemistry model, the evolution of two-dimensional detonations in thermo-chemical space was analyzed.

The computational cost of detailed chemistry often leads to the use of simplified chemical models in large scale detonation simulations. The continued development of tabulated chemistry models will improve the accuracy of practical simulations at low cost, which will aid in applications such as engine design.

7.3 Future work

The tabulated chemistry model introduced in Chapter 5 showed promising results for two-dimensional hydrogen detonations. To improve upon the methodology, there are a few areas that require future work:

- The numerical implementation of the chemistry table may be further optimized. The sensitivity of results to the table resolution, both in C and T coordinates, as well as the number of ZND solutions used to precompute to table, should be studied. The table lookup currently uses a bilinear interpolation in C and T; other interpolation methods should be considered.
- Additional detonation behavior such as detonation diffraction [65, 143] or quenching [19] should be compared across chemistry models. This has particular relevance to both safety and propulsion applications.
- The tabulated chemistry model should be validated against experiments, not only detailed chemistry simulation data. Such comparisons will require three-dimensional simulations, with channel dimensions and boundary conditions matching that of the comparison experiments.

The tabulation approach should also be expanded to include additional physics:

- Chemistry tables should be developed and validated for hydrocarbon fuels; some details of the current model are specific to hydrogen combustion, such as the definition of the progress variable and the tabulation of $\dot{\omega}_C/\rho^2$. A similar strategy for defining the progress variable is anticipated for hydrocarbon fuels; in addition to using major/minor product species [81], future work will identify the key radicals which influence the induction zone. In addition to their relevance to propulsion applications, hydrocarbons have larger detailed chemistry mechanisms and therefore would benefit from greater computational savings through tabulation.
- Thermal nonequilibrium effects have been suggested to have an impact on the detonation structure [18, 53]. Tabulated chemistry is an ideal modeling framework for incorporating these effects with minimal increase to the computational cost.
- As tabulated chemistry has proven useful for both flames and detonations separately, the possibility of chemistry tabulation for deflagration-to-detonation transition should be explored. This is relevant for predictive modeling to prevent accidental explosions.

There are two main areas of future work related to the filtering framework developed in Chapter 2-3:

- Three-dimensional detonations with turbulence should be investigated. First, the impact of the SFS viscosity on turbulence must be studied; modifications to the numerical implementation of the SFS terms may be required to prevent artificially early dissipation of turbulence. Then, the modeling framework may be used to study detonation-turbulence interactions.

- The impact of the filtering framework on the chemistry modeling should be explored. This could enable detonation simulations at coarser grid resolutions to further reduce the computational cost. A preliminary analysis is presented in Appendix A.

Appendix A

FILTERED TABULATED CHEMISTRY MODELS

This appendix presents an early investigation of the impact of spatial filtering on the chemistry modeling for detonations. In the filtering procedure in Sec. 2.1, it is assumed that the filter width, Δ, is much smaller than the chemical length scales; for detonations, $\Delta \ll \mathcal{L}$. Under this assumption, the shock can be filtered without impacting the reaction zone. However, if the filter width approaches the induction zone length, additional SFS terms may be required. The impact of the filtering on the chemistry will be discussed here in the context of tabulated chemistry.

The SFS terms in the progress variable transport equation are discussed in Sec. A.1. An a priori analysis of the filtering effects is presented in Sec. A.2, and modeling implications are discussed.

A.1 Analytical framework

Making no assumptions about the closure for the SFS terms, the filtered progress variable transport equation is

$$\frac{\partial(\overline{\rho}\tilde{C})}{\partial t} + \frac{\partial(\overline{\rho}\tilde{u}_i\tilde{C})}{\partial x_i} = \frac{\partial \overline{j}_i}{\partial x_i} + \frac{\partial j_{i,SFS}}{\partial x_i} + \overline{\dot{\omega}}_C, \tag{A.1}$$

where the SFS diffusion flux is

$$j_{i,SFS} = \overline{\rho}\tilde{u}_i\tilde{C} - \overline{\rho u_i C}. \tag{A.2}$$

Assuming there are no reactions taking place within the filtered shock, both ρu and C are constant across the shock, such that $j_{i,SFS} = 0$, and the source term is unaffected by the filtering, $\overline{\dot{\omega}}_C \approx \dot{\omega}_C$. This was the assumption made for the species transport equation (see Eq. (2.71)).

If the filtered shock thickness is comparable to the chemical length scales, C is no longer constant across the filtered shock, and therefore $j_{i,SFS} \neq 0$. Additionally, the effect on the progress variable source term is non-negligible, $\overline{\dot{\omega}}_C \neq \dot{\omega}_C$. Unfortunately, there is no analytical closure that may be derived for these terms. An a priori analysis of the effects of filtering on these terms will be conducted in the following section. For the tabulated chemistry approach, only two terms require closure ($j_{i,SFS}$ and $\overline{\dot{\omega}}_C$). In the detailed chemistry framework, closing the SFS terms would be impractical due to the number of species and reactions involved.

A.2 A priori analysis

The following a priori analysis relies on the $2H_2$-O_2-7Ar detonation case in Sec. 4.5.

A.2.1 One-dimensional detonation

First, the one-dimensional ZND solution for the CJ detonation is filtered with a Gaussian filter based on a fraction of the induction zone length: $\Delta = \mathcal{L}/10$, $\Delta = \mathcal{L}/5$, and $\Delta = \mathcal{L}/2$. The temperature and progress variable profiles are shown in Fig. A.1. As the filter width increases, the shock and reaction zone are no longer distinct regions; for $\Delta = \mathcal{L}/2$, the temperature continually increases without a thermally-neutral period, and the progress variable increases inside the shock. The convective SFS terms resulting from the filtered solutions are shown in Fig. A.2. As expected, the magnitude of the SFS term increases with the filter width. For the smaller filter widths, the term is negative in the reaction zone and zero elsewhere. For the larger filter width ($\Delta = \mathcal{L}/2$), there is also a positive SFS through the shock. Neglecting the SFS due to the shock itself, the convective SFS is similar for the momentum and energy equations. Analogous to the SFS viscosity and conductivity used in the momentum and energy equations, this convective SFS term could be tabulated in terms of a progress variable diffusivity to be added to the physical diffusivity, D.

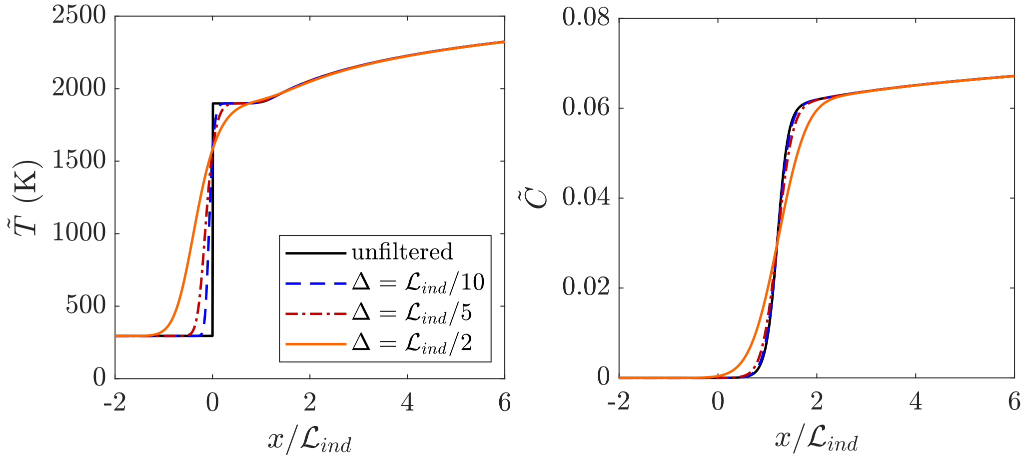

(a) Temperature.

(b) Progress variable.

Figure A.1: One-dimensional detonation; unfiltered (black solid line), filtered with $\Delta = \mathcal{L}/10$ (blue dashed line), $\Delta = \mathcal{L}/5$ (red dash-dotted line), and $\Delta = \mathcal{L}/2$ (orange solid line).

The budget for the filtered progress variable equation is shown in Fig. A.3 for two filter widths. The convective term and the source term dominate the budget, while the convective SFS term is small even for the larger filter width. This suggests that

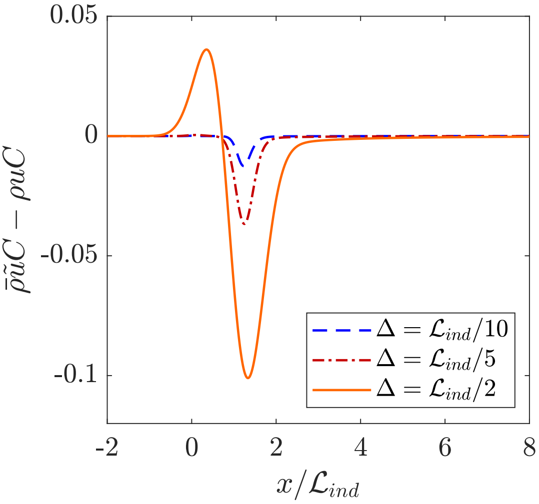

Figure A.2: Convective SFS flux for a one-dimensional detonation filtered with $\Delta = \mathcal{L}/10$ (blue dashed line), $\Delta = \mathcal{L}/5$ (red dash-dotted line), and $\Delta = \mathcal{L}/2$ (orange solid line).

the convective SFS term may be neglected with minimal impact on the progress variable transport. Similarly, any SFS due to the reaction zone may be neglected in the momentum and energy equations; the SFS terms computed for the shock are sufficient.

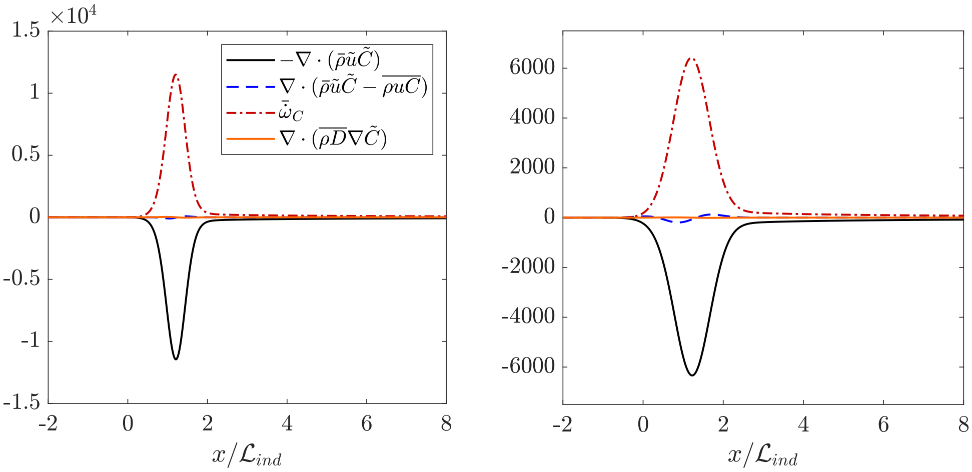

(a) $\Delta = \mathcal{L}/5$.

(b) $\Delta = \mathcal{L}/2$.

Figure A.3: Filtered progress variable equation budget for a one-dimensional detonation; convective term (black solid line), convective SFS term (blue dashed line), source term (red dash-dotted line), and diffusion term (orange solid line).

The filtered source term requires further discussion. Figure A.4 shows the filtered source term both in physical space and in progress variable space. As the filter width increases, the peak source term decreases and the width of the source term peak increases. For $\Delta = \mathcal{L}/2$, there is non-negligible source term within the shock. These substantial effects on the progress variable source term indicate that the filtering must be accounted for when tabulating the source term.

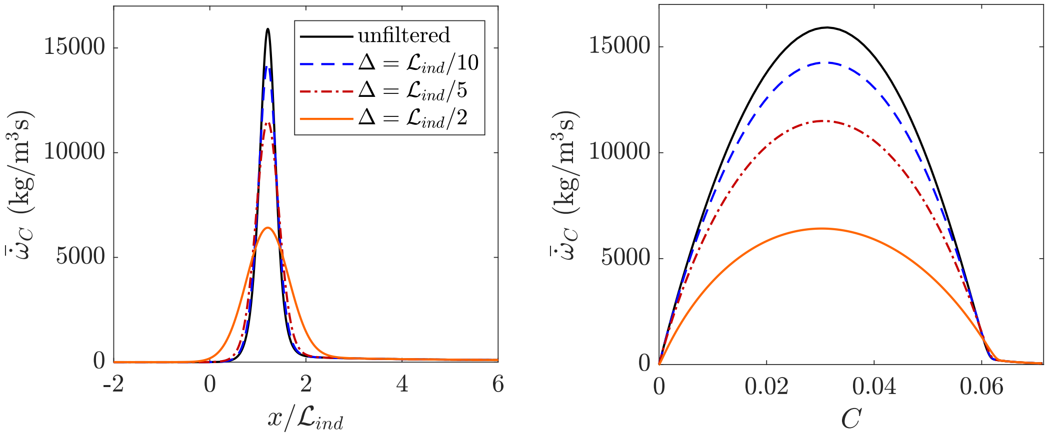

(a) Physical space.

(b) Progress variable space.

Figure A.4: Progress variable source term for a one-dimensional detonation; unfiltered (black solid line), filtered with $\Delta = \mathcal{L}/10$ (blue dashed line), $\Delta = \mathcal{L}/5$ (red dash-dotted line), and $\Delta = \mathcal{L}/2$ (orange solid line).

A.2.2 Two-dimensional detonation

In the previous section, the progress variable budget analysis indicated that the convective SFS term may be neglected, whereas the filtering of the source term must be included in the tabulation. The data from Sec. 4.5 will now be used to assess these assumptions in two-dimensional detonations.

The instantaneous convective term and source term fields are shown in Fig. A.5 before and after filtering the data with $\Delta = \mathcal{L}/2$. Qualitatively, the filtered fields resemble the unfiltered fields; the filtered source term is spread over a thicker region along the detonation front. The corresponding convective SFS field is shown in Fig. A.6a, and is nonzero in the lead shock and reaction zone.

Three y locations (indicated by the dashed lines in Fig. A.5 and A.6a) are examined in more detail for the budget analysis in Fig. A.6. Locations y_1 (Fig A.6b) and y_3 (Fig. A.6d) correspond to triple points on the primary detonation front, while y_2 (Fig. A.6c) is mid-way between triple points. At the triple points, the source term is the dominant term in the budget, followed by the convective term. Away from the triple points, the convective term is the largest in magnitude, followed

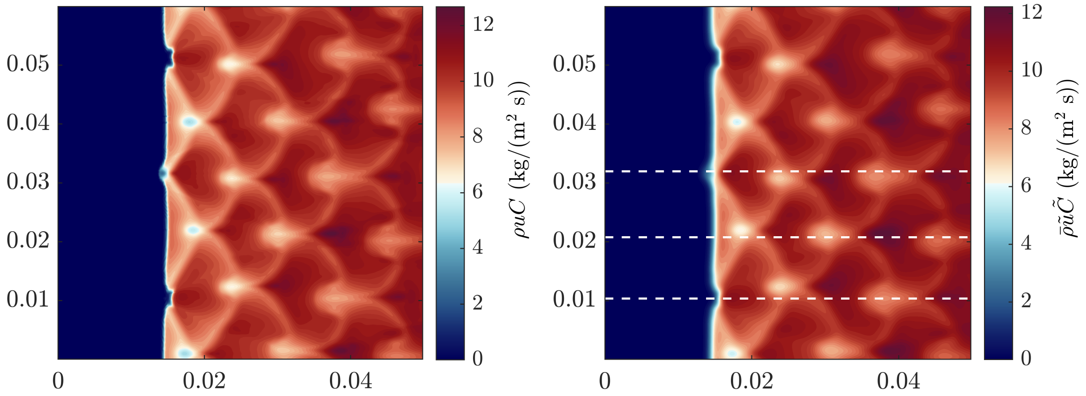

(a) Unfiltered convective term.

(b) Filtered convective term.

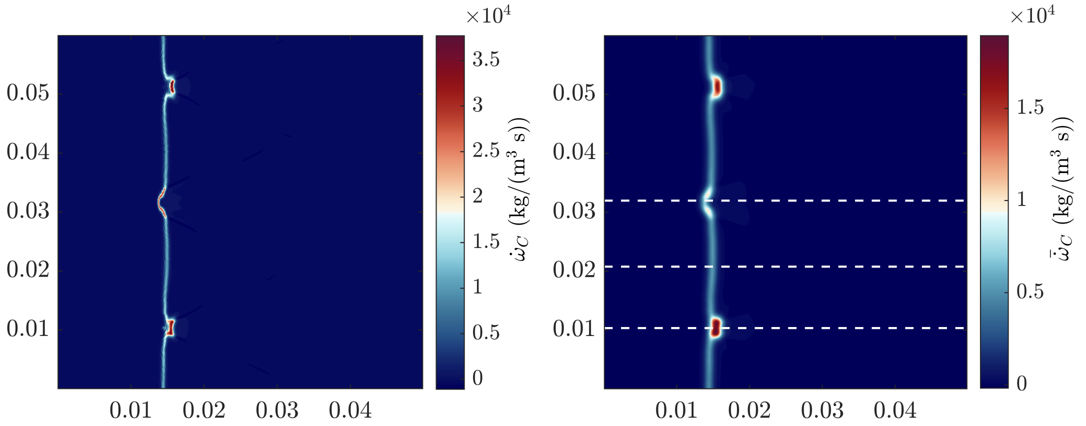

(c) Unfiltered source term.

(d) Filtered source term.

Figure A.5: Impact of filtering on a two-dimensional detonation, with $\Delta = \mathcal{L}/2$. White dashed lines correspond to the budget locations used in Fig. A.6.

by the source term. For all three locations, the convective SFS term is relatively small. The contribution of the unsteady term is not shown in the budget plots; this contribution expected to compensate for the imbalance between the source term and the convective term.

Although the two-dimensional detonation involves numerous shock collisions and transverse waves downstream of the primary shock front, the convective SFS for the progress variable does not have a major contribution to the overall budget. Therefore, as an initial attempt, the filtered tabulation model does not need to include an SFS progress variable diffusivity.

The conditional mean progress variable source term (conditioned on C) in Fig. A.7a shows a similar trend to that seen for the one-dimensional case in Fig. A.4. To quantify the impact of the filter width on the source term, the reduction in the peak

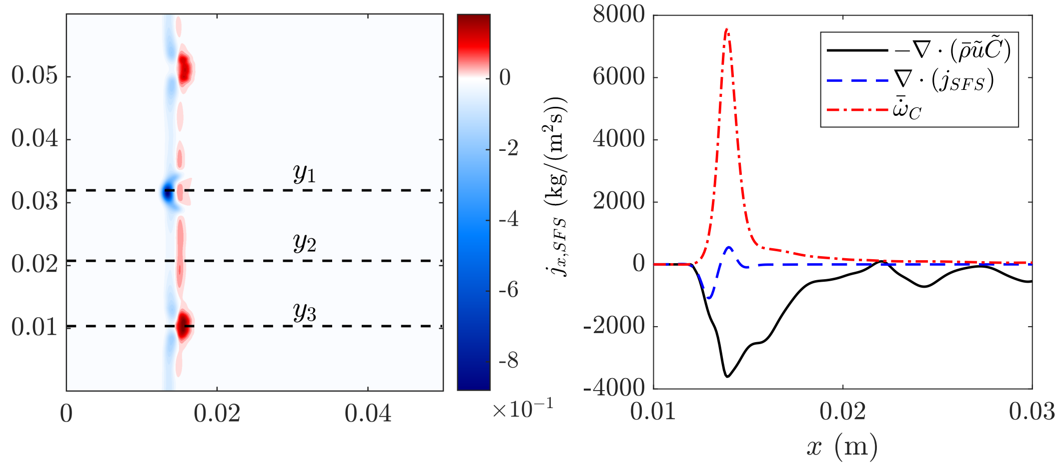

(a) Convective SFS term.

(b) Budget along y_1.

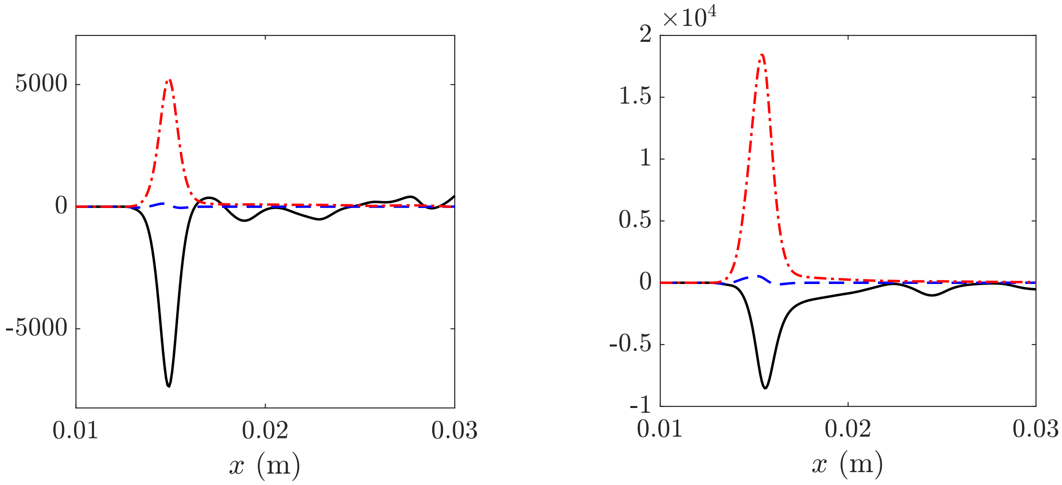

(c) Budget along y_2.

(d) Budget along y_3.

Figure A.6: Two-dimensional convective SFS term (a) and progress variable equation budget (b-d) along the y locations marked by the black dashed lines in (a). Convective term (black solid line), convective SFS term (blue dashed line), and source term (red dash-dotted line).

is computed as

$$f = \max\{\overline{\dot{\omega}}_C\}/\max\{\dot{\omega}_C\}. \tag{A.3}$$

The reduction factor f is shown in Fig. A.7b as a function of the filter width. For one-dimensional cases, f is based on the peak values from the ZND solution. For the two-dimensional case, f is evaluated using the peak values from the conditional mean, as well as the local values along the three y locations used for the budget analysis. Both the induction zone length, $\mathcal{L}$, and the width at half the max $\dot{\omega}_C$, δ, were considered as relevant length scales for normalizing the filter width. Normalization by δ resulted in a better collapse of the computed f values for the different cases.

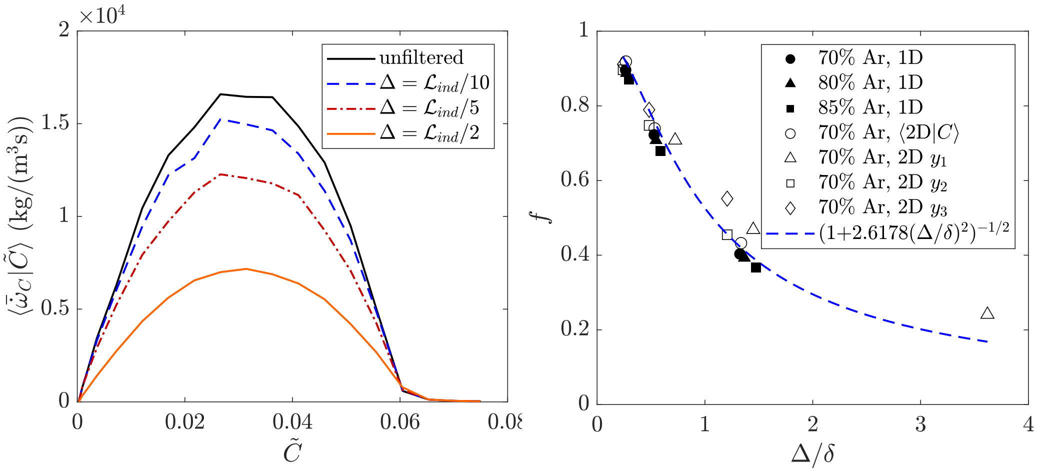

(a) Conditional mean source term.

(b) Peak source term reduction.

Figure A.7: Impact of filtering on the progress variable source term. Conditional mean source term from the two-dimensional 7Ar-diluted detonation (a); unfiltered (black solid line), filtered with $\Delta = \mathcal{L}/10$ (blue dashed line), $\Delta = \mathcal{L}/5$ (red dash-dotted line), and $\Delta = \mathcal{L}/2$ (orange solid line). (b) Reduction in peak source term due to filtering, $f = \max\{\dot{\omega}_C\}/\max\{\bar{\dot{\omega}}_C\}$ for different Ar-diluted mixtures in 1D and 2D (conditional mean).

BIBLIOGRAPHY

[1] F. Barthelemy et al. *Accident on the 21st of September 2001 at a factory belonging to the Grande Paroisse Company in Toulouse*. Tech. rep. IGE/01/034. Ministry for Regional Development and the Environment, 2001.

[2] K. Anzai et al. "Fukushima Daiichi Nuclear Power Plant accident: facts, environmental contamination, possible biological effects, and countermeasures". In: *Journal of clinical biochemistry and nutrition* 50.1 (2011), pp. 2–8.

[3] M. Santora. "Czech Coal Mine Explosion Kills at Least 13". In: *New York Times* (2018).

[4] Y. Luo, D. Wang, and J. Cheng. "Effects of rock dusting in preventing and reducing intensity of coal mine explosions". In: *International Journal of Coal Science & Technology* 4 (2017), pp. 102–109.

[5] K. Kailasanath. "Recent developments in the research on rotating-detonation-wave engines". In: *55th AIAA Aerospace sciences meeting*. 2017, p. 0784.

[6] B. A. Rankin et al. "Overview of performance, application, and analysis of rotating detonation engine technologies". In: *Journal of Propulsion and Power* 33.1 (2017), pp. 131–143.

[7] G. D. Roy et al. "Pulse detonation propulsion: challenges, current status, and future perspective". In: *Progress in Energy and Combustion Science* 30.6 (2004), pp. 545–672.

[8] E. S. Oran and V. N. Gamezo. "Origins of the deflagration-to-detonation transition in gas-phase combustion". In: *Combustion and Flame* 148.1-2 (2007), pp. 4–47.

[9] V. N. Gamezo, C. L. Bachman, and E. S. Oran. "Flame acceleration and DDT in large-scale obstructed channels filled with methane-air mixtures". In: *Proceedings of the Combustion Institute* 38.3 (2021), pp. 3521–3528.

[10] D. Schwer and K. Kailasanath. "Numerical investigation of rotating detonation engines". In: *46th AIAA/ASME/SAE/ASEE Joint Propulsion Conference & Exhibit*. 2010, p. 6880.

[11] J. Kindracki, P. Wolański, and Z. Gut. "Experimental research on the rotating detonation in gaseous fuels–oxygen mixtures". In: *Shock waves* 21 (2011), pp. 75–84.

[12] W. A. Hargus, S. A. Schumaker, and E. J. Paulson. "Air force research laboratory rotating detonation rocket engine development". In: *2018 joint propulsion conference*. 2018, p. 4876.

[13] Y. B. Zel'dovich. "On the theory of the propagation of detonation in gaseous systems". In: *Zh. eksp. teoret. fiz.* 10 (1940), pp. 542–568.

[14] J. von Neumann. "Theory of detonation waves". In: *John von Neumann, collected works* 6 (1942), pp. 203–218.

[15] W. Döring. "Über den detonationsvorgang in gasen". In: *Annalen der Physik* 435.6-7 (1943), pp. 421–436.

[16] D. L. Chapman. "VI. On the rate of explosion in gases". In: *The London, Edinburgh, and Dublin Philosophical Magazine and Journal of Science* 47.284 (1899), pp. 90–104.

[17] E. Jouguet. "Sur la propagation des réactions chimiques dans les gaz". In: *J. Maths. Pure Appl.* 7 (1905), p. 347.

[18] B. Taylor et al. "Numerical simulations of hydrogen detonations with detailed chemical kinetics". In: *Proceedings of the combustion Institute* 34.2 (2013), pp. 2009–2016.

[19] S. Taileb, J. Melguizo-Gavilanes, and A. Chinnayya. "Influence of the chemical modeling on the quenching limits of gaseous detonation waves confined by an inert layer". In: *Combustion and Flame* 218 (2020), pp. 247–259.

[20] C.-W. Shu and S. Osher. "Efficient implementation of essentially non-oscillatory shock-capturing schemes". In: *Journal of Computational Physics* 77.2 (1988), pp. 439–471.

[21] G.-S. Jiang and C.-W. Shu. "Efficient implementation of weighted ENO schemes". In: *Journal of Computational Physics* 126.1 (1996), pp. 202–228.

[22] E. Johnsen et al. "Assessment of high-resolution methods for numerical simulations of compressible turbulence with shock waves". In: *Journal of Computational Physics* 229.4 (2010), pp. 1213–1237.

[23] D. J. Hill and D. I. Pullin. "Hybrid tuned center-difference-WENO method for large eddy simulations in the presence of strong shocks". In: *Journal of Computational Physics* 194.2 (2004), pp. 435–450.

[24] B. Stevens and T. Colonius. "Enhancement of shock-capturing methods via machine learning". In: *Theoretical and Computational Fluid Dynamics* 34.4 (2020), pp. 483–496.

[25] C.-W. Shu and S. Osher. "Efficient implementation of essentially non-oscillatory shock-capturing schemes, II". In: *Journal of computational physics* 83.1 (1989), pp. 32–78.

[26] A. Harten. "The artificial compression method for computation of shocks and contact discontinuities. III. Self-adjusting hybrid schemes". In: *Mathematics of Computation* 32.142 (1978), pp. 363–389.

[27] H. Yang. “An artificial compression method for ENO schemes: the slope modification method”. In: *Journal of Computational Physics* 89.1 (1990), pp. 125–160.

[28] Z. Xu and C.-W. Shu. “Anti-diffusive flux corrections for high order finite difference WENO schemes”. In: *Journal of Computational Physics* 205.2 (2005), pp. 458–485.

[29] J. VonNeumann and R. D. Richtmyer. “A method for the numerical calculation of hydrodynamic shocks”. In: *Journal of Applied Physics* 21.3 (1950), pp. 232–237.

[30] A. W. Cook and W. H. Cabot. “A high-wavenumber viscosity for high-resolution numerical methods”. In: *Journal of Computational Physics* 195.2 (2004), pp. 594–601.

[31] B. Fiorina and S. K. Lele. “An artificial nonlinear diffusivity method for supersonic reacting flows with shocks”. In: *Journal of Computational Physics* 222.1 (2007), pp. 246–264.

[32] A. W. Cook. “Artificial fluid properties for large-eddy simulation of compressible turbulent mixing”. In: *Physics of Fluids* 19.5 (2007), p. 055103.

[33] S. Kawai and S. K. Lele. “Localized artificial diffusivity scheme for discontinuity capturing on curvilinear meshes”. In: *Journal of Computational Physics* 227.22 (2008), pp. 9498–9526.

[34] A. Mani, J. Larsson, and P. Moin. “Suitability of artificial bulk viscosity for large-eddy simulation of turbulent flows with shocks”. In: *Journal of Computational Physics* 228.19 (2009), pp. 7368–7374.

[35] S. Kawai, S. K. Shankar, and S. K. Lele. “Assessment of localized artificial diffusivity scheme for large-eddy simulation of compressible turbulent flows”. In: *Journal of Computational Physics* 229.5 (2010), pp. 1739–1762.

[36] C. Y. Lee and S. K. Lele. “Localized artificial diffusivity scheme for deflagrations and detonation waves”. In: *Computers & Fluids* 159 (2017), pp. 33–52.

[37] S. Premasuthan, C. Liang, and A. Jameson. “Computation of flows with shocks using the spectral difference method with artificial viscosity, I: basic formulation and application”. In: *Computers & Fluids* 98 (2014), pp. 111–121.

[38] S. Premasuthan, C. Liang, and A. Jameson. “Computation of flows with shocks using the spectral difference method with artificial viscosity, II: modified formulation with local mesh refinement”. In: *Computers & Fluids* 98 (2014), pp. 122–133.

[39] T. Haga and S. Kawai. “On a robust and accurate localized artificial diffusivity scheme for the high-order flux-reconstruction method”. In: *Journal of Computational Physics* 376 (2019), pp. 534–563.

[40] A. Leonard. “Energy cascade in large-eddy simulations of turbulent fluid flows”. In: *Advances in Geophysics*. Vol. 18. Elsevier, 1975, pp. 237–248.

[41] S. B. Pope and S. B. Pope. *Turbulent flows*. Cambridge University Press, 2000.

[42] N. A. Adams and S. Stolz. “A subgrid-scale deconvolution approach for shock capturing”. In: *Journal of Computational Physics* 178.2 (2002), pp. 391–426.

[43] N. A. Adams. “The use of LES subgrid-scale models for shock capturing”. In: *International journal for numerical methods in fluids* 39.9 (2002), pp. 783–797.

[44] V. C. Sousa and C. Scalo. “A unified Quasi-Spectral Viscosity (QSV) approach to shock capturing and large-eddy simulation”. In: *Journal of Computational Physics* 459 (2022), p. 111139.

[45] V. C. Sousa and C. Scalo. “A Legendre spectral viscosity (LSV) method applied to shock capturing for high-order flux reconstruction schemes”. In: *Journal of Computational Physics* 460 (2022), p. 111157.

[46] B. P. Leonard. “A stable and accurate convective modelling procedure based on quadratic upstream interpolation”. In: *Computer methods in applied mechanics and engineering* 19.1 (1979), pp. 59–98.

[47] H. Liu et al. “Numerical study of combustion effects on the development of supersonic turbulent mixing layer flows with WENO schemes”. In: *Computers & Fluids* 189 (2019), pp. 82–93.

[48] F. De Vuyst et al. “A geometrically accurate low-diffusive conservative interface capturing method suitable for multimaterial flows”. In: *Computers & Fluids* 227 (2021), p. 104897.

[49] S. Jaouen and F. Lagoutière. “Numerical transport of an arbitrary number of components”. In: *Computer methods in applied mechanics and engineering* 196.33-34 (2007), pp. 3127–3140.

[50] M. Ancellin, B. Després, and S. Jaouen. “Extension of generic two-component VOF interface advection schemes to an arbitrary number of components”. In: *Journal of Computational Physics* 473 (2023), p. 111721.

[51] E. S. Oran et al. “A numerical study of a two-dimensional H2-O2-Ar detonation using a detailed chemical reaction model”. In: *Combustion and Flame* 113.1-2 (1998), pp. 147–163.

[52] L. Shi et al. “Assessment of vibrational non-equilibrium effect on detonation cell size”. In: *Combustion Science and Technology* 189.5 (2017), pp. 841–853.

[53] J. Vargas et al. “Development of a steady detonation reactor with state-to-state thermochemical modeling”. In: *Shock Waves* 32.8 (2022), pp. 679–689.

[54] Z. Hong, D. F. Davidson, and R. K. Hanson. “An improved H2/O2 mechanism based on recent shock tube/laser absorption measurements”. In: *Combustion and Flame* 158.4 (2011), pp. 633–644.

[55] B. Savard, B. Bobbitt, and G. Blanquart. “Structure of a high Karlovitz n-C7H16 premixed turbulent flame”. In: *Proceedings of the Combustion Institute* 35.2 (2015), pp. 1377–1384.

[56] G. Blanquart, P. Pepiot-Desjardins, and H. Pitsch. “Chemical mechanism for high temperature combustion of engine relevant fuels with emphasis on soot precursors”. In: *Combustion and Flame* 156.3 (2009), pp. 588–607.

[57] G. Dong, B. Fan, and Y. Chen. “Acceleration of chemistry computations in two-dimensional detonation induced by shock focusing using reduced ISAT”. In: *Combustion Theory and Modelling* 11.5 (2007), pp. 823–837.

[58] J. Wu, G. Dong, and B. Li. “Parallel chemistry acceleration algorithms based on ISAT method in gaseous detonation computations”. In: *Computers & Fluids* 167 (2018), pp. 265–284.

[59] W. Fickett and W. W. Wood. “Flow calculations for pulsating one-dimensional detonations”. In: *Physics of Fluids* 9.5 (1966), pp. 903–916.

[60] C. L. Mader. “One-and two-dimensional flow calculations of the reaction zones of ideal gas, nitromethane, and liquid TNT detonations”. In: *Symposium (International) on Combustion*. Vol. 12. 1969, pp. 701–710.

[61] T. Jin et al. “Simulations of cellular detonation interaction with turbulent flows”. In: *AIAA Journal* 54.2 (2016), pp. 419–433.

[62] C. R. Kaplan, A. Özgen, and E. S. Oran. “Chemical-diffusive models for flame acceleration and transition-to-detonation: genetic algorithm and optimisation procedure”. In: *Combustion Theory and Modelling* 23.1 (2019), pp. 67–86.

[63] X. Lu, C. R. Kaplan, and E. S. Oran. “A chemical-diffusive model for simulating detonative combustion with constrained detonation cell sizes”. In: *Combustion and Flame* 230 (2021), p. 111417.

[64] X. Lu, C. R. Kaplan, and E. S. Oran. “Predictions of flame acceleration, transition to detonation, and detonation propagation using the Chemical-Diffusive Model”. In: *Combustion and Flame* 235 (2022), p. 111705.

[65] M. Peswani and B. Maxwell. “Detonation wave diffraction in stoichiometric C2H4/O2 mixtures using a global four-step combustion model”. In: *Physics of Fluids* 34.10 (2022), p. 106104.

[66] E. Oran et al. “Numerical simulations of detonations in hydrogen-air and methane-air mixtures”. In: *Symposium (International) on Combustion*. Vol. 18. 1. Elsevier. 1981, pp. 1641–1649.

[67] K. Kailasanath et al. “Determination of detonation cell size and the role of transverse waves in two-dimensional detonations”. In: *Combustion and Flame* 61.3 (1985), pp. 199–209.

[68] S. Taki and T. Fujiwara. “Numerical simulation of triple shock behavior of gaseous detonation”. In: *Symposium (International) on Combustion*. Vol. 18. 1. Elsevier. 1981, pp. 1671–1681.

[69] E. S. Oran, D. A. Jones, and M. Sichel. “Numerical simulations of detonation transmission”. In: *P. R. Soc. A.* 436.1897 (1992), pp. 267–297.

[70] M. Lefebvre et al. “The influence of the heat capacity and diluent on detonation structure”. In: *Combustion and Flame* 95.1-2 (1993), pp. 206–218.

[71] M. e. Sichel et al. “A two–step kinetics model for numerical simulation of explosions and detonations in H2–O2 mixtures”. In: *P. R. Soc. A.* 458.2017 (2002), pp. 49–82.

[72] G. J. Sharpe and M. Short. “Detonation ignition from a temperature gradient for a two-step chain-branching kinetics model”. In: *Journal of Fluid Mechanics* 476 (2003), pp. 267–292.

[73] J. Li et al. “Numerical simulations of cellular detonation diffraction in a stable gaseous mixture”. In: *Propuls. Power Res.* 5.3 (2016), pp. 177–183.

[74] P. Yang et al. “Effects of inflow Mach number on oblique detonation initiation with a two-step induction-reaction kinetic model”. In: *Combustion and Flame* 193 (2018), pp. 246–256.

[75] B. Varatharajan et al. “Two-step chemical-kinetic descriptions for hydrocarbon–oxygen-diluent ignition and detonation applications”. In: *Proceedings of the Combustion Institute* 30.2 (2005), pp. 1869–1877.

[76] F. Veiga-Lopez, L. M. Faria, and J. Melguizo-Gavilanes. “Influence of chemistry on the steady solutions of hydrogen gaseous detonations with friction losses”. In: *Combustion and Flame* 240 (2022), p. 112050.

[77] G. Floring, M. Peswani, and B. Maxwell. “On the role of transverse detonation waves in the re-establishment of attenuated detonations in methane–oxygen”. In: *Combustion and Flame* 247 (2023), p. 112497.

[78] C. D. Pierce and P. Moin. “Progress-variable approach for large-eddy simulation of non-premixed turbulent combustion”. In: *Journal of Fluid Mechanics* 504 (2004), pp. 73–97.

[79] E. Knudsen and H. Pitsch. “A general flamelet transformation useful for distinguishing between premixed and non-premixed modes of combustion”. In: *Combustion and Flame* 156.3 (2009), pp. 678–696.

[80] J. Schlup and G. Blanquart. “Reproducing curvature effects due to differential diffusion in tabulated chemistry for premixed flames”. In: *Proceedings of the Combustion Institute* 37.2 (2019), pp. 2511–2518.

[81] S. K. Menon, P. A. Boettcher, and G. Blanquart. “Enthalpy based approach to capture heat transfer effects in premixed combustion”. In: *Combustion and Flame* 160.7 (2013), pp. 1242–1253.

[82] M. Oevermann. “Numerical investigation of turbulent hydrogen combustion in a SCRAMJET using flamelet modeling”. In: *Aerospace Science and Technology* 4.7 (2000), pp. 463–480.

[83] R. Vicquelin et al. “Coupling tabulated chemistry with compressible CFD solvers”. In: *Proceedings of the Combustion Institute* 33.1 (2011), pp. 1481–1488.

[84] A. Saghafian, V. E. Terrapon, and H. Pitsch. “An efficient flamelet-based combustion model for compressible flows”. In: *Combustion and Flame* 162.3 (2015), pp. 652–667.

[85] E. Cisneros–Garibay and M. E. Mueller. “Consistent Coupling of Compressibility Effects in Manifold-Based Models for Supersonic Combustion”. In: *AIAA Journal* 62.2 (2024), pp. 590–601.

[86] H. Zhang, Y. Chen, and Y. Lv. “Development and validation of a combustion large-eddy-simulation solver based on fully compressible formulation and tabulated chemistry”. In: *Aerospace Science and Technology* 127 (2022), p. 107693.

[87] A. Saghafian et al. “Large eddy simulations of the HIFiRE scramjet using a compressible flamelet/progress variable approach”. In: *Proceedings of the Combustion Institute* 35.2 (2015), pp. 2163–2172.

[88] Z. Gao, C. Jiang, and C.-H. Lee. “Representative interactive flamelet model and flamelet/progress variable model for supersonic combustion flows”. In: *Proceedings of the Combustion Institute* 36.2 (2017), pp. 2937–2946.

[89] L. Shunn et al. “GPU-Accelerated High-Fidelity Rotating Detonation Engine Simulations Using an Extended Flamelet Progress Variable Approach”. In: *Turbo Expo: Power for Land, Sea, and Air*. Vol. 86953. American Society of Mechanical Engineers. 2023, V03AT04A031.

[90] A. Favre. “Turbulence: Space-time statistical properties and behavior in supersonic flows”. In: *The Physics of fluids* 26.10 (1983), pp. 2851–2863.

[91] B. Vreman, B. Geurts, and H. Kuerten. “Large-eddy simulation of the turbulent mixing layer”. In: *Journal of Fluid Mechanics* 339 (1997), pp. 357–390.

[92] G. Sidharth and G. V. Candler. “Subgrid-scale effects in compressible variable-density decaying turbulence”. In: *Journal of Fluid Mechanics* 846 (2018), pp. 428–459.

[93] M. D. Salas and A. Iollo. "Entropy jump across an inviscid shock wave". In: *Theoretical and computational fluid dynamics* 8.5 (1996), pp. 365–375.

[94] G. Beardsell and G. Blanquart. "A cost-effective semi-implicit method for the time integration of fully compressible reacting flows with stiff chemistry". In: *Journal of Computational Physics* 414 (2020), p. 109479.

[95] O. Desjardins et al. "High order conservative finite difference scheme for variable density low Mach number turbulent flows". In: *Journal of Computational Physics* 227.15 (2008), pp. 7125–7159.

[96] T. J. Poinsot and S. Lele. "Boundary conditions for direct simulations of compressible viscous flows". In: *Journal of Computational Physics* 101.1 (1992), pp. 104–129.

[97] C. S. Yoo et al. "Characteristic boundary conditions for direct simulations of turbulent counterflow flames". In: *Combustion Theory and Modelling* 9.4 (2005), pp. 617–646.

[98] F. Ismail and P. L. Roe. "Affordable, entropy-consistent Euler flux functions II: Entropy production at shocks". In: *Journal of Computational Physics* 228.15 (2009), pp. 5410–5436.

[99] H. W. Liepmann and A. Roshko. *Elements of gasdynamics*. Courier Corporation, 2001.

[100] A. W. Cook and W. H. Cabot. "Hyperviscosity for shock-turbulence interactions". In: *Journal of Computational Physics* 203.2 (2005), pp. 379–385.

[101] B. Engquist and B. Sjögreen. "The convergence rate of finite difference schemes in the presence of shocks". In: *SIAM journal on numerical analysis* 35.6 (1998), pp. 2464–2485.

[102] S. Browne, J. Ziegler, and J. Shepherd. "Numerical solution methods for shock and detonation jump conditions". In: *GALCIT report FM2006* 6 (2008), p. 90.

[103] D. G. Goodwin et al. *Cantera: An Object-oriented Software Toolkit for Chemical Kinetics, Thermodynamics, and Transport Processes*. `https://www.cantera.org`. Version 2.5.1. 2021. DOI: `10.5281/zenodo.4527812`.

[104] P. Woodward and P. Colella. "The numerical simulation of two-dimensional fluid flow with strong shocks". In: *Journal of Computational Physics* 54.1 (1984), pp. 115–173.

[105] S. Simon and J. Mandal. "A simple cure for numerical shock instability in the HLLC Riemann solver". In: *Journal of Computational Physics* 378 (2019), pp. 477–496.

[106] J. J. Quirk. "A contribution to the great Riemann solver debate". In: *Upwind and High-Resolution Schemes*. Springer, 1997, pp. 550–569.

[107] H. Tang. “On the sonic point glitch”. In: *Journal of Computational Physics* 202.2 (2005), pp. 507–532.

[108] G. A. Sod. “A survey of several finite difference methods for systems of nonlinear hyperbolic conservation laws”. In: *Journal of Computational Physics* 27.1 (1978), pp. 1–31.

[109] B. Fryxell and F. Timmes. *Exact Riemann Solver*. `http://cococubed.asu.edu/code\_pages/exact\_riemann.shtml`. 2021.

[110] R. Anderson et al. “High-order local maximum principle preserving (MPP) discontinuous Galerkin finite element method for the transport equation”. In: *Journal of Computational Physics* 334 (2017), pp. 102–124.

[111] Z. Hong et al. “On the rate constants of OH+ HO2 and HO2+ HO2: A comprehensive study of H2O2 thermal decomposition using multi-species laser absorption”. In: *Proceedings of the Combustion Institute* 34.1 (2013), pp. 565–571.

[112] K.-Y. Lam, D. F. Davidson, and R. K. Hanson. “A shock tube study of H2+ OH$\rightarrow$ H2O+ H using OH laser absorption”. In: *International Journal of Chemical Kinetics* 45.6 (2013), pp. 363–373.

[113] J. M. Austin. *The role of instability in gaseous detonation*. California Institute of Technology, 2003.

[114] N. Tsuboi, S. Katoh, and A. K. Hayashi. “Three-dimensional numerical simulation for hydrogen/air detonation: Rectangular and diagonal structures”. In: *Proceedings of the Combustion Institute* 29.2 (2002), pp. 2783–2788.

[115] V. Deledicque and M. V. Papalexandris. “Computational study of three-dimensional gaseous detonation structures”. In: *Combustion and Flame* 144.4 (2006), pp. 821–837.

[116] S. Taileb, J. Melguizo-Gavilanes, and A. Chinnayya. “The influence of the equation of state on the cellular structure of gaseous detonations”. In: *Physics of Fluids* 33.3 (2021), p. 036105.

[117] J. H. Lee. *The detonation phenomenon*. Cambridge University Press, 2008.

[118] B. J. McBride. *NASA Glenn coefficients for calculating thermodynamic properties of individual species*. National Aeronautics and Space Administration, John H. Glenn Research Center, 2002.

[119] J. Van Oijen, R. Bastiaans, and L. De Goey. “Low-dimensional manifolds in direct numerical simulations of premixed turbulent flames”. In: *Proceedings of the Combustion Institute* 31.1 (2007), pp. 1377–1384.

[120] Z. Liang et al. “Detonation front structure and the competition for radicals”. In: *Proceedings of the Combustion Institute* 31.2 (2007), pp. 2445–2453.

[121] S. Desai et al. “Effects of non-thermal termolecular reactions on wedge-induced oblique detonation waves”. In: *Combustion and Flame* 257 (2023), p. 112681.

[122] J. S. Salinas et al. “Non-thermal termolecular reactions effects on hydrogen-air planar detonation”. In: *AIAA SCITECH 2024 Forum*. 2024, p. 2783.

[123] S. Ramachandran and S. Yang. “Micro-jetting and Transverse Waves in Oblique Detonations”. In: *Combustion and Flame* 265 (2024), p. 113506.

[124] H. Pitsch. *FlameMaster: A C++ computer program for 0D combustion and 1D laminar flame calculations*. `https://www.itv.rwth-aachen.de/downloads/flamemaster/`.

[125] N. Peters. “Fifteen lectures on laminar and turbulent combustion”. In: *Ercoftac summer school* 1428 (1992), p. 245.

[126] J. J. Erpenbeck. “Stability of idealized one-reaction detonations”. In: *The Physics of Fluids* 7.5 (1964), pp. 684–696.

[127] H. Lee and D. S. Stewart. “Calculation of linear detonation instability: one-dimensional instability of plane detonation”. In: *Journal of Fluid Mechanics* 216 (1990), pp. 103–132.

[128] L. He and J. H. Lee. “The dynamical limit of one-dimensional detonations”. In: *Physics of Fluids* 7.5 (1995), pp. 1151–1158.

[129] G. Sharpe. “Linear stability of idealized detonations”. In: *Proceedings of the Royal Society of London. Series A: Mathematical, Physical and Engineering Sciences* 453.1967 (1997), pp. 2603–2625.

[130] M. Short and D. S. Stewart. “Cellular detonation stability. Part 1. A normal-mode linear analysis”. In: *Journal of Fluid Mechanics* 368 (1998), pp. 229–262.

[131] P. Hwang et al. “Numerical resolution of pulsating detonation waves”. In: *Combustion Theory and Modelling* 4.3 (2000), p. 217.

[132] G. Sharpe and S. Falle. “Numerical simulations of pulsating detonations: I. Nonlinear stability of steady detonations”. In: *Combustion Theory and Modelling* 4.4 (2000), p. 557.

[133] H. Ng et al. “Nonlinear dynamics and chaos analysis of one-dimensional pulsating detonations”. In: *Combustion Theory and Modelling* 9.1 (2005), pp. 159–170.

[134] A. K. Henrick, T. D. Aslam, and J. M. Powers. “Simulations of pulsating one-dimensional detonations with true fifth order accuracy”. In: *Journal of Computational Physics* 213.1 (2006), pp. 311–329.

[135] M. Short and J. J. Quirk. “On the nonlinear stability and detonability limit of a detonation wave for a model three-step chain-branching reaction”. In: *Journal of Fluid Mechanics* 339 (1997), pp. 89–119.

[136] M. Short and G. J. Sharpe. “Pulsating instability of detonations with a two-step chain-branching reaction model: theory and numerics”. In: *Combustion Theory and Modelling* 7.2 (2003), p. 401.

[137] F. N. Egolfopoulos et al. “Advances and challenges in laminar flame experiments and implications for combustion chemistry”. In: *Progress in Energy and Combustion Science* 43 (2014), pp. 36–67.

[138] A. Bourlioux, A. J. Majda, and V. Roytburd. “Theoretical and numerical structure for unstable one-dimensional detonations”. In: *SIAM Journal on Applied Mathematics* 51.2 (1991), pp. 303–343.

[139] C. Romick, T. D. Aslam, and J. Powers. “The effect of diffusion on the dynamics of unsteady detonations”. In: *Journal of Fluid Mechanics* 699 (2012), pp. 453–464.

[140] A. Bourlioux and A. J. Majda. “Theoretical and numerical structure for unstable two-dimensional detonations”. In: *Combustion and Flame* 90.3-4 (1992), pp. 211–229.

[141] D. N. Williams, L. Bauwens, and E. S. Oran. “Detailed structure and propagation of three-dimensional detonations”. In: *Symposium (International) on Combustion*. Vol. 26. 2. Elsevier. 1996, pp. 2991–2998.

[142] J. Lee. “The propagation mechanism of cellular detonation”. In: *Shock Waves: Proceedings of the 24th International Symposium on Shock Waves Beijing, China July 11–16, 2004*. Springer. 2005, pp. 19–30.

[143] J. Melguizo-Gavilanes et al. “Dynamics of detonation transmission and propagation in a curved chamber: a numerical and experimental analysis”. In: *Combustion and Flame* 223 (2021), pp. 460–473.